

**EXPERIMENTAL STUDIES OF ZINC OXIDE
AND SILICA PEPTIDE INTERACTIONS**

ANNA SOLÀ RABADÀ

A thesis submitted in partial fulfilment of the requirements of Nottingham
Trent University for the degree of Doctor of Philosophy

January 2016

This work is the intellectual property of the author. You may copy up to 5% of this work for private study, or personal, non-commercial research. Any re-use of the information contained within this document should be fully referenced, quoting the author, title, university, degree level and pagination. Queries or requests for any other use, or if a more substantial copy is required, should be directed in the owner of the Intellectual Property Rights.

Abstract

In nature, mineral-forming organisms achieve outstanding control over the assembly and properties of minerals. Understanding interactions during biomolecule-mediated synthesis is key to addressing the challenges that arise when designing new materials and synthesizing superior nanostructures, especially under aqueous conditions. The studies of peptide-mineral interactions presented in this thesis aimed to identify the peptide-surface affinity and its binding mechanism(s) as well as the effect of peptides on mineral formation by *in vitro* studies. The minerals; crystalline zinc oxide (ZnO) and amorphous silica (SiO₂) and their specific binding peptides identified by phage display were chosen for this investigation.

Firstly, the growth of ZnO was investigated via a hydrothermal synthesis route. Product formation, precipitation processes and phase transformation was then compared in the presence of two peptides; EAHVMHKVAPRP (EM-12, a ZnO-binding peptide) and its mutant EAHVCHKVAPRP (EC-12). Both peptides affected the crystal formation process; however, their effect and mechanism of interaction was shown to follow different pathways. X-Ray Photoelectron Spectroscopy (XPS) revealed that the peptide EC-12 interacted with the Zn²⁺ species in the solid phase through the thiol group (from cysteine). This interaction caused a drastic change in the mineral morphology with sphere-like ZnO crystals being formed. In contrast, the delay and/or suppression of ZnO formation in the presence of the EM-12 peptide was shown to be not due to peptide-mineral interactions (proved by XPS) and, instead, interactions with Zn²⁺ species in solution were proposed. As ZnO properties and applications are directly related with its morphology, these outcomes can be applied for the design of advanced material.

For silica, the effect of particle size and surface chemistry on peptide binding response was studied, with specific emphasis on the effect of level of functionalization on binding. Exhaustive characterisation of the silica surfaces, particularly by XPS, was crucial for knowledge of the chemistry and topography of the solid surface under study; and thus, to understand their impact on peptide adsorption. Peptide interactions at the aqueous interface were influenced by the surface chemistry and by the extent of functionalization where a 'switch' of peptide adsorption behaviour was observed. These new insights into silica-peptide interactions may facilitate the synthesis of novel organic/inorganic nanocomposite materials for biomedical applications.

Dedication

To my husband, parents and sister, for your endless love, encouragement and support.

“Life isn’t about finding yourself, life is about creating yourself”

George Bernard Shaw.

Acknowledgements

First, my most sincere thanks to Professor Carole C. Perry for her helpful advice, guidance and encouragement over the years. Also special thanks to Dr David J. Belton for the valuable discussions we have shared since I arrived at the Nottingham Trent University. I am very grateful to the US Air Force Office of Scientific Research (AFOSR) for funding FA9550-13-1-0040.

Extra thanks to those who have somehow contributed to this thesis, specially, Dr Graham Hickman for his assistance on mass spectrometry, Jasmine Almond (undergraduate researcher) for the synthesis of micro-scaled silica particles and their functionalization, Martin Roe from University of Nottingham for XPS data collection and Dr Marion Limo for the time spent together comparing our mineral studies.

I would also like to thank all members of the Biomolecular and Materials Interface Group with whom I always shared great time, past and present, Dr Valeria Puddu, Dr Marco Demurtas, Mithun Parambath, Matthew Nicklin, Veeranjanyulu Thota, Zayd Westcott, Ben Hanby, Cyrille Delneuve, Cassandra Toni, Akshay Bhadwal, Victor Labib, Olga Verkhozina, Hannah Priest, Sophie Prentice and Elisa Tonoli.

Extra special thanks to Maria Papageorgiou and Robyn Plowright for their support, never-ending chats, gym sessions and worthy coffee breaks.

My gratitude to the technicians at the Nottingham Trent University who helped in using instrumentation and with whom I also shared nice chats; Mary Smith, David Edwards and Gordon Arnott; and generally everybody who have made my time spent in Nottingham Trent University rewarding and also enjoyable.

On a more personal level, I want to thanks my family for all their love and for always believing in me. Thanks to all my closest friends and especially to my dear friend Dr Estefania Boix for always being there; even if thousands miles away. And, finally, I am most grateful to my husband for his patience, encouraging, support and unconditional love. You are my inspiration, my everything.

Table of Contents

Abstract	i
Dedication	ii
Acknowledgments	iii
CHAPTER I: INTRODUCTION	1
1.1 BIOINORGANIC MATERIALS: AN OVERVIEW	1
1.2 MINERAL BINDING PEPTIDES	2
1.2.1 Phage Display Technique.....	2
1.2.2 Mineral Binding Peptides Identified by Phage Display	3
1.3 OVERVIEW OF ZINC OXIDE (ZNO)	5
1.3.1 Properties and Applications of ZnO	5
1.3.2 ZnO Crystal Growth and Synthesis Methods.....	6
1.3.3 The Role of Biomolecules during ZnO Synthesis.....	9
1.4 OVERVIEW OF SILICA (SiO ₂).....	10
1.4.1 Properties and Applications of SiO ₂	10
1.4.2 Silicification Process and Synthesis Methods	13
1.4.3 The Role of Biomolecules during Biosilicification Process.....	16
1.4.3.1 Bio-inspired SiO ₂ Studies.....	18
1.5 MOTIVATION AND OBJECTIVES	20
CHAPTER II: EXPERIMENTAL METHODS	21
2.1 ELECTRON MICROSCOPY	21
2.1.1 Transmission Electron Microscope.....	21
2.1.2 Scanning Electron Microscope Coupled to Energy Dispersive X-Ray Analysis.....	22
2.2 ATTENUATED TOTAL REFLECTANCE INFRARED SPECTROSCOPY	24
2.3 THERMOGRAVIMETRIC ANALYSIS.....	26
2.4 POWDER X-RAY DIFFRACTION	27
2.5 X-RAY PHOTOELECTRON SPECTROSCOPY	29
2.6 DYNAMIC LIGHT SCATTERING AND ZETA POTENTIAL	32
2.7 NITROGEN GAS ADSORPTION.....	35

2.8 INDUCTIVELY COUPLED PLASMA-OPTICAL EMISSION SPECTROMETRY	37
2.9 SOLID PHASE PEPTIDE SYNTHESIS	38
2.10 HIGH PERFORMANCE LIQUID CHROMATOGRAPHY.....	41
2.11 ISOTHERMAL TITRATION CALORIMETRY.....	43
2.12 FLUORESCENCE SPECTROSCOPY	46
CHAPTER III: MECHANISM OF ZnO FORMATION FROM	
AQUEOUS SOLUTION OF ZINC ACETATE.....	48
3.1 INTRODUCTION	48
3.2 EFFECT OF PH ON ZNO MORPHOLOGY.....	53
3.3 MATERIALS.....	56
3.4 ZNO SYNTHESIS.....	56
3.5 CHARACTERIZATION	57
3.6 RESULTS AND DISCUSSION.....	58
3.6.1 Zinc Oxide Formation via Intermediate(s).....	58
3.6.2 Comparison of Different Mechanisms of ZnO Growth via LBZs.....	68
3.7 CONCLUSIONS	72
CHAPTER IV: ZnO-BINDING PEPTIDES STUDIES	73
4.1 INTRODUCTION	73
4.2 MATERIALS.....	76
4.3 ZNO SYNTHESIS IN THE PRESENCE OF PEPTIDES	76
4.4 PEPTIDE SYNTHESIS	76
4.5 CHARACTERIZATION	77
4.6 ITC STUDIES	78
4.7 RESULTS AND DISCUSSION.....	80
4.7.1 Peptide EM-12: Delay/Suppression of ZnO Formation	80
4.7.2 Peptide EC-12: Stronger Complexation Capability with Zn ²⁺	87
4.7.3 Study of the Peptide-Mineral Interactions.....	90
4.7.4 Effects of EM-12 and EC-12 on ZnO Morphology.....	100
4.8 CONCLUSIONS	104
CHAPTER V: SiO₂-BINDING PEPTIDES STUDIES.....	106
5.1 INTRODUCTION	106

5.2 MATERIALS.....	108
5.3 SOLID PHASE PEPTIDE SYNTHESIS	109
5.4 PREPARATION OF SILICA SAMPLES.....	109
5.4.1 Silica Synthesis Methods.....	109
5.4.2 Silica Functionalization.....	112
5.4.3 Preparation of samples for the binding studies (Fluorescamine assay).....	113
5.5 CHARACTERIZATION	114
5.6 RESULTS AND DISCUSSION.....	115
5.6.1 Silica Particles Synthesis and Properties.....	115
5.6.2 Silica Particle Functionalization and Properties.....	122
5.6.3 Silica-Peptide Binding Studies.....	129
5.6.3.1 Effect of Silica Particle Size on Binding.....	130
5.6.3.2 Effect of Silica Functionalization on Binding	132
5.6.3.3 Effect of Level of Functionalization on Binding.....	134
5.7 CONCLUSIONS	141
CHAPTER VI: CONCLUSIONS AND FUTURE WORK	142
6.1. CONCLUSIONS	142
6.2. FUTURE WORK	148
References.....	150
Appendices	169
Glossary.....	202
Publications.....	206

Chapter I

Introduction

1.1 Bioinorganic Materials: an Overview

The ability of nature to produce minerals with both crystalline and amorphous structures under ambient conditions and giving to such minerals specific and unique properties is much envied by scientists (Lopez *et al.*, 2005; Mann, 1998; Simkiss and Wilbur, 2012). Through a process called biomineralization, biomolecules composed of lipids, proteins, and/or carbohydrates are involved in the growth mechanisms of many biominerals (Lowenstam and Weiner, 1989; Williams, 1984) into designs that confer exceptional properties, such as ordered hierarchical porous structures applicable for catalysis, biosensing and biomedical applications (Davis, 2002; Slowing *et al.*, 2007). Understanding how biological systems control the final size, shape and properties of minerals is key to addressing the challenges that arise when designing new materials and synthesizing superior nanostructures, especially under aqueous conditions.

Proteins in particular have been found to significantly influence biosynthesis and the templating of numerous natural composites including bones, seashells and opal (Perry *et al.*, 2009; Sanford and Kumar, 2005). Many different biomolecules have been identified to play a crucial role when minerals are formed (Crenshaw, 1982; Dove *et al.*, 2003; Kroger *et al.*, 2002; Lowenstam and Weiner, 1989; Poulsen and Kroger, 2004; Sumper and Kroger, 2004; Weiner *et al.*, 1983; Weiner and Addadi, 2002). For example, in biosilification (formation of biogenic silica), the biomineral-associated organic molecules identified that are involved in the mineral biogenesis process typically include highly phosphorylated proteins (silaffins, silacidins) (Kroger *et al.*, 1999; Richthammer *et al.*, 2011) or the protein Lustrin A which is responsible for calcium carbonate mineralization (Shen *et al.*, 1997). *In vitro* studies have shown that either these proteins or their shorter sequence (peptides) have control not only just over the biomineral they were extracted from but other materials (Sewell and Wright, 2006; Sumerel *et al.*, 2003). Accordingly, such natural biomineralization processes have inspired 'biomimetic' strategies for the synthesis of novel materials with complex shape, hierarchical organization and controlled size, shape and polymorph under

ambient conditions in aqueous environments (Dickerson *et al.*, 2008; Naik *et al.*, 2004; Nudelman and Sommerdijk, 2012; Xu *et al.*, 2007). Of interest in this thesis is to study the role of peptides during mineral formation and to explore the peptide binding mechanisms.

1.2 Mineral Binding Peptides

To mimic the naturally occurring biomineral forming proteins and create artificial biomolecules for technological applications combinatorial biology techniques, such as phage display (PD), ribosome display (RD) and cell-surface display (CSD) can be employed. Combinatorial biology techniques are used to identify those peptides that preferentially bind to a target material substrate by molecular recognition (Smith and Petrenko, 1997), hereafter named mineral-binding peptides (BPs). Among them, PD is the most popular technique which generates and displays a large diversity of peptide sequences (Golec *et al.*, 2012; Naik *et al.*, 2002; Rothenstein *et al.*, 2012).

1.2.1 Phage Display Technique

Phage selection procedure (or biopanning) takes place through a reiterative process of: (1) incubation, (2) washing, (3) elution and (4) amplification (Figure 1.1) (Huang *et al.*, 2012; Smith and Petrenko, 1997).

First, the target surface is incubated for several hours to a combinatorial peptide library and it is then that the binding occurs. The non-binders are eliminated by a washing process followed by elution of the bound phage using either mild acid or basic conditions (Huang *et al.*, 2012). These steps are commonly repeated one or more times in order to enrich the binding clones. Finally, the recovered phage population is amplified (Huang *et al.*, 2012; Smith and Petrenko, 1997). Peptide libraries are displayed on the phage coat protein (i.e. M13), a virus able to infect bacteria and replicate within it (Smith and Petrenko, 1997).

Phage displayed peptide libraries have been utilized for the selection of BPs for a high number of materials. These substrates can be classified as metal, metal oxide, metal alloy, metal compounds, mineral, semiconductor, carbon material and polymer binders (Smith and Petrenko, 1997).

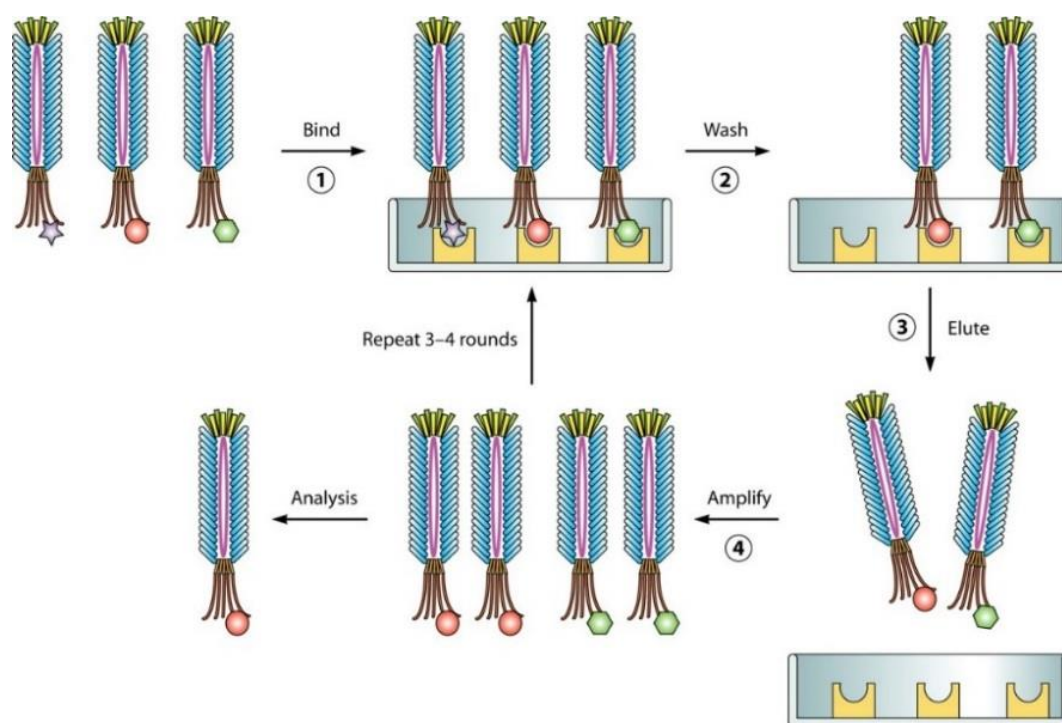


Figure 1.1 Schematic representation of biopanning of a PD library to select phage binding to an immobilized target from Huang *et al.* (2012).

1.2.2 Mineral Binding Peptides Identified by Phage Display

To date, several peptides have been identified to bind ZnO and SiO₂ surface. In Table 1.1 are listed amino acids sequences that have shown high affinity for these surfaces (ZnO and SiO₂).

Many of the ZnO-BPs identified showed histidine in their sequences (Table 1.1). Sequences with low amount of histidine residues; however, generally contain residues such as glutamic acid (E), cysteine (C) and/or aspartic acid (D) which are known to interact with Zn²⁺ in zinc enzymes of living organism (Vallee and Auld, 1990). Further, ZnO-BPs synthesized by two different research groups, Tomczak *et al.*(2009) and Umetsu *et al.*(2005), showed two highly similar sequences, ZnO-1 and Z1, respectively. In both cases the libraries used were of M13 pIII coat protein; however, the ZnO targets were of different size (Table 1.1). Note that, using PD pH 7.5, most of the ZnO-BPs identified have a high isoelectronic point and are, therefore, positively charged at physiological pH (Rothenstein *et al.*, 2012; Tomczak *et al.*, 2009; Umetsu *et al.*, 2005). This observation suggests that ionic interactions are important in the binding of these peptides sequences to ZnO surface.

For SiO₂-BPs, Pep1 and Si4-1 also showed certain similarity (Table 1.1). In general, high fractions of histidine and/or serine were identified in these SiO₂-BPs. Ser-rich peptides have been shown to be involved in the silicification process as well as Lys and Arg (Belton *et al.*, 2004). For SiO₂-BPs, other than electrostatic interactions (i.e. hydrophobic or hydrogen bonding) have been reported as the peptide binding mechanisms (Naik *et al.* 2002, Eteshola *et al.* 2005 and Patwardhan *et al.* 2012, Puddu *et al.* 2012).

Table 1.1 Summary of ZnO-BPs and SiO₂-BPs identified using combinatorial phage display. Peptides used for this investigation are highlighted. Amino acids structures and properties are given in Appendix 1.1.

Peptide Sequence of ZnO-BPs	Peptide name	ZnO Substrate	Reference
EAHMHKAPRP	ZnO-1	1 µm particles	(Umetsu <i>et al.</i> , 2005)
EAHMHKAPRP-GGGSC	TZnO-1	1 µm particles	(Umetsu <i>et al.</i> , 2005)
GLHVMHLVAPPR	Z1	Nanopowder	(Tomczak <i>et al.</i> , 2009)
GLHVMHLVAPPR-GGGC	TZ1	Nanopowder	(Tomczak <i>et al.</i> , 2009)
HSSHHQPKGTNP	Pep31	ZnO (0001)/(0001)	(Rothenstein <i>et al.</i> , 2012)
HHGHSPTSPQVR	Pep44	ZnO (0001)/(0001)	(Rothenstein <i>et al.</i> , 2012)
TMGANLGLKWPV	PG-7	Powdered ZnO	(Golec <i>et al.</i> , 2012)
Peptide Sequence of SiO ₂ -BPs	Peptide name	Silica Particle Size (nm)	Reference
MSPHPHPRHHHT	Si4-1	400-600	(Naik <i>et al.</i> , 2002)
RGRRRRLSCRLL	Si4-10	400-600	(Naik <i>et al.</i> , 2002)
HPPMNASHPHMH	Et1	100*	(Eteshola <i>et al.</i> , 2005)
HTKHSHTSPPL	Et2	100*	(Eteshola <i>et al.</i> , 2005)
CHKKPSKSC	SiC1	50	(Chen <i>et al.</i> , 2006)
RLNPPSQMDPPF	DS202	Quartz-binder	(Tamerler and Sarikaya,
QWPPPLWFSTS	DS189	Quartz-binder	(Tamerler and Sarikaya,
YITPYAHLRGGN	Pep2	15.0±0.4	(Patwardhan <i>et al.</i> , 2012)
KSLSRHDHIIHH	Pep1	82.1±3.6	(Patwardhan <i>et al.</i> , 2012)
LDHSLHS	7 mer	82.1±3.6	(Patwardhan <i>et al.</i> , 2012)
MHRSDLMSAAVR	Pep4	450±22	(Patwardhan <i>et al.</i> , 2012)
KLPGWSG	S1	82±4	(Puddu and Perry, 2012)
AFILPTG	S2	82±4	(Puddu and Perry, 2012)

*Thickness of Silica films.

1.3 Overview of Zinc Oxide (ZnO)

1.3.1 Properties and Applications of ZnO

ZnO has been used already in the Bronze Age as a byproduct of copper ore smelting and was used for healing of wounds (Ellmer *et al.*, 2008). Its major application for many centuries was for the production of brass (Cu-Zn alloy) (Ellmer *et al.*, 2008). Nevertheless, it has been in the last century when this material has been highly investigated. The interest in ZnO reached its peak in the 1960s, with the discovery of its good piezoelectric properties (Hutson, 1960). ZnO is a wide bandgap semiconductor ($E_g = 3.437$ eV) with an excitation binding energy of 60 meV. Due to an optically forbidden transition of the fundamental gap, ZnO is transparent in the visible part of the electromagnetic spectrum (Nie *et al.*, 2002). In Table 1.2 properties of mineral wurtzite ZnO are summarized (Madelung *et al.*, 1998; Pearton *et al.*, 2005). The piezoelectric property is caused by the polarity of ZnO, i.e. the absence of inversion symmetry in the crystal lattice. Hence, ZnO has a wide range of applicability in the manufacturing of solar cells, blue light-emitting diodes (LEDs) and nanolasers amongst others (Klingshirn, 2007). ZnO possesses a large family of highly crystalline nanostructures that can adopt a great variety of morphologies which are predicted to play an important role for many applications, such as ZnO nanowires for gas sensors (Wan *et al.*, 2004) or ZnO nanoplates for dye-sensitive solar cells (Qiu *et al.*, 2010). ZnO nanostructures are being increasingly used as photocatalysts for degrading harmful contaminants such as pesticides from ground water (Baruah and Dutta, 2009). In its polycrystalline form, ZnO present low toxicity and biodegradability (Brayner *et al.*, 2006), which makes this material also interesting for biomedical applications (Zhang *et al.*, 2013). In the pharmaceutical (or cosmetic) industry, ZnO nanoparticles are used as an additive for sunscreen or facial powders as they reflect and scatter UV light without damaging human skin (Nohynek *et al.*, 2007). ZnO nanoparticles have also been investigated for their use in the food industry since it shows significant antimicrobial activity against 3 pathogens (*Listeria monocytogenes*, *Salmonella Enteritidis*, and *Escherichia coli* O157:H7) in growth media and thus inclusion in food systems like coating surfaces and packaging processes may be effective in inhibiting certain pathogens (Jin *et al.*, 2009). Other biomedical applications that have been taking much attention are the use of ZnO nanoparticles for drug delivery, gene delivery, biosensing and biomedical imaging

(Zhang *et al.*, 2013). For this, studies on ZnO-biomolecule interfaces have been of great importance in the recent years, such as protein binding on specific ZnO crystal planes for the design ZnO-based materials and biosensors (Xie *et al.*, 2015), or the synthesis of ZnO Nanoparticles (NPs) in the presence of glucose, sucrose and polysaccharides to improve the immobilization of the antibodies on the surface of the cellulose fiber sheets (Khatri *et al.*, 2014), and also the use of DNA linked to ZnO@CdS to improve energy transfer between ZnO@CdS and graphene oxide (GO) for detection of DNA sequences (Sun *et al.*, 2014). Therefore, fundamental understanding of biomolecule adsorption on ZnO surfaces is key for addressing specific applications of such material.

Table 1.2 Basic properties of mineral wurtzite ZnO.

Parameter	ZnO	Units
Naturally occurring mineral	Zincite	
Abundance Earth's crust	40	ppm
Energy gap (E_g)	3.437 (d)	eV
Lattice	Hexagonal	
Structure ^a	Wurtzite	
Space group	P6 ₃ mc	
a, c	0.3250, 0.5207	nm
Density	5.606	$\text{g}\cdot\text{cm}^{-3}$
Melting point, T_m	1975	$^{\circ}\text{C}$
Boiling point, T_b	2360	$^{\circ}\text{C}$
Enthalpy of formation, ΔH_f	3.6	eV
Excitation binding energy	60	meV
Static dielectric constant	8.656	
Refractive index	2.008, 2.029	
Electron effective mass	0.24	

^a Stable phase at 300K.

1.3.2 ZnO Crystal Growth and Synthesis Methods

ZnO is an inorganic compound which occurs naturally as the mineral zincite. The first fine specimens were found at the Franklin/Sterling Hill deposit in New Jersey (USA) in 1810. This mineral typically crystallizes in the hexagonal wurtzite structure (Figure 1.2a) and belongs to the space group P6₃mc in the Hermann-Mauguin notation

(Wyckoff, 1963). Another less thermodynamically stable structure for ZnO under ambient conditions is zinc blende. Wurtzite and zinc blende structures have tetrahedral coordination where an O^{2-} ion is surrounded by four Zn^{2+} ions. Figure 1.2a shows the primitive cell (heavy lines) of the Wurtzite-structure lattice placed within a hexagonal prism where a and c are the lattice constants (Ellmer *et al.*, 2008). The primitive translation vectors a and b include an angle of 120° and are situated in the base plane, with c orthogonal to them. There are four atoms per unit cell and every atom of one type is tetrahedrally coordinated with four atoms of another type, and *vice versa*. The tetrahedral coordination in ZnO results in a non-centrosymmetric structure (Wang, 2004). The orientation relation between planes and ZnO crystals exhibit several typical surface orientations (Figure 1.2b). The basic low index surface terminations are (0001), (000 $\bar{1}$), (10 $\bar{1}$ 0) and (11 $\bar{2}$ 0) (Figure 1.2b). The (0001) and the (000 $\bar{1}$) represent the zinc- and the oxygen-terminated surfaces, respectively, of the polar {0001} direction, which are perpendicular to the c -axis (Ellmer *et al.*, 2008). The other two facets are non-polar surfaces parallel to the c -axis and have lower energy than the {0001} direction (Wang, 2004).

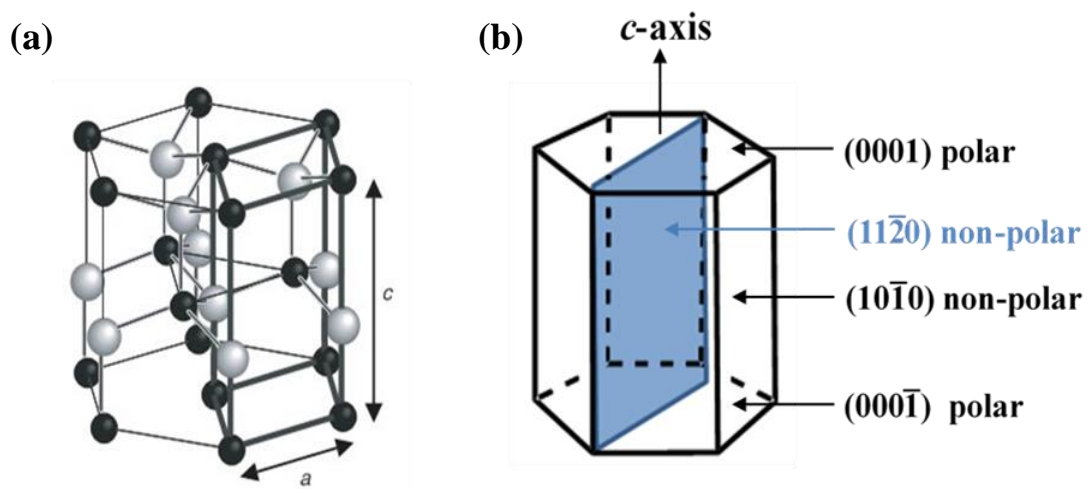


Figure 1.2 (a) Primitive cell of the Wurtzite-structure lattice where the light grey spheres correspond to oxygen and the dark spheres to zinc (Ellmer *et al.*, 2008) ; and (b) ZnO crystal typical surface orientations.

The crystal growth morphology is controlled by a combination of energetic and kinetic factors. Under thermodynamic equilibrium conditions, the morphologies formed tend to maximize the areas of low surface energy planes, i.e. (10 $\bar{1}$ 0) plane. Therefore, low

energy faces (thermodynamically more stable) are preferentially expressed. On the other hand, the slowest growing faces become the largest, and the rapidly growing faces either become small or disappear altogether. Generally, the low energy faces tend to also be those that grow slowly (Yoreo and Vekilov, 2003). As a result ZnO crystals are inherently elongated along the *c*-axis as shown in Figure 1.2b.

The most common methods to synthesize ZnO nanostructures are either vapour route (usually at high temperatures, from 500 - 1500 °C) or solution route synthesis (typically at temperatures below 200 °C). Typically used vapour routes techniques are vapour phase transport, which includes vapour solid (VS) and vapour liquid solid (VLS) (Umar *et al.*, 2005; Wang *et al.*, 2013; Wu and Yang, 2001); physical vapour deposition which includes radiofrequency (RF) sputtering (Lim *et al.*, 2006); and chemical vapour deposition (Minegishi *et al.*, 1997), which includes microwave plasma-assisted (Chen *et al.*, 1998) and metal organic chemical vapour deposition (MOCVD) (Lee *et al.*, 2004). Solution route syntheses are frequently via hydrothermal methods (Baruah and Dutta, 2009), chemical bath deposition (CBD) (Govender *et al.*, 2004), spray pyrolysis (Krunk and Mellikov, 1995), electrophoresis (Wong and Searson, 1999) and microwave assisted thermal decomposition (Lagashetty *et al.*, 2007). Hydrothermal methods are commonly chosen for the synthesis of ZnO due to their simplicity, low cost and green chemistry approach (low energy consumption, closed system, etc.) and also due to the nucleation control during the crystallization process. For ZnO, layered basic zinc salts (LBZs) have been identified as intermediate products during solution route synthesis via the hydrothermal method (Jang *et al.*, 2010; Tokumoto *et al.*, 2003; Wang *et al.*, 2006; Wang *et al.*, 2011). A more detailed review of hydrothermal methods is given in Chapter 3 section 3.1. This synthesis route has been shown to generate a wide range of 1D nanometer through micrometer ZnO structures by simply tuning reaction parameters such as pH, temperature, precursors and solvents. Morphology modification has also been achieved by using structure directing agents (SDAs) like citrate ions, amines and polymers (Tian *et al.*, 2003), as well as, biomolecules such as peptides (Bai *et al.*, 2009; Baier *et al.*, 2012; Gerstel *et al.*, 2006; Liang *et al.*, 2011; Limo and Perry, 2015; Rothenstein *et al.*, 2012; Sola-Rabada *et al.*, 2015; Togashi *et al.*, 2011; Tomczak *et al.*, 2009).

1.3.3 The Role of Biomolecules during ZnO Synthesis

It has not been until the last 15 years where investigations using biomolecules for controlling ZnO crystal morphology have been developed. For example, the formation of ZnO hexagonal disks was achieved by addition of arabic gum into the system (Jitianu and Goia, 2007). In another case, the presence of histidine generated different ZnO structures (prismlike, flowerlike and hollow microspheres) depending on the reactants molar ratios employed (Wu *et al.*, 2008). The growth of ZnO nanoshells at room temperature was demonstrated by using the enzyme urease (De La Rica and Matsui, 2008). ZnO-BPs have also been studied to understand their interaction mechanisms, the effects thereof and possible applications (Bai *et al.*, 2009; Baier *et al.*, 2012; Liang *et al.*, 2011; Limo and Perry, 2015; Rothenstein *et al.*, 2012; Sola-Rabada *et al.*, 2015; Togashi *et al.*, 2011; Tomczak *et al.*, 2009). ZnO morphology modification has been shown to be peptide directed but also influenced by the ZnO synthesis growth conditions and precursors employed (Limo *et al.*, 2015; Togashi *et al.*, 2011). Besides this, the use of biomolecular templates for the growth of ZnO hierarchical structures has been shown not only to impact ZnO morphology but also to suppress (Gerstel *et al.*, 2006) or catalyse (Umetsu *et al.*, 2005) ZnO formation. In Chapter 4 section 4.1, an in-depth review of ZnO-BPs controlling ZnO formation is given. Further, as explained in section 1.3.1, generation of nanocomposites by capping ZnO particles with biomolecules can give additional functionality for a variety of applications (Cho *et al.*, 2011; Huang *et al.*, 2008; Khatri *et al.*, 2014; Sun *et al.*, 2014; Zou *et al.*, 2008). For example, the green photoluminescence of ZnO particles was enhanced by its synthesis in the presence of spider silk peptides which can be directly used as biosensors or in optoelectronic devices (Huang *et al.*, 2008). Cho and co-workers generated Fe₃O₄-ZnO nanoparticles by using a ZnO-BP (RPHRKGGA) (Cho *et al.*, 2011). This nanocomposite was shown to be an efficient carrier to deliver target antigens to dendritic cell (DC) for cancer immunotherapy (Cho *et al.*, 2011). Although investigations have shown the effect of the presence of biomolecules during ZnO synthesis only in a few cases, the role of certain amino acids (i.e. histidine) has been proposed (Limo *et al.*, 2015; Wu *et al.*, 2008) and/or specific biomolecule binding sites (Okochi *et al.*, 2010). The mechanisms by which biomolecules attach to the ZnO surface and/or modulate nucleation and crystal growth processes to direct ZnO formation is yet to be fully understood and, is therefore, a challenge for scientists.

1.4 Overview of Silica (SiO₂)

1.4.1 Properties and Applications of SiO₂

SiO₂ is one of the most common materials in nature and is the second most common biogenic mineral after carbonates (Lowenstam and Weiner, 1989). Silica can be found in nature either in amorphous or crystalline forms (i.e. quartz, cristoblite, tridymite). Crystalline silica, commonly α -quartz, is a basic compound of soil, sands and rocks whereas amorphous silica is commonly deposited in living organisms, including land plants (i.e. rice, cucumber), single cellular organisms such as diatoms and animals such as sponges (Iler, 1979). Silica produced by living organisms (also known as biogenic silica) can be found in a wide range of highly ordered structures with a variety of pores diameters conferring this material exceptional mechanical properties. The biosilicification process involves complex inorganic polymerization reactions in the presence of organic species such as proteins and proteoglycans which are considered as possible control molecules during the biomineralisation process (Perry and Keeling-Tucker, 2003). The role of the organic matrix during silica formation and an understanding of the overall biosilicification process have been widely studied to address the design of new materials inspired by nature (Coradin and Livage, 2007; Patwardhan *et al.*, 2012; Perry and Keeling-Tucker, 2003; Poulsen and Kröger, 2005; Sanchez *et al.*, 2005). Synthetic amorphous silica nanoparticles (SiNPs) have received much attention in recent years for a variety of technological and biomedical applications due to their relatively large surface area and permeability through many biological pathways resulting in high interaction with biological systems (De Jong and Borm, 2008). Their biocompatibility and bioresorbable character and easy functionalisation also makes SiNPs ideal candidates for biomedical applications. The cytotoxicity character of SiNPs on cells is known to be dependent on the amount of material used, time of exposure on the cells, and size of the nanoparticles; where smaller particles (< 20 nm) showed higher toxicity (Kumar *et al.*, 2015). Parameters such as size, shape, chemical composition, surface properties and crystallinity determine the viability of using SiNPs as drug delivery supports. On the other hand, micron scaled silica particles have been extensively use as inorganic supports (i.e. chromatography columns) for a variety of applications, including isolation of polypeptides, proteins, nucleic acids or DNA fragments (Kirkland *et al.*, 2000). In the

last decades, the use of chromatography columns made with either non-porous or porous silica has also been investigated. Pore diameters can vary from microporous (< 2 nm) to mesoporous (< 50 nm) to finally macropores (> 50 nm). Micropores (or non-porous) stationary phases have shown outstanding speed for separation of macromolecules due to excellent mass transfer characteristics (Kirkland *et al.*, 2000). Moreover, porous silica-based materials have attracted great attention for enzyme immobilization since they can be hosted within the pores of mesoporous supports allowing expensive biological catalysts to be used repeatedly for as long as they remain active (Girelli and Mattei, 2005; Zucca and Sanjust, 2014). The chemistry of synthesized silica particles is mainly composed by siloxanes (Si-O-Si), silanols (Si-OH) and ionic siloxide (Si-O⁻) and/or the presence of water molecules adsorbed on the surface. Depending on the extent of these species on the silica surface, a more hydrophilic (silanol) or hydrophobic (siloxane) character of the particles can be achieved. Silanol groups can be found in different forms: isolated, geminal, vicinal and internal (Figure 1.3a). In general, an increase of the surface ionization with particle size is believed to be by the presence of a higher population of isolated silanol groups (Si-OH), leading to a higher surface acidity (Patwardhan *et al.*, 2012). Aggregation (or agglomeration) of silica particles can occur due to hydrogen bonding through surface silanol groups on adjacent particles. Depending on the reaction conditions, the silica units can interconnect forming chains (known as a gel) or stay separated (known as a sol or powder) (Figure 1.3b).

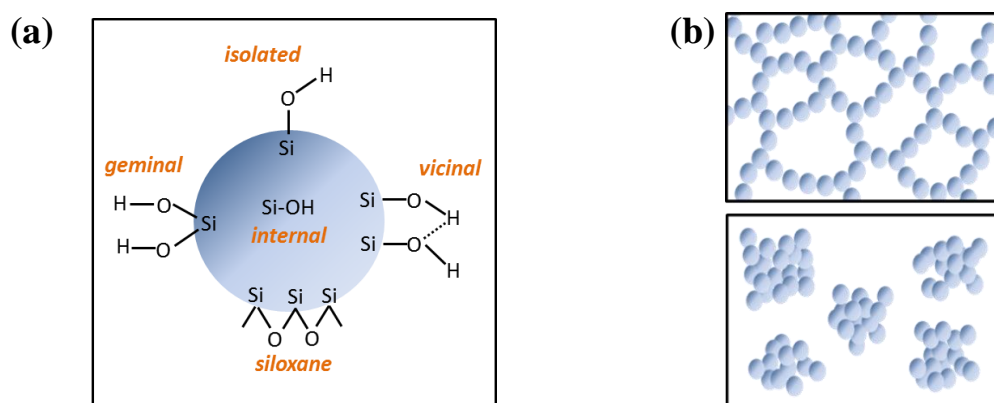


Figure 1.3 (a) The silanol chemistry of silica particles is composed: isolated, geminal, vicinal and internal. Illustration adapted from Zhuravlev *et al.* 2000, and (b) Two-dimensional representation of silica units distribution in a gel (top) and a precipitate (bottom). Illustration adapted from Iler 1979.

The abundant number of hydroxyl groups on SiNPs allows their functionalization leading to specific or higher reactive groups including carboxyl (An *et al.*, 2007), amine (Asenath Smith and Chen, 2008), methyl (Luechinger *et al.*, 2005), phenyl (Wu *et al.*, 2006) or thiol (Yang *et al.*, 2005). Therefore, these groups can be used to change the particles affinity for specific surfaces or (bio)molecules by, for example, hydrogen bonding (Asenath Smith and Chen, 2008). A great interest on amine-functionalized silica surfaces has developed as their nucleophilic nature make them good candidates to serve as solid base catalysts or good linkers between silica and organic species (i.e. DNA, enzymes, polypeptides) and/or metals. Thus, amino-functionalized silica surfaces have been used in a wide range of applications such as waste water treatment by immobilization of catalytically active transition metals (Aguado *et al.*, 2009) or gene delivery (Bharali *et al.*, 2005), amongst others. Moreover, through particle functionalisation, their hydrophobic character can be increased by linking alkyl groups on the particles surface (Luechinger *et al.*, 2005). Methyl-functionalized silica surfaces are attractive for industrial applications due to abrasion resistance (Das *et al.*, 2014) and anti-sticking or self-cleaning properties (Sanjay *et al.*, 2012). The hydrophobic/hydrophilic ratio of silica materials is of high importance for its application in wastewater treatment (Aguado *et al.*, 2009). The functionalization of tissue culture polystyrene (TCP) with silica has also been studied for biomedical applications (Hickman *et al.*, 2015). For example, generating a silica surface upon TCP and applying it as a platform for subsequent functionalization using a fluorinated alkoxy silane has been shown to produce a material with a differential adsorption profile of serum factors derived from the cell culture media; producing better control of cancer cell aggregation-disaggregation events *in-vitro* (Nicklin *et al.*, 2014). Further studies showed that an appropriate surface chemistry (i.e. hydrophilic or super-hydrophobic silica films) could facilitate the adhesion and proliferation of cells (Hickman *et al.*, 2012). Henceforth, the wide range of silica forms including precipitated, fused quartz, crystal, fumed silica, colloidal silica, silica gel and aerogel, its low-toxicity and easy surface modification; confers to this material a vast array of applications such that it has become a vital compound in daily life. In Figure 1.4 silica applications according to its properties are shown.

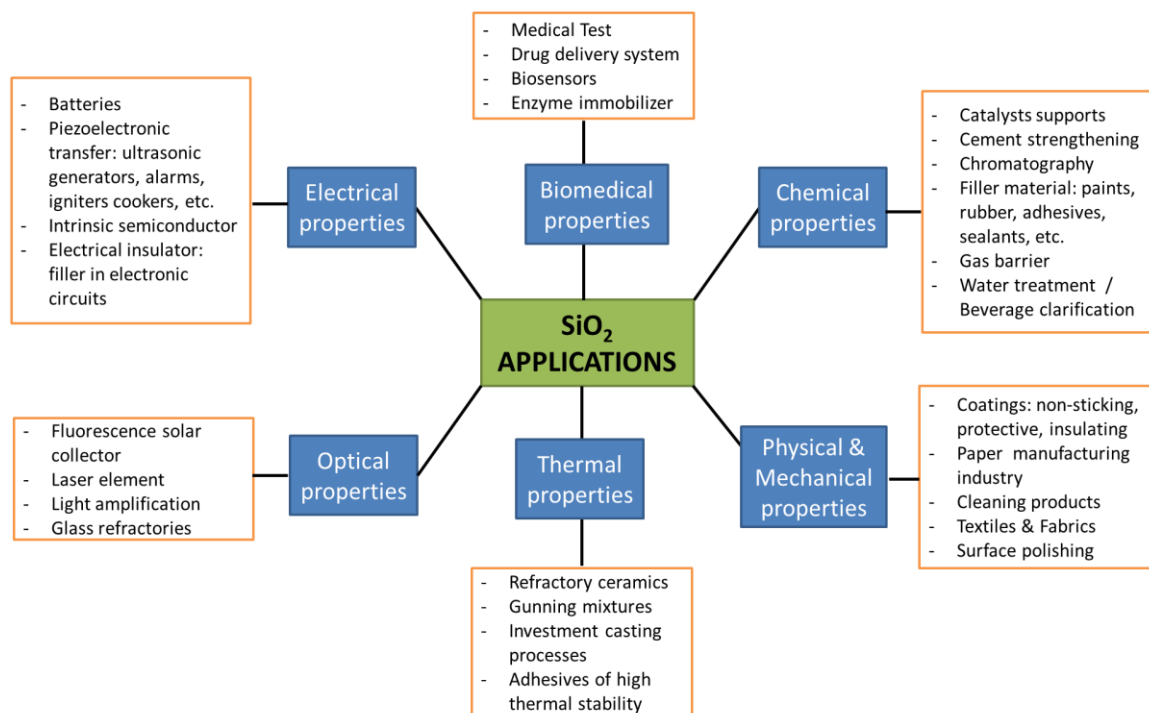


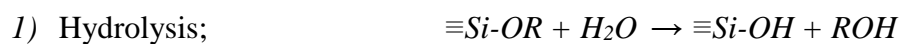
Figure 1.4 Applications of SiO₂ based materials.

1.4.2 Silicification Process and Synthesis Methods

Monodispersed silica particles (at the nano- and micro-scale) have been widely synthesized using the sol-gel method which implies the hydrolysis of a silica precursor followed by the condensation into oligomers for further formation of silica particles (Brinker and Scherer, 1990). The final size of the synthesized particles depends on the hydrolysis (rate of nucleation) and the condensation process (rate of growth) (Van Blaaderen *et al.*, 1992). The rate of hydrolysis can be promoted by the addition of an acid (i.e. HCl) or a base (i.e. NH₃) due to the increase of either hydronium or hydroxide groups into the system. In 1968, Stöber and Fink reported an effective route for the synthesis of silica particles in basic conditions where the particle size, from 10 nm to 2 μm, was simply controlled by changing the concentrations of the reactants (Stöber *et al.*, 1968). Early in the 90s, Osseoassare and Arriagada developed a microemulsion method (also in basic conditions) for the synthesis of SiNPs by controlling the hydrolysis of the silica precursor in an inverse microemulsion system (Osseo-Asare and Arriagada, 1990). The growth of silica microparticles has also been investigated under acidic conditions by using acetic acid (Karmakar *et al.*, 2000), tartaric acid (Izutsu *et al.*, 1997) or nitric acid (Kawaguchi and Ono, 1990). In general, at low pH structures

with low porosity are obtained and, consequently, these are more dense particles; whereas in alkaline conditions, mesoporous spheres (from 2 to 50 nm) are typically achieved. More recently, SiNPs have been prepared through microwave–assisted acid catalysis using HCl (Lovingood *et al.*, 2013). SiNPs have also been commercially produced by chemical vapour condensation (CVC), which implies the decomposition of metal-organic precursors, such as SiCl₄, in a high temperature flame (Vansant *et al.*, 1995).

In the sol-gel process, silica condensation can be performed by the hydrolysis of silicon alkoxides such as tetraethoxysilane (TEOS) or tetramethoxysilane (TMOS) to form silicon hydroxide, Si(OH)₄, and subsequent condensation of SiO₂, as shown in the following equations:



In the first steps of polymerisation, siloxane bonds form into cyclic structures and further formation of three-dimensional molecules that result in particles (Figure 1.5) with a majority of Si-O-Si bonds and a minority of silanols (Si-OH) (Iler, 1979; Perry and Keeling-Tucker, 2003). As the small silica particles (<5 nm) are more soluble than bigger spheres, when dissolution occurs, small oligomers are deposited on the bigger spheres by a process known as ‘Ostwald ripening’, a term commonly applied to the formation of crystals (Iler, 1979; Yoreo and Vekilov, 2003). Mechanisms for silica formation have been shown to follow different pathways in an acid- or a base-catalysed reaction (Appendix 1.2). The silica polymerisation process for aqueous systems strictly depends on the pH of the media and, if applicable, also on the presence of salts, as summarised schematically by Iler (1979) in Figure 1.5.

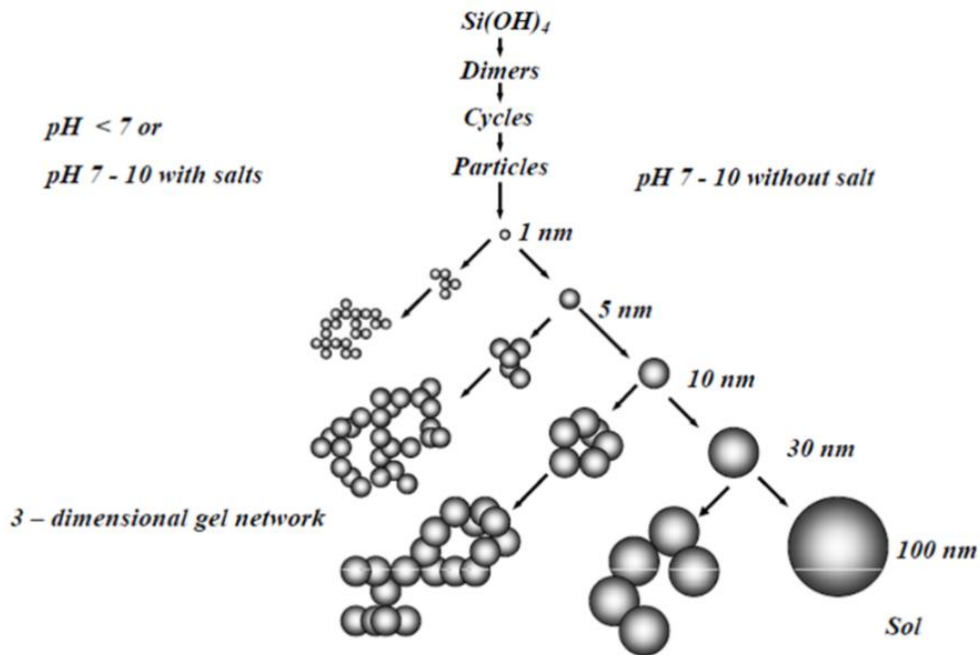


Figure 1.5 Silica polymerisation from monomer to particles and gel or powders for different solution conditions. Adapted from Iler (1979).

First, condensation of monomers into oligomers takes place spontaneously for concentrations of SiO_2 above 100-200 ppm, which is higher than the amorphous silica solubility limit. Since condensation polymerisation is an ionic process, for $\text{pH} > 2$ the rate of the reaction depends on the concentration of OH^- ions whereas for $\text{pH} < 2$, the condensation rate depends on the concentration of H^+ . Note that, at the isoelectronic point (pI) of silica ($\text{pH} = 2$), reaction rate becomes extremely low as the electric mobility of silica is zero and silicic acid solutions may present stability as it corresponds to the point of zero charge of silica surface (Cihlár, 1993). Therefore, the condensation of silanols (Si-OH) in base-catalysed reaction ($\text{pH} > 2$) proceeds by a rapid deprotonation of the silanol, followed by slow attack of the resulting silanolate on another silanol group as shown in Appendix 1.2 (Osterholtz and Pohl, 1992). At this pH, silica species become negative and charge density increases along with the pH. At pH 7 the rate of dissolution and silica deposition is high and leads to a fast formation of particles (from 5-10 nm), with further particle growth taking place at a slower rate. The condensation rate reaches its maximum at $\text{pH} = 7.5$ (Wu *et al.*, 2013). Above this pH, the rate of condensation decreases until dissolution of silicates can be observed ($\text{pH} > 10.5$). Besides this, the presence of a cationic surfactant can stabilize silicates up to $\text{pH} = 12$ due to strong electrostatic interactions (Wu *et al.*, 2013). The obtained colloid

suspension (sols) results in the formation of uniform spherical particles. At this range of basic pH, where silica carries a negative charge, there is repulsion among particles which results in the formation of discrete units. Nonetheless, the presence of salts above 0.2 - 0.3 N can neutralise the negative charge of the silica particles allowing gelation to occur (Iler, 1979). On the other hand, the acid catalyzed ($\text{pH} < 2$) condensation of silanols most likely proceeds by rapid protonation of the silanol followed by slow attack on a neutral molecule shown in Appendix 1.2 (Osterholtz and Pohl, 1992). At this pH, silica species are positively charged and charge density increases with decreasing the pH which also favours condensation rate by nucleophilic attack (Wu *et al.*, 2013). At low pH, smaller particles are obtained (from 2 - 4 nm) due to the low rate of condensation and dissolution, and growth of bigger particles can only be achieved if temperature or pH is raised. As at acidic pH the particles are less negatively charged, there is a minimum repulsion and they can aggregate into gel networks (Iler, 1979). Henceforth, the rate of reaction for hydrolysis depends on pH which directly affects the charge of the silica species in solution. The nature of the alkyl groups in the silica precursor also affects the reaction rate. Generally, larger alkyl groups slow the rate of hydrolysis and due to steric effects they hinder condensation (Lofgreen and Ozin, 2014). Finally, it has been shown that the water content strongly influences the hydrolysis and condensation kinetics, there being observed low SiO_2 yields for low water:TEOS molar ratio (Milea *et al.*, 2011).

1.4.3 The Role of Biomolecules during Biosilicification Process

Silica biomineralization on Earth is controlled by unicellular organisms like diatoms, radiolarian and synurophytes as well as by multicellular sponges (Lowenstam and Weiner, 1989). These organisms produce silica structures which serve as the organism's skeleton and which accounts for the majority of their body mass (Sumper and Kroger, 2004). Diatoms, for example, exhibit intricate cell wall patterns in the nano- to micrometer range composed of hydrated, amorphous silica (Sumper and Kroger, 2004). Evidence for genetic influence over the production of diatom silica cell walls (termed *frustules*) came from observations that the patterning of these structures is species-specific and is precisely replicated in diatom progeny (Sumper and Kroger, 2004). Henceforth, biosilica producers have become extensively studied for the understanding of biosilicification processes since this could unravel the paradigm for the fabrication of

controlled nanostructures under conditions that are much milder than those used in traditional material-processing techniques. Important insights into diatom biosilicification have been made by isolating and characterizing specific biomolecules entrapped within the amorphous silica of the frustule, i.e. long-chain polyamines (LCPAs) (Kroger *et al.*, 2000) and cationic polypeptides termed silaffins (Kroger *et al.*, 1999). Both silica-associated biomolecules have been demonstrated to accelerate silica formation from a silicic acid solution *in vitro* (Kroger *et al.*, 1999; Kroger *et al.*, 2000). Silaffins are composed by a large number of phosphorylated serine residues and post-translationally modified lysines which carry oligo-propyleneamine functionalized side chains (Kroger *et al.*, 2002). Sumper and Kroger (2004) proposed the mechanism by which cationic molecules and hydrogen bonding polymers (hydroxyl amino acids: serine and tyrosine) can interact with anionic silica and neutral silanol groups, respectively; and thus, induce silica condensation (Sumper and Kroger, 2004).

Later studies also showed that the silica precipitation process is affected by either the synthetic polyamine structure or amino acid composition (Belton *et al.*, 2008; Bernecker *et al.*, 2010; Wieneke *et al.*, 2011). Remarkably, small changes on the KXXX peptide motif (X = A, G, S, or E in Silaffin 3) occurring repeatedly in silaffins could determine the morphology as well as the amount of precipitated silica (Wieneke *et al.*, 2011). Highly acidic phosphopeptides, termed silacidins, have also been identified from the diatom shell of *Thalassioria pseudonana*, and their role on silica precipitation was also demonstrated *in vitro* studies (Wenzl *et al.*, 2008). From the silica spicules of the sponge *Thetya aurantia*, proteins termed silicateins were also shown to catalyze silica formation from tetraethoxysilane *in vitro* (Cha *et al.*, 1999). The same year, Zhou *et al.* (1999) proposed a mechanism by which silicatein- α (70% of the silicatein filament obtained from sponges) catalyses the hydrolysis of alkoxy silanes at neutral pH via an acid/base reaction through the activity of the serine and histidine side chains, specifically, between the hydroxyl group of serine-26 and the imidazole side group of histidine-165. Due to the high structural homology of silicatein- α to the hydrolytic enzyme, cathepsin L; this reaction (Figure 1.6) was based on the mechanism of peptide bond hydrolysis by the analogous well known protease Cathepsin-L (Zhou *et al.*, 1999).

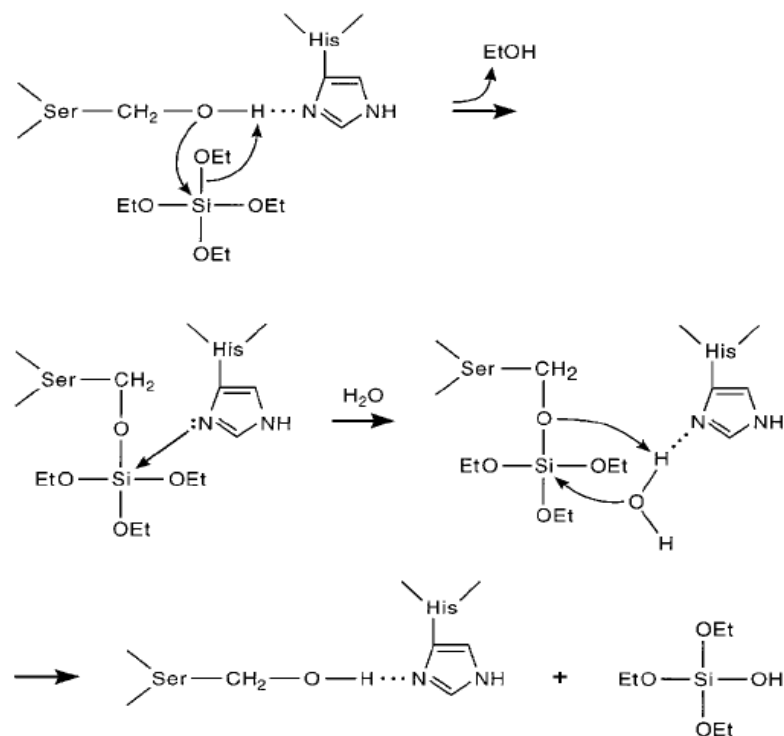


Figure 1.6 Mechanism proposed for alkoxy silane catalytic hydrolysis by silicatein active sites (serine and histidine) according to Zhou *et al.* (1999).

1.4.3.1 Bio-inspired SiO₂ Studies

Inspired by nature, studies on the effect of biomolecules such as amino acids, polypeptides, and oligo-peptides have arisen in materials science. Extensive studies have been done on a 19-mer peptide from the silaffin Sil-1A₁, termed R5 (SSKKSGSYSGSKGSKRRIL), for its capability of precipitating silica at neutral pH (Kroger *et al.*, 1999); and remarkably, the RRIL motif was shown to be essential for silica precipitation *in vitro* (Knecht and Wright, 2003). As previously mentioned, Wieneke *et al.* demonstrated that small variations in the isolated KXXK domains (peptide motifs occurring repeatedly in silaffins) could significantly change the morphology of silica precipitates (Wieneke *et al.*, 2011). Specifically, silica formation in the presence of the KASK peptide motif showed the presence of silica spheres of hundreds of nanometres together with grainy silica structures (Wieneke *et al.*, 2011). On the other hand, synthesis in the presence of the KAEK peptide motif showed mainly the presence of grainy silica while in the presence of the KAAK peptide motif, silica spheres (~ 100 nm) were mainly detected. Further, an increase of the silica spheres was observed by decreasing the polarity of the side chains in the order Glu, Ser and Ala

(Wieneke *et al.*, 2011) . Lysine and polylysine (PLL) have been widely studied for their ability to catalyse silica formation and growth at near-neutral pH, and remarkably, silica morphology modification, from spheres to hexagonal plates, occurred by increasing the degree of polymerisation (DP) of PLL (Tomczak *et al.*, 2005) . This effect on silica morphology was suggested to be by the α -helical secondary structure adopted by PLL at DP > 100, as opposed to random coil for PLL with DP < 100 (Tomczak *et al.*, 2005) . According to Coradin and Livage the presence of amino acids such as serine, lysine, proline and aspartic or polypeptides of such amino acids favoured silicic acid condensation via hydrogen binding and electrostatic interactions, showing the later a more pronounced effect (Coradin and Livage, 2001). Patwardhan *et al.* demonstrated that positively charged peptides are strongly attracted to anionic silica surfaces and, further polar groups in the peptides can attach to silanol or siloxide groups by hydrogen bonding, ion-dipole, dipole-dipole and van-der-Waals interactions (Patwardhan *et al.*, 2012) . Puddu and Perry proved that small changes on the silica surface (i.e. low degree of functional groups) can significantly modulate the binding mechanism at the silica-peptide interface (Puddu and Perry, 2014). Molecular recognition of a solid by a peptide has also been studied combining bioinformatics and molecular simulations. For example, Oren and co-workers, showed that strong crystalline SiO₂-BPs (specifically quartz) always had at least one each of Pro, Leu, and Trp in direct surface contact (Oren *et al.* 2010). Rimola *et al.* demonstrated by computed adsorption energies that amino acids containing side chains with either polar or large aliphatic groups have the most favourable interactions energies towards hydroxylated amorphous silica and suggested hydrogen bonds and London dispersive interactions as the main driving forces (Rimola *et al.*, 2009) . Most recent computational studies performed by Emami *et al.* have shown that the adsorption of charged peptides is highly influenced by the working pH (Emami *et al.*, 2014) . In contrast, no significant difference was observed for neutral peptides which were more weakly bound by hydrogen bonds and hydrophobic interactions (Emami *et al.*, 2014) . Although great advances have been made in the mechanisms concerning silica-biomolecule interactions, the control of selective recognition of biomolecules is still unclear and is a challenge for the fabrication of drug delivery systems and new catalysts, amongst others.

1.5 Motivation and Objectives

The main inspiration for this investigation is how mineral-forming organisms achieve their outstanding control over the assembly and properties of minerals. The studies of peptide-mineral interactions presented in this thesis aimed to identify (a) surface peptide affinity and binding mechanism(s) and/or (b) the effect of peptides on mineral formation. Crystalline ZnO and amorphous SiO₂ were the two materials chosen. The interest in ZnO emerged as this mineral can adopt a great variety of morphologies directly related with its properties/applications and which can be easily modified by the presence of additives (i.e. peptides) into the synthesis system. Amorphous SiO₂ was selected as this mineral has attractive interest for the synthesis of organic/inorganic nanocomposite materials due to its low-toxicity and remarkable colloidal stability in physiological fluids. Further, silica surface modification has been shown to enhance and/or control immobilization of biomolecules (i.e. proteins, and DNA) which can give additional functionality for a variety of applications.

General objectives:

- Synthesize and characterize minerals and mineral-BPs
- Study the mechanisms concerning biomolecule-mineral interactions

Specific aims for ZnO:

- Understand the mechanism of ZnO formation through a hydrothermal method.
- Study the effect of mineral-BPs on ZnO morphology.
- Determine the mechanisms by which these peptides modulate nucleation and crystal growth processes to direct ZnO formation, i.e. the significance of sequence composition and the order and characteristics of the amino acids.

Specific aims for SiO₂:

- Study the properties of different silica particle sizes obtained by two different synthesis methods.
- Determine the level of functionalization that can be achieved for specific functional groups and particle size.
- Study the effect of particle size, surface functionalization and extent of functionalization on SiO₂-peptide interactions.

Chapter II

Experimental Methods

This chapter describes the analysis methods and characterisation techniques used in this thesis. Information on sample preparation and conditions of operation is provided.

2.1 Electron Microscopy

In an electron microscope, the illumination source is produced by a beam of accelerated electrons which allows for the generation of high resolution images at high magnification (up to $\times 10^7$). Therefore, this technique is suitable for the analysis of samples containing particles within the micro- and nano-meter scale. Common techniques using this type of microscopy are transmission electron microscope (TEM) or scanning electron microscope (SEM). Both SEM and TEM can be used to study the morphology of micro- and nanoparticles, including particle size, orientation, aggregation and interconnection. SEM is primarily used to study the surface or near surface structure of bulk specimens, where TEM is more suitable for samples which are smaller (< 100 nm) or where higher resolution is required.

2.1.1 Transmission Electron Microscope

In a TEM, a thin specimen is irradiated with a beam of electrons that transmit through the sample. The electron beam with an accelerating potential of 200 keV is generated by heating a filament, usually made of tungsten or LaB₆. This filament serves as a cathode; and, when a positive potential is applied to the anode, the electrons are accelerated travelling down the column (Figure 2.1). The electrons then pass through the anode into a set of condenser lenses which reduce the aperture of the beam emitted, controlling its diameter and convergence angle when it hits the specimen. Once the beam reaches the sample and goes through, it crosses an objective lens (to form the first intermediate image) with a controlled aperture to eliminate scattered electrons. This first image produced by the objective usually has a magnification of 50-100 times. Finally, the image is magnified through a series of intermediate and projector lenses before striking a phosphor screen or an electronic camera for imaging.

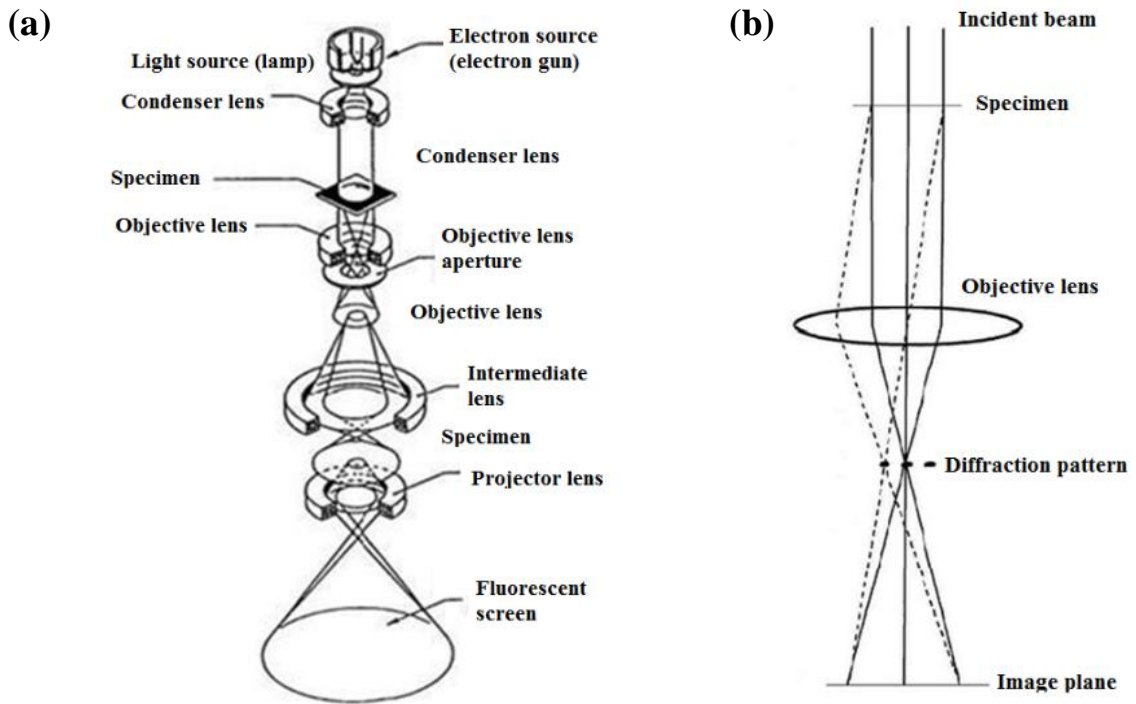


Figure 2.1 (a) Main elements of a TEM and (b) X-ray diagram of the diffraction mechanism (Goldstein, 1981).

Sample analysis was performed by using JEOL JEM-2010 with LaB₆ filament. Samples were suspended in ethanol and sonicated with an ultrasonic bath for 5 minutes before dispersion prior to addition (2-3 drops) onto holey carbon-coated TEM support grids and analyzed after drying.

2.1.2 Scanning Electron Microscope Coupled to Energy Dispersive X-Ray Analysis

Similarly to TEM, SEM is an electron-based imaging technique to study materials. The electron gun, condenser lenses and vacuum system, are similar in both. SEM uses scattered electrons as a basis for image generation. SEM is primarily used to study the surface, or near surface structure of bulk solids. In a SEM, electrons are also generated by a heated filament (generally made of tungsten) and accelerated down the column (towards the sample) at energy between 2 keV and 40 keV. Then, the electrons go through a system of electromagnetic lenses and scanning coils (or pairs of deflector plates) near the end of the column, directing and positioning the focused beam on the target. The high energy incident electrons interact with the atoms of the sample

producing the ionisation of low-energy electrons. The ionised electrons, known as “secondary electrons” (SE), then leave the specimen atom with reduced kinetic energy (5 eV). Each incident electron can produce several secondary electrons but due to their low energy, only secondary electrons that are very near the surface (< 10 nm depth) can escape the sample and be collected at the collector/detector and an image is then generated. In addition, reflected high-energy electrons from the beam produce back-scattered electrons (BSE) along with the emission of characteristic X-rays (< 2 μm depth) with the latter giving compositional information on the sample. Specifically, the intensity of BSE can be correlated to the atomic number of the element giving qualitative elemental information whereas EDX analysis gives more quantitative elemental information. In Figure 2.2 the different interactions that can occur depending on the depth of penetration of the incident beam and types of signal produced are shown; which are SE, BSE, characteristic X-rays, cathodoluminescence (CL), specimen current and transmitted electrons. All these signals can be measured and interpreted providing information about the surface topography and composition of the sample (Goldstein, 2003; Skoog *et al.*, 1998).

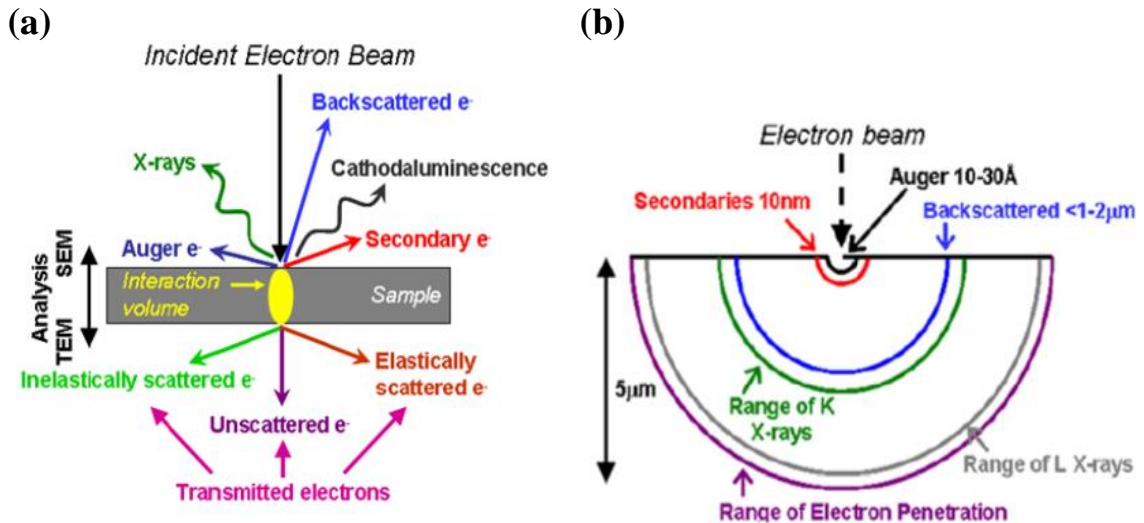


Figure 2.2 (a) Main interactions involved in electron microscopy and (b) depth of penetration (Goldstein, 2003).

In this work, the morphology of the samples was studied with a JEOL JSM-A840A scanning electron microscope (SEM) at an accelerating voltage of 20 kV (Figure 2.3). The SEM had two Faraday Cup-like detectors, a BSE electron and a SE detector. Image

capture, processing system and image-file storage was provided by 'INCA' software (Oxford Instruments). Elemental composition was studied using EDX.

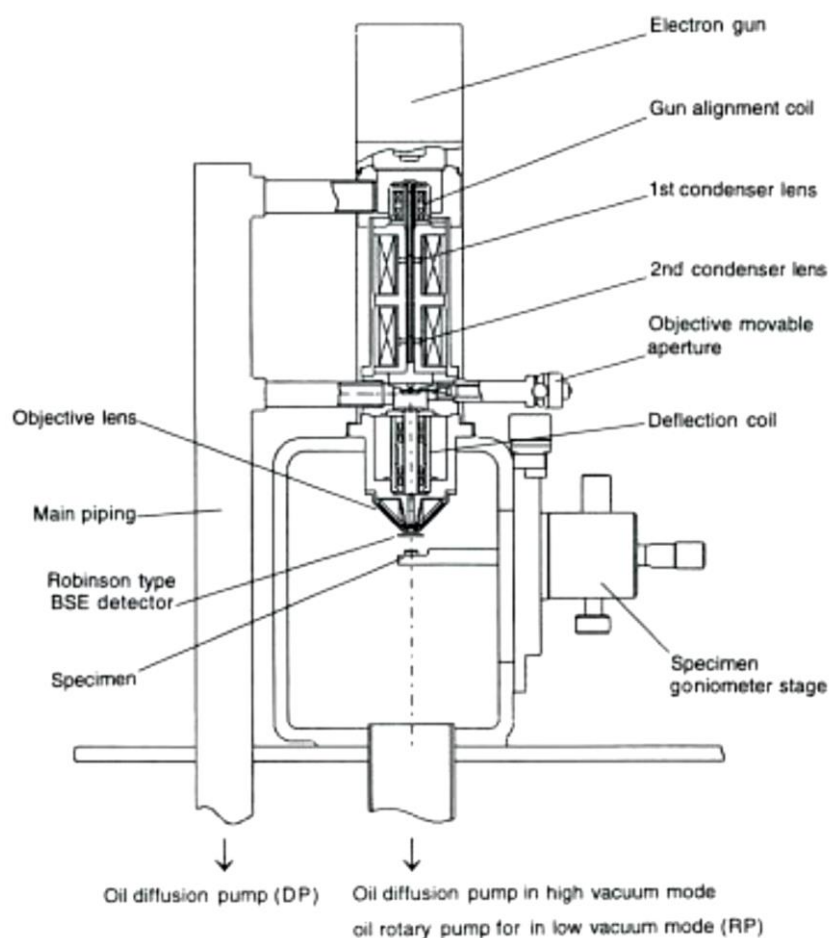


Figure 2.3 Cross section of a SEM (Russell *et al.*, 2001) .

2.2 Attenuated Total Reflectance Infrared Spectroscopy

Attenuated Total Reflectance (ATR) is a technique used in combination with infrared (IR) spectroscopy. The IR radiation has a longer wavelength (λ) and lower frequency (ν) than visible light, corresponding to the region of the electromagnetic spectrum between $14000\text{--}10\text{ cm}^{-1}$ (Figure 2.4). This region is divided in three subregions: the near, mid and far IR. The energy of the radiation in the mid IR region ($4000\text{--}200\text{ cm}^{-1}$) is commonly used in organic chemistry as induces vibrational and rotational transitions in covalently bonded molecules. Only molecules with an electric dipole moment that change during vibration are 'IR-active'. When a specimen is irradiated with IR radiation, molecules/materials absorb specific wavelengths that are characteristic of

their structure. Consequently, the frequency of vibration can be associated with a particular bond type or functional group present in the molecule. Vibrations can involve either a change in the bond length (stretching vibration, ν) or bond angle (bending vibration, σ) (Stuart, 2004).

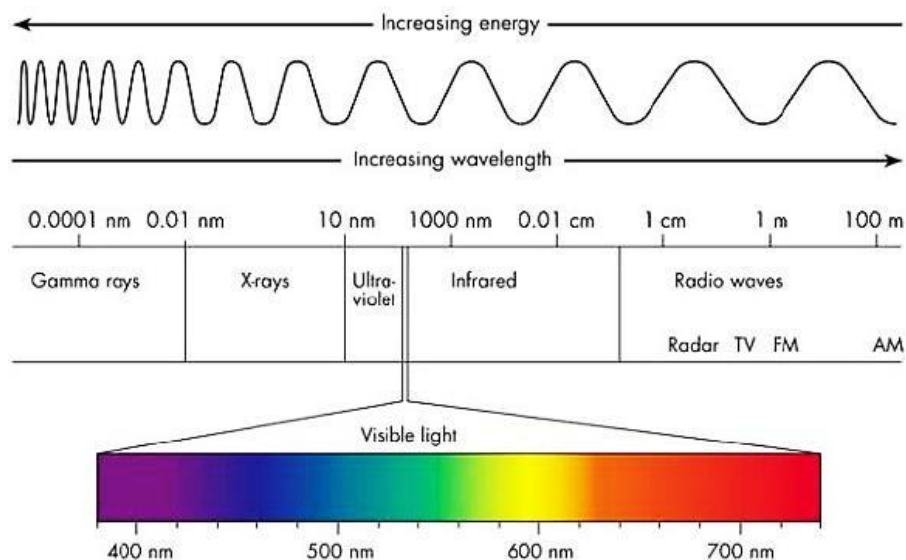


Figure 2.4 The electromagnetic spectrum. Picture taken from <http://serc.carleton.edu>.

ATR spectroscopy employs the phenomenon of *total internal reflection*. A beam of IR radiation penetrates the ATR crystal of a relatively high refractive index and it is reflected from the internal surface of the crystal. As the beam bounces off the crystal, an evanescent wave is established at the crystal interface and is projected into the sample. Some of the energy of the evanescent wave is absorbed by the sample and the reflected radiation (or the resultant attenuated radiation) is returned to the detector (Figure 2.5).

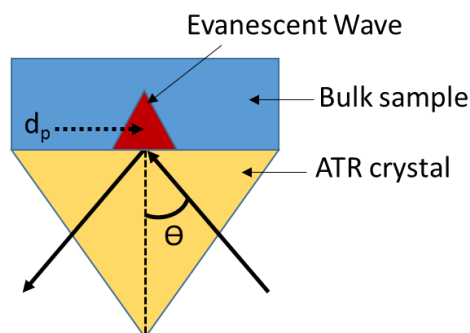


Figure 2.5 Graphical representation of a single reflection in ATR.

The depth of penetration (d_p) is a function of the wavelength (λ), the angle of incidence of the IR beam (θ) and the refractive index of both, the sample (n_1) and the crystal (n_2):

$$d_p = (\lambda/n_1)/\{2\pi[\sin\theta - (n_1/n_2)^2]^{1/2}\} \quad \text{Eq. 2.1}$$

A Perkin Elmer Spectrum 100 Series spectrometer equipped with Deuterated Triglycine Sulphate (DTGS) detector was used for analysis. Data collection over a total range of 4000-650 cm^{-1} and 16 scans were measured at a spectral resolution of 4 cm^{-1} . After, the crystal area was cleaned and the background spectrum collected, the solid material was placed onto the small crystal area (Internal Reflection Element, IRE) and held in place by the Calibrated Pressure Applicator (ASI Applied Systems) to ensure even and reproducible contact between the sample and the IRE (Diamond/KRS-5 crystal) surface. Instrument control and data collection was done using a Compaq 486-DX/66 MHz computer. Data was acquired using Nicolet OMNIC software.

2.3 Thermogravimetric Analysis

Thermogravimetric analysis (TGA) is used for the study of the thermal stability of materials. In this technique the sample is subjected to a temperature rate program under a controlled atmosphere and the change of sample weight is monitored as a function of temperature or time (Skoog *et al.*, 1998). TGA allows for the quantification of water content and/or solvent content, decarboxylation, pyrolysis, decomposition, oxidation, and weight % ash. The instrument is composed of a highly sensitive precision balance to operate in the micro-gram scale, a furnace typically working in a range between 20 to 1000 $^{\circ}\text{C}$, a sample purge gas control with an inert gas such as nitrogen, argon or clean dry air and a computer for data collection and analysis (Figure 2.6). Depending on the atmosphere used different reactions can be studied and vary according to the material analysed (Skoog *et al.*, 1998). For example, in the presence of an inert gas, sample decomposes with temperature (pyrolysis), whereas in the presence of oxygen combined with heat, an oxidative reaction can take place.

In this work, the samples were analysed with a Mettler Toledo TGA/SDTA851^e equipment with an auto sampling unit. Data was acquired and analysed using the STARe DB V9.10 software. Two types of graphs will be show in this thesis: (i) TGA

curve; normalized total % of sample weight loss versus temperature (°C) and (ii) DTG curve; 1st derivative of sample weight loss versus temperature °C.

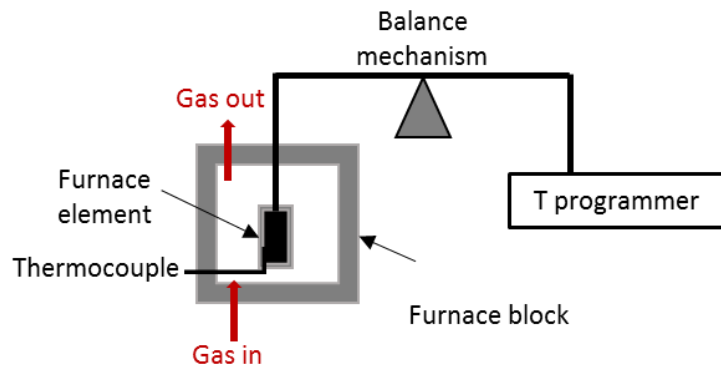


Figure 2.6 Scheme of a thermogravimetric balance.

2.4 Powder X-Ray Diffraction

Powder X-ray Diffraction (PXRD, hereafter named XRD) is a powerful technique for the identification of the crystallinity of a solid-phase sample. A crystalline material has its characteristic diffraction peaks and, therefore, its own characteristic XRD pattern. A crystalline phase consists of elements, such as atoms, molecules or ions, which are highly ordered arranged along its crystal lattice (in all three directions). The diffraction occurs when the X-ray radiation interacts with a crystalline phase and is scattered uniformly in all directions. First, when the X-ray beam strikes the surface of the crystal at an angle θ , a portion of the beam is scattered by the atoms on the surface. The remaining unscattered portion of the beam penetrates the second layer of atoms where another fraction is scattered; this process is repeated throughout further layers of atoms, as shown in Figure 2.7 (Klug and Alexander, 1974; Skoog *et al.*, 1998). For an incident wave of radiation (wavelength, λ), the scattered X-rays from the first layer of atoms travel less distance than the X-rays that penetrate to the internal layers. This distance, known as interplanar distance (d), is the crystal lattice plane separation. Hence, the scattered X-rays from a lower layer of atoms, traverse an extra length of $2d \cdot \sin\theta$, where θ is the scattering angle. This was expressed in an equation known as Bragg's Law, where 'n' is an integer of waves reflected from the different layers (Klug and Alexander, 1974):

$$n \cdot \lambda = 2d \cdot \sin \theta \quad \text{Eq. 2.2}$$

The data acquired from XRD is essentially a plot of diffracted beam intensity against twice the incident angle or 2θ . A diffraction pattern describes then a number of peaks which correspond to reflections from a crystal. The 2θ position of the peaks is a function of the interplanar distance, or d-spacing. From the XRD data, it can also be determined the mean crystallite size (diameter) of the particles by the applying Scherrer equation (Klug and Alexander, 1974):

$$D = \frac{K \cdot \lambda}{\beta \cdot \cos\theta} \quad \text{Eq. 2.3}$$

$$\beta = B_b - B_x \quad \text{Eq. 2.4}$$

Where D is the crystallite domain size (\AA); K is the crystalline shape constant which is generally taken as 0.9 for an approximately spherical crystal; θ is the Bragg diffraction angle (radians); λ is the X-ray wavelength (\AA ; usually from a copper source: $\text{CuK}\alpha$ with $\lambda = 1.5406 \text{ \AA}$); β is the line broadening at half the maximum intensity (FWHM), after subtracting the instrumental line broadening, B_x (radians).

The Scherrer equations is, however, an estimation (not exact value) of the crystallite size due to different morphologies and mean particle sizes can be present within the sample (Klug and Alexander, 1974). It is recommended to use lower angles peaks for calculation of the crystallize size when analysing small particles since peak broadening occurs for smaller particles when increasing the angle.

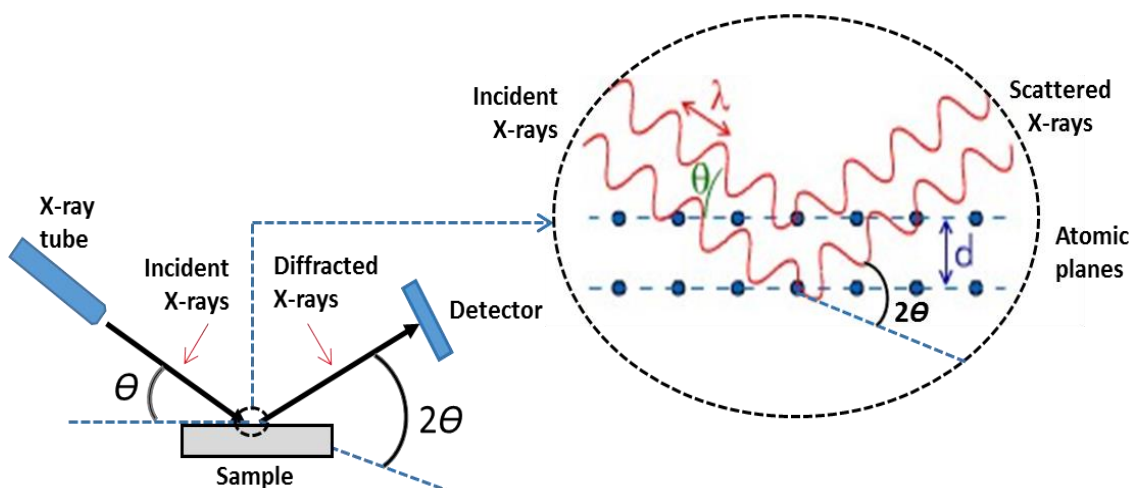


Figure 2.7 Schematic representation of crystallinity study using the X-ray diffraction technique. Illustration adapted from Klug and Alexander (1974).

The crystal phase of the solid samples was identified by using a PANalytical X'Pert PRO X-Ray diffractometer (CuK α radiation with wavelength of 1.54060 Å). Ground samples (if necessary) were packed into an aluminium sample holder and scanned from 5° to 90° of 2 θ (with spinning) at an accelerating voltage of 45 kV, 40 mA filament current, using a scan speed of 0.02 ° s⁻¹ at room temperature. Diffraction patterns were analysed using X'Pert-HighScore Plus (Version 2.0a) programme for diffractogram manipulation, background determination and peak identification. Due to the small amount of sample (in some cases), a little piece of polypropylene (PP) was fitted into the aluminum holder, so less amount of sample was needed for analysis. The characteristic peaks of the holder with the piece of PP material are given in Appendix 2.1. The mean crystallite size (grain size) ratio was estimated using the Scherrer equation (Klug and Alexander, 1974).

2.5 X-Ray Photoelectron Spectroscopy

X-Ray Photoelectron Spectroscopy (XPS), also known as Electron Spectroscopy for Chemical Analysis (ESCA), is a powerful technique that investigates the surface chemistry of a sample providing the elemental composition and the electronic state of such elements. Using the XPS technique, the sample is first placed into a preparation chamber (Figure 2.8) of a moderate vacuum system prior to be transferred to the ultra-high vacuum chamber (UHV). Conditions of UHV are required to minimize the scatter of photoelectrons and contamination of the sample surface. The sample is then irradiated with an X-ray source (either Al K α or Mg K α rays) to excite the electronic states of atoms on the surface. Although X-rays may penetrate deep into the sample, for a standard XPS system using an Al or Mg anode, the energy of the emitted photoelectrons is in the range of 100-1400 eV. Hence, for energies around 1400 eV, photoelectrons from depths higher than 10 nm have low probability of leaving the surface (Fairley, 2009). The emitted photoelectrons pass then through a system of lenses (electrostatic and/or magnetic) that have two main purposes: (i) to define the analysis area by using electrostatic steering plates and metal apertures and (ii) to correct their energy by applying a retard voltage (Hofmann, 2013). The photoelectrons are filtered via the hemispherical analyser (HSA) that only allows the pass of electrons of a given energy, called Pass Energy (PE). As photoelectrons pass through the HSA, they are dispersed radially accordingly to their respective kinetic energy (KE) and recorded

by the detector. The KE of the photoelectrons measured is used to determine the binding energy (E_B or EB) of the emitted electrons by using the following equation:

$$E_B = h \cdot \nu - KE - \Phi \quad \text{Eq. 2.5}$$

Where h is the Planck constant (6.62×10^{-34} J·s); ν , is the frequency of the radiation (Hz); and Φ , is the work function of the analyser.

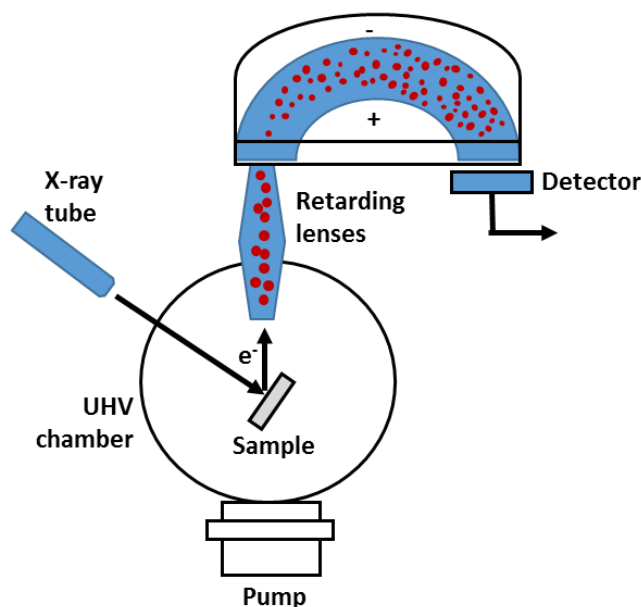


Figure 2.8 Conventional X-rays source for an XPS instrument. Illustration adapted from Hofmann (2013).

The generated spectrum shows the binding energy against the intensity of a photoelectron peak. A single peak is observed for electron transitions from energy level s , whereas a doublet peak is observed for levels p , d and f due to the unpaired electron left after photoemission having either a parallel or antiparallel orientation to the orbital momentum (spin-orbital coupling), thus, there is an energy difference (Hofmann, 2013). The energy separation of the two adjacent peaks of the same orbital (same n , l) increases with the atomic number and decreases for the same n with higher l values. The relative intensities of the doublet peaks are given by the ratio of their degeneracy ($2j + 1$). A chemical shift of the photoelectron peak energy is observed when there is a change in the bonding state of an atom compared to the pure element. For example, when an atom is bonded to another of higher electronegativity, charge transfer occurs and the effective charge becomes positive, increasing the binding energy. During

analysis, surface charging occurs, and consequently, the energy of the peaks is shifted. Hence, charging correction is required by usually using adventitious carbon ($E_B = 285.0 \pm 0.2$ eV) as a reference standard peak. As each element has a characteristic binding energy associated to each core atomic orbital, the elemental identity, chemical state, and quantity of a detected element can be determined. In addition, the spectrum will also contain Auger peaks which are generated by auto-ionization. When a core photoelectron is ejected from an inner shell, the vacancy created can be filled by an electron from a higher energy orbital (Figure 2.9). During this process, the energy released may aid a second electron to be ejected as a photoelectron. This secondary photoelectron is referred to as an Auger electron. Auger peaks reflect the geometry and electronic structure of a molecule; thus, an Auger spectrum gives information to distinguish between protonated states. Like core photoelectron peaks, Auger peaks can be used for quantification and determination of chemistry (Hofmann, 2013).

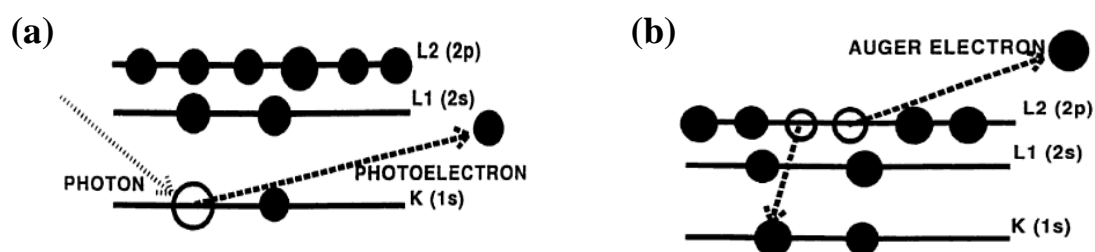


Figure 2.9 (a) Electronic transitions for the photoelectron process and (b) the Auger electron process (bottom) (Hofmann, 2013).

The basic line shape of the XPS peak is given by Lorentzian function where the line width ΔE_0 is determined by the lifetime of the core hole state left by photoemission; however, in crystalline materials, atomic vibrations create a small Gaussian broadening generally caused by the analyser. Hence, the line shape of the XPS peak is fitted by using a mixed Gaussian-Lorentzian function (Hofmann, 2013).

For this study, samples were analysed by Mr Martin Roe from Advanced Materials Research Group, X-ray Photoelectron Spectroscopy, Faculty of Engineering at University of Nottingham. The XPS employed to investigate the chemical constitution of the samples was a VG Scientific ESCALab MkII X-Ray photoelectron spectrometer with Al K α X-ray source ($h\nu = 1483.6$ eV) (Figure 2.10). Samples were ground and then mounted on standard sample holders. Survey spectra were collected covering the

full binding energy (BE) range from 0-1200 eV using a step size of 0.2 eV and pass energy of 50 eV. To compensate for surface charging effects in the insulating samples, all binding energies were corrected with reference to the saturated hydrocarbon C1s peak at 285.0 eV. Core level spectra of desired elements were deconvoluted and fitted according to mixed Gaussian–Lorentzian components using CASAXPS software (Fairley, 2009).

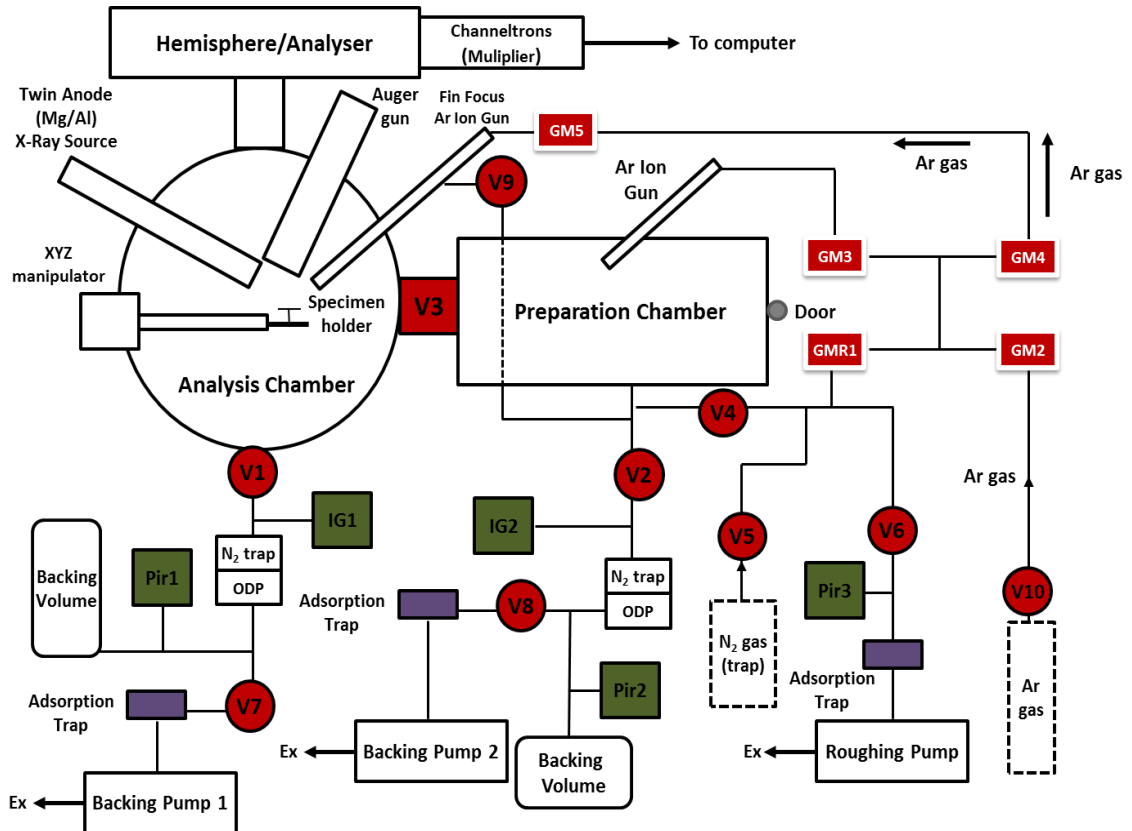


Figure 2.10 Schematic diagram of the VG ESCALab MarkII system.

2.6 Dynamic Light Scattering and Zeta potential

Particle size can be determined by measuring the Brownian motion of particles in a sample using dynamic light scattering (DLS). The relationship between the particle size (spherical) and its diffusion rate is defined in the Stokes-Einstein equation for diffusion in solution (Malvern Instruments Ltd., 2004):

$$D = \frac{K_B \cdot T}{6 \cdot \pi \cdot \eta \cdot r} \quad \text{Eq. 2.6}$$

Where D , is the diffusion constant; μ , is the flow velocity of the particles due to an applied force ($\mu = Vd/F$); K_B , is the Boltzmann's constant ($1.38 \cdot 10^{-23} \text{ J}\cdot\text{K}^{-1}$); T , is the absolute temperature; π , is the constant pi (3.1415); η , is the dynamic viscosity; and r , is the radius of the spherical particle.

In a typical DLS experiment, the sample is irradiated with a monochromatic laser light beam. The particles from the sample scatter the light in all directions which is then recorded by a photomultiplier. The observed scattered intensity fluctuates along the time axis (Figure 2.11), providing information about the motion of the dispersed particles. Finally, the particle size distribution is calculated using a size distribution processor (SDP).

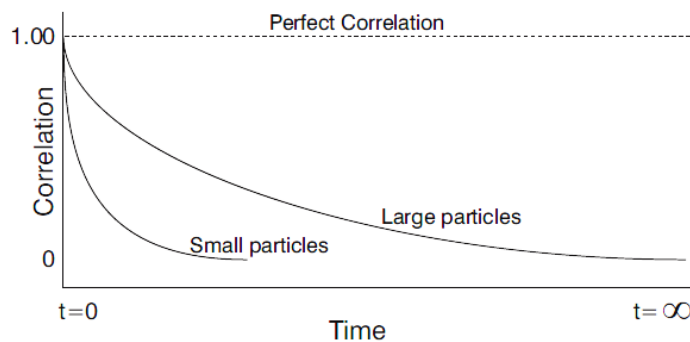


Figure 2.11 Time autocorrelation function of the scattered intensity for large and small particles (Malvern Instruments Ltd., 2004).

Although the size distribution generated by DLS is an intensity distribution, this can be converted to a volume distribution and, further, to a number distribution. The type of distribution chosen will depend on the information needed from the sample. Hence, it is important to distinguish between the three types of distribution (intensity, volume and number) provided by the instrument. The example below (Figure 2.12) shows an easy way to differentiate between them. When there is the same population of two different particle sizes, for example 5 and 50 nm, the number distribution gives the same signal for both particle sizes as the number of particles for each size is the same. However, when plotting volume distribution, the volume of a sphere is defined by $V = 4/3 \cdot \pi \cdot r^3$, thus, the volume of the larger particles is 1000 times higher than for the smaller particles. For intensity distribution, larger particles will scatter much more light (Rayleigh's approximation) giving a much higher signal (Malvern Instruments Ltd., 2004).

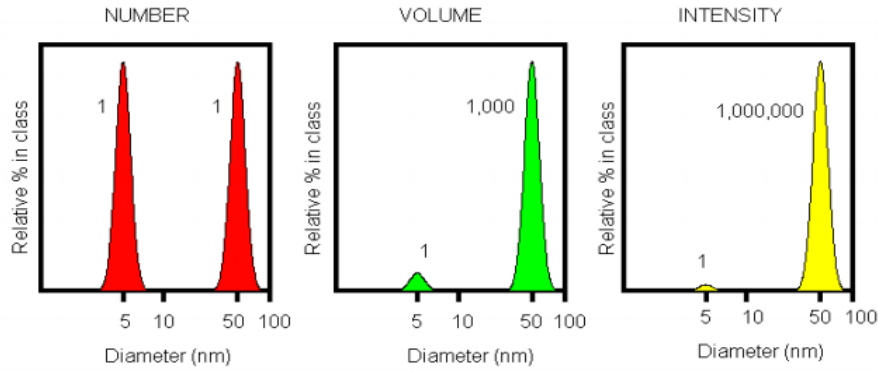


Figure 2.12 Time autocorrelation function of the scattered intensity for large and small particles (Malvern Instruments Ltd., 2004).

Zeta potential measurements are used to determine the surface charge of the particles in a solution. This method measures how fast a particle moves in a liquid when an electric field is applied (i.e. velocity). By knowing the viscosity (η), the dielectric constant (ϵ) and the velocity (or electrophoretic mobility, μ), the zeta potential (ξ) can be determined (Malvern Instruments Ltd., 2004):

$$\xi \approx \frac{4 \cdot \pi \cdot \eta \cdot \mu}{\epsilon} \quad \text{Eq. 2.7}$$

The basic of this technique is that suspended particles in a solution are electrically charged. The development of a net charge at the particle surface will increase the concentration of ions of opposite charge, the so called counter ions, creating an electrical double layer around each particle (Figure 2.13a). Hence, the liquid surrounding the particle presents an inner region (Stern layer) and an outer region (diffusion layer). Ions are more strongly attached in the inner region than in the outer region. When a particle moves (e.g. due to gravity), the ions within the electrical double layer migrate accompanying the particle, whereas the ions beyond the slipping plane (Figure 2.13a) do not. The potential existing at the slipping plane is the so called Zeta potential. As shown in Figure 2.13a (bottom), electric potential decays almost exponentially, which allows introduction "Debye length" (distance from particle surface) as estimate of the electrical double layer thickness. Since the Debye length depends on the ionic strength of the electrolyte; the zeta potential will vary with electrolyte concentration. Another important factor to be considered during zeta potential measurements is the pH of the solution. The pH of the solution at which the

zeta potential will be zero (no charge) is the isoelectric point (pI). Therefore, above the isoelectric point (higher pH), the zeta potential values are negative and get more negatively with increasing pH and *viceversa* (Figure 2.13b).

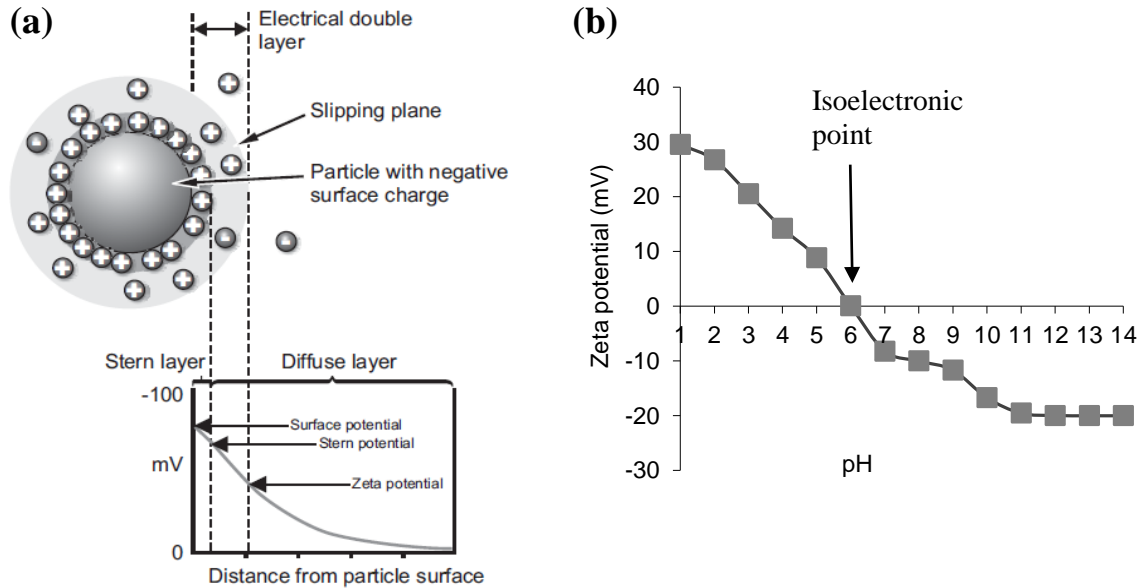


Figure 2.13 (a) Schematic diagram showing the electrical double layer (Malvern Instruments Ltd., 2004) and (b) an example of zeta potential values against pH where the isoelectric point is indicated with an arrow.

In this study, a Zeta Sizer Nano Series (Malvern, UK) was employed to determine the particle size and zeta potential values. For particle size analysis sample were generally suspended in a 5% ethanol solution and size values were obtained from the number distribution in order to show the most populated size. For zeta potential determination, particles were analysed straight from the solution prepared for the study, in this case, phosphate buffer saline solution (pH = 7.4).

2.7 Nitrogen Gas Adsorption

Nitrogen (N_2) gas adsorption is used to determine the surface area and pore size of a given solid material. Samples are first degassed under heat and vacuum to remove adsorbed contaminants, such as water or carbon dioxide, present in the solid due to atmospheric exposure. The temperature and pressure are carefully chosen to avoid any structural change to the sample. After degassing, the atmosphere in the sample container (or sample cell) is sustained at a temperature similar to the boiling point of the

adsorbate gas, commonly N_2 . Hence, the sample cell is immersed in liquid nitrogen under vacuum (77 K, $-195\text{ }^\circ\text{C}$). Once the temperature is equilibrated, a small amount of adsorbate gas (N_2) is introduced into the sample cell and the relative pressure (P/P_0) monitored. This process is repeated several times until a P/P_0 value of 1 is achieved. The quantity adsorbed at each pressure point (from 0 to 1) is then calculated and an adsorption isotherm is constructed. Conversely, desorption isotherms are obtained by measuring the quantities of gas removed from the sample as the relative pressure is lowered (P/P_0 value from 1 to 0). The resulting isotherms can be defined as a measure of the amount of adsorbate (gas) required for forming a monolayer over the external surface of the solid over a range of relative pressures (Brunauer *et al.*, 1938). The final shape of the isotherm is affected by the nature of the surface and the adsorbate and which Brunauer, Deming, Deming and Teller (BDDT) classified into 5 different types (Figure 2.14) (Brunauer *et al.*, 1938).

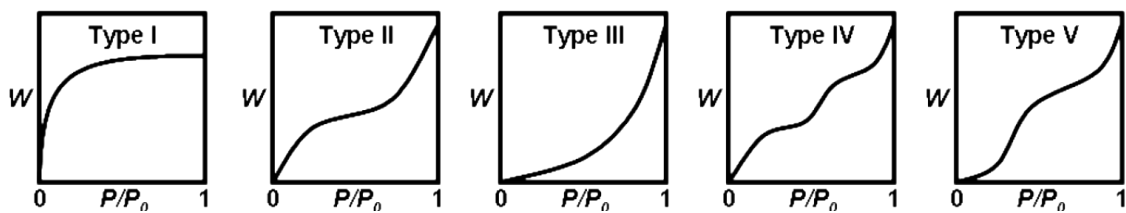


Figure 2.14 Isotherm types as classified by BDDT. W is the mass of adsorbate and P/P_0 the relative (partial) pressure (Brunauer *et al.*, 1938).

The main characteristics of each type of isotherms are:

- Type I: Also known as Langmuir isotherms correspond to microporous solids with relatively small surface area.
- Type II: From non-porous or macroporous materials. The linear horizontal section of the plot is used to determine the P/P_0 at which monolayer coverage is complete.
- Type III: Is a rare isotherm that occurs when the interaction between adsorbate-adsorbate is stronger than the adsorbate-adsorbent.
- Type IV: Same as Type II but with further capillary condensation in mesopores.
- Type V: The most rare isotherm, it is a type III where there are also pores in the mesoporous range.

Surface area measurements are typically done following the Brunauer, Emmet and Teller (BET) method (Brunauer *et al.*, 1938). With this approach, the monolayer coverage by nitrogen as adsorbate is determined from the 0.05-0.35 P/P_0 range. Total pore volume can be calculated from Barret, Joyner and Halenda (BJH) method where the amount of gas adsorbed at a P/P_0 is around 1 (Barrett *et al.*, 1951). Total pore volume allows the estimation of average pore size. For adsorption/desorption plots, hysteresis is generally present; depending on the shape of the plot this can be related to different pore shapes (Figure 2.15):

- Type A: Cylindrical pores.
- Type B: Slit-shaped pores.
- Type C: Wedge-shaped pores with open ends.
- Type D: Wedge-shaped pores with narrow necks at least at one end.
- Type E: “Ink bottle”.

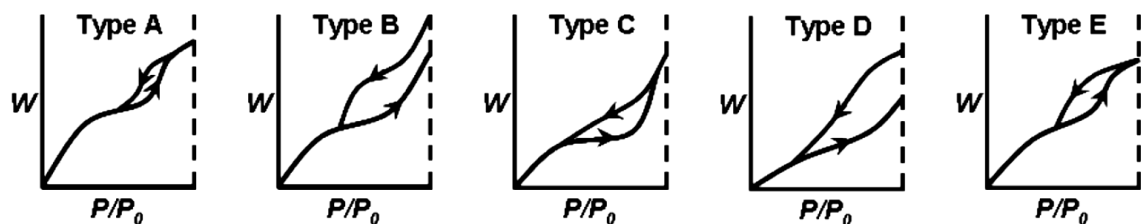


Figure 2.15 Hysteresis types as classified by deBoer. W is the mass of adsorbate and P/P_0 the relative (partial) pressure (deBoer, 1958).

In this study, sample surface area and the N_2 adsorption-desorption isotherms were obtained on approximately 100 mg of sample powder. A Quantochrome Nova 3200e was employed using N_2 as adsorbate. Samples were degassed at 100 °C overnight prior to each analysis. The surface area was determined by BET method using five-point adsorption isotherm in the relative pressure range of $P/P_0 = 0.05/0.3$ at 77.35 K. Pore size distribution was obtained by the BJH method from the desorption branch of the isotherm.

2.8 Inductively Coupled Plasma-Optical Emission Spectrometry

Inductively coupled plasma optical emission spectrometry (ICP-OES), is a powerful technique used for the detection of trace elements, mainly metals. Although, it has wide

element coverage (over 70 elements), there are some elements whose analysis is difficult at the trace level due to their high excitation energies (i.e. halogens) or not possible due to the presence of air in the plasma discharge (i.e. H, N, O and C). Beside this, elemental composition and concentration can be determined for a large number of elements; hence, either quantitative or qualitative information can be obtained. ICP-OES uses inductively coupled plasma to excite atoms or ions that emit electromagnetic radiation at the characteristic wavelength of an element. Therefore, qualitative information is obtained from the wavelengths at which the electromagnetic radiation is emitted by the atoms or ions in the sample and quantitative information is acquired from the amount of electromagnetic radiation (intensity) emitted by the atoms or ions of a particular element. The instrument is composed mainly by two sections: the ICP torch and the optical spectrometer (Cazes and Ewing, 2005). The ICP torch is usually an assembly of three quartz glass tubes and the high-temperature plasma is commonly generated by flowing Argon (Ar) gas through the torch that with the spark of a Tesla coil (an electric field) generates electrons and ions which are then accelerated by the aid of magnetic field, and, finally, collide with other Ar atoms (known as inductive coupling), causing further ionization. Liquid samples are introduced into the nebulizer by a peristaltic pump and converted into an aerosol when impacted with the high-temperature Ar gas. Gaseous molecules in the sample break into atoms. The subsequent excitation or ionization of the atoms generates electrons which emit radiation at the characteristic wavelengths of the elements involved (Cazes and Ewing, 2005).

In this study, a Perkin Elmer ICP-OES Optima 2100DV was employed for element detection and quantification. Standard solutions of elements of interest were prepared from a stock solution (1000 ppm) from BDH Laboratory Supplies. Calibration standard curves were obtained by plotting intensity signal against concentration (ppm) and accepted when the correlation coefficient (R^2) was at least 0.999.

2.9 Solid Phase Peptide Synthesis

In solid Phase Peptide Synthesis (SPPS), the formation of a peptide chain starts on an amino acid (aa) covalently attached to an insoluble solid support (resin) and subsequent incorporation of a desired aa takes place through a series of coupling and deprotection steps (Merrifield, 1963). This process is repeated step-by-step until the desired peptide

length is achieved. At the end of the synthesis, the solid support and ‘usually’ the side-chain protecting groups are all removed from the peptide in a final step known as cleavage. This technique revolutionized the peptide chemistry since purification and characterization is no longer required at the end of each aa addition due to the peptide remaining attached to the resin throughout the synthesis; hence, minimal loss of peptide occurs. Further, successful formation of the peptide is generally achieved as an excess of reagents can be used and the non-reacted products can be easily washed out. This methodology allows its operation in an automated manner, being also a time-saving technique compared with the classical method (Merrifield, 1963). However, a number of variables should be considered to get to the desired final product such as the nature of the resin and its linkage, type of protection groups and coupling chemistries (i.e. single coupling is commonly used but aa like arginine requires a double coupling). Figure 2.16 shows the stepwise SPPS where the C-terminal amino acid is attached to the resin via a carboxyl group. Therefore, the synthesis proceeds in the C→N direction. Any functional group in the aa side chain is usually protected with 9-fluorenylmethyl carbamate (Fmoc) group, in order to direct the aa chain in the C→N direction (avoiding side chain reactions), whereas the α -amino group can be protected with a tertiary butyl-based side chain protection group (*t*Bu), among others (Albericio and Kates, 2000). During the initial loading, the temporary protection group (X) is removed from the aa residue, and therefore, a second aa with the carboxylic group activated is able to form a bond with the already deprotected α -amino group of the initial peptide. After coupling, the excess of reagents is eliminated by washing and the temporary protecting group of the second aa (already attached forming a dipeptide) is then removed. The process is repeated until the desired peptide length is attained (Albericio and Kates, 2000). Finally, the cleavage step for the detachment of the resin and recovery of the peptide can be made using strong acids (i.e. hydrofluoric acid, HF), moderate acids (i.e. trifluoroacetic acid, TFA) or mild acids (i.e. low % of TFA) combined with nucleophilic reagents, known as scavengers (water, thioanisole, phenol, etc.). The use of scavengers is needed as during the cleavage process cationic species are generated from the protecting groups and resin linkers which can react aa containing electron-rich functional groups, as is the case of tyrosine, tryptohan, methionine, and cysteine. The cleaved peptide is then usually re-precipitated in chilled diethyl ether and washed several times with the same solvent. The solvent can be removed either by using a

vacuum oven at low temperature or by bubbling nitrogen into the chilled diethyl ether (Albericio and Kates, 2000).

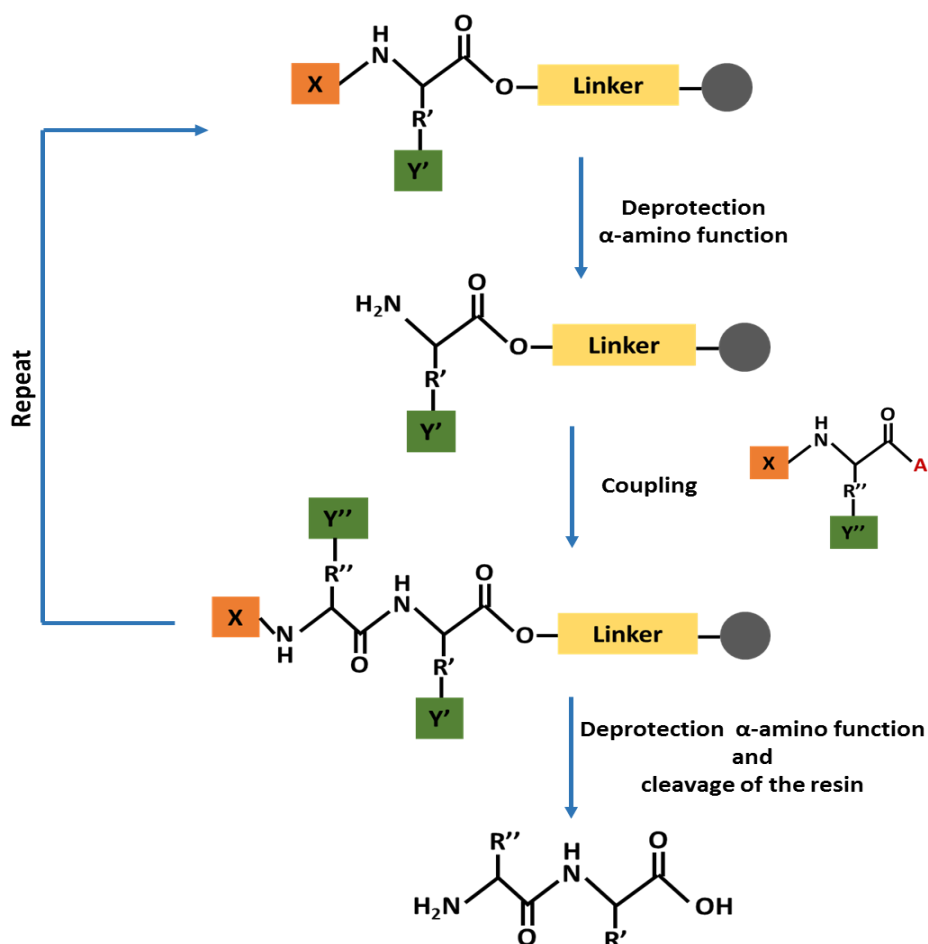


Figure 2.16 Scheme of the stepwise SPPS where, X is the temporary amino protecting group; Y is the permanent side-chain protecting group; A, is the activating group; and the grey circle is the resin. Illustration reproduced from Albericio and Kates (2000).

For this study, peptides were prepared by solid phase methods using a microwave-assisted solid phase peptide synthesizer (CEM Corporation) via Fmoc chemistry (Collins *et al.*, 2009). TGT resin preloaded with protected Fmoc was used as the solid support. The following side chain protections were used: 2,2,4,6,7-pentamethyl-dihydrobenzofuran-5-sulfonyl (Pbf) for arginine; triphenylmethyl (Trt) for cysteine and histidine; t-butyl ester (OtBu) for glutamic acid; and t-butyloxycarbonyl (Boc) for lysine. For the coupling, O-Benzotriazole-N,N,N',N'-tetramethyl-uronium-hexafluorophosphate (HBTU) in N,N-dimethylformamide (DMF) and N,N'-Diisopropylethylamine (DIPEA) in N-methyl-2-pyrrolidinone (NMP) were used as

activator and activator base, respectively. The couplings were single except for arginine where a double coupling was used. Piperazine in DMF was used for N-terminal deprotection prior to each coupling. The cleavage of the peptide from the resin and the final deprotection (side chains) were achieved in one step by treating the peptide resin with a cleaving agent containing TFA, thioanisole, 3,6-Dioxa-1,8-octanedithiol (DODT) and distilled-deionized water (ddH₂O). The cleaved peptides were re-precipitated in chilled diethyl ether and washed three times with the same solvent. Once solvent was evaporated, a few milliliters of water were added and lyophilisation at -70 °C using a Virtis-110 freeze-dryer.

2.10 High Performance Liquid Chromatography

High Performance Liquid Chromatography (HPLC) is an analytical technique based on the separation of molecules (analytes) due to the differences in their structure and/or composition (Kupiec, 2004). By HPLC, the purity and/or content of the analytes in a solution can be determined. In general, the sample and a pressurised liquid (mobile phase) are continuously pumped through a column filled with a solid adsorbent material (solid stationary phase). The components of the sample are separated due to the affinity with the different phases, which depends on the chemical nature of the molecules, the nature of the stationary phase and the composition of the mobile phase. Therefore, analytes travel through the column at different velocities and are eluted (from the column) at different times, known as retention time, which under particular conditions is characteristic of a given analyte (Kupiec, 2004). The retention time is also described as column capacity factor (k'):

$$k' = \frac{T_A - T_0}{T_0} = \frac{V_A - V_0}{V_0} \quad \text{Eq. 2.8}$$

Where V_A , is the elution volume of the component A and, V_0 , is the elution volumes of a non-retained compound. At constant flow rate, the retention times ($T_A - T_0$) can be used instead the elution volumes.

Chromatographic separations can be performed using a variety of stationary phases, including immobilized silica or alumina. The chemistry of the columns can be modified with functional groups (such as phenyl, cyano and alkyl) for best separation results. For example, pristine silica surface (negatively charged surface) is recommended when the

sample contains ionized molecules as electrostatic interactions will be involved during separation (Kupiec, 2004). Stationary phases such as ‘cyano’ enhance the retention of polar compounds by dipole-hydrogen interactions. The separation of hydrophobic molecules is best achieved by the presence of alkyl ligands on the silica surface (Kupiec, 2004). The type and composition of the mobile phase also affects the separation of the components. The mobile phase is commonly made from a mixture of polar and non-polar liquid components. Two types of HPLC methods can be applied depending on the solid stationary and mobile phases employed: normal-phase (NP) or reverse-phase (RP). When the stationary phase is more polar than the mobile phase, the separation is considered NP-HPLC and, conversely, RP-HPLC when it is less polar. RP-HPLC is commonly applied to separate molecules based on their hydrophobic properties; thus, it is a useful technique for the analysis of peptides and proteins.

HPLC instrumentation consists of a pump, mobile phase reservoir, injector, column, detector and integrator or acquisition and display system (Figure 2.17). A high-pressure pump is required to move the mobile phase through the column as the solid stationary phase is composed of micro-sized porous particles. The injector can be a single injection or an automated injection system within a volume range of 0.1-100 ml. The main types of detectors are UV-vis, refractive index (RI) and fluorescence. The response of each component detected is displayed on a computer screen and is known as a chromatogram. The chromatogram is represented by the intensity of the signal (y axis) and the retention time (x axis).

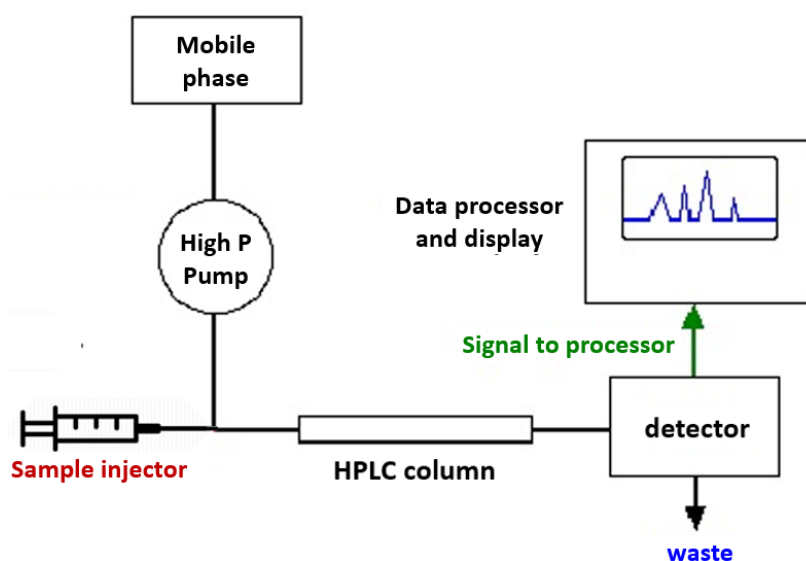


Figure 2.17 Scheme of the parts of a HPLC.

For this study, the purity of the synthesized peptides was determined by using a Dionex HPLC with a UV detector (set at 214 nm) and a Jupiter 4u Proteo 90A C12 Reverse Phase column (Phenomenex). Data processing was performed with the Chromeleon® software. The solid stationary phase consisted of tightly packed silica particles. The mobile phase consisted of two eluents made up of a mixture of solvents: (a) 95 % HPLC grade distilled water with 5% HPLC grade acetonitrile (more polar mobile phase) and (b) 5 % HPLC grade distilled water with 95% HPLC grade acetonitrile and 0.1% formic acid (less polar mobile phase). Both eluents were primed through the column separately for equal periods of time. A control sample made of 50% HPLC grade acetonitrile and 50% HPLC grade water was run before and after sample analysis.

2.11 Isothermal Titration Calorimetry

Isothermal Titration Calorimetry (ITC) is a unique and highly sensitive technique used for the study of biochemical interactions. ITC measures the energy released (exothermic) or absorbed (endothermic) by the system when a reaction takes place. Experiments are performed by titration of a reactant (i.e. biomolecule) into a sample solution containing the other reactant (i.e. substrate). After each addition, heat changes are recorded allowing quantitative characterization of the energetic processes (i.e. binding reaction) (Freire *et al.*, 1990). As a result, a binding isotherm is obtained from the plot of heat of formation against the molar ratio of the substrate to biomolecule giving information about the enthalpy (ΔH), association or binding constant (either K_a or K_B) and stoichiometry (n) of binding. The Gibbs free energy (ΔG) can be then determined applying:

$$\Delta G = -R \cdot T \cdot \ln K_B = \Delta H - T \cdot \Delta S \quad \text{Eq. 2.9}$$

Where T , is the experimental temperature; R , is the gas constant ($8.314 \text{ J mol}^{-1} \text{ K}^{-1}$) and ΔS is the change in entropy.

ITC system mainly consists of a calorimeter and a syringe assembly (Figure 2.18). The calorimeter is composed by a reference cell and a sample cell which are enclosed in an adiabatic jacket. The cells are made of a thermally conducting and chemically inert material such as Hastelloy¹ alloy or gold. The reference cell usually contains the same solvent in which the sample has been prepared in.

¹Hastelloy is the trademark of Haynes International Inc. and is prefixed to a series of highnickel alloys designed for corrosion resistance (Philip 2004).

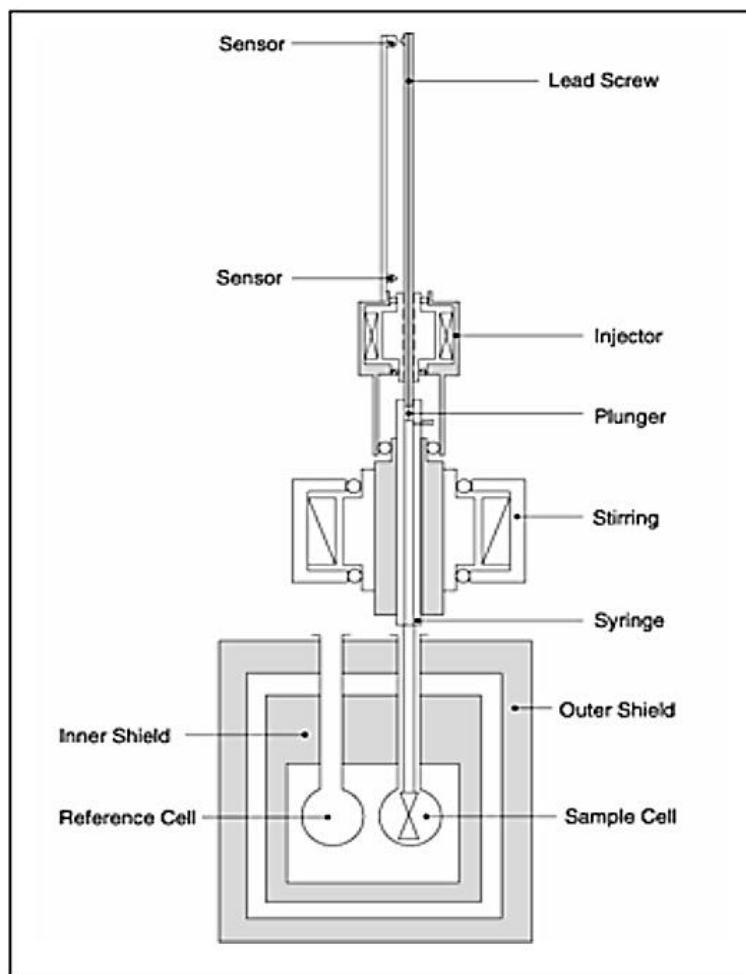


Figure 2.18 Scheme of VP-ITC from MicroCal VP-ITC Microcalorimeter User's Manual (Freire *et al.*, 1990).

Temperature differences between the reference cell and the sample cell are measured and calibrated to power units ($\mu\text{cal}\cdot\text{s}^{-1}$), known as differential power (DP) signal. It is important that the temperature of the reference cell and sample are at equilibrium before titration begins. The syringe assembly mainly involves an injection syringe and an automated pipette injector, accompanied with a stirring system and a high precision syringe pump for efficient titrant delivery. For each injection, a DP signal is recorded as a result of the energy absorbed or released in the system when the reaction occurs between the substrate and the biomolecule. The extent of heat change depends on whether an interaction occurs or not. If no interaction takes place, heat changes will be similar to those observed when titrating the solvent with the solvent (Blank reaction). On the other hand, when interaction occurs, the heat changes in the Blank reaction will be subtracted to the heat changes of the 'true' reaction in order to study the magnitude of these interactions. Optimization of the method is required to (i) reach

saturation-endpoint of the reaction, (ii) to minimize interference in heats measured and (iii) to obtain sufficient measurements for prediction of curve shape. Experimental optimization is achieved by varying a number of experimental parameters: total number of injections, cell temperature ($^{\circ}\text{C}$), reference power ($\mu\text{cal}\cdot\text{s}^{-1}$), stirring speed (rpm), injection volume (μl), injection duration (s), spacing between injections (s), syringe concentration (mM) and cell concentration (mM).

Once the titration is completed, the heat changes (in $\mu\text{cal}\cdot\text{s}^{-1}$) during a certain period of time are integrated by the instrument software (Figure 2.19a). The resulting ITC binding isotherm is obtained by the plot of the normalized integrated heat change in $\text{Kcal}\cdot\text{mol}^{-1}$ of injectant against the molar ratio of the biomolecule (Figure 2.19b). The accuracy of the K_B value is evaluated by the critical parameter (C) which is product of the total concentration of the cell component (K_B) and the stoichiometry (n). The C parameter ideally lie between 10 and 100 (Cliff *et al.*, 2004) and determines the shape of the isotherm. Depending on the shape of the isotherm, the data can be fitted using either identical or two independent sites binding model. The main difference between the models is that the binding sites can have the same ΔH and K_B values (one set of identical sites model) or have two different binding sites with separate values of ΔH and K_B (two sets of independent sites model) (Freyer and Lewis, 2008; Limo *et al.*, 2014).

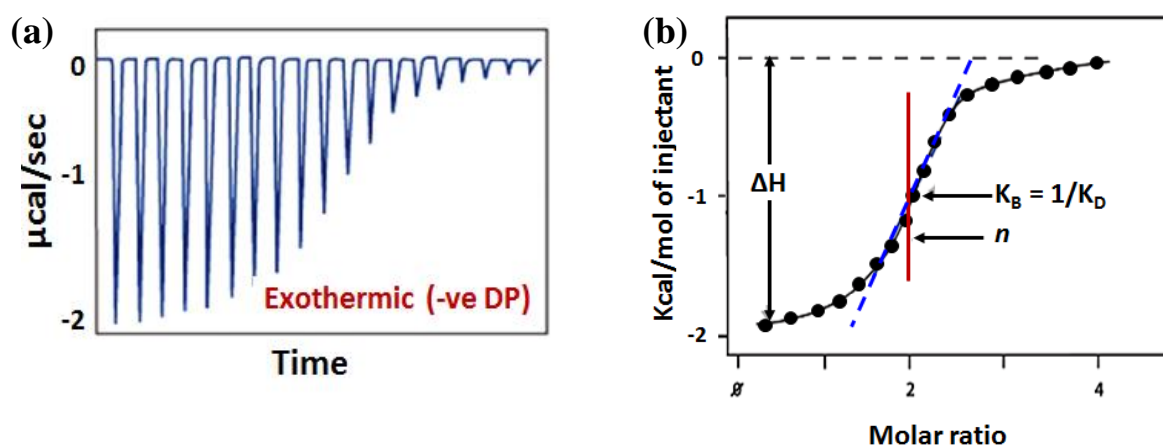


Figure 2.19 ITC data for (a) raw data showing an exothermic reaction and (b) ITC isotherm fitted to a one independent site model. Adapted from (Milev, 2013).

The instrument used to carry out ITC studies was a MicroCal VP-ITC. Data analysis was conducted using ORIGIN v7.0 software. For fitting, a non-linear least-square algorithm with binding sites models available by MicroCal was used.

2.12 Fluorescence Spectroscopy

Fluorescence spectroscopy is based on the electronic and vibrational states of molecules. At room temperature most molecules occupy the lowest vibrational level of the ground electronic state (Figure 2.20). A beam of light, commonly UV light, excites the electrons in molecules to a higher vibrational state, known as excited vibrational state. These electrons then drop down to the lowest levels of the excited vibrational state dissipating part of the energy absorbed during excitation, process known as internal conversion. Fluorescence emission occurs when these electrons (in the lowest vibrational levels of the excited state) return to the ground state. During this process, photons are released emitting at different wavelength depending on the vibrational level of the ground state they move in. Hence, each transition occurs at specific and single wavelength, being the transition energy:

$$E = h \cdot \nu = \frac{h \cdot c}{\lambda} \quad \text{Eq. 2.10}$$

Where h , is the Planck constant (6.63×10^{-34} J·s); ν , is the light frequency (s^{-1} or Hz); c , is the light velocity (3.00×10^8 m·s $^{-1}$) and; λ , is the wavelength (nm).

Therefore, the detection of the different frequencies of light emitted in fluorescent spectroscopy, allows for the determination of the structure of the different vibrational levels in molecules.

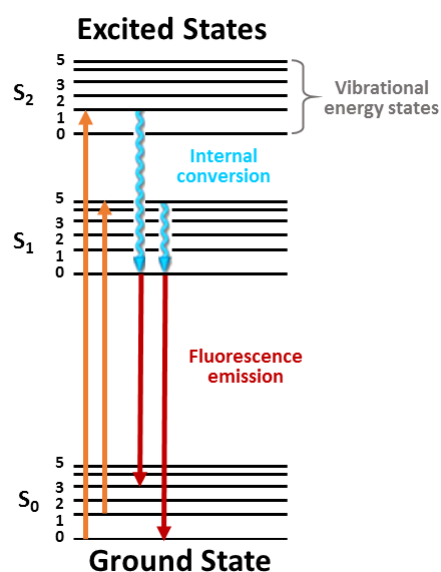


Figure 2.20 Representation of transitions giving rise to fluorescence emission. Adapted from (Lakowicz, 2013).

Chapter III

Mechanism of ZnO Formation from Aqueous Solution of Zinc Acetate

3.1 Introduction

The structure and/or morphology of ZnO is predicted to play an important role in its applications due to control over the physical and chemical properties of the material (Djurišić *et al.*, 2012). Its controlled synthesis has been an interesting area of research either to develop more simple, cost-effective, reproducible and eco-friendly fabrication routes (Yoshimura and Byrappa, 2008) or for the growth of crystals with a specific size and shape (Liu and Zeng, 2003; Masuda *et al.*, 2007; Singh *et al.*, 2012). Solution synthesis methods involving the hydrolysis of metal alkoxides or simple inorganic salts have become of considerable importance in the growth of metal oxides like SiO₂ and ZnO (Masuda *et al.*, 2007; Ohya *et al.*, 1994; Stöber *et al.*, 1968). Particularly, hydrothermal methods are attractive for their simplicity, low cost and green chemistry approach (low energy consumption, closed system, etc.) and also due to the nucleation control during the crystallization process. Although hydrothermal methods only contribute to about the 6% among all solution syntheses routes (Yoshimura and Byrappa, 2008), this technique presents the advantage of using hot fluids that offer high diffusivity and low viscosity which facilitates mass transport and; hence, enhance the kinetics of reaction (Yoshimura and Byrappa, 2008). This synthesis approach has been shown to generate a wide range of highly crystalline structures by simply tuning reaction parameters. Parameters such as solution composition (precursors and solvents), temperature, pressure and pH have been carefully monitored to obtain the desired ZnO structures (Amin *et al.*, 2011; Dove *et al.*, 2003; Govender *et al.*, 2004; Masuda *et al.*, 2007). ZnO rods, belts, wires, plates, rings, tetrapods, prisms, pyramids, spheres, cubes, hollow structures, pot-like, flower-like and multi-needle shaped crystals have been synthesized using solution routes (Baruah and Dutta, 2009; Hamada *et al.*, 2011; Jang *et al.*, 2008; Kimitsuka *et al.*, 2013; Liu and Zeng, 2003; Masuda *et al.*, 2007; Wang *et al.*, 2007; Wang *et al.*, 2004; Yin *et al.*, 2014; Zhou *et al.*, 2002). Figure 3.1, shows some of

the ZnO structures that have been reported up to date by using solution route synthesis via the hydrothermal method.

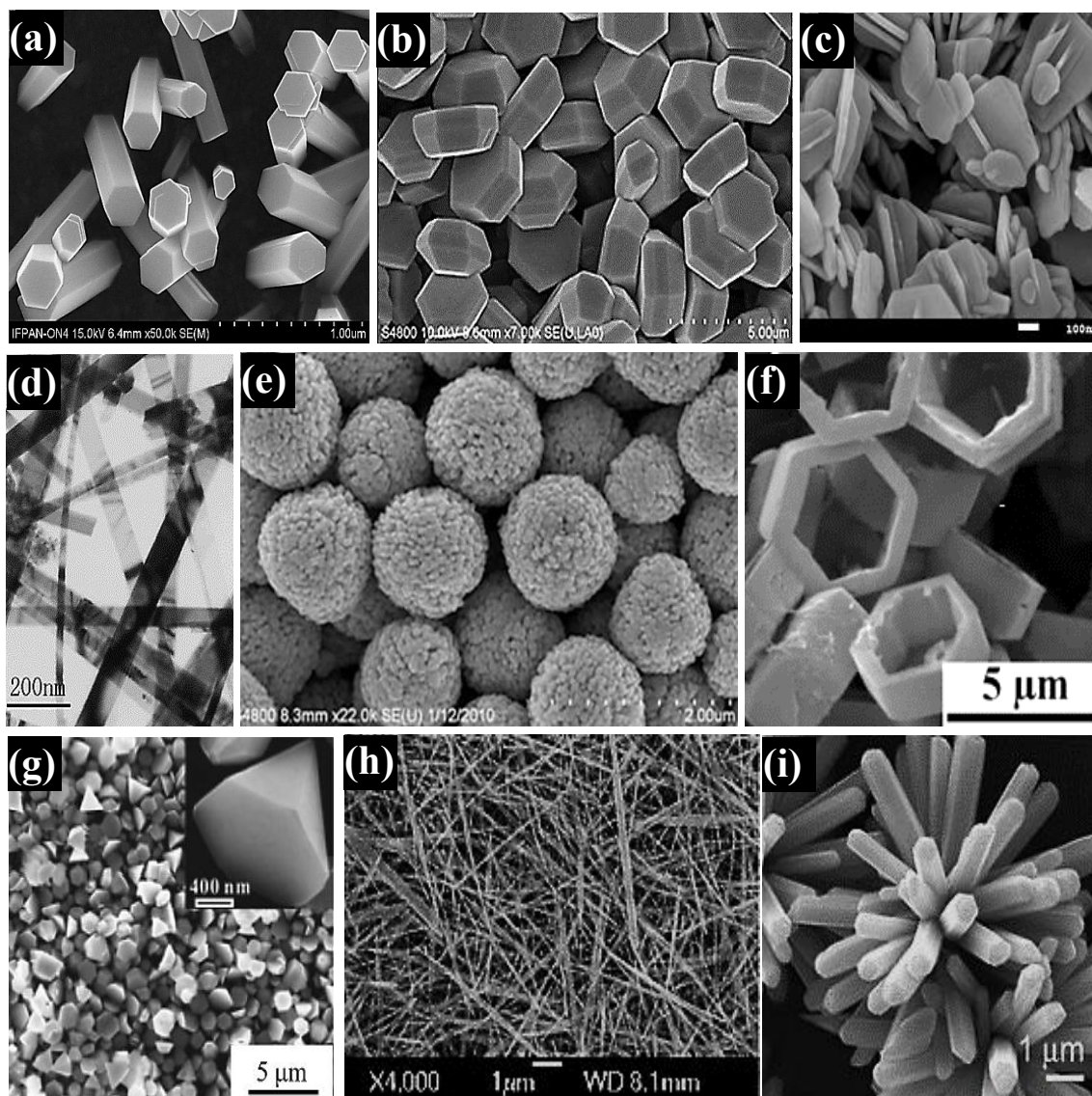


Figure 3.1 ZnO structures synthesized via hydrothermal method (a) nanorods (Pietruszka *et al.*, 2014), (b) pot-like (Yin *et al.*, 2014), (c) nanoflakes (Ramimoghdam *et al.*, 2012), (d) nanobelts (Hu *et al.*, 2007), (e) spheres (Yin *et al.*, 2014), (f) micro-rings (Lian *et al.*, 2011), (g) pyramids (Zhou *et al.*, 2005), (h) nanowires (Hu *et al.*, 2007) and (i) flowerlike (Sun *et al.*, 2010).

To understand the different morphologies obtained, there is the need to know the processes behind the formation of a crystal. Crystallization only occurs when supersaturation is reached in the system since the spontaneous appearance of a new phase occurs only in non-equilibrium conditions (Erdemir *et al.*, 2009). Therefore, the

rate and mechanism of crystal formation in liquid solution depends on the solubility, diffusivity (molecular or ionic transport) and solid-liquid interfacial tension (Rodríguez-hornedo and Murphy, 1999). Likewise, supersaturation can be created by a change in the temperature, pressure and pH of the system (Rodríguez-hornedo and Murphy, 1999). Once the solution is supersaturated, crystallization takes place by two major events: nucleation and crystal growth. The initial nucleation process occurs when a sufficient number (critical size) of molecules, atoms or ions in the solution are brought together generating a new thermodynamic phase (nuclei) as defined by classical nucleation theory. Although, the free energy of the system increases due to the increase of the surface energy (ΔG_s), when the critical size (r_c) is reached (Figure 3.2a), the total free energy of the system starts to decrease due to the higher stability of the solid state in respect to the liquid (ΔG_v) and; thereby, growth becomes energetically favourable (Erdemir *et al.*, 2009; Gibbs, 1878; Zeng *et al.*, 2011). Henceforth, the arrangement of these molecules, atoms or ions in a highly ordered structure and subsequent growth of the nuclei gives rise to the crystal growth process. The direction of crystal growth depends on the surface energy of the growing facets, with the low energy faces (thermodynamically more stable) being preferentially expressed. Moreover, nucleation can occur through two different mechanisms; homogeneous and heterogeneous nucleation. Each mechanism will give place to a rate of crystal growth and in like manner the final crystal morphology can be modified (Cox *et al.*, 2013; Govender *et al.*, 2004). The main difference between the two mechanisms is that the energy barrier (ΔG) needed for nucleation is reduced in the case of heterogeneous nucleation (Figure 3.2b) due to the presence of an active surface site, for example, the wall of the bottle or the presence of impurities facilitating the nucleation process (Rodríguez-Hornedo and Murphy, 1999; Zeng *et al.*, 2011). While homogeneous nucleation occurs spontaneously and randomly, heterogeneous nucleation can be considered as an interface catalysed process (Bhat, 2015; Turnbull, 1950).

For ZnO, the crystallization process at low levels of supersaturation is dominated by heterogeneous nucleation and well-defined polyhedral crystals are commonly formed, whereas for homogeneous nucleation (high level of supersaturation), a dendritic to spherulitic morphology is typically achieved (Baruah and Dutta, 2009; Govender *et al.*, 2004). The presence of nanoparticles (fine ZnO powders) can be observed at very high levels of supersaturation as to minimize the overall energy of the system; crystals tend

to agglomerate losing its well-defined morphology (Singh *et al.*, 2012). Commonly used hydrothermal methods work at low levels of supersaturation, as allows for the formation of particles with a regular polyhedral crystal face and facilitates the study of the growth habit of the crystals (Li *et al.*, 1999) .

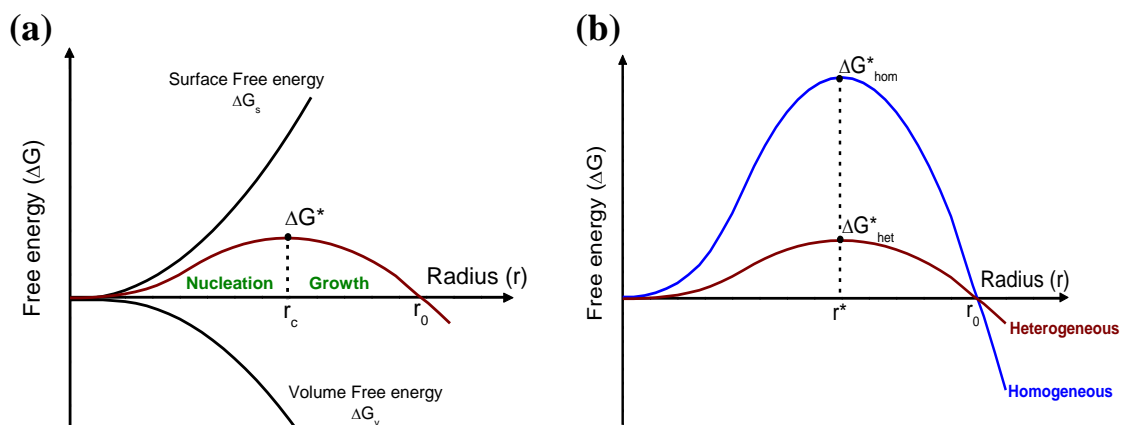


Figure 3.2 (a) Nucleation pathways under thermodynamic control in classical nucleation theory; and (b) energy barrier for a homogeneous and heterogeneous nucleation. Images have been adapted from Zeng *et al.* (2011).

Nevertheless, nucleation and growth may occur by more complicated pathways than suggested by the classical nucleation theory as observed by biomineralization studies in which not only thermodynamic contributions are present but also kinetic driving forces (Mann, 1998; Teng, 2013). Kinetically driven crystallization often involves the formation of a metastable solid phase (reached with loss of free energy) that may be nonstoichiometric, hydrated, and easily phase transformed (Cölfen and Mann, 2003; Rodríguez-Hornedo and Murphy, 1999). As shown in Figure 3.3, a change of the activation-energy barriers of nucleation, growth, and phase transformation is, in principle, achieved by kinetic control (Cölfen and Mann, 2003; Xu *et al.*, 2007). Note that, the activation energy barrier is the minimum energy required to reach the transition state. Thus, the crystallization process occurs through a multi-step route which implies structural and compositional transformation from amorphous precursors in solution to the crystalline solid state through the formation of intermediates in a phenomenon referred to as Ostwald's Law of phases (Cölfen and Mann, 2003; Liu and Zeng, 2004; Teng, 2013; Yoreo and Vekilov, 2003). Generally, these intermediates present higher solubility than the final solid phase (more thermodynamically stable phase) leading to a

faster precipitation (higher nucleation rate). Consequently, phase transformation usually takes place through dissolution and re-nucleation processes, known as Ostwald ripening (Cölfen and Mann, 2003; Liu and Zeng, 2004; Rodríguez-Hornedo and Murphy, 1999; Yoreo and Vekilov, 2003). As a result, the final crystal morphology is thought to be dictated by both thermodynamic and kinetic contributions (Erdemir *et al.*, 2009; Yoreo and Vekilov, 2003).

For ZnO, layered basic zinc salts (LBZs) have been identified as intermediate products during solution route synthesis via the hydrothermal method (Jang *et al.*, 2010; Tokumoto *et al.*, 2003; Wang *et al.*, 2006; Wang *et al.*, 2011). LBZs also have attracted attention due to its proposed brucite-like structure which confers to this material good properties for its application in anion exchange (Morioka *et al.*, 1999). LBZs have become favored bottom-up compounds in catalysis, separation technology, intercalation and drug delivery (Arizaga *et al.*, 2007; Inoue and Fujihara, 2011; Morioka *et al.*, 1999; Newman and Jones, 1999).

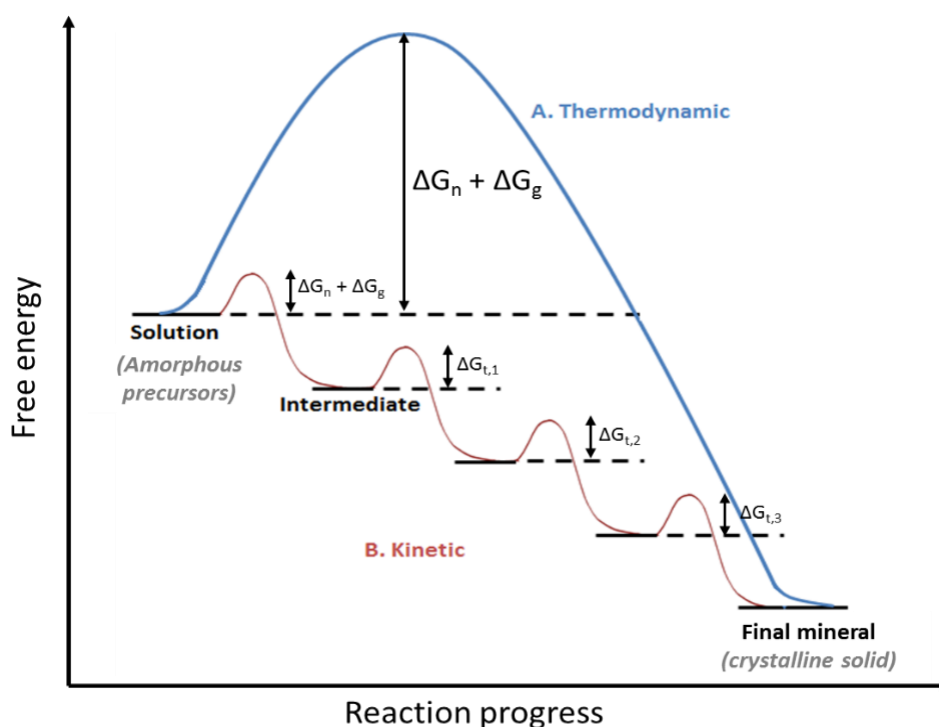


Figure 3.3 Proposed crystallization pathways under thermodynamic control (A) by one-step route (classical nucleation theory) and kinetic control (B) by multi-step routes where proceeds by sequential precipitation (Ostwald's Law of phases). The free energy of activation is associated with nucleation (n), growth (g), and phase transformation (t). Image has been adapted from Cölfen and Mann (2003).

Ultimately, the direction of crystal growth depends on the surface energy of the growing facets, with the low energy faces (thermodynamically more stable) preferentially expressed, and as a result ZnO crystals are inherently elongated along the *c*-axis. However, crystal growth habits can be highly influenced by the presence of impurities/additives. Since ZnO morphology modification is investigated in the presence of peptides (Chapter 4); in this study, the product formation and phase transformation was monitored over time in order to understand the ZnO crystal growth mechanism for the selected synthesis conditions. Further, phase transformation processes were studied by comparison of another solution synthesis route which also results in the formation of wurtzite structured twinned hexagonal rods of ZnO (Liang *et al.*, 2014).

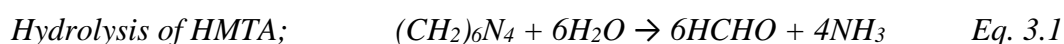
3.2 Effect of pH on ZnO Morphology

ZnO possesses a large family of highly crystalline nanostructures that can adopt a great variety of morphologies which are predicted to play an important role for their applications (Wan *et al.*, 2004; Wang, 2004). The growth of the ZnO crystals can be influenced by many factors; such as temperature, pH, reaction time, precursors, etc. Through the hydrothermal method, the change of pH has been shown to play an important role on the ZnO morphology (Amin *et al.*, 2011; Baruah and Dutta, 2009; Masuda *et al.*, 2007), with the growth rate of ZnO crystal being faster in basic pH conditions (Baruah and Dutta, 2009). As previously mentioned (section 3.1), supersaturation of the system is the driving force for such nucleation and crystal growth processes. Low levels of supersaturation indicate that ZnO is crystallized by heterogeneous nucleation whereas for higher levels of supersaturation homogeneous nucleation dominates (Govender *et al.*, 2004; Lu and Yeh, 2000). Lu *et al.* observed that when changing the basicity of a system (zinc nitrate and ammonia solutions under thermal treatment in a range of 100-200 °C); crystallization occurred through heterogeneous nucleation at pH < 11, where basic Zn precursors were partially dissolved; whereas at pH > 11 basic Zn precursors were dissolved (a clear solution was observed) and, hence, ZnO was crystallized through homogeneous nucleation (Lu and Yeh, 2000). It was also observed that the yield of products decreased with higher pH values as the probability of nucleation in a homogenous solution is less favourable than in an heterogeneous solution (Lu and Yeh, 2000). Solution syntheses routes using other

Zn precursors have also shown a change in the morphology of ZnO formed by varying the pH. Singh *et al.* used zinc chloride in an aqueous solution of ammonia. The pH of the reaction from 8-11 was increased by addition of ammonia. The morphology of the ZnO precipitates changed from nanorods (pH = 8) to nanoparticles (pH = 11). The morphology change was attributed to the dominance of a dissolution effect and homogeneous nucleation (Singh *et al.*, 2012).

Dissolution processes are controlled by Zn-O hydrolysis reactions. Kinetic control of metal ion hydrolysis may proceed by (i) forced hydrolysis or (ii) controlled release of hydroxide (Matijevic, 1993). The precipitation of metal oxides through forced hydrolysis involves the deprotonation of the hydrated ions formed during the ageing of the aqueous metal salt solution at elevated temperatures (80-100 °C) and as a result the pH decreases throughout the course of the reaction. In the case of Zn²⁺, a not easily hydrolysable cation, precipitation can be induced by increasing the pH with a weak base (Govender *et al.*, 2004; Matijevic, 1993). On the other hand, a slow release of hydroxide ions into the metal salt solution can promote the hydrolysis of cations (Govender *et al.*, 2004). This process generates basic metal salts, such as LBZs, that are later transformed to the oxide phase.

Ammonia and hexamethylenetetramine (HMTA) have been extensively used as base sources to release the hydroxide ions into the solution for the ZnO formation (Amin *et al.*, 2011; Govender *et al.*, 2004; Polsongkram *et al.*, 2008; Tokumoto *et al.*, 2003). In the case of HMTA, a slower release of hydroxide ions into the system occurs due to, first, hydrolyses forming ammonia (Equation 3.1) which subsequently acquires hydrogen ions from H₂O to generate ammonium and hydroxide ions (Equation 3.2).



Henceforth, morphology modification caused by pH variation is believed to be due to the reactions taking place during ZnO formation (Equation 3.3-3.4). A study carried out by Amin *et al.* using zinc acetate and ammonia as precursors showed that the increase of pH by adding sodium hydroxide into the system (pH ~ 9) resulted in the formation of ZnO nanotetrapods instead ZnO nanorods (pH~7) (Amin *et al.*, 2011). This modification was attributed to the increase of hydroxide concentration in the initial

solution which led to the formation of a new growth precursor (Equation 3.5), causing anisotropic growth at the active site of ZnO seeds (Amin *et al.*, 2011) .



ZnO morphology modification can be also conducted by simply varying the ratio of the reagents employed (which also leads to a change in the pH), as shown by Masuda *et al.* In like manner, an increase of hydroxide concentration in the initial solution is produced giving for $[\text{NH}_3]/[\text{Zn}(\text{CH}_3\text{COO})_2] = 2$ (pH ~ 7) rod-like structures and for $[\text{NH}_3]/[\text{Zn}(\text{CH}_3\text{COO})_2] = 6$ (pH ~ 9) multi-needle shape structures (also named ZnO nanotetrapod) (Masuda *et al.*, 2007) .

Hereafter, a similar study was conducted following Masuda *et al.* methodology in order to ensure control of pH in the reaction vessel could be achieved before performing the final experiments for this study. The control reactions at different pH values, showed a drastic morphology change over a small pH variation, as seen in Figure 3.4.

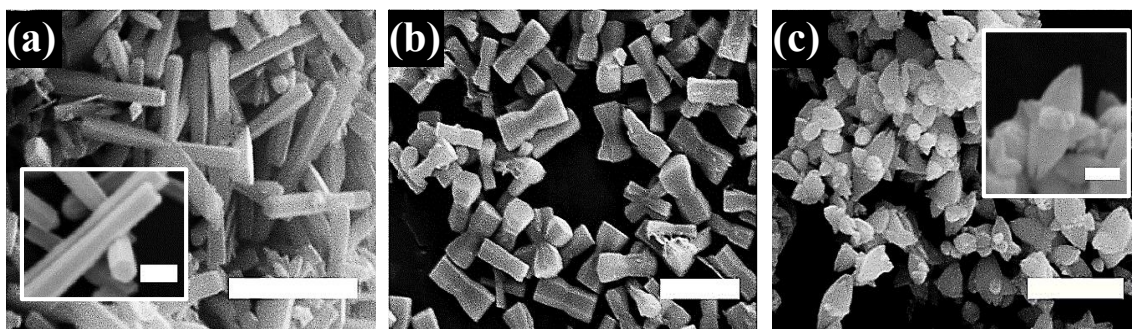


Figure 3.4 SEM images of precipitates of the Blank at (a) pH = 7.1, (b) pH = 7.2 and (c) pH > 8. All scale bars are 2 μm and inset scale bars at 0.5 μm .

The hydrothermal synthesis method chosen for this study was the reaction of zinc acetate and ammonia at neutral pH. This system was chosen for two main reasons. Firstly, the hydrothermal method working at low levels of supersaturation allows for the growth of well-defined crystal facets which facilitates the study of the growth habit of the crystals. For a bath containing zinc acetate (at 25 $^{\circ}\text{C}$), the system gets supersaturated (with respect to the hydroxide) at pH 6.68 (Govender *et al.*, 2004); therefore, working at

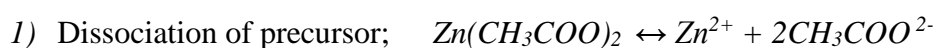
pH = 7 the supersaturation in the system was ensured and was more likely to proceed through heterogeneous nucleation (low supersaturation) which allowed for the growth of 1D ZnO structures. And, secondly, the influence of synthesis conditions on product formation, precipitation processes and phase transformation was demonstrated by comparison with another hydrothermal synthesis route using zinc nitrate and HMTA as a precursors and also known to result in the formation of wurtzite-structured, twinned hexagonal rods of ZnO.

3.3 Materials

Zinc acetate ($\text{Zn}(\text{CH}_3\text{COO})_2$) 99.99%, 1 M hydrochloric acid (HCl), 1 M potassium hydroxide volumetric standard (KOH) and Zinc atomic absorption standard solution (1000 ppm) were purchased from Sigma-Aldrich; ammonia solution (NH_3 , 35%) from Fisher Scientific. All chemicals were used without further treatment. And, ddH₂O with conductivity less than $1 \mu\text{S cm}^{-1}$ (25 °C) was used as the solvent for all ZnO synthesis reactions.

3.4 ZnO Synthesis

ZnO crystals were synthesized in aqueous solution using as a zinc precursor $\text{Zn}(\text{CH}_3\text{COO})_2$ following previously described hydrothermal synthesis methods in which twinned hexagonal rods were formed with the thermodynamically stable wurtzite structure. Following the methodology of Masuda *et al.*, 30 mM of $\text{Zn}(\text{CH}_3\text{COO})_2$ (hereafter labeled as ZnAc₂) in 50 °C water and 30 mM of NH_3 were prepared as stock solutions (Masuda *et al.*, 2007). For accurate preparation of the required NH_3 stock concentration, the concentration of a 5% NH_3 solution used for the stock solution preparation was determined by titration prior to each experiment. For all reactions, the 30 mM NH_3 stock solution at room temperature was vigorously stirred into an equal volume of 30 mM ZnAc₂ solution (at 50 °C). The pH of the reaction solutions was 7.0 ± 0.1 . The mixtures were sealed and placed in a water-bath set at 50 °C for up to 48 hours. ZnO precipitation took place in three steps, where equal molar ratio between zinc ions and hydroxyl ions was achieved in the system:



- 2) Protonation of base; $NH_3 + H_2O \leftrightarrow NH_4^+ + OH^-$
- 3) Precipitation of Zn^{2+} ions; $Zn^{2+} + 2OH^- \rightarrow ZnO + H_2O$

During the course of the reactions, samples were taken from the reaction vessels at selected times (± 2 min). Samples were collected in triplicate and centrifuged at 13000 rpm for 3 minutes to separate precipitates from the supernatants. The precipitates were washed three times with ddH₂O. Cleaned precipitates were dried at -70 °C using a Virtis-110 freeze-dryer.

3.5 Characterization

The crystallinity of the precipitates obtained was characterized using XRD (PANalytical X'Pert PRO, Cu K α radiation with wavelength of 1.54056 Å). Ground samples (if necessary) were packed into an aluminium sample holder and scanned from 5° to 80° of 2θ at an accelerating voltage of 45 kV, 40 mA filament current, using a scan speed of 0.02° s⁻¹ at room temperature. Diffraction patterns were analyzed using X'Pert-HighScore Plus (Version 2.0a) program for diffractogram manipulation, background determination and peak identification. The morphology and size of selected precipitates were studied using SEM (JEOL JSM-840A, 20 kV, gold sputter-coated samples). For ZnO crystal size analysis, more than 30 crystals were studied for each sample and the aspect ratio ($L/D = \text{length/average diameter}$) of each individual crystal was determined using the Java-based image processing program (*ImageJ* software). ATR (Perkin Elmer Spectrum 100 Series Spectrometer with Diamond/KRS-5 crystal) was used to detect the functional groups present in the lyophilized precipitates. Spectra were averaged from 32 scans at 2 cm⁻¹ resolution with air as background. The amount of non ZnO component in the precipitates was determined by TGA (Mettler Toledo TGA/SDTA 851^e) where samples were heated at 10 °C·min⁻¹ from 30 °C to 900 °C in air to ensure complete combustion of all organic material. The chemical constitution of the precipitates was investigated by XPS using a VG Scientific ESCALab MkII X-ray photoelectron spectrometer with Al K α X-ray source ($h\nu = 1483.6$ eV). Synthesized precipitates as well as control samples (purchased ZnO (99.999%) and ZnAc₂ (99.99%)) were ground and then mounted on standard samples holders. Survey spectra were collected covering the full BE range from 0-1200 eV using a step size of 1 eV, a dwell time of 0.2 seconds and a PE of 50 eV. To compensate for surface charging

effects in the insulating samples, all binding energies were corrected with reference to the saturated hydrocarbon C 1s peak at 285.0 eV. High resolution core level spectra of the Zn 2p, C 1s and O 1s peaks were collected using a PE of 20 eV and step size of 0.2 and a dwell time of 0.4 s, which were subsequently deconvoluted and fitted using standard mixed Gaussian-Lorentzian components using CASAXPS software.

3.6 Results and Discussion

3.6.1 Zinc Oxide Formation *via* Intermediate(s)

Previous studies in our group by Dr Liang (Liang, 2010) showed that the reaction of $\text{ZnAc}_2\text{-NH}_3$ occurs *via* an intermediate, a layered structure that only later transforms to the oxide phase with ZnO being the major compound in the sample at 16 hours and beyond. In this study, the presence of the intermediate, identified as Layered Basic Zinc Acetate (LBZA) with formula $(\text{Zn}_5(\text{OH})_8(\text{CH}_3\text{COO})_2 \cdot 2\text{H}_2\text{O})$, was studied by SEM, XRD, ATR, TGA and XPS. SEM results showed two different species within the 1 hour precipitate and 24- or 48-hours precipitates, characterized as LBZA (Figure 3.5a) and ZnO (Figure 3.5b-c), respectively. The anisotropic growth of the crystals was observed since the aspect ratio (L/D) of the ZnO crystals showed an increase from ~ 4 at 24 hours to ~ 7 at 72 hours (Appendix 3.1).

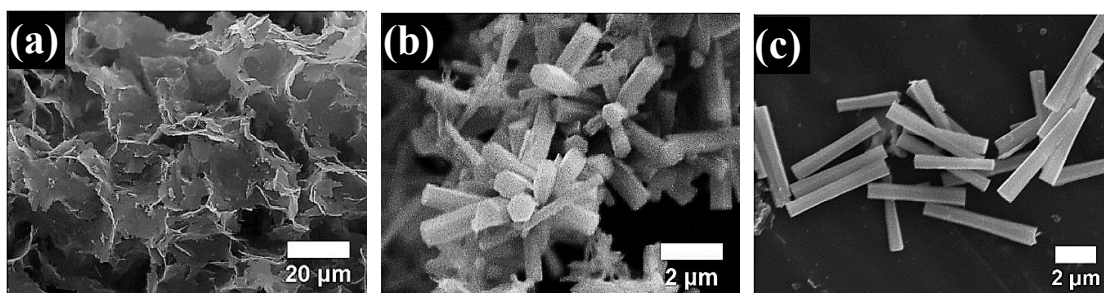


Figure 3.5 SEM images of precipitates of the Blank at (a) 1 hour, (b) 24 hours and (c) 48 hours.

XRD diffraction peaks of ZnO, corresponding to the hexagonal wurtzite structure (JCPDS card No. 36-1451, space group $P6_3mc$), were detected in the 24- and 48-hours precipitates (Figure 3.6a). Peaks at 31.6° , 34.2° , and 36.1° matched with the (1010), (0002), and (1011) planes of ZnO respectively (Bragg, 1920; Govender *et al.*, 2004; Masuda *et al.*, 2007), as well as other characteristic peaks within 2θ of $40\text{-}80^\circ$. For the early stage precipitate (1 hour precipitate), a series of diffraction peaks spaced by 2θ of

6.8°, 13.4° and 20.1° typical for LBZA were observed (Cui *et al.*, 2008; Hosono *et al.*, 2004; Morioka *et al.*, 1999; Poul *et al.*, 2000; Tokumoto *et al.*, 2003). The most intense peak at 2θ of $6.8 \pm 0.1^\circ$ assigned to the (001) plane of LBZA (Cui *et al.*, 2008; Hosono *et al.*, 2004; Morioka *et al.*, 1999; Poul *et al.*, 2000; Tokumoto *et al.*, 2003) exhibits an interlayer spacing of $13.0 \pm 0.1 \text{ \AA}$ which is in agreement with the reported interlayer spacing values from ~ 12 to $\sim 15 \text{ \AA}$ for LBZA (Cui *et al.*, 2008; Hosono *et al.*, 2004; Kasai and Fujihara, 2006; Morioka *et al.*, 1999; Poul *et al.*, 2000). A broad peak at $\sim 33.2^\circ$ of 2θ was also observed in the 1 hour precipitate (Figure 3.6b), which corresponds to the (100) diffraction in LBZA (Inoue and Fujihara, 2011; Xia *et al.*, 2011). Interestingly as the reaction progressed, there was a shift towards low angle as a peak was observed at $\sim 32.9^\circ$ of 2θ in the 24- and 48-hour precipitates (Figure 3.6b). This new peak could be attributed to the formation of an additional intermediate phase with intercalated carbonate anions besides the acetate anions (Jang *et al.*, 2010; Patrinoiu *et al.*, 2013) and/or $\text{Zn}(\text{OH})_2$ species which can be present at the later stages of ZnO formation (Jang *et al.*, 2010; McBride *et al.*, 2003; Patrinoiu *et al.*, 2013; Shaporev *et al.*, 2007; Wang *et al.*, 2011). ATR analysis gave further evidence corroborating the formation of a zinc hydroxyl double salt containing both, acetate and carbonates groups and is discussed in detail below.

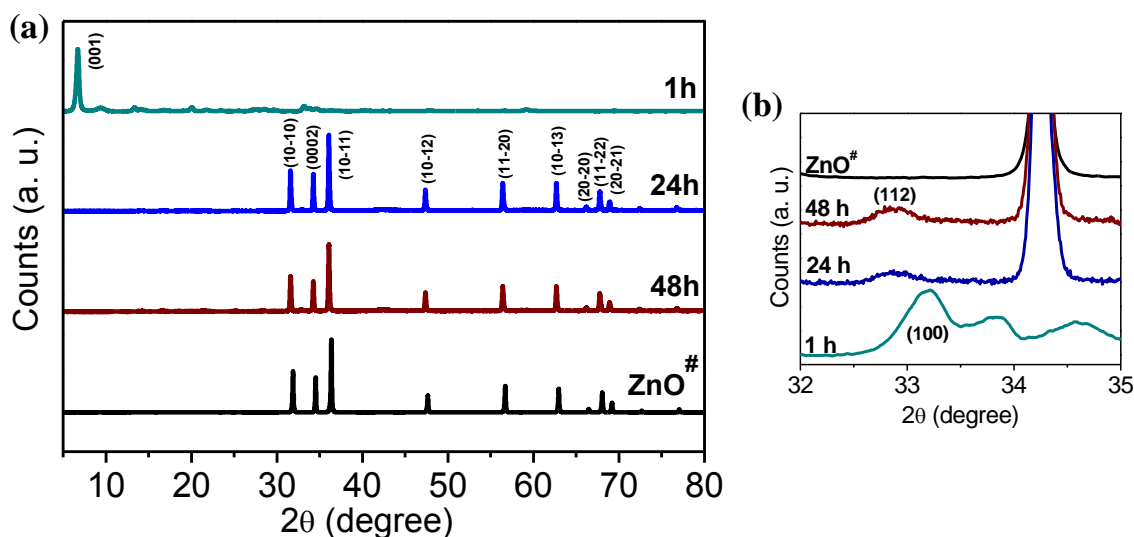


Figure 3.6 (a) XRD characterization of precipitates collected at different reaction times; the four-digit and three-digit Miller indices correspond to the crystal planes of ZnO and LBZA, respectively; and (b) the region from 32° to 35° of 2θ has been highlighted where peaks found confirm the formation of intermediates. Purchased ZnO is designated with a hash.

The crystallization process was believed to be by the phenomenon known as Ostwald's Law of phases, as described in Section 3.1, in which a metastable phase, more soluble and unstable, is formed prior to the formation of the stable phase (Cölfen and Mann, 2003; Rodríguez-Hornedo and Murphy, 1999). Although the characterization of the precipitates gave information about what was present in the sample, without necessarily explaining how it was formed, the observation of ZnO crystals growing out of the layered structures gave evidence of LBZA being an intermediate of the reaction (Figure 3.7). These results (SEM and XRD data) confirmed that ZnO formation in this ZnAc₂-NH₃ reaction occurred via the formation of an intermediate compound as follows: Zn(Ac)₂ → LBZA → ZnO. Even though LBZA was not detected by XRD from precipitates collected at 24 hours and beyond; ATR, TGA and XPS data showed the presence of trace amounts of acetate in these precipitates even though the major component was ZnO.

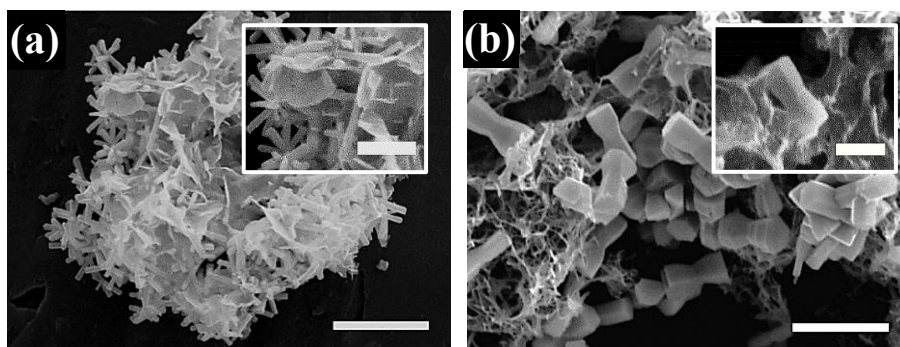


Figure 3.7 SEM analysis showing growth of ZnO rods from layered structures for the ZnAc₂-NH₃ system at (a) pH = 7.0 and (b) pH = 7.2. All scale bars are 5 μm and inset 2 μm.

ATR analysis confirmed the formation of intermediates by observation of characteristic acetate peaks in the region from 1800 to 1300 cm⁻¹ (Figure 3.8). The whole ATR spectra of the precipitates are shown in Appendix 3.2. ATR spectrum for the 1 hour precipitate (Figure 3.8) showed the presence of acetate (from LBZA) by peaks detected at 1548 cm⁻¹ (peak ii) and 1392 cm⁻¹ (peak iv) corresponding to the vibrational modes of carboxyl group, asymmetric (ν_{as}) and symmetric stretching (ν_s) of COO⁻, respectively (Aisawa *et al.*, 2001; Cui *et al.*, 2008; Gardener and Perry, 2000; Koleva and Stoilova, 2002; Nakamoto, 1986; Nara *et al.*, 1996; Ogata *et al.*, 1998) and the peak detected at 1337 cm⁻¹ (peak v) corresponded to the in-plane bending (δ_s) or deformation of -CH₃ (Jang *et al.*, 2010). A broad absorption peak in the 3000-3600 cm⁻¹ region

assignable to the O-H group of hydroxide or intercalated water in LBZA was also observed (Appendix 3.2). Besides this, for 24- and 48-hour precipitates, the $\nu_{as}(\text{COO}^-)$ was practically non-existent (or absent) and instead a peak at $\sim 1505 \text{ cm}^{-1}$ (peak iii) was observed. This peak was attributed to the asymmetric stretching (ν_{as}) of CO_3^{2-} also known as $\nu_3(\text{CO}_3^{2-})$ (Jang *et al.*, 2010). The $\nu_3(\text{CO}_3^{2-})$ peak is split into two peaks at 1507 and 1391 cm^{-1} . Hence, the peak observed at $\sim 1391 \text{ cm}^{-1}$ for the 24- and 48-hour precipitates does no longer correspond to the $\nu_s(\text{COO}^-)$ at 1392 cm^{-1} found in the 1 hour precipitate. Other peaks characteristic of the carbonate group were observed (Appendix 3.2.), corresponding to the symmetric stretching (ν_s) of CO_3^{2-} (1045 cm^{-1}), also known as $\nu_1(\text{CO}_3^{2-})$, and out-of-plane deformation of CO_3^{2-} (831 cm^{-1}) (Jang *et al.*, 2010). The CO_3^{2-} species in the samples are believed to originate from the dissolved carbon dioxide (CO_2) present in the solution (Jang *et al.*, 2010) and are incorporated in the crystalline mineral forming a layered basic zinc hydroxyl double salt containing acetate and carbonate hereafter referred to as layered basic zinc acetate-carbonate (LBZAC) with formula $\text{Zn}_5(\text{OH})_x(\text{CH}_3\text{COO})_y(\text{CO}_3)_z \cdot n\text{H}_2\text{O}$ ($x + y + z = 10$) (Patrinoiu *et al.*, 2013). An additional peak at $\sim 1628 \text{ cm}^{-1}$ (peak i) was observed for both precipitates which was previously assigned to the O-H vibrational mode attributed to the hydroxide slab in LBZA/LBZAC (Morioka *et al.*, 1999; Poul *et al.*, 2000) or in this case, to the hydroxide slab in LBZAC as this peak was mainly observed when carbonates were detected. A peak at 831 cm^{-1} previously attributed to CO_3^{2-} can also be associated with $\text{Zn}(\text{OH})_2$ (Srivastava and Secco, 1967). However, this peak became prominent with the appearance of the other CO_3^{2-} peaks, suggesting that it is more likely to be associated with CO_3^{2-} species rather than $\text{Zn}(\text{OH})_2$. It is however not clear whether LBZAC was an intermediate product in the formation of ZnO or only a byproduct formed as a consequence of the reaction conditions; nevertheless, anticipating the results discussed in section 3.6.2, XRD and ATR analysis suggests that LBZAC was present when dissolution of some of the solid phase initially formed was observed using ICP-OES analysis (Liang *et al.*, 2014). The remaining undissolved solid phase (LBZA and LBZAC) could undergo phase transformation into ZnO. Hence, ZnO formation in this $\text{ZnAc}_2\text{-NH}_3$ reaction occurred via the formation of intermediate compounds as follows: $\text{Zn}(\text{Ac})_2 \rightarrow \text{LBZA} \rightarrow \text{ZnO}$, with LBZAC being a ‘plausible’ intermediate.

From the ATR data, the coordination mode of acetate anions to Zn^{2+} ions was deduced from the difference in frequency (wavenumber) between $\nu_{as}(\text{COO}^-)$ and $\nu_s(\text{COO}^-)$, $\Delta\nu_{as-s}$ (Nakamoto, 1986; Nara *et al.*, 1996; Wang *et al.*, 2011). The $\Delta\nu_{as-s}$ value for the 1 hour precipitates was $\sim 163 \text{ cm}^{-1}$, which implied that the COO^- has coordination type to Zn^{2+} either forming an ionic metal complex (Nakamoto, 1986; Nara *et al.*, 1996; Wang *et al.*, 2011) or as a bridging ligand (Nara *et al.*, 1996). Therefore, the acetate present in the samples did not arise from free ions, corroborating the claim that LBZA (contains zinc hydroxide layers held together by acetate ions and intercalated water molecules) is the intermediate compound for ZnO formation in this reaction. The coordination mode of CO_3^{2-} ions to Zn^{2+} ions was determined from the difference between $\nu_3(\text{CO}_3^{2-})$ peaks, $\Delta\nu_3$ (Jang *et al.*, 2010). The $\Delta\nu_3$ value in precipitates with carbonate present (24- and 48-hour precipitates) was $\sim 115 \text{ cm}^{-1}$ which is associated with unidentate coordination to Zn^{2+} ions (Jang *et al.*, 2010).

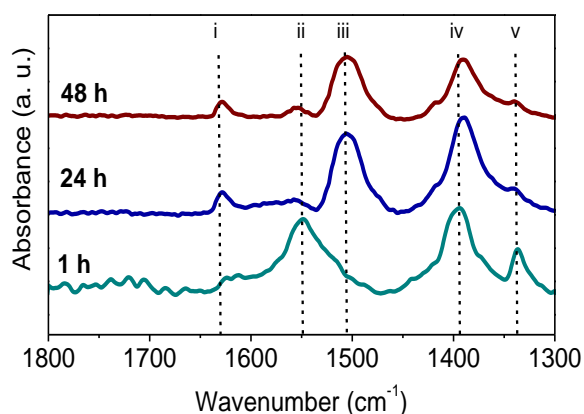


Figure 3.8 ATR spectra of precipitates collected at (a) 1 hours, (b) 24 hours and (c) 48 hours.

TGA analysis showed three stages of weight loss for all the precipitates (Figure 3.9). In the first stage, the release of physisorbed water occurred at temperatures below $100 \text{ }^\circ\text{C}$ (Hosono E *et al.*, 2004; Poul *et al.*, 2000). The weight loss in this region was mainly observed in the 1 hour precipitates; however, the 24 hour precipitates showed still a small presence of water. The second stage showed two overlapping weight loss regions between 100 and $250 \text{ }^\circ\text{C}$, attributed to the dehydration of intercalated water ($100 \text{ }^\circ\text{C}$ - $168 \text{ }^\circ\text{C}$) and the the dehydroxylation of zinc hydroxide layers in LBZA or LBZAC to form ZnO ($168 \text{ }^\circ\text{C}$ - $250 \text{ }^\circ\text{C}$). From the analysis of the precursor, ZnAc_2 , it was observed that the decomposition of acetate groups occurred within the third stage of

weight loss at higher temperatures from 250 to 400 °C (Patrinoiu *et al.*, 2013; Poul *et al.*, 2000; Wang *et al.*, 2011; Xia *et al.*, 2011). Phase transformation of intermediates was clearly observed in Stage 2 (Figure 3.9) where the 1 hour precipitate had the major weight loss in the first region (100 °C - 168 °C) while the 48 hours precipitate had the major weight loss within the second region (168 °C - 250 °C) (Liang *et al.*, 2014). The thermal decomposition of the precipitates taken at 1 hour of reaction resulted in a $33.3 \pm 1.5\%$ (Figure 3.9 inset) weight loss which is very close to the 34 - 38% weight loss reported for LBZA in the literature (Hosono *et al.*, 2004; Xia *et al.*, 2011). This data further supports LBZA being the major component of the initial precipitate. With progression of the reaction, the total weight loss decreased with the 24 hours precipitate losing $10.8 \pm 2.2\%$ and the 48 hours precipitate losing $4.52 \pm 1.7\%$ (Figure 3.9 inset). These results indicated that for the latest stage of precipitation most of the LBZA was converted to ZnO.

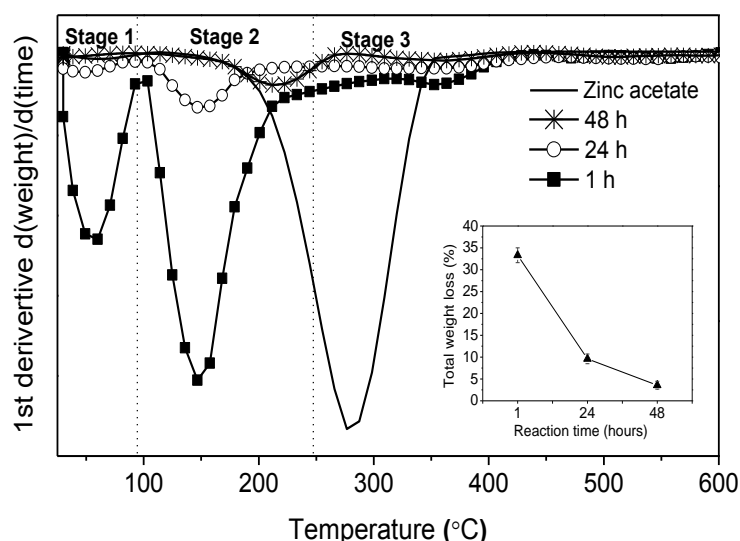


Figure 3.9 TGA 1st derivative weight loss curves of the precipitates collected during the course of reaction. Inset is the plot of the total percentage loss against time.

XPS results confirm the incorporation of Zn, O and C in all the precipitates studied by detailed analysis of the Zn 2p_{3/2}, O 1s and C 1s, at 1021.6 ± 0.1 eV, 531.6 ± 0.1 eV, 285.0 ± 0.0 eV, respectively; cf. the survey scan of the 48 hour precipitate (Figure 3.10). XPS analysis of the starting material, ZnAc₂ 99.99% purchased from Sigma-Aldrich, and the samples at different times of reaction, 1- and 48-hour precipitate, would seem to support the reaction of ZnO formation occurring *via* intermediates by showing a corresponding reduction in the atomic percentage of C with time due to the

LBZs being consumed during the reaction (Figure 3.10). These results also include traces of the ubiquitous carbonaceous contamination (C 1s peak) - the so called ‘adventitious carbon’ present even on the cleanest and purest of samples. Practical detection limits for most elements are of the order of 0.5 - 1.0 atomic %. Hence, a sample of purchased 99.999% ZnO was analysed by XPS in order to show that the C 1s peak detected in 48 hours precipitate was not just from trace contamination during the analysis but was also from LBZs in the sample (Table 3.1).

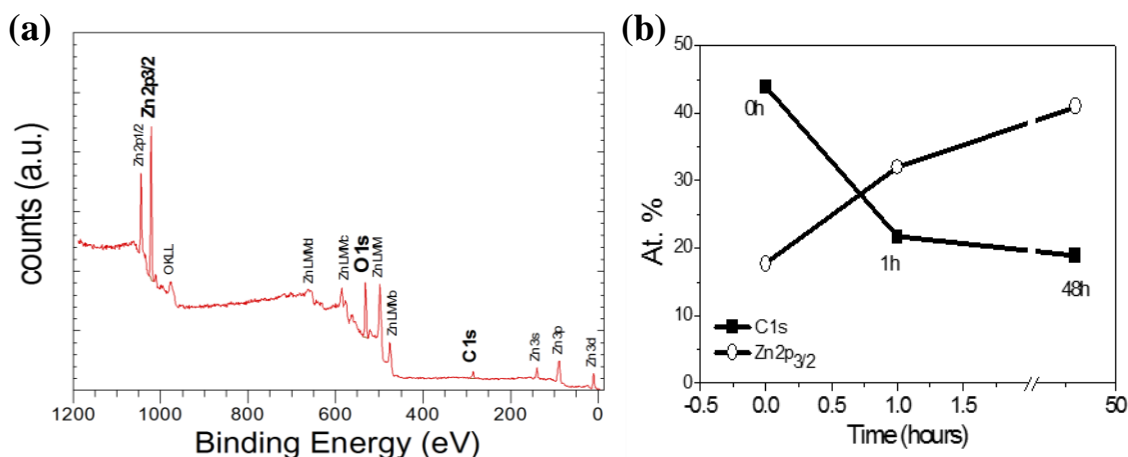


Figure 3.10 (a) XPS survey spectrum recorded from an as-deposited 48 hour-precipitate and (b) from XPS data: atomic % of carbon and zinc in the precursor (ZnAc₂), 1- and 48-hour precipitates.

Table 3.1 Atomic percentages of C 1s, Zn 2p_{3/2}, and O 1s peaks obtained from XPS and the relative ratio of Zn/O.

<i>Sample Description</i>	<i>At % C 1s</i>	<i>At % Zn 2p_{3/2}</i>	<i>At % O 1s</i>	<i>Relation Zn:O</i>
Starting material (ZnAc ₂)	43.9	17.7	38.4	0.5
1 hour-precipitate	21.7	32.0	46.3	0.7
48 hour-precipitate	18.9	41.0	47.6	0.9
ZnO 99.999%	13.0	44.5	42.4	1.0

Core-level spectra of as-deposited precipitates were carefully studied for Zn 2p_{3/2}, O 1s and C 1s regions. The measured Zn 2p_{3/2} region, in Figure 3.11a, was fitted with three components for the 1 hour precipitate, with BE values of 1021.5 eV, 1022.6 eV and 1019.9 eV whereas for the 48 hours precipitate only two peaks were required, with BE values of 1021.8 eV and 1022.5 eV. The BE value of 1021.7 ± 0.2 eV is very close to

the corresponding reference value of 1021.9 ± 0.1 eV for crystalline ZnO (Wagner *et al.*, 1979) and the BE value found for the purchased ZnO (99.999%) as shown in Appendix 3.3. A recent study has shown that depending on the ZnO morphology the BE can vary ± 0.3 eV, with lower values attributed to ZnO nanoparticles and higher values to ZnO nanorods (Al-Gaashani *et al.*, 2013). The different local chemical states of the Zn ions in the precipitates indicate the presence of Zn ions in a mixed environment, as is the case for LBZA/LBZAC. The presence of a higher binding energy component, such as the BE value of 1022.6 ± 0.1 eV, can be attributed either to acetate Zn groups (Zn-OCOCH₃) or hydrated Zn (Zn-OH) (Huang *et al.*, 2010). The study of Zn 2p_{3/2} region for ZnAc₂ (Appendix 3.3) indicates this higher BE value corresponds to carboxyl groups present in either in LBZA or LBZAC. The other lower binding energy component at 1019.9 eV for the 1 hour precipitate is in accordance with the corresponding BE values (1019.7 ± 0.6 eV) of LBZs with a general formula $[(\text{Zn}^{\text{octa}})_3(\text{Zn}^{\text{tetra}})_2(\text{OH})_8]^{2+} \cdot 2(\text{A}^-) \cdot n\text{H}_2\text{O}$ (Baier *et al.*, 2012). The absence of the last peak at 1019.7 ± 0.6 eV in the 48 hours precipitate and the increase of the % Area of the Zn 2p_{3/2} peak corresponding to crystalline ZnO (1021.5 ± 0.3 eV) indicates the LBZs were consumed and most of the intermediates were converted to ZnO. The O 1s region was fitted with three peaks for both precipitates (Figure 3.11). For the 1 hour precipitate a peak was detected at 529.9 eV, a value which is in between that of the BE values for O in crystalline ZnO (530.1 eV) (Moulder *et al.*, 1992) or/and condensed zincoxane ($-(\text{Zn-O})_x-$) bonds (529.7 eV) (Huang *et al.*, 2010). For the 48 hours precipitate, this peak was shifted to 530.1, being closer to lattice oxygen from ZnO (Appendix 3.3). A second peak at 531.6 ± 0.2 eV oxygen was assigned to a hydroxylated oxide surface (Zn-OH) (Deroubaix and Marcus, 1992; Huang *et al.*, 2010; Jing *et al.*, 2006) also present in LBZs. The third peak at 532.5 ± 0.2 eV, was close to the BE value of 532.3 eV reported for carboxyl groups (COO⁻) (Lofgren *et al.*, 1997), which was proved by the XPS spectra of ZnAc₂ where the same peak (at 532.2 eV) was observed in the sample (Appendix 3.3). Further observation of the % Area of the peaks, where the increase of the O 1s peak area attributed to crystalline ZnO was proportional to the decrease of the Zn-COO⁻ and/or Zn-OH area which indicates that the reaction of hydrolysis and condensation of ZnAc₂ has occurred. The C 1s peaks for the precipitates consisted in two principal components (Figure 3.11) at 285.3 ± 0.1 eV and 288.9 ± 0.3 eV corresponding to the methyl group and the carboxyl group (Ballerini *et al.*, 2007; Clark *et al.*, 1976), respectively; which was confirmed by analysis of ZnAc₂ (Appendix 3.3).

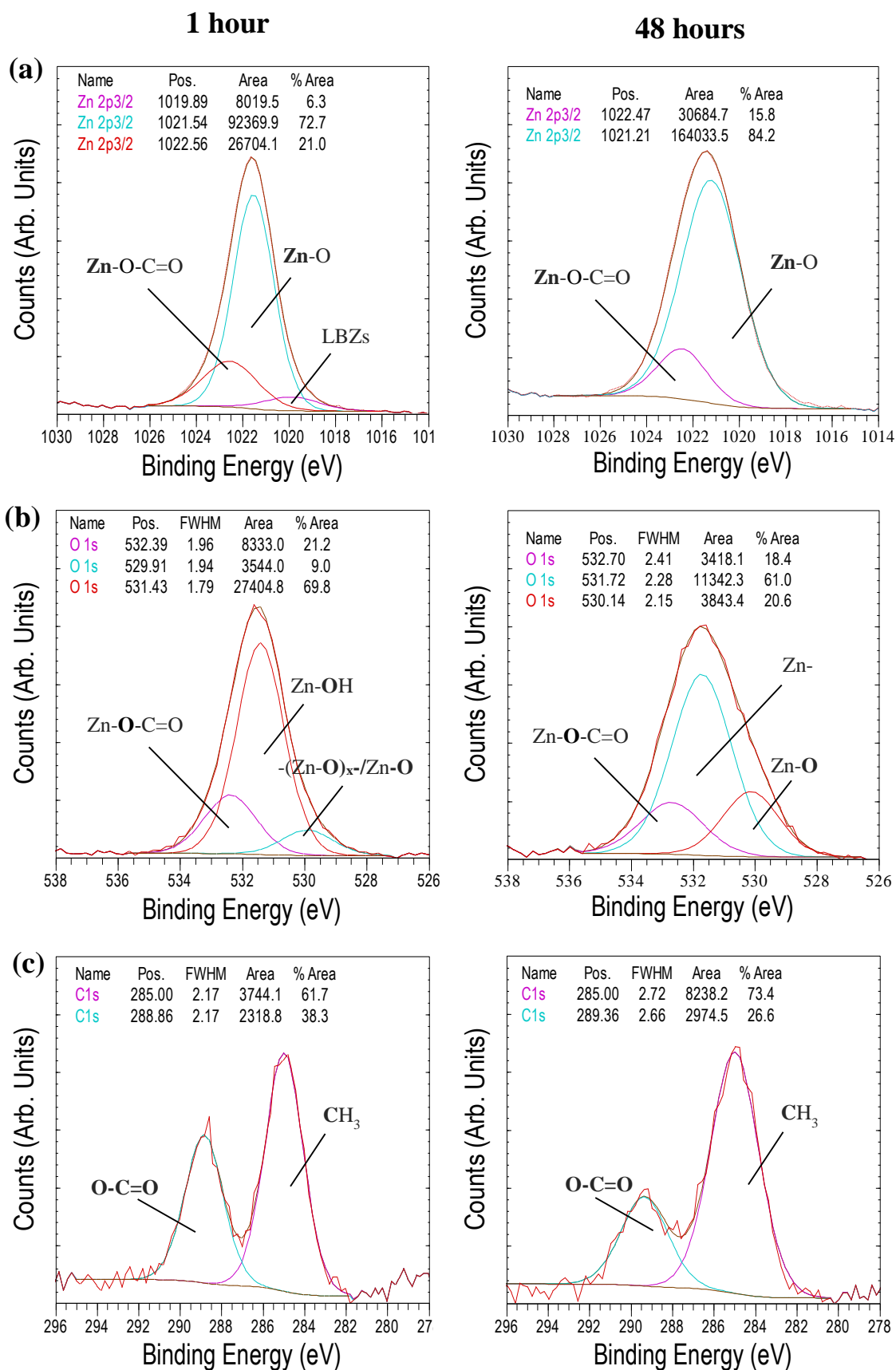


Figure 3.11 Core level spectra of as deposited precipitates collected at 1 and 48 hours of reaction for (a) Zn 2p_{3/2}, (b) O 1s and (c) C 1s.

For clarification, the BE values of the Zn 2p_{3/2} peak for crystalline ZnO can vary by ± 0.9 eV and there is a small difference between the BE values in Zn metal and ZnO (Table 3.2). Although the presence of Zn metal is discarded due to the reaction system conditions and neither was it detected by any other technique employed during sample characterization; for example, XRD would show the characteristic diffraction peaks of Zn metal at around 20.4° 2 θ degrees ZnO (Singh and Gopal, 2007); to discard the presence of Zn metal in our system, it was far better to look at the Zn Auger peak (Zn LMM) using values of kinetic energy (KE) where there exists a much greater chemical shift of > 3eV, being these two element environments (Zn metal and ZnO). The XPS survey spectra and the Zn Auger high resolution scan (Figure 3.12) showed a Zn LMM peak at ~988 eV which is attributed to ZnO (Amekura *et al.*, 2007), whereas the KE peak for metallic Zn would be expected at 992 eV (Amekura *et al.*, 2007).

Table 3.2 Literature reported values of the Zn 2p_{3/2} binding energy of ZnO and Zn metal.

Zn 2p _{3/2} BE (eV)	Reference	Zn 2p _{3/2} BE (eV)	Reference
ZnO		Zn metal	
1022.0	Wagner 1979	1021.6	Wagner 1979
1022.2	Kim 2005	1021.7	Biesinger
1021.0	Biesinger 2010	1021.5	Kim 2005
1021.2	Gaashani 2012		
1021.5			

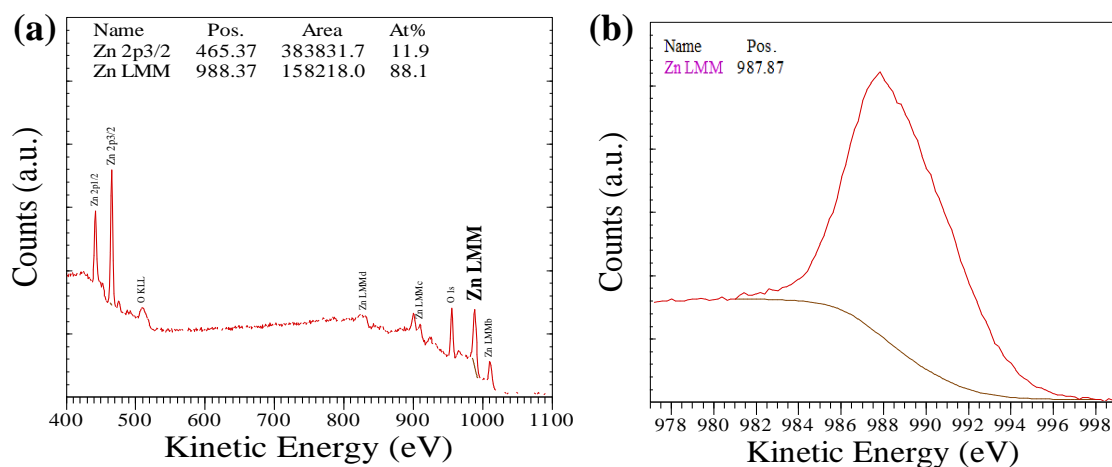


Figure 3.12 (a) XPS Survey spectra of a sample collected at 48 hours of reaction and (b) the Zn Auger high resolution scan.

Although, the presence of LBZA/LBZAC was confirmed by ATR, TGA and XPS by identification of acetate groups, it has been shown that acetate groups can be adsorbed on the positive Zn faces of ZnO and suppress growth along the polar (001) plane (Golić *et al.*, 2011). Therefore, a study of the methodology followed for the washing of the precipitates was carried out to ensure the acetates detected were not only surface adsorbed but from the intermediate(s) phases present. Further, this experiment was needed as for XPS the values that have been reported for acetate ($-\text{COO}^-$) and carboxylic acids ($-\text{COOH}$) are too close to tell apart, i.e. C1s peak for carboxylic acids are 289.0 - 289.3 eV (Briggs and Beamson, 1992) and C1s peak for acetate are 289.1 eV (Ballerini *et al.*, 2007; Clark *et al.*, 1976). Hence, a ZnAc_2 solution was added to a sample containing pure ZnO and incubated for a period of time in order to quantify the amount of acetate that could be absorbed (Appendix 3.4). Samples were subjected to thermal decomposition and the weight loss was determined after being treated in a three different ways: (a) not washed, (b) washed once and (c) washed trice (Appendix 3.4). The last procedure corresponded to the one followed in this study. Results showed, in Appendix 3.4, the amount of organic material found in tested precipitates was lower than the amount observed in the samples collected during the ZnO synthesis process (between 4 - 33%). Therefore, it was believed that the acetates detected largely originated from intermediate(s) species rather than adsorbed acetates on the surface of the particles present.

XRD, ATR, TGA and XPS analyses (and also SEM results) confirmed that for the reaction between ZnAc_2 and NH_3 at 50 °C and pH 7.0 ± 0.1 the synthesis of ZnO occurs through the formation of intermediate compounds: LBZA and possibly LBZAC.

3.6.2 Comparison of Different Mechanisms of ZnO Growth *via* LBZs

For a better understanding of the ZnO growth mechanism *via* intermediates, LBZs, the results obtained using the $\text{ZnAc}_2\text{-NH}_3$ system were compared with another hydrothermal method described by Tomczak and co-workers (Tomczak *et al.*, 2009) using zinc nitrate hexahydrate ($\text{Zn}(\text{NO}_3)_2 \cdot 6\text{H}_2\text{O}$) and 1,3-hexamethylenetetramine (HMTA) as precursors which in this case the intermediate formed through the reaction was Layered Basic Zinc Nitrate (LBZN), with formula $\text{Zn}_5(\text{NO}_3)_2(\text{OH})_8 \cdot x\text{H}_2\text{O}$. For both systems, equal molar ratio between zinc ions and hydroxyl ions was achieved. The concentration of Zn precursor and base used in the $\text{ZnAc}_2\text{-NH}_3$ system (15 mM) was

lower than the concentration used in the $\text{Zn}(\text{NO}_3)_2 \cdot 6\text{H}_2\text{O}$ -HMTA system (50 mM); however, these concentrations were necessary to maintain neutral pH where the formation of elongated hexagonal ZnO rods occurs as explained/shown in section 3.2. For clarification, the ICP-OES data was obtained by Dr Liang (Liang, 2010) and Dr Limo (Limo, 2014) for the ZnAc_2 - NH_3 system and the $\text{Zn}(\text{NO}_3)_2 \cdot 6\text{H}_2\text{O}$ -HMTA system; respectively. Note that, Figure 3.13 is a schematic representation with average values; graphs with error bars can be found in the above mentioned theses. Both synthesis routes supported the growth of twinned hexagonal rods. However, the progression of solid phase transformation from LBZs to ZnO showed a dissolution/precipitation process in the $\text{Zn}(\text{CH}_3\text{COO})_2$ - NH_3 system, which did not occur for $\text{Zn}(\text{NO}_3)_2 \cdot 6\text{H}_2\text{O}$ -HMTA system (Liang *et al.*, 2014).

By monitoring the Zn^{2+} remaining in solution using ICP-OES technique, it was observed in the $\text{Zn}(\text{CH}_3\text{COO})_2$ - NH_3 system that immediate precipitation of LBZA occurred when mixing the reagents consuming a high fraction of zinc ions present in the solution (Figure 3.13). As explained in Section 3.1, the formation of more soluble and unstable precipitates establishes a metastable phase that with time recrystallizes to more stable phase (Ostwald's Law of phases); in this case, precipitation of LBZA may have been facilitated by the ready availability of hydroxide ions (OH^-) from the hydrolysis of NH_3 (Amin *et al.*, 2011; Hosono *et al.*, 2004). As previously showed; XRD, ATR, XPS and TGA analysis gave evidence of the transformation of LBZA to ZnO over time. As acetate groups in the LBZA structure were continuously liberated (Baruah and Dutta, 2009; Wang *et al.*, 2011), dissolved carbon dioxide could have gradually been incorporated forming LBZAC. It should be noted that a fraction of the dissolved carbon dioxide could be readily in aqueous solution since initiation of reaction, hence also aiding for the formation of LBZAC. With the progression of the reaction to 24 hours, partial dissolution was observed releasing Zn^{2+} ions back into solution (Figure 3.13) which was believed to be due to the formation of LBZAC. This was supported by findings from XRD (Figure 3.6b) and ATR analysis (Figure 3.8) which showed that LBZAC was present when dissolution was observed (ICP-OES data). The amount that was dissolved may have been the amount needed to sustain the growth of ZnO. Particularly in such a zinc ion deficient system, the dissolution of intermediate phases which are thermodynamically unstable and soluble (Govender *et al.*, 2004) may have been induced to sustain the growth of more stable ZnO hexagonal crystal rods

(Govender *et al.*, 2004; Liu and Zeng, 2004; Yoreo and Vekilov, 2003). The amount of LBZs that decreased over time as shown by TGA analysis cannot be accounted for by the dissolution process, thus, it is believed that the bulk of the intermediate was phase transformed into ZnO (Figure 3.7). In the second method, $\text{Zn}(\text{NO}_3)_2 \cdot 6\text{H}_2\text{O}$, Zn^{2+} ions in solution were gradually consumed over time (Figure 3.13), thus, phase transformation of intermediates and growth of ZnO occurred with no evidence of dissolution and re-precipitation of zinc ions.

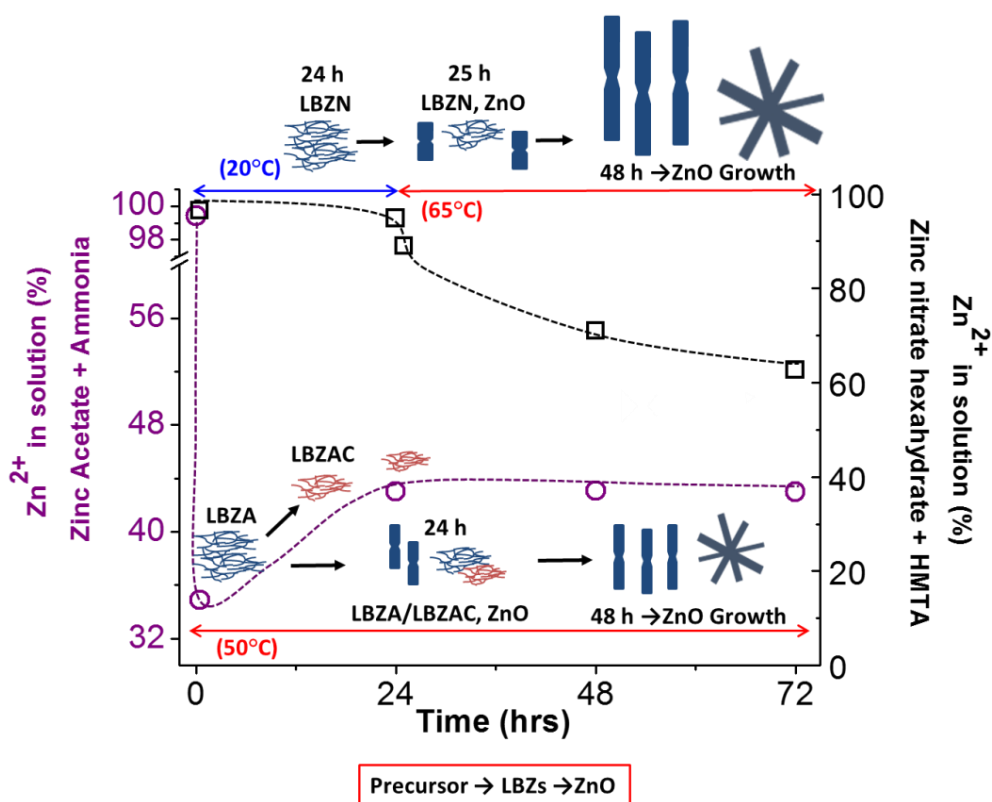


Figure 3.13. ICP-OES analysis showing percentage of Zn^{2+} in solution with respect to the initial concentration of Zn^{2+} as a function of reaction time for synthesis of ZnO hexagonal rods using two methods: (a) 15 mM ZnAc_2 + 15 mM NH_3 , pH 7.0 ± 0.1 (circular marker points) and (b) 50 mM $\text{Zn}(\text{NO}_3)_2 \cdot 6\text{H}_2\text{O}$ + 50 mM HMTA, pH 6.9 ± 0.1 (square marker points). Schematic representation of solid phases present is also shown. Images of ZnO rods are drawn to scale; ZnAc_2 - NH_3 system ($L/D_{24\text{hrs}} = 4.4 \pm 1.8$; $L/D_{48\text{hrs}} = 5.9 \pm 0.9$) and $\text{Zn}(\text{NO}_3)_2 \cdot 6\text{H}_2\text{O}$ -HMTA system ($L/D_{25\text{hrs}} = 2.6 \pm 1.3$; $L/D_{48\text{hrs}} = 8.9 \pm 3.3$). Figure from Liang *et al.* (2014).

As explained in Section 3.2, the hydrolysis of HMTA and the slow release of OH^- ions may drive the process of ZnO precipitation (Govender *et al.*, 2004; McPeak *et al.*, 2011; Strano *et al.*, 2014). Though, there are different views in the literature on the precise

role of HMTA in the solution synthesis of ZnO, it is suggested that the anisotropic growth of ZnO crystals can be due to HMTA either buffering the pH of the solution and controlling the saturation index (McPeak *et al.*, 2011) or attachment to the nonpolar facets of ZnO acting as a capping agent and, hence, promoting the vertical growth of ZnO nanorod along the *c*-axis (Sugunan *et al.*, 2006). Other recent studies have shown that both events happen simultaneously and suggested the double role of HMTA in the growth of ZnO nanorods (Kumar *et al.*, 2015; Strano *et al.*, 2014). Speciation calculations by Govender *et al.* showed that the pH at which the bath is supersaturated with respect to the hydroxide containing zinc nitrate–HMTA or zinc acetate-ammonia in a molar ratio of 1:1 was exactly the same, ~6.8 (Govender *et al.*, 2004). However, the working pH for the zinc nitrate system in this current study was slightly lower ($\text{pH} = 6.9 \pm 0.1$) than in the zinc acetate system ($\text{pH} = 7.0 \pm 0.1$). It is believed that small differences in supersaturation at a given pH could affect the ZnO precipitation points (Govender *et al.*, 2004). It has been shown, that depending on the counter ion present for a given system, the periods for ZnO precipitation may be different, such that for a bath containing zinc acetate longer periods are required than for zinc nitrate. Thus, smaller ZnO particles are commonly formed when using acetate salts compared to ZnO particles generated in the presence of nitrate salts (Kumar *et al.* 2015). This current work, may give evidence the longer periods required in zinc acetate baths are due to the ZnO growth mechanism going through a dissolution/ reprecipitation process which does not occur in the case of zinc nitrate baths; however, it should not be discounted that the difference in the concentration of Zn^{2+} ions present in the $\text{Zn}(\text{NO}_3)_2 \cdot 6\text{H}_2\text{O}$ -HMTA system had a higher concentration which may allow for further growth of the ZnO crystals. ZnO crystals obtained using the $\text{Zn}(\text{NO}_3)_2 \cdot 6\text{H}_2\text{O}$ -HMTA system had a greater aspect ratio, 8.9 ± 3.3 , than those obtained from the ZnAc_2 - NH_3 system, 5.9 ± 0.9 , for the 48 hours precipitates.

The grain sizes from XRD data calculated using the Scherrer equation also supported the observation of bigger particles in the nitrate system, since an increase in crystallite size was shown for the $\text{Zn}(\text{NO}_3)_2 \cdot 6\text{H}_2\text{O}$ -HMTA system with respect to the ZnAc_2 - NH_3 system (Liang *et al.*, 2014). In both systems, values obtained for the *c*-axis associated with the (0001) plane were greater than the values for the *a*-axis associated with the (1010) plane which could be correlated to anisotropic growth of ZnO rods (Liang *et al.*, 2014).

3.7 Conclusions

The ZnO growth mechanism was investigated via a hydrothermal synthesis method using as precursors ZnAc_2 and NH_3 . Through this hydrothermal method, it was shown that a change of pH can play an important role on ZnO morphology. Therefore, the reaction was conducted at 7.0 ± 0.1 to initiate nucleation (reach supersaturation) and to ensure the growth of wurtzite structured ZnO hexagonal rods. Thorough characterization of precipitates formed during the reaction processes, it was shown that this synthesis route occurs *via* intermediate(s), layered structures that only later transform to the oxide phase. The identities of the solid-phases formed were confirmed by data from SEM, XRD, ATR, XPS and TGA analysis. The first intermediate identified was LBZA, followed by the formation of LBZAC where carbonates originated from dissolved CO_2 present in solution. The observation of ZnO crystals growing out of the layered structures gave further evidence of LBZA being an intermediate in the reaction.

The influence of synthesis conditions on product formation, precipitation processes and phase transformation was demonstrated by comparison with another hydrothermal synthesis route using zinc nitrate and HMTA as precursors and also known to result in the formation ZnO hexagonal rods. As demonstrated, depending on reaction conditions ZnO growth can take place via dissolution/re-precipitation processes and/or solid-phase transformation. In the $\text{ZnAc}_2\text{-NH}_3$ system, solid-phase transformation from intermediates to ZnO involved a dissolution and re-precipitation process; resulting in an immediate precipitation of LBZA, partial dissolution of LBZAC releasing Zn^{2+} ions back into solution, consequently leading to a re-precipitation process facilitating further growth of ZnO crystals. For the $\text{Zn}(\text{NO}_3)_2 \cdot 6\text{H}_2\text{O}\text{-HMTA}$ system, no dissolution/re-precipitation process was observed; and growth of ZnO crystals occurred via solid-phase transformation from an intermediate identified as LBZN.

Chapter IV

ZnO-binding peptides studies

4.1 Introduction

The identification of biomineral-associated biomolecules has shed light on how biominerals are formed in living organisms. This has also led to the use of the bioinspired/biomimetic approach for materials synthesis (Mann, 1998; Sanchez *et al.*, 2005), even for non-biologically produced minerals such as ZnO (Tian *et al.*, 2002). Despite ZnO not being found in living organisms, to date, more than twenty ZnO-binding peptides (ZnO-BPs) have been identified from either cell surface display (Tomczak *et al.*, 2009; Umetsu *et al.*, 2005) or phage display libraries (Golec *et al.*, 2012; Rothenstein *et al.*, 2012; Tomczak *et al.*, 2009; Umetsu *et al.*, 2005). However, only a few peptides such as GLHVMHKVAPPR (G-12) (Liang *et al.*, 2011; Limo *et al.*, 2015), EAHVMHKVAPRP (EM-12) (Togashi *et al.*, 2011; Umetsu *et al.*, 2005) and derivatives GLHVMHKVAPPR-GGGC (GT-16) (Liang *et al.*, 2011; Muthukumar, 2009) and EAHVMHKVAPRP-GGGSC (ET-17) (Muthukumar, 2009; Umetsu *et al.*, 2005) have been studied further. The addition of GT-16 during ZnO synthesis has been shown to reduce the aspect ratio of the ZnO crystals formed (Tomczak *et al.*, 2009). In order to unravel the cause(s) of aspect ratio reduction by this ZnO-BP, our group conducted some studies using G-12 (Liang *et al.*, 2011; Limo *et al.*, 2015) and/or GT-16 (Liang *et al.*, 2011; Limo *et al.*, 2015). The direct evidence obtained suggested that (i) ZnO aspect ratio reduction occurs via an adsorption-growth inhibition mechanism, (ii) G-12 adsorbing on both (0001) and (10-10) planes of ZnO is sufficient to reduce the ZnO aspect ratio (the GGGC-tag is not essential); and, (iii) the GGGC-tag is responsible for the selective adsorption of GT-16 on the (0001) plane of ZnO crystals. Also, the addition of G-12 in different ZnO experimental systems led to modification of the growth mechanisms (Liang *et al.*, 2011; Limo *et al.*, 2015). Studies by others have shown that the addition of ET-17 into stable Zn(OH)₂ sols catalyzes ZnO formation, directing a flower-type anisotropic crystal growth (Umetsu *et al.*, 2005). The catalytic effect of ET-17 is generated either by the presence of the EM-12 segment or

GGGSC-tag (Umetsu *et al.*, 2005). The catalytic effect of ET-17 was further confirmed as ET-17 attached to a genetically modified-collagen template was able to generate ZnO nanowires (Bai *et al.*, 2009). In general, well-studied ZnO-BPs are strongly basic. Recently, Moon *et al.* have performed *in vitro* studies of an acidic sequence, VPGAAEHT, identified by phage-display. The presence of this peptide strongly influenced ZnO morphology (from needle-like structures to microspheres) as well as optical emission properties (Moon *et al.*, 2015). A green emission decrease was observed in the presence of such peptide due to surface-related oxygen and zinc vacancies in the ZnO structure and, further, when adding higher concentration of peptide blue emission emerged from oxygen and zinc interstitials defects (Moon *et al.*, 2015). A study proposed to understand the interactions taking place between the ZnO surface and EM-12 showed that conformational changes as well as charged amino acids and residues adjacent to the charged aminoacids are critical to the binding to ZnO (Yokoo *et al.*, 2010). It was concluded that the electrostatic interaction between ZnO particles and ZnO-BPs was enthalpy-driven, and involved hydrogen bonding, as also suggested by Patwardhan *et al.* (Patwardhan *et al.*, 2012). The specific binding sites of the EM-12 peptide have been explored (Okochi *et al.*, 2010), with the shorter sequences; HVMHKV and HKVAPR having either high specificity and/or affinity for ZnO nanoparticles. Additionally, it was proposed that ZnO binding did not depend on hydrophobicity or other physical parameters but ZnO recognition of the specific amino acid alignment of these peptides (Okochi *et al.*, 2010). Morphology changes observed for ZnO growth in the presence of ZnO-BPs did not lead to random morphologies. For example, the addition of EM-12 or dipeptides from its sequence (i.e. Met-His or His-Lys) during solution synthesis using Zn(OH)₂ as a precursor, suppressed crystal growth of ZnO in the (0001) direction (Togashi *et al.*, 2011).

The coordination of Zn²⁺ with proteins plays an important role for the structural stability and functionality of proteins in living organisms as evidenced in metalloproteins such as metallothioneine and zinc fingers of DNA-binding proteins (Bertini, 2007). Zn²⁺-protein complexation occurs at specific domain(s) via the side chains of amino acid residues namely; sulphur atoms of cysteine and methionine, nitrogen atoms of histidine, and oxygen atoms of aspartic acid and glutamic acid (Bertini, 2007). In experimental studies using a Zn(NO₃)₂-HMTA hydrothermal reaction, Gerstel *et al.* demonstrated that the presence of

aspartic acid, glutamic acid, and their corresponding dipeptides produced LBZs (layered basic zinc salts) as opposed to the expected ZnO (Gerstel *et al.*, 2006). They also observed the formation of soluble complexes when higher concentrations of these additives were used and proposed that Zn^{2+} -additive complexation via electrostatic interaction was responsible for LBZs or soluble complex formation (Gerstel *et al.*, 2006). More recently, it has been shown that the presence of peptides with different isoelectric points (in the acid, basic and neutral range) using a $\text{Zn}(\text{NO}_3)_2\text{-NaOH}$ hydrothermal reaction also formed LBZs as a metastable phase during the precipitation process. It was suggested that negatively charged peptides intercalated easily in metastable LBZs (Baier *et al.*, 2012). Previous studies have shown that the formation of ZnO (without additives) occurs via intermediate(s), LBZs, that only later transform to the oxide phase (ZnO) (Hosono E *et al.*, 2004; Jang *et al.*, 2010; Patrinoiu *et al.*, 2013; Poul *et al.*, 2000; Tokumoto *et al.*, 2003; Wang *et al.*, 2006; Wang *et al.*, 2011). This crystallization process usually occurs by a phenomenon known as Ostwald's Law of phases (Yoreo and Vekilov, 2003) in which a metastable phase is formed prior to the formation of the stable phase. In a recent study conducted by our group, the ZnO growth mechanism without the presence of additives has been described and compared for two different hydrothermal methods: (a) zinc acetate ($\text{Zn}(\text{CH}_3\text{COO})_2$) and ammonia (NH_3) and (b) zinc nitrate hexahydrate ($\text{Zn}(\text{NO}_3)_2 \cdot 6\text{H}_2\text{O}$) and 1,3-hexamethylenetetramine (HMTA) (Liang *et al.*, 2014). Both synthesis routes supported the growth of twinned hexagonal rods. However, the progression of solid phase transformation from LBZs to ZnO showed a dissolution/reprecipitation process in the $\text{Zn}(\text{CH}_3\text{COO})_2\text{-NH}_3$ system, which did not occur for the $\text{Zn}(\text{NO}_3)_2 \cdot 6\text{H}_2\text{O}\text{-HMTA}$ system (Liang *et al.*, 2014).

In the current study, the effect of the peptide EM-12 (identified by phage display technique) and its mutant EC-12 during ZnO formation was investigated using the $\text{Zn}(\text{CH}_3\text{COO})_2\text{-NH}_3$ hydrothermal method (Masuda *et al.*, 2007). A specific aim of the investigation was to explore the effect of increasing the number of potential complexing groups on ZnO formation, for instance, the replacement of methionine (M_5) with cysteine (C_5) in the peptide sequence. Although both peptides affected the crystal formation process, only EC12 was shown to interact with the solid phase(s) formed during the reaction. From the results of detailed materials characterization and changes in the morphology observed,

the interactions between the peptide(s) and solution and solid state species present during the process of ZnO crystal formation in the presence of EM-12 and EC-12 are proposed.

4.2 Materials

Zinc acetate ($\text{Zn}(\text{CH}_3\text{COO})_2$, 99.99%), piperazine ($\text{C}_4\text{H}_{10}\text{N}_2$), DIPEA ($\text{C}_8\text{H}_{19}\text{N}$), TFA ($\text{C}_2\text{HF}_3\text{O}_2$), thioanisole ($\text{C}_7\text{H}_8\text{S}$), DODT ($\text{C}_6\text{H}_{14}\text{O}_2\text{S}_2$), 1 M HCl, Zinc atomic absorption standard solution (1000 ppm), 1 M KOH potassium hydroxide volumetric standard, acetonitrile (ACN) and sodium chloride (NaCl) were purchased from Sigma-Aldrich; ammonia solution (NH_3 , 35%), Ethanol ($\text{C}_2\text{H}_6\text{O}$), DMF, dichloromethane (DCM), NMP, and diethyl ether were purchased from Fisher Scientific; HBTU and all Fmoc-protected amino acids required for peptide synthesis were purchased from CEM Corporation while the proline-preloaded-TGT resins were obtained from Novabiochem[®]. All chemicals were used without further treatment. The solvent for all ZnO synthesis reactions was ddH₂O with conductivity less than $1 \mu\text{S cm}^{-1}$.

4.3 ZnO Synthesis in the Presence of Peptides

ZnO crystals were synthesized following the methodology described in Section 3.4. In this case, 24 ml of 31.25 mM of NH_3 stock solution at room temperature was vigorously stirred into 25 ml of 30 mM ZnAc_2 solution (at 50 °C) followed immediately by the addition of 1 ml of the prepared peptide solutions; giving final peptide concentrations in a range of 0 to 0.5 mM. The pH was also checked and regardless of the peptide identity and the concentration of the peptide used, the pH of the reaction solutions was maintained to 7.0 ± 0.1 . For this study, samples were taken from the reaction vessels at 24 and 48 hours (± 2 minutes).

4.4 Peptide Synthesis

EM-12 and EC-12 were prepared by solid phase methods using a microwave-assisted solid phase peptide synthesizer (CEM Corporation) via Fmoc chemistry following methodology described in Section 2.9, Chapter 2. The purity of the lyophilized peptides was analyzed

with a Dionex HPLC equipped with a UV detector (set at 214 nm) and a Jupiter 4u Proteo 90A C12 Reverse Phase column (Phenomenex) (see Section 2.10, Chapter 2 for analysis details). The purity of EM-12 and EC-12 was determined as 88% and 93% respectively. The m/z (mass to charge ratio) of the peptides was measured by Dr Graham Hickmann (The John Van Geest Cancer Research Centre, NTU) using a Bruker UltraflexIII TOF/TOF mass spectrometer and analysed with Bruker DaltonicflexAnalysis software. The molecular weight (Mw) of EM-12 and EC-12, 1371.8 g/mol and 1343.7 g/mol, respectively; was confirmed with their measured m/z of 1371.6 m/z and 1343.6 m/z, respectively (Appendix 4.1).

4.5 Characterization

The crystallinity of the precipitates obtained was characterized using XRD (PANalytical X'Pert PRO, Cu K α radiation with wavelength of 1.54056 Å). Ground samples (if necessary) were packed into an aluminium sample holder and scanned from 5° to 90° of 2 θ at an accelerating voltage of 45 kV, 40 mA filament current, using a scan speed of 0.02 ° s⁻¹ at room temperature. Diffraction patterns were analyzed using X'Pert-HighScore Plus (Version 2.0a) program for diffractogram manipulation, background determination and peak identification. The mean crystallite size (grain size) ratio of c- and a-axis i.e. (0001) plane was estimated using the Scherrer equation: $d = 0.9\lambda/(\beta \cdot \cos \theta)$, where d, λ , β , and θ are the grain size, X-ray wavelength, the full-width at-half-maximum (fwhm), and the Bragg angle, respectively. The morphology and size of selected precipitates were studied using SEM (JEOL JSM-840A, 20 kV, gold sputter-coated samples). For ZnO crystal size analysis, more than 30 crystals were studied for each sample and the aspect ratio (L/D = length/diameter average) of each individual crystal was determined using the Java-based image processing program (*ImageJ* software). ATR (Perkin Elmer Spectrum 100 Series Spectrometer with Diamond/KRS-5 crystal) was used to detect the functional groups present in the lyophilized precipitates. Spectra were averaged from 32 scans at 4 cm⁻¹ resolution with air as background. The amount of non-ZnO component in the precipitates was determined by thermogravimetric analysis, TGA (Mettler Toledo TGA/SDTA 851°) where samples were heated at 10 °C·min⁻¹ from 30 °C to 900 °C in air to ensure complete

combustion of all organic material. The chemical constitution of the precipitates was investigated by XPS using a VG Scientific ESCALab MkII X-ray photoelectron spectrometer with an Al K α X-ray source ($h\nu = 1486.6$ eV). Samples were ground and then mounted on standard sample holders. Before analysis of the samples, the calibration and linearity of the binding energy scale was checked with a pure silver sample using the peak positions of the Ag 3d $_{5/2}$ photoelectron line (at 368.26 eV) and the AgM $_4$ NN Auger line (at 1128.78 eV). Survey spectra of precipitates were collected covering the full BE range from 0 - 1200 eV using a step size of 1 eV, a dwell time of 0.2 seconds and PE of 50 eV. High resolution core level spectra of the Zn 2p $_{3/2}$, C 1s, O 1s, N 1s and S 2p peaks were collected using a PE of 20 eV, a step size of 0.2 and a dwell time of 0.4 seconds, which were subsequently deconvoluted and fitted using standard mixed Gaussian-Lorentzian components using CasaXPS software. To compensate for surface charging effects in the insulating samples, all binding energies were corrected with reference to the saturated hydrocarbon C 1s peak at 285.0 eV using the CasaXPS software.

4.6 ITC studies

Isothermal Titration Calorimetry (ITC) was used to study peptide-mineral interactions. ZnO crystals for this study were calcined at up to 500 °C using a heating rate of 10 °C/min during 30 minutes in order to eliminate any presence of organic material such as acetates from possible intermediates of reaction. The calcined ZnO was then characterised by ATR, XRD and SEM analysis to ensure no other compounds apart from ZnO were present in the sample (Appendix 4.2). A stock solution of ZnO (0.015 M) was prepared by suspending a known weight of ZnO particles in HPLC grade water (1.2 mg·ml $^{-1}$) and followed by sonication for 30 minutes. ITC ZnO solutions (0.05 mM) were prepared from the stock solution. The concentration of these samples was checked using ICP-OES (Perkin Elmer ICP-OES Optima 2100DV). The average concentration of Zn $^{2+}$ ions present in the samples prepared ($n = 6$) was 0.050 ± 0.004 mM. The instrument used to carry out these ITC studies was a MicroCal VP-ITC developed by GE Healthcare. The experimental optimization was achieved by varying a number of experimental parameters: the total number of injections, cell temperature (°C), reference power ($\mu\text{cal}\cdot\text{s}^{-1}$), stirring speed (rpm), injection volume (μl), injection duration (s), spacing between injections (s), syringe concentration (mM) and

cell concentration (mM). Optimization was required to (i) reach the saturation-endpoint of the reaction, (ii) to minimize interference in measured heats and (iii) to obtain sufficient measurements for prediction of curve shape. The parameters selected for the experiments were; cell temperature at 25 °C, reference power of 15 $\mu\text{cal}\cdot\text{s}^{-1}$ and stirring speed of the syringe of 394 rpm to maintain ZnO particles in suspension. Total volumes in the cell and syringe were 1.4 ml and 280 μl , respectively. Periodical injections of 10 μl were executed every 1200 s for the first 10 injections and 1000 s for the remaining experiment. The spacing between each injection in seconds was programmed to allow for equilibrium to be reached after each injection. Each experiment had a total duration of around 8 hours. The concentrations of ZnO in the cell and peptide in the syringe were chosen to reach saturation. Previous studies in our group (Limo and Perry, 2015) showed that saturation can be attained using a relation of $[\text{ZnO}]/[\text{peptide}]$ between 0.025 - 0.050. Thus, 1.2 mM peptide (EC-12) was prepared for a ZnO concentration of 0.05 mM.

For this study, several experiments were carried out prior to the titration of the ZnO solution with peptide (Figure 4.1). Firstly, the water-water method was run before and after each experiment to make sure both syringe and cell were clean and exempt of any residues that could remain from a previous analysis. Secondly, a water-ZnO method was performed in order to check possible interactions between the ZnO crystals and the solvent used in the system (water). And finally, as peptide-peptide interactions can occur in water (Limo and Perry, 2015), the heat changes measured in the peptide-water method were subtracted from the heat changes during the titration of ZnO particles with peptide; therefore, the observation of heat changes in the final titration (peptide-ZnO method) can be only attributed to the binding reaction of the peptide with the mineral. Data analysis was conducted using ORIGIN v7.0 software. For fitting, a non-linear least-square algorithm with binding sites models available by MicroCal was used. Depending on the shape of the isotherm, the data could be fitted using either identical or two independent sites binding model. The main difference between the models is that the binding sites can have the same ΔH and K_B values (one set of identical sites model) or have two different binding sites with separate values of ΔH and K_B (two sets of independent sites model) (Freyer and Lewis, 2008; Limo *et al.*, 2014).

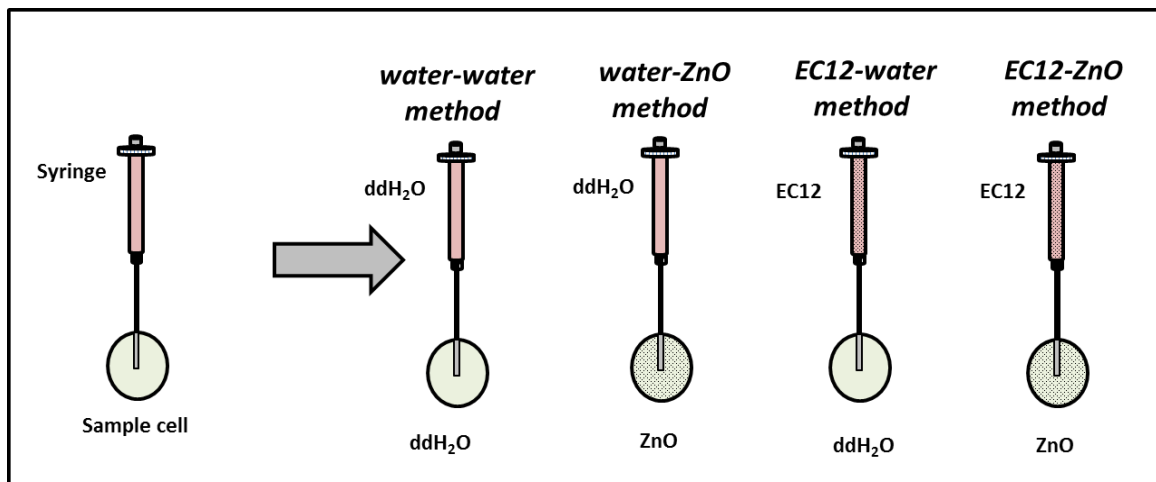


Figure 4.1 Scheme of the methodology followed for ITC studies.

4.7 Results and Discussion

4.7.1 Peptide EM-12: Delay/Suppression of ZnO Formation

The role of EM-12 in affecting ZnO formation was explored by characterization of the precipitates at a series of reaction times (24 and 48 hours). The previous study (Chapter 3) has shown that in the system using ZnAc_2 and NH_3 as precursors the formation of ZnO occurs via intermediate(s), layered structures that only later transform to the oxide phase, which have been identified as LBZA (Hosono *et al.*, 2004; Jang *et al.*, 2010; Patrinoiu *et al.*, 2013; Poul *et al.*, 2000; Tokumoto *et al.*, 2003; Wang *et al.*, 2006; Wang *et al.*, 2011) and LBZAC (Jang *et al.*, 2010; Liang *et al.*, 2014; Patrinoiu *et al.*, 2013) with formulae, $\text{Zn}_5(\text{OH})_8(\text{CH}_3\text{COO})_2 \cdot 2\text{H}_2\text{O}$ and $\text{Zn}_5(\text{OH})_x(\text{CH}_3\text{COO})_y(\text{CO}_3)_z \cdot n\text{H}_2\text{O}$ ($x + y + z = 10$), respectively.

Based on the characterization of the 24 hours precipitates using SEM (Figure 4.2), the addition of EM-12 caused the delay of ZnO crystal growth when increasing the peptide concentration in the reaction solution, with LBZA being the major compound present at higher concentrations of EM-12. The addition of 0.1 mM of EM-12 (Zn-to-peptide ratio = 150:1) did not affect ZnO formation significantly as ZnO crystals were observed in the precipitates (Figure 4.2a). However, in the presence of EM-12 at higher concentrations (Figure 4.1b-c), either a delay or suppression of ZnO formation was perceived since a

layered structure with irregular shapes was observed instead of the hexagonal rods. Although, the layered structures found in all the samples corresponded to LBZA, a significant difference between LBZA structures in the precipitates from 0.2 to 0.5 mM of EM-12 was observed (more SEM images are shown in Appendix 4.3), being star-like structures for the highest concentration.

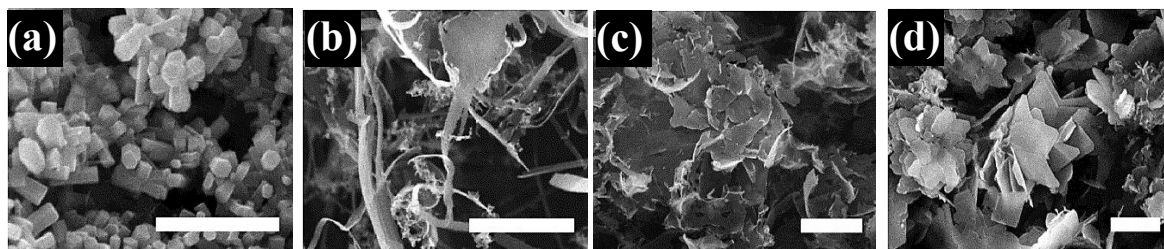


Figure 4.2 SEM images of precipitates in the presence of EM-12 at 24 hours: (a) 0.1 mM, (b) 0.2 mM, (c) 0.4 mM and (d) 0.5 mM. All scale bars are 5 μm .

ZnO delay formation was clearly observed in the 0.2 mM precipitate due to the detection of ZnO as the major component being delayed to 48 hours (Figure 4.3). This effect will be referred to as “delayed-formation” hereafter. Further, EM-12 not only caused the delayed formation of ZnO (conversion from LBZA to ZnO) but it also caused the inhibition of the crystal growth along the c-axis corresponding to the (0002) plane which is discussed later in Section 4.7.4 (‘Effect of EM-12 and EC-12 on ZnO morphology’).

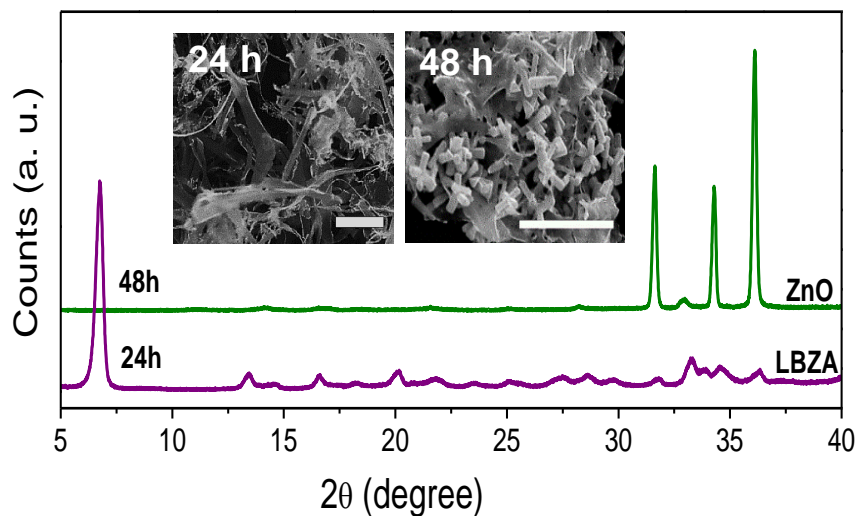


Figure 4.3 XRD diffractograms of precipitates in the presence of 0.2 mM of EM-12 collected at 24 hours and 48 hours. Inset SEM images of these precipitates. All scale bars are 5 μm .

XRD diffractograms for all precipitates at 48 hours (Figure 4.4) showed that for higher concentrations of peptide added LBZA remained the main compound. In the presence of 0.4 mM EM-12, either characteristic peaks of LBZA or ZnO were detected and for the highest EM-12 concentration studied; 0.5 mM, LBZA remained the major phase at 48 hours (Figure 4.4) suggesting the suppression of ZnO formation. The presence of LBZAC (as a main compound) was discounted as $00l$ reflections would have had a larger interlayer spacing (~ 19 Å) produced by the co-intercalation of both acetate and carbonate ions (Jang *et al.*, 2010; Patrinoiu *et al.*, 2013).

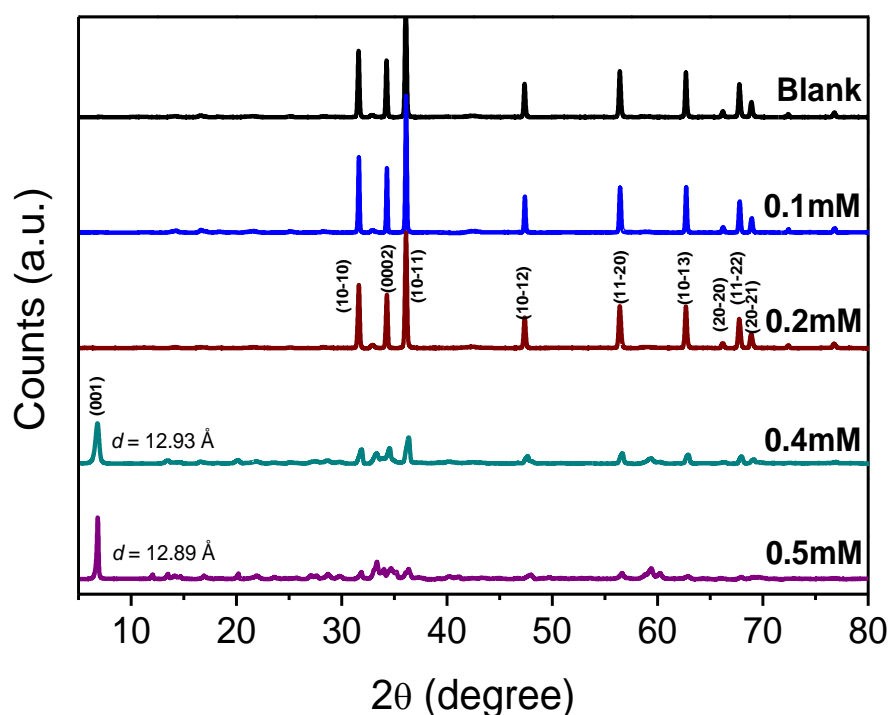


Figure 4.4 XRD diffractograms of the precipitates collected at 48 hours of reaction for the Blank, 0.1 mM, 0.2 mM, 0.4 mM and 0.5 mM of EM-12. Four-digit and three-digit Miller indices were assigned to crystal planes of ZnO and LBZA, respectively.

TGA results also confirmed the delayed-formation of ZnO and its suppression when higher concentration of peptide was employed (Figure 4.5a). The weight losses observed in the presence of 0.2 mM EM-12 and above ($> 25\%$), supported the presence of LBZA in the samples (Figure 4.5a). The reduction in weight loss from 24 to 48 hours was due to the phase transformation from LBZA to ZnO. However, less reduction of weight loss was

observed for the sample containing 0.4 mM of EM-12, which is believed to be due to a mixture of LBZA/ZnO phases present in the samples as shown by XRD results (Figure 4.4). Additionally, for 0.5 mM of EM-12, LBZA remained the major phase up to 48 hours (Figure 4.5a). Previous studies by our group, showed that LBZA was still the main phase present in the precipitates after 168 hours of reaction (Liang, 2010; Liang *et al.*, 2014). Hence, the addition of 0.5 mM peptide suppressed ZnO formation to the extent that LBZA remained stable for longer periods of time while lower EM-12 concentrations still formed ZnO crystals but slowed down the rate of conversion of LBZA to ZnO. The delayed-formation of ZnO was also supported with the TGA 1st derivative weight loss curves (Figure 4.5b) which resulted in three stages of weight loss. For the 24 hours precipitates containing 0.2 mM of EM-12, the curve was very similar to that found for the 1 hour precipitates in the Blanks (Section 3.6.1), where LBZA was the main phase present in the samples. With progression from 24 to 48 hours, a change of the weight loss region in Stage 2, could be attributed to the phase transformation of intermediates was observed. Samples synthesized in the presence of peptide showed a higher weight loss attributable to acetate groups (Stage 3) compared with weight loss from the Blank samples.

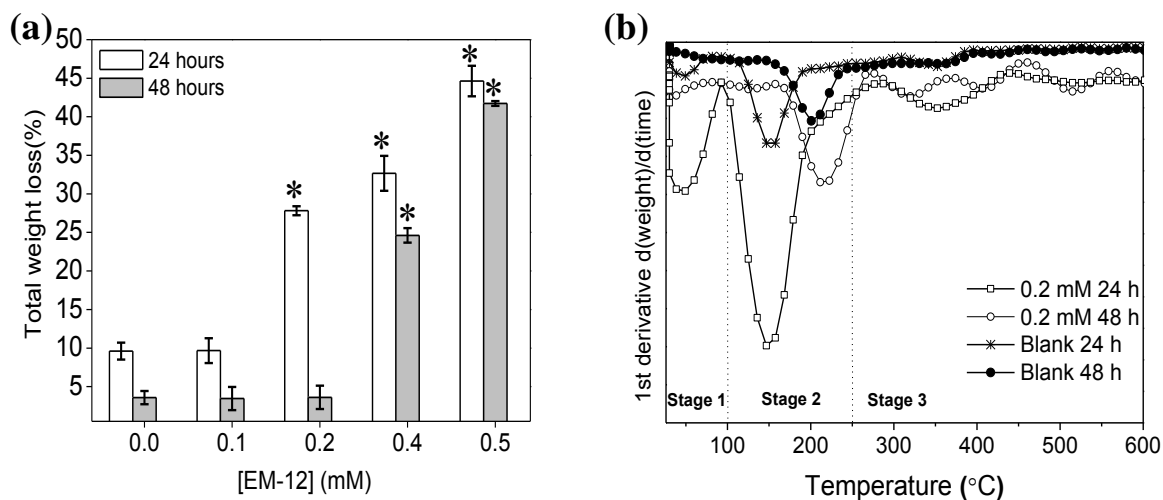


Figure 4.5 (a) Total weight loss (%) of precipitates collected in the presence of different concentrations of EM-12 (0.1-0.5 mM) at 24 hours and 48 hours. The starred bars correspond to samples that are mainly LBZA as observed by XRD and; (b) representative TGA 1st derivative weight loss curves of precipitates collected at 24 and 48 hours with [EM-12] of 0 mM (Blank) and 0.2 mM; where Stage 1 (< 100 °C) corresponds to the release of physisorbed water; Stage 2,

dehydration of intercalated water (100 °C - 168 °C) and/or the dehydroxylation of zinc hydroxide layers in LBZA or LBZAC (168 °C - 250 °C) and; the Stage 3 (250 - 400 °C), the decomposition of acetate/carbonates groups.

As explained in Chapter 3, acetate groups in LBZA can be gradually replaced by carbonate groups originating from dissolved CO₂ present in solution, hence a new intermediate can be observed, LBZAC. At the later stages of ZnO formation (i.e. 48 hours) carbonate species can be dominant over acetate species, albeit in traces amounts relative to the amount of ZnO present (Liang *et al.*, 2014). In Figure 4.6, it can be observed that for the sample containing 0.1 and 0.2 mM of EM-12, the peaks identified were similar to those for the Blank, and arose from traces of carbonate present in the sample (peaks iii and iv) even though ZnO was the dominant compound detected by XRD. For higher concentrations of peptide studied, 0.4 and 0.5 mM, characteristic acetate peaks were detected (peaks ii, iv and v), confirming the delayed-formation of ZnO.

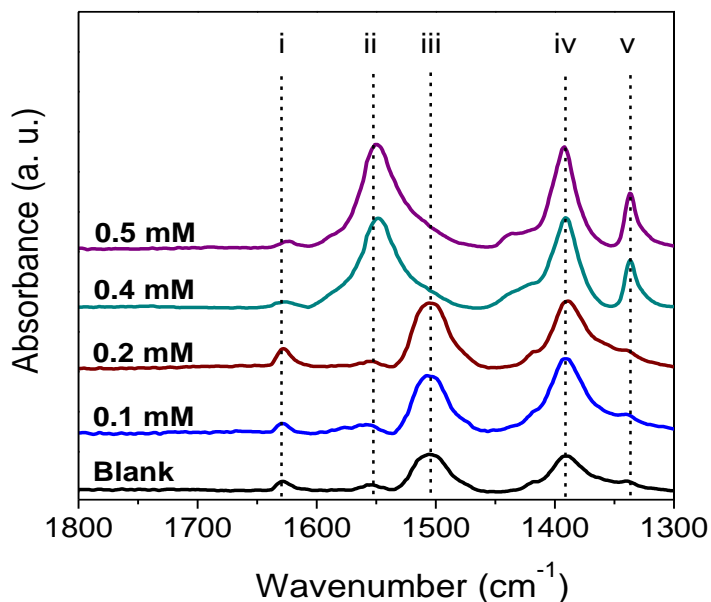


Figure 4.6 ATR spectra of precipitates collected at 48 hours for Blank, 0.1 mM, 0.2 mM, 0.4 mM and 0.5 mM of EM-12 were peaks correspond to (i) O-H vibrational mode attributed to the hydroxide slab in LBZA/LBZAC, (ii) ν_{as} of COO⁻, (iii) ν_{as} of CO₂³⁻, (iv) ν_s of COO⁻ and/or ν_3 of CO₂³⁻ and (v) δ_s of -CH₃.

By XPS, analogous experiments to those performed on the Blanks as in chapter 3 were carried out. The survey spectra showed the presence of Zn, O and C in all the precipitates studied (Blanks, 0.2 mM and 0.4 mM of EM-12), with peaks in the Zn 2p_{3/2}, O 1s and C 1s regions; having BE values of 1021.7 ± 0.2 eV, 531.6 ± 0.1 eV, 285.0 ± 0.0 eV, respectively; (Figure 4.7a). From the plot of % area of the C 1s and Zn 2p_{3/2} peaks at different concentrations of peptide, an increase of the C 1s region with peptide addition can be observed (Figure 4.7b) supporting the supposition that the presence of EM-12 slowed down the rate of conversion of LBZA to ZnO, as more C is expected with the presence of the intermediate. For clarification, the data obtained include traces of ‘adventitious carbon’, usually present in the XPS experiment (Section 3.6.1); however, the remaining carbon was thought to be from LBZA, as identified by XRD and TGA.

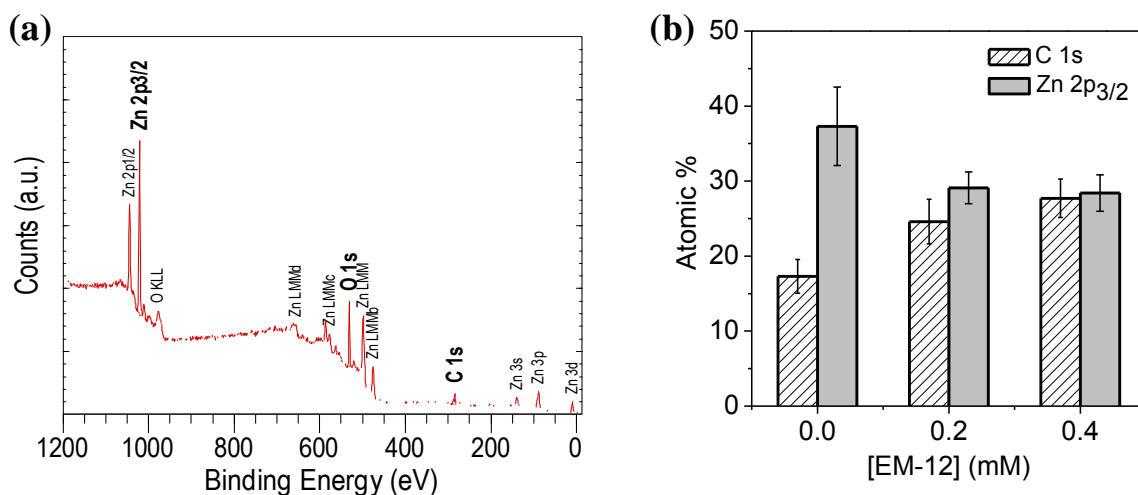


Figure 4.7 (a) XPS survey spectrum recorded from an as-deposited precipitate collected at 24 hours with [EM-12] of 0.4 mM and (b) atomic % of carbon and zinc for the 48 hours precipitate with 0.0 mM (Blank), 0.2 mM and 0.4 mM of EM-12.

The analysis of core-level spectra for Zn 2p_{3/2}, C 1s and O 1s regions, Figure 4.8, showed the different local chemical states of each element in the precipitates indicating the presence of the elements in a mixed environment. In this case, the precipitate with 0.2 mM of EM-12 was chosen due to the different solid phase present at 24 hours and 48 hours, being LBZA and ZnO, respectively.

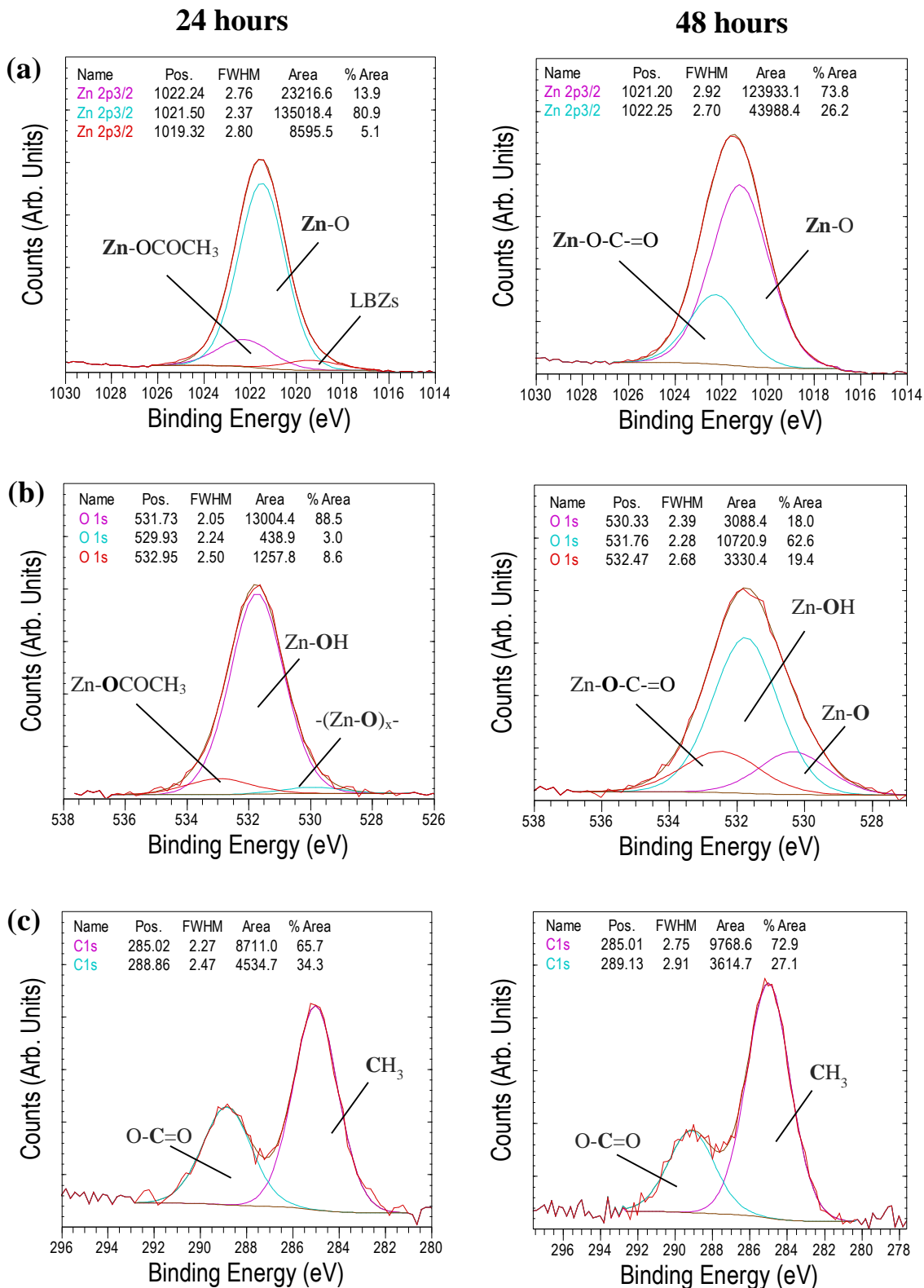


Figure 4.8 Core level spectra of as deposited precipitates collected at 24 and 48 hours of reaction for (a) Zn 2p_{3/2}, (b) O 1s and (c) C 1s for 0.2 mM of EM-12.

Core-level spectra for the Zn 2p_{3/2} region (Figure 4.8a) showed similar BE values as found in the Blanks (Section 3.6.1) for 1 hour precipitates (LBZA) and 48 hours precipitate (ZnO), as well as the same number of peaks fitted, corroborating the presence of the different solid phases present in the samples. The O 1s region (Figure 4.8b) also showed a peak at 529.9 eV shifted to 530.3 eV for 24- and 48-hours precipitates, respectively. Core-level spectra for C 1s (Figure 4.8c) showed peaks corresponding to the methyl (~285 eV) and carboxyl (~289 eV) groups (Ballerini *et al.*, 2007; Clark *et al.*, 1976) as expected from the composition of the materials.

The SEM, XRD, XPS, TGA and ATR analyses confirmed that for the reaction between ZnAc₂ and NH₃ at 50 °C and pH 7.0 ± 0.1 the synthesis of ZnO in the presence of EM-12 slowed down the rate of conversion of LBZA to ZnO; to the extent that ZnO formation was suppressed for the highest concentration of peptide present in the system (0.5 mM of EM-12). The mechanisms in which EM-12 causes this delay/suppression effect can be due to either EM-12 stabilized LBZA or retained Zn²⁺ ions in solution; in both cases LBZA is favoured and is discussed in more detail later in this chapter.

4.7.2 Peptide EC-12: Stronger Complexation Capability with Zn²⁺

A comparison study was carried out using the peptide EC-12, obtained by replacing methionine (M₅) with cysteine (C₅). Residues such as histidine (H), cysteine (C), and methionine (M) are able to coordinate with Zn²⁺ species (Gerstel *et al.*, 2006; Rombach *et al.*, 2002; Vogler *et al.*, 2002). For instance, the imidazole substituent in histidine residues can act as a bridging ligand and coordinate with metal ions as is the case of metalloproteins (Bertini, 2007). Cysteine can bind to metal ions through its thiolate group, for example, it is able to serve as a ligand in ferric heme iron most frequently in its deprotonated cysteinate form (Bertini, 2007) while non-deprotonable methionine is known to coordinate Cu(I) through its sulphur lone pair (Bertini, 2007). Due to the presence of a deprotonable sulphur atom, cysteine is proposed to have a stronger complexation capability with Zn²⁺ compared to methionine.

In this study, experiments were performed using two different concentrations of EC-12. First, 0.2 mM of EC-12 was chosen due to the observation of a delay in the formation of

ZnO in the presence of 0.2 mM of EM-12, where the main compound for the precipitates collected at 24 hours and 48 hours were LBZA and ZnO, respectively. And secondly, the presence of 0.4 mM of EC-12 was also studied in order to see if there was a delay and/or inhibition of ZnO formation at higher concentrations of peptide added. In the presence of 0.2 mM of EC-12, XRD results were different from the precipitates containing EM-12 as LBZA was not detected in the 24 hours precipitates (Figure 4.9a) suggesting that no delay in the formation of ZnO occurred at this peptide concentration. However, ZnO crystals generated in the presence of 0.2 mM of EC-12 were morphologically different from those obtained for the Blanks, showing flatter and shorter structures with less well-defined facets of the crystals (Figure 4.9b(i)-(ii)). For the higher concentration of peptide added, 0.4 mM of EC-12, samples showed twinned spherical crystals (no facets of the crystals) (Figure 4.9b(iii)-(iv)) instead of twinned hexagonal rods commonly observed for the Blanks and no evidence of delayed-formation of ZnO was observed in the precipitates (Figure 4.9a).

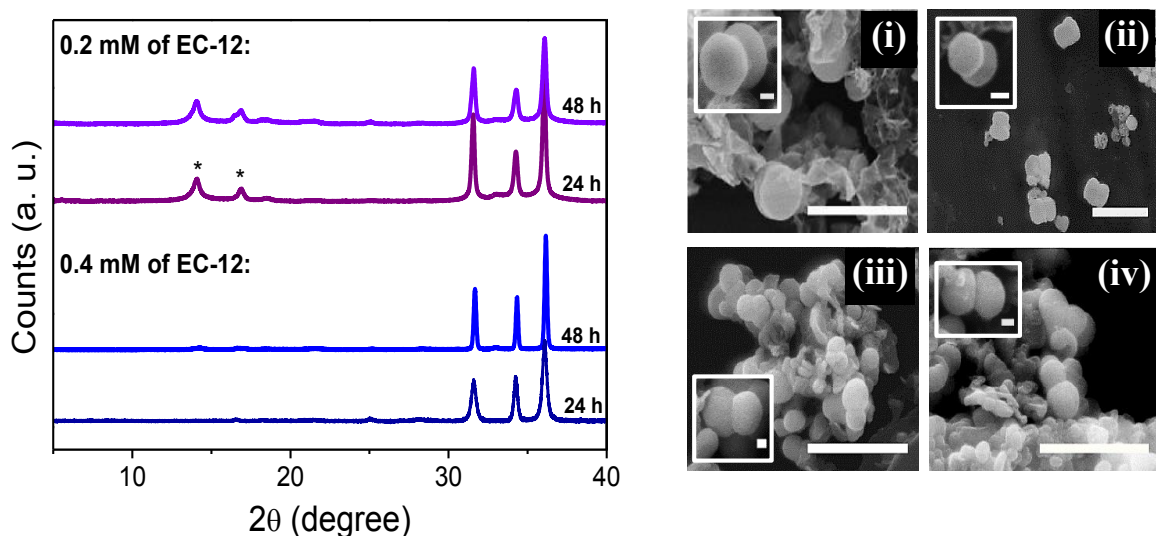


Figure 4.9 (a) XRD diffractograms of precipitates in the presence of EM-12 at different reaction times for (i) 0.2 mM 24 hours, (ii) 0.2 mM 48 hours, (iii) 0.4 mM 24 hours and (iv) 0.4 mM 48 hours. All scale bars are 5 μm and inset bar 0.5 μm . The position of the diffraction peaks originating from the PP holder are marked with asterisks (*) (Appendix 2.1).

TGA results showed an increase in weight loss up to ~25% for the 24 hours precipitates which suggested that weaker delayed-formation of ZnO occurred compared with materials

formed in the presence of EM-12 (Figure 4.10). Even so, the higher complexation capability of EC-12 proposed due to the presence of the cysteine, did not lead to a stronger delay/suppression effect on ZnO formation as seen for EM-12 (~34%). With progression of the reaction (48 hours), both concentrations showed a % weight loss comparable with the Blanks (< 10%). The weaker but still delayed-formation of ZnO in the presence of EC-12 was perhaps surprisingly caused when lower concentrations of EC-12 were used (Sola-Rabada *et al.*, 2015). This was suggested to be due to a balance between the catalytic effect and a delay/suppression effect.

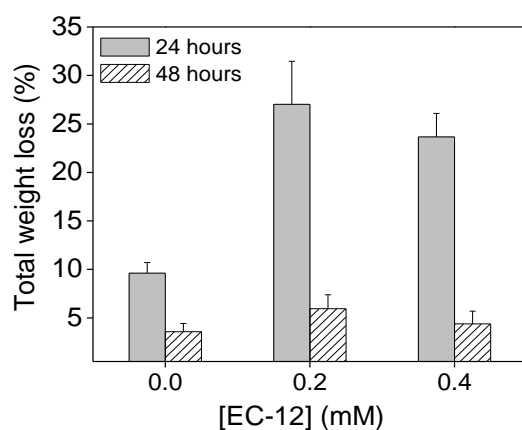


Figure 4.10 Total weight loss for 24- and 48-hours precipitates at different EC-12 concentrations.

As explained in Section 4.1, the incorporation of the peptide ET-17 (EAHVMHKVAPRP-GGGSC) into $\text{Zn}(\text{OH})_2$ sols could catalyse the formation of ZnO. Although, a catalytic activity was not shown in presence of EC-12, a change in the catalytic activity of a surface (the grain size) can affect the rate of mineral formation (Thiele, 1939). As different crystal morphology is growing in the system when EC-12 is present, there might be a change between the rates of crystal formation and growth. Therefore, the similar combination of amino acid side chain functionalities (for ET-17, EC-12 and EM-12) but with structural differences arising from peptide sequence suggests that there might be a tuneable strength of these effects.

ATR and XPS results for EC-12 studies are shown in Section 4.7.3, as data revealed the presence of this peptide in the solid phase which made possible the study of the possible interactions taking place between the solid phase and the peptide.

4.7.3 Study of the Peptide-Mineral Interactions

ATR spectra of precipitates should reveal the presence or not of the peptide in the samples (precipitates) by the detection of the amide-I band at $\sim 1700\text{-}1600\text{ cm}^{-1}$ associated mainly with the stretching vibration of the C=O in peptides (Kong and Yu, 2007). ATR analysis of the lyophilised precipitates for samples containing EM-12 and EC-12 was carried out, as well as the analysis of the peptides itself (Figure 4.11).

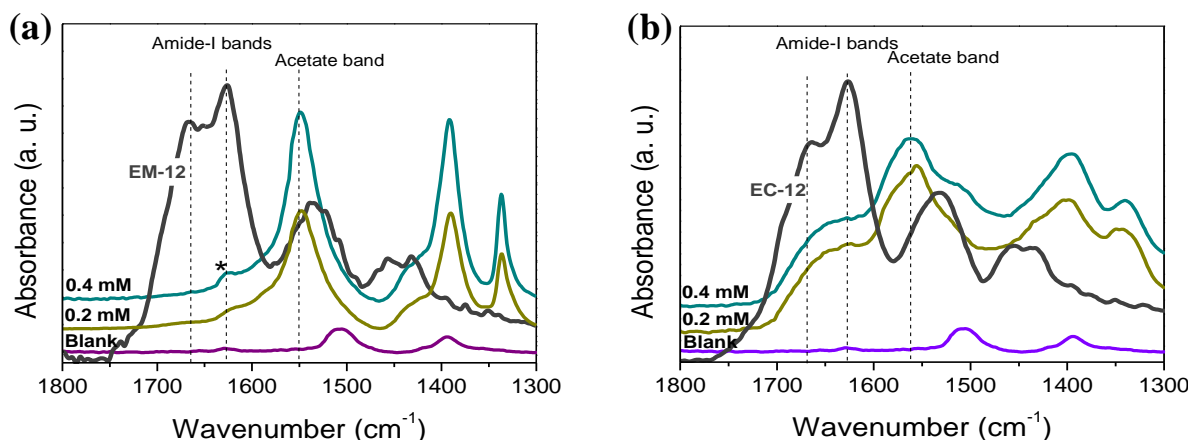


Figure 4.11 ATR spectra of lyophilised precipitates collected at 24 hours in the presence of (a) EM-12 and (b) EC-12. The peak arising with an asterisk (*) is attributed to the O-H vibrational mode (corresponding to the hydroxide slab in LBZA/LBZAC).

For EM-12, peaks corresponding to the amide-I band were detected at $\sim 1667\text{ cm}^{-1}$ and 1628 cm^{-1} (Figure 4.11a). Notice that, the shape of the amide-I band for proteins or polypeptides consist of overlapping component bands, representing α -helices, β -sheets, turns and random structure; correlated to the secondary structural conformation adopted by proteins or polypeptides (Goormaghtigh *et al.*, 1990). ATR spectra of precipitates in the presence of EM-12 (Figure 4.11a) showed there is no detectable peptide in the samples. The peak at 1620 cm^{-1} (*) did not correspond to the peptide as showed in Section 4.2. In contrast, the presence of the EC-12 was observed in all the precipitates as assessed by the detection of the amide-I band (Figure 4.11b), suggesting that this peptide may interact with the Zn^{2+} species in the solid-phase. Nevertheless, the exact solid phase(s) which EC-12 interacted with could not be uniquely identified as acetate groups are detected in the

precipitates indicating that LBZA and/or LBZAC in addition to ZnO were present in the solid phase.

Since EM-12 was not present in the precipitates, it was decided to analyse the supernatants in order to check whether this peptide, with a weaker complexation capability, could be washed out of precipitates through the cleaning process. Thus, supernatants were centrifuged following the same conditions described in Section 3.3 for the precipitates, and an aliquot was carefully taken from the middle of the tube (to avoid collection of any precipitate remaining at the bottom) and freeze-dried. ATR results showed the presence of the amide-I peaks in lyophilized supernatants (Figure 4.12) at the higher concentrations of EM-12 added (0.4 mM and 0.5 mM), implying that EM-12 only interacts with Zn^{2+} species in solution and not with Zn^{2+} species in the solid phase. The absence of the amide-I band from the spectra of samples prepared in the presence of 0.1 mM and 0.2 mM of EM-12 can be explained by it being present at concentration levels below the detection limit of the ATR technique.

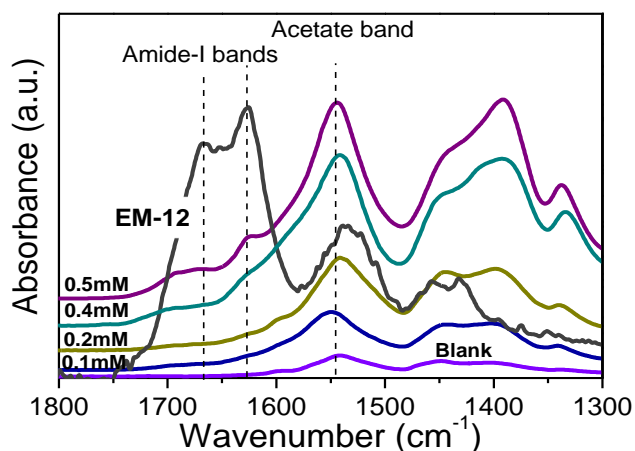


Figure 4.12 ATR spectra of lyophilised supernatants in the presence of EM-12.

The presence of the peptide EC-12 in the samples was also studied by XPS. The incorporation of Zn, O and C was observed in all the precipitates, similar to the XPS survey spectra when studying EM-12, with a peak in the N 1s region (Figure 4.13a) also being detected. The N 1s high resolution core level spectrum showed a peak at 399.5 ± 0.4 eV (Figure 4.13b) attributed to the presence of amino groups in the peptide (Baier *et al.*, 2012).

These results were further supported with the presence of an extra peak (not found when studying EM-12) in the C 1s region at 287.0 eV (Figure 4.13c) corresponding to the tertiary carbon connected with the nitrogen atom of the amino group (Cavalleri *et al.*, 2004; Clark *et al.*, 1976; Gao *et al.*, 2009).

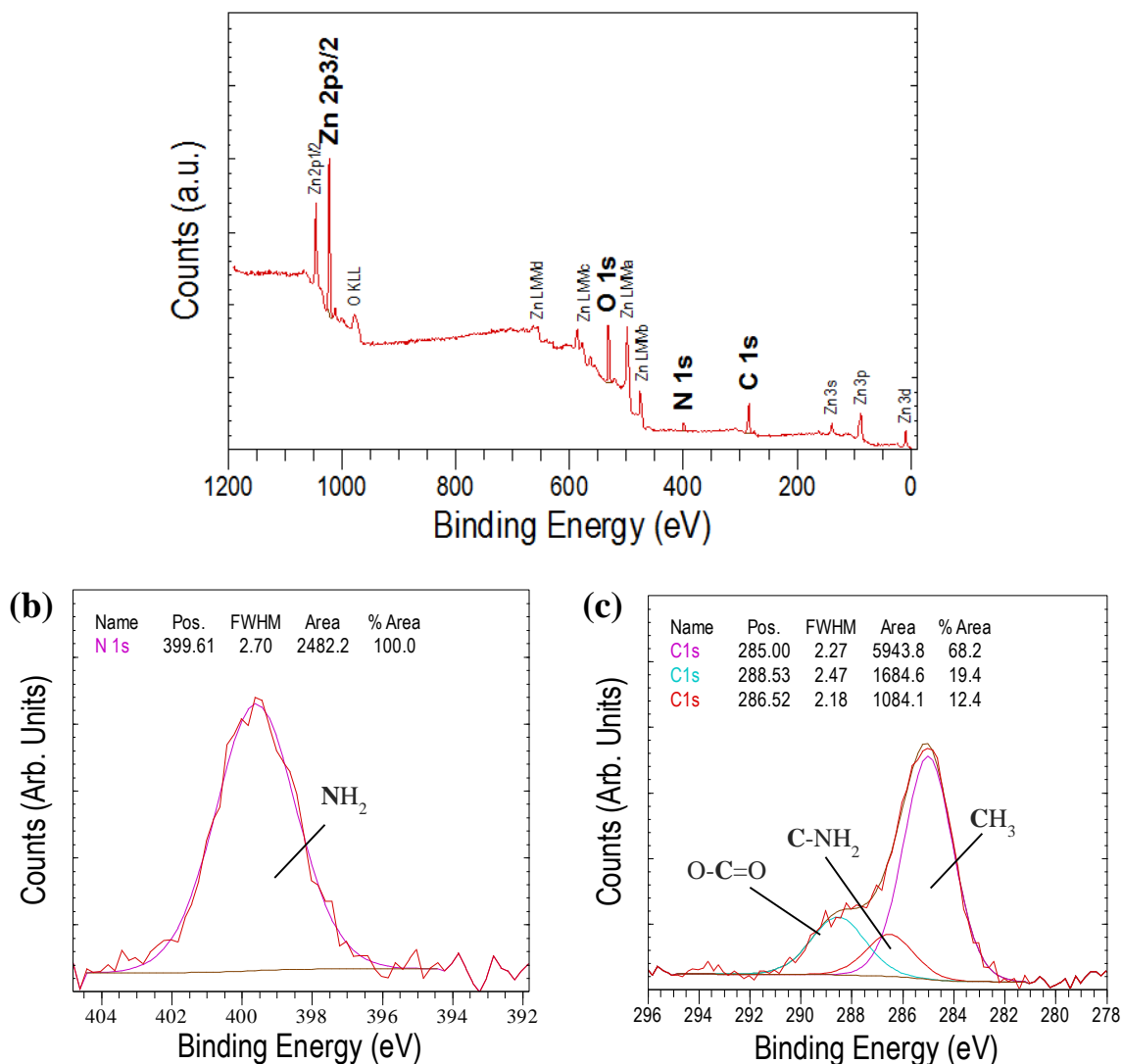


Figure 4.13 (a) XPS survey spectrum recorded from an as-deposited precipitate collected at 24 hours with [EC-12] of 0.4 m and the high resolution core level spectra of (b) N1s and (c) C 1s region.

Based on the ATR and XPS results, it can be concluded that EM-12 interacts with Zn^{2+} species in solution, whereas EC-12 was able to interact with Zn^{2+} species in the solid phase.

Previous studies by our group have shown that retention of Zn^{2+} in solution was proportional to EM-12/EC-12 concentration, suggesting Zn^{2+} -peptide complexation in solution (Liang, 2010). The results also showed that the addition of EC-12 increased the % Zn^{2+} in solution with respect to the peptide EM-12 (Liang, 2010).

As previously mentioned, cysteine is proposed to have a stronger complexation capability with Zn^{2+} compared to methionine, which was confirmed by detection of a higher fraction of Zn^{2+} in solution (Appendix 4.4) and by the detection of this peptide in the solid-phase (ATR and XPS results). Henceforth, the interaction of the Zn^{2+} species in the solid phase(s) with the peptide EC-12 could be studied by XPS. It is proposed that peptides may interact via the side chains of amino acids (i.e. sulphur atoms from methionine or cysteine; oxygen atoms from glutamic acid; and/or nitrogen atoms from histidine) by electron donation. The presence of peptide in the precipitates made it possible to identify the different elements present in the amino acid sequence. For instance, the amide groups contained in EC-12 were detected by ATR (amide-I bands) and XPS (N 1s and C 1s peaks). The main difference between EM-12 and EC-12 is the methionine and cysteine amino acids, respectively (Appendix 1.1). Note that, both peptides at the reaction pH have identical side chain and termini charges and their (positive) net charges are the same (Appendix 4.5). Despite the presence of a sulphur atom in both amino acids, the thiol group from cysteine has been shown to readily react with heavy metal ions (Zn^{2+} , Cd^{2+} , Pb^{2+} , Hg^{2+} , Ag^+) due to the high affinity of the soft sulphide and the soft metal, as is the case of the mercuric mercapto-cysteine (Stricks and Kolthoff, 1953). Cysteine residues also play an important role in biology; for example, stabilization of protein structure through disulfide bonds (Guzzo, 1965) or catalytic activity in biochemical reactions (Guan and Dixon, 1991). Thereafter, the presence of EC-12 in the precipitates was thought to an interaction between the thiol group present in the cysteine group and the Zn^{2+} species in the solid phase(s). In support of this, S 2p high core level spectra was performed for precipitates in the presence of EC-12 (Figure 4.14). As expected, a peak was observed in the S 2p region, which could arise from the cysteine thiol group (Dodero *et al.*, 2000) present in EC-12. This broad peak at around 162.2 eV (Figure 4.14) was deconvoluted into two peaks, $2p_{3/2}$ and $2p_{1/2}$ at 161.8 and 163.0 eV, respectively. The S 2p doublet separation could be fitted using a peak area ratio of 2:1 and a separation of 1.18 eV. Generally, in the S 2p region, the presence of a

doublet corresponding to the $2p_{3/2}$ and $2p_{1/2}$ peaks should be observed; however, overlap of the two peaks may occur due to the small amount of sulphur in the samples (Bae *et al.*, 2004). Previous studies have showed that the binding energy of the S $2p_{3/2}$ signal determines whether sulphur is present as a thiol (unbound) or thiolate (bound to the surface), the BE values being at ~ 163 eV and ~ 162 eV, respectively (Castner *et al.*, 1996; Cavalleri *et al.*, 2004; Clark *et al.*, 1976; Dodero *et al.*, 2000; Volmer *et al.*, 1990). The presence of sulphur-sulphur interactions within the peptide solution was discarded as S $2p_{3/2}$ values were lower than those reported for disulphides, which can be found between 162.5 to 163.5 eV (Castner *et al.*, 1996; Nesbitt *et al.*, 1998). The S $2p_{3/2}$ signal found at 161.8 eV, suggested that the interaction of EC-12 with the solid phase could be via Zn^{2+} -sulphur (from cysteine).

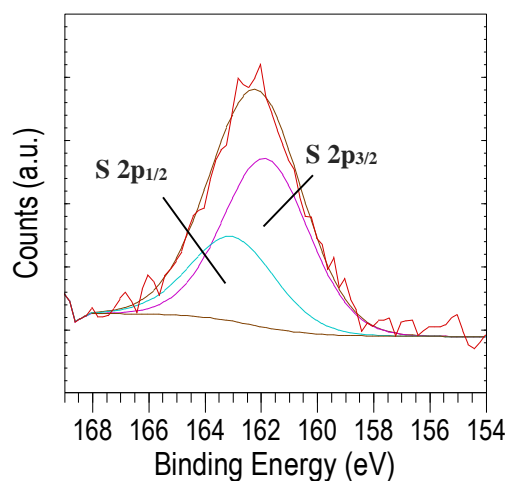


Figure 4.14 XPS high resolution core-level spectra of the S 2p region.

As previously mentioned, the modification of ZnO morphology via the adsorption of EC-12 on ZnO crystals could not be confirmed due to the presence of other solid phase(s), LBZs. The intercalated acetate anions into LBZs have been shown to be oriented preferentially towards the positive (0001) plane of ZnO crystal (Jang *et al.*, 2011). Therefore, the possibility of EC-12 intercalating into LBZA and causing the drastic morphological change of ZnO crystals was studied. The interlayer spacing of LBZA formed in the presence of EC-12 did not change significantly compared to the Blank (Figure 4.15). Despite this fact, an approximation of the peptide dimensions was

investigated using ChemDraw 3D software to see if EC-12 could be fitted into the zinc hydroxide layers (Appendix 4.6). The lack of change in the interlayer spacing and dimensions of the peptide (larger than spacing measured) implied that either EC-12 was not intercalated or it was oriented parallel to the zinc hydroxide layer whilst intercalated. Thus, the possibility of EC-12 intercalating into LBZA formed could not be discounted.

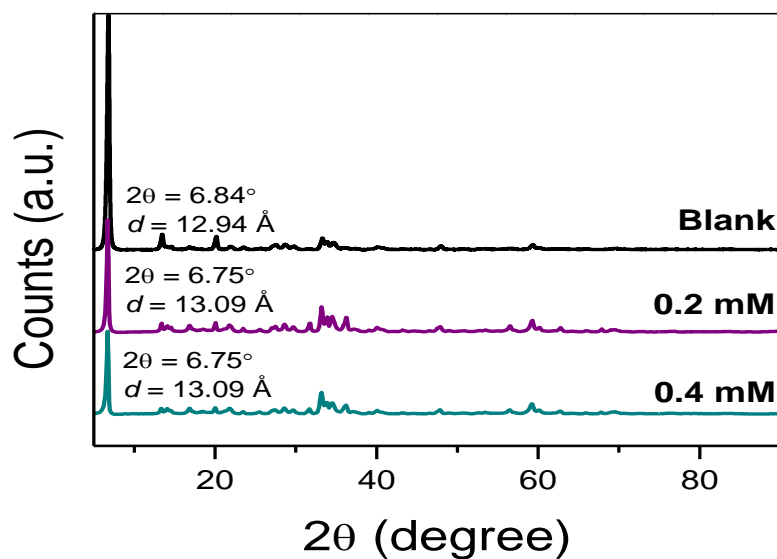


Figure 4.15 XRD diffractograms of the 1 hour precipitates for the Blank, 0.2 mM and 0.4 mM of EC-12 precipitate.

A recent study has shown that some common amino acids can be incorporated into the ZnO lattice (Brif *et al.*, 2014); particularly, amino acids containing S or Se, as are the case of cysteine and selenocysteine, respectively. This study also showed that incorporation of the amino acids led to a change in the optical and paramagnetic properties of the material as well as the crystal morphology. Particularly, the incorporation of cysteine into the ZnO lattice gave rise to the formation of ZnO spheres crystals instead of rods (Brif *et al.*, 2014). Therefore, the possibility that EC-12 could have been incorporated into the lattice of ZnO was investigated. In this case, studies were performed using an X-ray diffractometer and accurate d-spacing values were obtained (calculated) by running a reference Silicon standard prior to each analysis (Appendix 4.7). ZnO lattice strain modification was observed when EC-12 was added into the system (Figure 4.16). The values for the (1010), (0002) and (1011) planes were 0.108%, 0.039% and 0.128%, respectively, suggesting the

possibility of EC-12 being incorporated into the lattice of ZnO. Note that, the (0002) plane (or c-axis) did not show much lattice strain modification and the crystals look shorter; however, this is not surprising as for precipitates prepared in the presence of EM-12 no lattice strain modification was observed (Appendix 4.8) and yet crystal growth along the c-axis was significantly affected (see next Section 4.7.4).

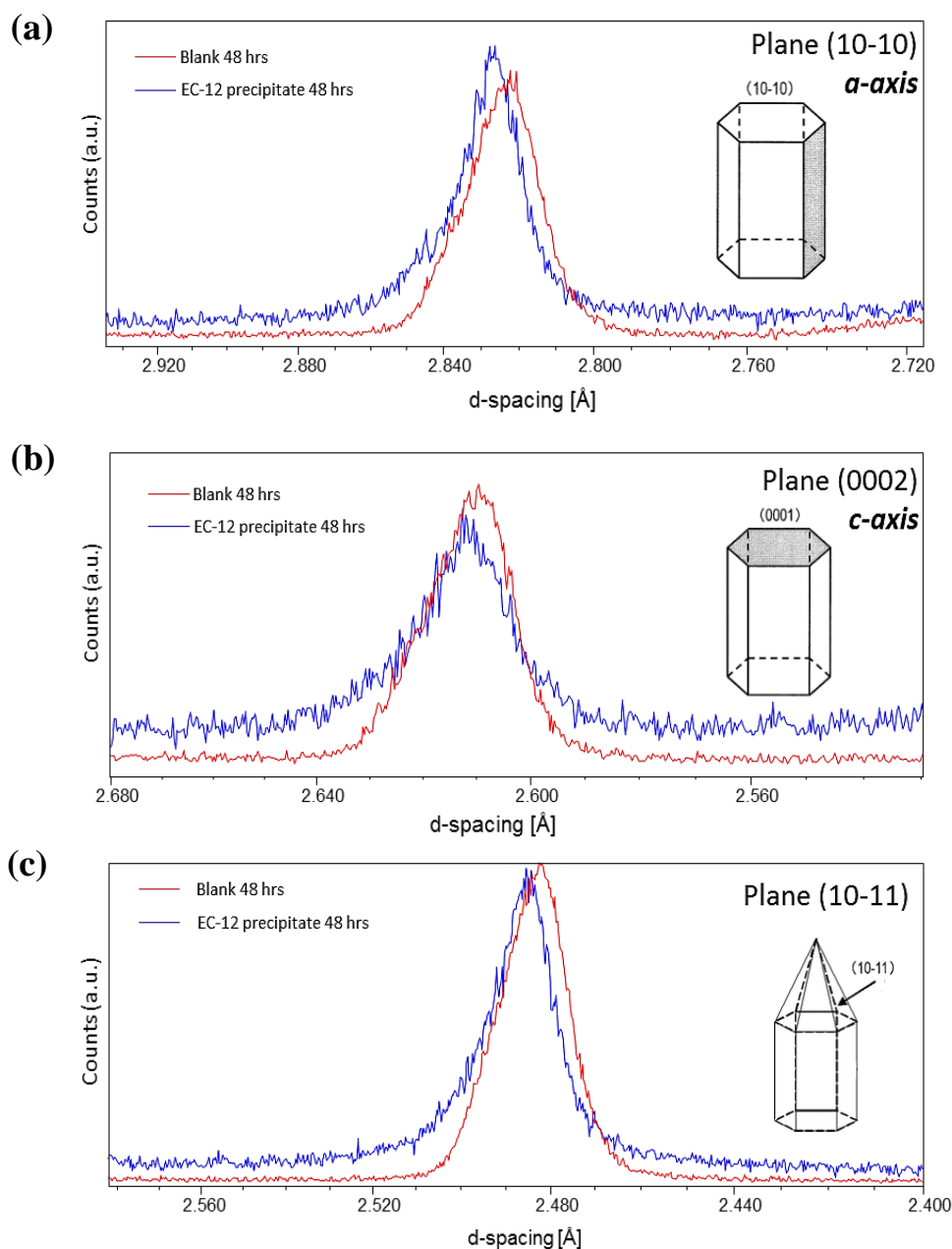


Figure 4.16 XRD diffraction peaks of ZnO crystals for the Blank and in the presence of 0.4 mM of EC-12 for (a) (10 $\bar{1}$ 0) plane, (b) (0002) plane and (c) (10 $\bar{1}$ 1) plane.

However, due to the dimensions of this peptide and the small lattice strain modification, it could not be discounted that ZnO morphology modification was due to EC-12 being adsorbed onto ZnO surface instead being intercalated. It has been reported that stronger bonds lead to a smaller interfacial free energy due to the enthalpic contribution to the free energy comes primarily from chemical bonding (Yoreo and Vekilov, 2003). Hence, as Zn^{2+} in the crystal can form bonds with those in the peptide that are stronger than the bonds of solvation; a decrease of the interfacial free energy may occur, allowing for the growth of spherical shape ZnO crystals. As mentioned by Yoreo and Vekilov “this may well be the key physical phenomenon that allows living organisms to delineate both location and orientations of crystallites” (Yoreo and Vekilov, 2003). In Section 4.7.4, the crystallite domain sizes for ZnO in the presence of different concentrations of EC-12 are shown.

The ITC technique was also used to study interactions between the mineral ZnO and the peptide EC-12. The isotherm graphs for the water-water method prior to each other method are shown in Appendix 4.9. The titration of the ZnO with ddH₂O showed negligible heat measurements (Figure 4.17a), whereas the titration of ddH₂O with EC-12 showed measurable heat changes (Figure 4.17b), which would indicate peptide-peptide interactions in water (Limo and Perry, 2015).

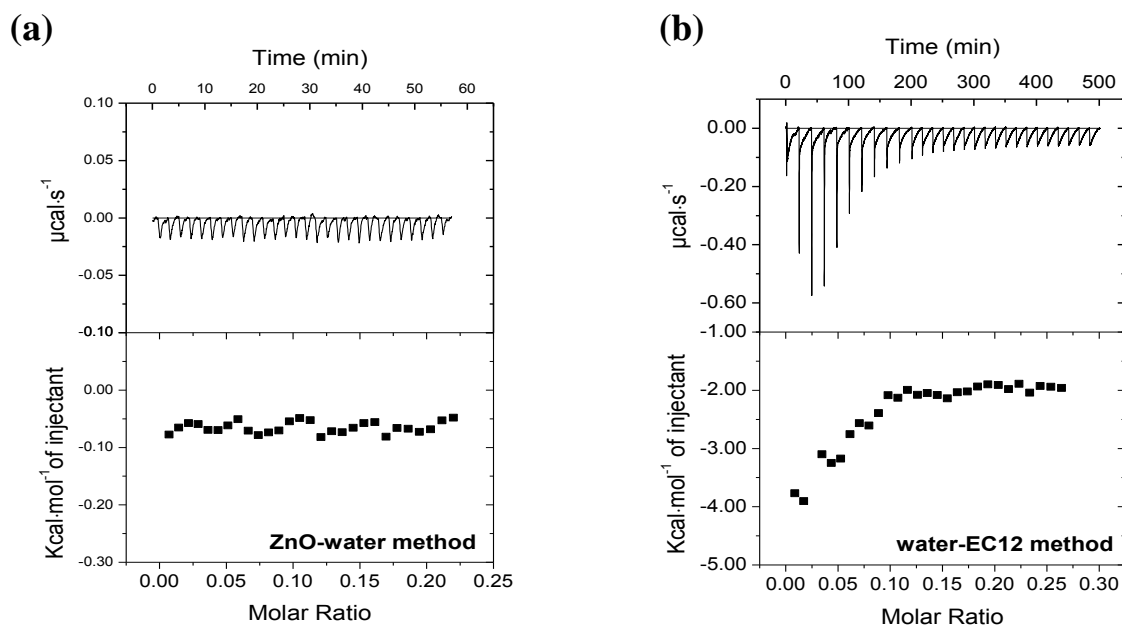


Figure 4.17 Isothermal profiles showing (a) titration of ddH₂O into ZnO (water-ZnO method), (b) titration of EC-12 into ddH₂O (EC12-water method).

Finally, the EC12-ZnO study was performed and heat changes measured in the EC-12-water experiment were subtracted from the heat changes measured during the titration of ZnO nanoparticles with EC-12. Binding isotherms are shown in Figure 4.18. In this case, data was fitted using the two sets of independent sites model as peptide-mineral interactions showed two different events of opposite heat change; an endothermic process at the early stage of the titration (few data points) followed by an exothermic process until the end of the analysis. Conformational changes in peptides (as they move closer to ZnO surface) can give rise to an endothermic interaction due to a variation of the entropy in the system (conformational entropy) affected by the structure and chemical composition of the peptide (Limo *et al.*, 2014). Also the observation of an endothermic process can be due to hydrophobic interactions (Chiad *et al.*, 2009) such as the rupture of hydrogen bonds by the interaction of water molecules with a polar hydroxylated ZnO surface (Limo *et al.*, 2014). On the other hand, exothermic interactions are associated with non-covalent interactions such as electrostatic interactions, Van der Waals interactions and/or hydrogen bonding (Ababou and Ladbury, 2007; Cliff *et al.*, 2004; Limo *et al.*, 2014).

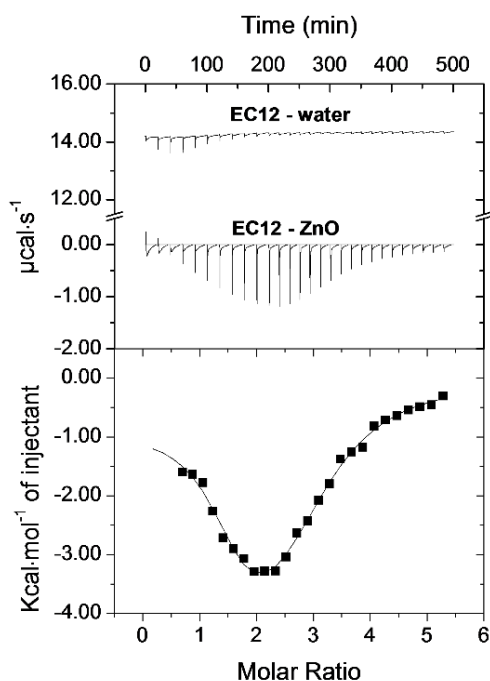


Figure 4.18 Binding isotherms for the titration of ZnO solution with EC-12 (experiment b) and the titration of the water with EC-12. Heat changes measured in the EC12-water experiment were subtracted.

From the data fitting, ITC MicroCal provided the parameters (ΔH , ΔS and K) to resolve the free energy of the system (ΔG) (Table 4.1). Data evaluation revealed that the interaction between EC-12 and ZnO particles was favoured since the reaction took place spontaneously ($\Delta G < 0$) and based on the high affinity values (K) observed. Generally, negative ΔH and positive ΔS indicates spontaneous reaction, whereas positive ΔH and positive ΔS indicates spontaneity depending on temperature.

Table 4.1 Thermodynamic parameters obtained by ITC analysis of ZnO nanoparticles titrated with the peptide EC-12. Endothermic and exothermic processes are labeled as (+ve) and (-ve), respectively.

Parameters	Dp	K ($L \cdot mol^{-1}$)	ΔH ($Kcal \cdot mol^{-1}$)	$T\Delta S$ ($Kcal \cdot mol^{-1}$)	ΔG ($Kcal \cdot mol^{-1}$)
EC12-ZnO	+ve	$1.22 \times 10^6 \pm 7.25 \times 10^5$	-0.89 ± 0.33	7.42	-8.30
	-ve	$7.24 \times 10^4 \pm 1.36 \times 10^4$	-5.77 ± 0.10	0.86	-6.63

From these results, it was concluded that this reaction was not temperature dependent to be favoured. In the endothermic process (+ve), positive values of ΔS could be due to peptide conformational changes and either incorporation or displacement of water molecules (Chiad *et al.*, 2009; Cliff *et al.*, 2004; Limo *et al.*, 2014). The exothermic process (-ve) was attributed to peptide-mineral interactions, although peptide-peptide interactions can also be present and are difficult to distinguish within the process (Limo *et al.*, 2014). The ΔH values generally reflect the strength of non-covalent interactions (electrostatic interactions, solvation and hydrophobic interactions, hydrogen bonding and Van der Waals interactions) and, in this case, the negative values suggested the presence of a large number of van der Waals interactions or hydrogen bonds (Chiad *et al.*, 2009). Van der Waals forces are driven by induced electrical interactions between very close atoms or molecules. Although, it is the weakest of all intermolecular attractions between molecules, this can be very strong when lots of Van der Waals forces are interacting between two molecules. Further, water tends to form ordered cages around non-polar molecules and this leads to a decrease in ΔS (Tanford, 1991). The adsorption affinity values observed in these results were close to those recently investigated for other peptides with high similarly sequence with EC-12

(Table 4.2). However, comparison with previous studies may not be ideal as ZnO crystals synthesized by other hydrothermal routes may affect parameters such as surface area and hydroxyl groups on the ZnO surface and, therefore, the mineral-peptide interactions. Ultimately, further experimental proof (reproducibility of the results) is also needed to validate the data above showed in Table 4.1.

Table 4.2 ITC studies of ZnO rods ($L/D = 8.92 \pm 3.26$) titrated with the peptides G-12 (Limo and Perry, 2015) and EM-12 (Limo, 2014).

Parameters	Dp	K ($L \cdot mol^{-1}$)	ΔH ($Kcal \cdot mol^{-1}$)	$T\Delta S$ ($Kcal \cdot mol^{-1}$)	ΔG ($Kcal \cdot mol^{-1}$)
G-12-rods	+ve	$1.40 \times 10^6 \pm 0.33 \times 10^6$	2.36 ± 0.68	10.73 ± 0.55	-8.37 ± 0.13
	-ve	$9.01 \times 10^4 \pm 0.32 \times 10^4$	-7.55 ± 1.09	-0.79 ± 1.06	-6.76 ± 0.02
EM-12-rods	+ve	$8.60 \times 10^5 \pm 4.98 \times 10^5$	0.27 ± 1.33	7.84	-8.37 ± 0.13
	-ve	$1.08 \times 10^5 \pm 1.50 \times 10^4$	-6.83 ± 0.68	0.03	-6.76 ± 0.02

4.7.4 Effects of EM-12 and EC-12 on ZnO Morphology

ZnO crystals generated in the presence of EM-12 were different from those obtained in the presence of EC-12 (Figure 4.19). Although the addition of EM-12 delayed/inhibited the formation of ZnO formation, rod-like structures were still observed, while for EC-12 studies, the ZnO crystals presented less well defined facets showing sphere-like structures.

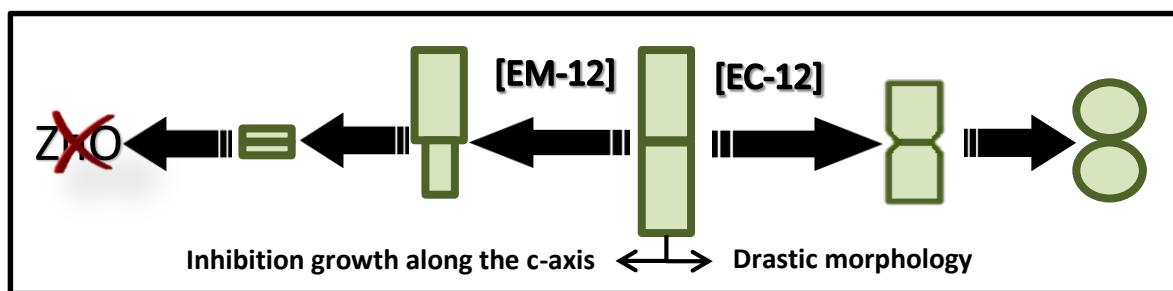


Figure 4.19 Illustration of ZnO morphology changes in the presence of EM-12 and EC-12 at different concentrations of peptide added. Non-scaled images.

In the presence of EM-12, ZnO crystals generally transformed from symmetrical twinned ZnO crystals (Blank) to asymmetric twinned crystals (in the majority) followed by un-

twinned crystals as EM-12 concentration was increased from 0.1 mM to 0.4 mM (Figure 4.20). These observations suggested that ZnO crystals were formed by two hexagonal rods (R_{1st} and R_{2nd}). The generation of shorter crystals (along the c-axis) was observed with EM-12 addition. It is believed that the reduction of the aspect ratio is due to specific polypeptides playing a role in the competitive adsorption-nucleation process by interacting with specific crystal planes (Muthukumar, 2009). For ZnO, theoretical and experimental studies (Liang, 2010; Muthukumar, 2009) suggested that polypeptides can interact with the (0002) plane corresponding to the c-axis with a reduction in the aspect ratio being observed. In this current work, the changes in twinning behaviour with increasing amount of EM-12 can be explained as follows. The complexation of Zn^{2+} and EM-12 reduced the amount of Zn^{2+} ions available for crystal growth (Sola-Rabada *et al.*, 2015). At lower EM-12 concentrations (0.1 - 0.2 mM), the growth of the second rod (R_{2nd}) was not complete resulting in the formation of asymmetrically twinned ZnO crystals. In the presence of 0.4 mM EM-12, crystal growth equilibrated before/at the end of growth of the first rod (R_{1st}), thus, untwinned ZnO crystals were obtained, which was supported by the observation of untwinned crystals being shorter but having comparable diameters with those (larger side of asymmetrical twinned crystals) formed at lower EM-12 concentrations (Figure 4.20). The ZnO crystallisation mechanism process seems to be by the formation of a first hexagonal rod (R_{1st}) followed by the growth of a second rod (R_{2nd}) on the first one (Zhang *et al.*, 2007; Zhang *et al.*, 2008) in which the addition of R_{2nd} could be considered as a secondary nucleation process (Muthukumar, 2009) being, in this case, inhibited by the presence of EM-12.

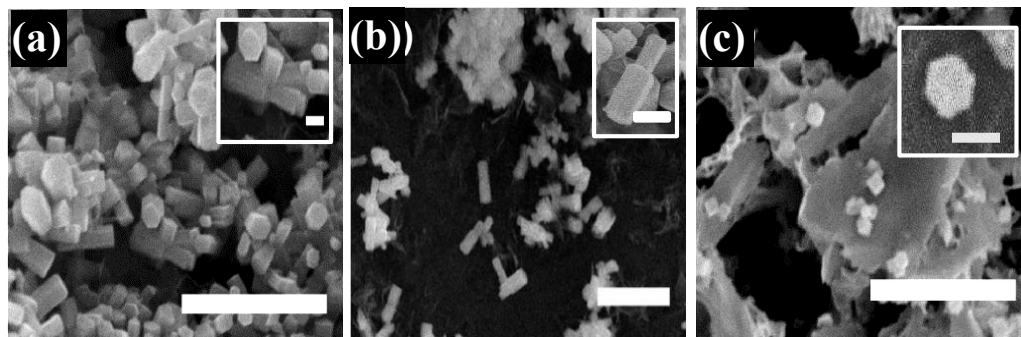


Figure 4.20 SEM images of precipitates collected at 48 hours for (a) 0.1 mM, (b) 0.2 mM and (c) 0.4 mM of EM-12. All scale bars are 5 μ m and inset scale bars at 0.5 μ m.

The aspect ratio (L/D) was studied for all precipitates containing ZnO crystals and showed the reduction of L/D with the addition of peptide (Figure 4.21). The presence of EM-12 not only caused the delayed formation of ZnO (conversion from LBZA to ZnO) but also caused the inhibition of crystal growth as seen in Figure 4.21 inset, where the Blank increased its aspect ratio with time and for samples containing EM-12 the aspect ratio was maintained over time. In the presence of EC-12, the aspect ratio could not be compared as hexagonal rods were no longer formed in the system and the spherical shape did not present a uniform diameter of the crystals along their c-axis ($\sim 1.5 \mu\text{m}$ for EC-12 and $\sim 0.5 \text{ nm}$ for EM-12). Even so, the aspect ratio for the ZnO crystals was calculated ($n > 15$), taking as the diameter the middle of the sphere where the two spheres are attached together. The values (at ≥ 24 hours) for 0.2 mM and 0.4 mM of EC-12 were $L/D = 1.7 \pm 0.2$ and $L/D = 1.8 \pm 0.3$, respectively, being much lower compared with the L/D value of ~ 6 (at ≥ 24 hours) for the Blanks. Further, the increase of peptide did not significantly modify the aspect ratio of the crystals suggesting no inhibition of crystal growth was achieved with increasing the concentration of EC-12.

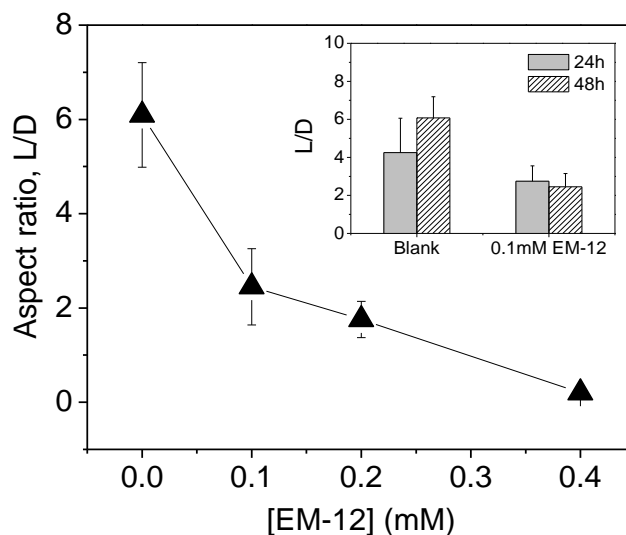


Figure 4.21 Average aspect ratio (L/D) of ZnO crystal rods ($n \geq 30$) as a function of [EM-12]. Inset shows aspect ratio as a function of time for the Blank and 0.1 mM of EM-12.

Although, it has been proposed that twinned hexagonal rods are formed by the aggregation of two approximately spherical particles (Verges *et al.*, 1990), the observation of twinned

crystals with a second rod or sphere slightly smaller than the first one, either in the presence of EM-12 and EC-12 (Appendix 4.10), suggested that ZnO crystals were generated by a 1st nucleation in which the formation of the R_{1st} or S_{1st} took place, followed by a 2nd nucleation which started the growth of the R_{2nd}/S_{2nd} on the first one.

The ZnO morphology transformation in the presence of EC-12 is believed to be due to interaction with the solid-phase. On the other hand, the weaker but still delayed-formation of ZnO due to the presence of EC-12 was remarkably caused when lower concentration of EC-12 was used. The fact EC-12 is able to interact with species in solution (Sola-Rabada *et al.*, 2015) but also with species in the solid-phase is the key to this behavior. Biomolecules involved during biomineralisation can modify the growth stage of minerals and also control the nucleation process (Yoreo and Vekilov, 2003). As explained in Chapter 3, the nucleation process occurs when a critical size (interfacial energy) for the nuclei to be formed is reached; followed by the subsequent growth of these nuclei (crystal growth). Both processes occur simultaneously while supersaturation exists. Note that, the smaller the interfacial energy, the smaller the critical size and the more likely nucleation becomes for any given supersaturation (Yoreo and Vekilov, 2003). Hence, the effect of EC-12 on ZnO formation can be explained as follows. EC-12 can interact covalently with the solid-phase, which may affect the nucleation process, as evidenced by the formation of crystals with drastically modified shape (compared with the Blank) and the reduction of the aspect ratio (from ~6 to ~2). Hence, supersaturation may be achieved more easily in the system as a lower interfacial energy is required for a smaller critical size. The crystalline domain size was calculated from the (0001) plane as is the thermodynamically favored axis for crystal growth using Scherrer equation (as described in Section 2.4). Table 4.3 shows the crystallite domain sizes calculated (Scherrer equation) for all precipitates studied, showing a smaller crystallite size for the precipitates where higher concentrations of EC-12 were added. Though, lower concentrations of peptide may have a weaker effect on the nucleation process (less peptide interacting with the solid phase) and crystal growth is predominantly dependent on the amount of Zn²⁺ available in the system, causing a delayed-formation of ZnO when a lack of Zn²⁺ ions exists for the growth of similar crystallites; whereas for higher concentrations of peptide employed, the nucleation process is strongly affected, being (in this case) the conditions of the system favorable to reach saturation and,

therefore, ZnO crystal growth can carry on without suppression. This would also explain why, in the case of EM-12 there is a delayed-formation of ZnO but not a change in the ZnO structures growing (rods).

Table 4.3 ZnO crystallite domain sizes calculated using the Scherrer equation, $k = 0.9$, $\lambda = 1.5406 \text{ \AA}$ and $B = \text{FWHM}$.

<i>ZnAc₂-NH₃ system</i>	Blank	0.2 mM	0.4 mM
(0001) plane	33.08 ± 1.67	33.49 ± 1.34	30.95 ± 0.85

4.8 Conclusions

The effect of the peptides EM-12 and EC-12 during ZnO formation via the $\text{ZnAc}_2\text{-NH}_3$ reaction, showed that the presence of the peptide EM-12 causes a delay and/or suppression of ZnO formation when increasing the peptide concentration, with LBZA being the major compound present at the highest concentration of EM-12 added. Further, addition of EM-12 not only caused the delayed formation of ZnO (conversion from LBZA to ZnO) but also caused the inhibition of crystal growth (wurtzite structured hexagonal rods) along the c-axis (or (0002) plane). The presence of EC-12; however, caused a more drastic change in the mineral morphology with sphere-like ZnO crystals being formed, and remarkably, no ZnO suppression was observed for the highest EC-12 concentrations added. The data presented appears to show that the mechanism of ZnO crystallisation occurs by the formation of a first hexagonal rod (R_{1st}) followed by the growth of a second rod (R_{2nd}) on the first one, considering the addition of R_{2nd} as a secondary nucleation process. With increasing EM-12 concentration, the growth of R_{2nd} was firstly inhibited followed by R_{1st} and final suppression of crystals at the highest concentration of peptide was observed. For EC-12 studies, ZnO crystals presented less well defined facets to the point that instead of being formed by two hexagonal rods (R_{1st} and R_{2nd}), crystals were formed by two spheres (S_{1st} and S_{2nd}).

From mineral-peptide interaction studies, it was observed that EM-12 interacts with Zn^{2+} species in solution, whereas EC-12 interacts with Zn^{2+} species in solution and in the solid

phase(s). The interaction of peptide with the solid-phase cannot be observed when using EM-12 although weak interactions cannot be discounted. From experimental data, the EC-12 interaction mechanism is proposed to include Zn^{2+} -sulphur (from cysteine) interactions. The exact solid phase(s) which EC-12 interacted with could not be uniquely identified due to the presence of other solid phases (LBZs) in the samples. The interlayer spacing of LBZA formed in the presence of EC-12 did not change significantly compared with the Blanks which implied that either EC-12 was not intercalated or it was oriented parallel to the zinc hydroxide layer while intercalated. Finally, ZnO lattice strain modification was observed when EC-12 was added into the system and it is suggested that this peptide may be incorporated into the lattice of ZnO. However, due to the dimensions of the peptide EC-12 and the small changes in the lattice strain, it was also suggested that the ZnO morphology modification was due to adsorption of EC-12 onto ZnO surface. As Zn^{2+} in the crystal can form bonds with those in the peptide that are stronger than the bonds of solvation; a decrease of the interfacial free energy could occur, allowing for the growth of spherical shape ZnO crystals. A smaller interfacial energy was demonstrated by the smaller crystallite domain sizes obtained for ZnO when increasing concentration of EC-12 into the system.

Chapter V

SiO₂-binding peptides studies

5.1 Introduction

Synthetic NPs have received much attention in recent years for a variety of technological and biomedical applications. The unique properties of NPs to some extent lie in their reduced size that confers on them high specific surface area. Therefore, NPs present a greater fraction of surface atoms and increased surface energy affecting both their chemical and physical properties (Rao *et al.*, 2006). The use of NPs in drug delivery systems is attractive due to their relatively large surface and permeability through many biological pathways resulting in high interaction with biological systems (De Jong and Borm, 2008). Thus, organic/inorganic nanocomposite materials have been employed as they combine the advantages of the inorganic material (i.e. rigidity, thermal stability) and the organic polymer (i.e. flexibility, dielectric, ductility, and processability) (Zou *et al.*, 2008). As mentioned in Chapter 1 Section 1.4.1, amorphous silica nanoparticles (SiNPs) have been extensively used due to their low-toxicity, easy surface modification and remarkable colloidal stability in physiological fluids (Natte, 2013). Immobilization of organic polymers (i.e. proteins, DNA, and enzymes) or dyes onto functionalized surface SiNPs have also been investigated since this enhances and/or controls interactions between the NPs and the molecule of interest (Natte, 2013; Roach *et al.*, 2005; Zou *et al.*, 2008). Besides this, the effects of functional groups on the surface properties of the SiNPs, and further, the mechanisms concerning nanoparticle-biomolecule interactions are not fully understood. Therefore, a specific emphasis and novel aspect of the present study is to investigate the effect of surface functionalization on binding. Essentially, amino- and methyl-functionalized silica particles since this allow the study of the effect of (positive) electrostatic interactions and hydrophobic interactions, respectively. This enhanced cell compatibility and opening the possibility to bind molecules that could be used for drug delivery (i.e. peptides, ligand) (Kumar *et al.*, 2015).

For the fabrication of surface modified silica particles two methods have been generally applied: (i) post modification (or grafting) and (ii) *in situ* modification (or co-condensation), with the latter route mainly used for aminopropylethoxysilanes since their bifunctional nature quickly induces hydrolysis and condensation of TEOS in solution due to the presence of aminopropyl and alkoxy silane groups. The presence of positively charged amine groups ($-\text{NH}_3^+$) at the aminopropyl site can attract more negatively charged species ($\equiv\text{Si}-\text{O}^-$) catalysing the sol-gel process and the alkoxy silane site is capable of co-condensing with TEOS due to the presence of the ethoxy moiety (Wang *et al.*, 2012). However, silica precipitation cannot uniquely be promoted by only using aminopropylethoxysilanes since their hydrolysis may lead to the formation of six- or five-membered chelate rings through intramolecular hydrogen bonds that hinder condensation (Hüsing *et al.*, 1999). Commonly used aminopropylethoxysilanes are 3-aminopropyl dimethylethoxysilane (APDMES) and 3-Aminopropyltriethoxysilane (APTES), the latter being preferred due to its lower cost. Besides this, the presence of aminopropylalkoxysilanes in the system may give rise to other type of reactions/interactions that should be taken into account when looking at the effectiveness of surface functionalization. The higher reactivity of aminoalkoxysilanes towards water (compared with alkylalkoxysilanes) can induce uncontrolled polymerization/oligomerization in solution, such that molecule are no longer available to attach onto the silica surface (Asenath Smith and Chen, 2008). Further, the aminoalkoxysilanes sitting on the silica surface may follow different interaction mechanisms (Figure 5.1). Typically, covalent interactions through ethoxy moieties are achieved (i); however, the same molecule may bind via hydrogen bonding between the silanol groups on the silica surface and the amine group (ii), occupying more particle surface and, thus, decreasing the silanol sites available for functionalization. No covalent attachment of aminoalkoxysilanes on the silica surface but hydrogen bonding with the surface silanol groups (iii-v) results in weak interactions that can be easily broken by the washing procedures applied after synthesis (Asenath Smith and Chen, 2008). Therefore, careful characterization of levels of surface functionalization is needed in order to study biomolecule-surface interactions.

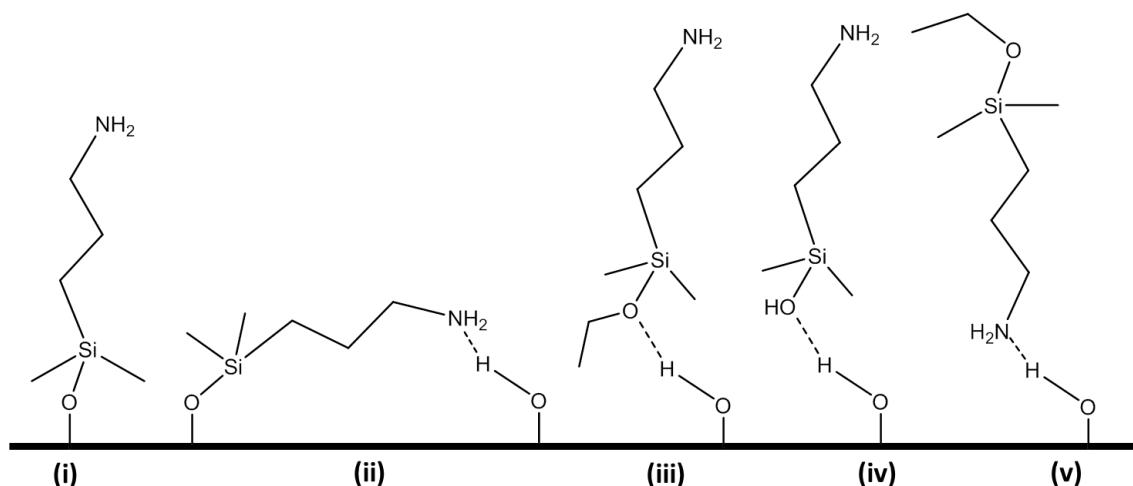


Figure 5.1 Types of interactions between aminoalkoxysilanes molecules and silicon oxide substrate. Adapted from Asenath Smith and Chen (2008).

Since nanodelivery systems are designed to have drugs absorbed onto the particle surface, the level of functionalization of the SiNPs is to be investigated as it may affect the amount of biomolecules absorbed and/or mechanisms of interaction. Further, a comparison study with micro scaled silica particles was also taken into consideration since recent studies in our group have shown that either the particle size or surface modified silica influence the mineral-peptide binding response (Puddu and Perry, 2014). And remarkably, it was observed that there was a higher interaction when increasing particle size independent of the properties of the peptides (Puddu and Perry, 2014). Henceforth, the specific aims of this chapter are to investigate the effect of (i) surface functionalization, (ii) level of functionalization and (iii) particle size on binding.

5.2 Materials

For the silica synthesis and functionalization, tetraethyl orthosilicate (TEOS, 98%, reagent grade), aminopropyltriethoxysilane (APTES, 99%) and tetramethyl orthosilicate (MTEOS, 98%) were purchased from Sigma-Aldrich; ammonia solution (NH₃, 35%) and acetic acid (CH₃COOH, > 99%) from Fisher Scientific and ethanol (EtOH, anhydrous, ≥ 99.5%) from Hayman Ltd. For the back titration of the ammonia stock solution prepared 1 M HCl and 1 M KOH volumetric standard from Sigma-Aldrich were used. For the peptide synthesis and

characterization, piperazine (C₄H₁₀N₂), DIPEA (C₈H₁₉N), TFA (C₂HF₃O₂), thioanisole (C₇H₈S), DODT (C₆H₁₄O₂S₂) were purchased from Sigma-Aldrich; DMF, DCM, NMP, and diethyl ether were purchased from Fisher Scientific; HBTU and all Fmoc-protected amino acids required for peptide synthesis and the proline-preloaded-TGT resins were obtained from Novabiochem[®]. Sample preparation for HPLC and Mass Spectrometry employed ACN and TFA, both purchased from Sigma-Aldrich. For binding studies, solutions were prepared with phosphate buffered saline (PBS) tablets from Fisher Scientific in ddH₂O with conductivity less than 1 μS·cm⁻¹.

5.3 Solid Phase Peptide Synthesis

The peptides KLPGWSG (K7), AFILPTG (A7) and LDHSLHS (L7) were prepared using a microwave-assisted solid phase peptide synthesizer (CEM Corporation) via Fmoc chemistry as previously described in Chapter 2 Section 2.9. The purity of K7, A7 and L7 determined with a Dionex HPLC with a UV detector (set at 214 nm) and a Jupiter 4u Proteo 90A C12 Reverse Phase column (Phenomenex) (see Chapter 2 Section 2.10 for analysis details) was 80%, 88% and 98%, respectively (Appendix 5.1). The m/z of the peptides was measured by Dr Graham Hickmann (The John Van Geest Cancer Research Centre, NTU) using a Bruker UltraflexIII TOF/TOF mass spectrometer and analysed with BrukerDaltonicflexAnalysis software. The Mw of K7, A7 and L7, 743.4 g/mol, 717.8 g/mol and 807.4 g/mol, respectively; was confirmed with their measured m/z of 744.4 m/z, 718.4 m/z and 808.1 m/z, respectively (Appendix 5.2).

5.4 Preparation of Silica Samples

5.4.1 Silica Synthesis Methods

SiO₂ condensation *in vitro* was performed through two different synthesis routes to achieve of the desired particle size (Figure 5.2). The growth of silica particles at the nanoscale (from 28 to 210 nm) was carried out using a modified Stöber synthesis method (Stöber *et al.*, 1968); whereas for the growth of bigger particles (> 2 μm), the synthesis route

proposed by Karmakar *et al.*; hereafter called Karmakar method (Karmakar *et al.*, 2000) was followed.

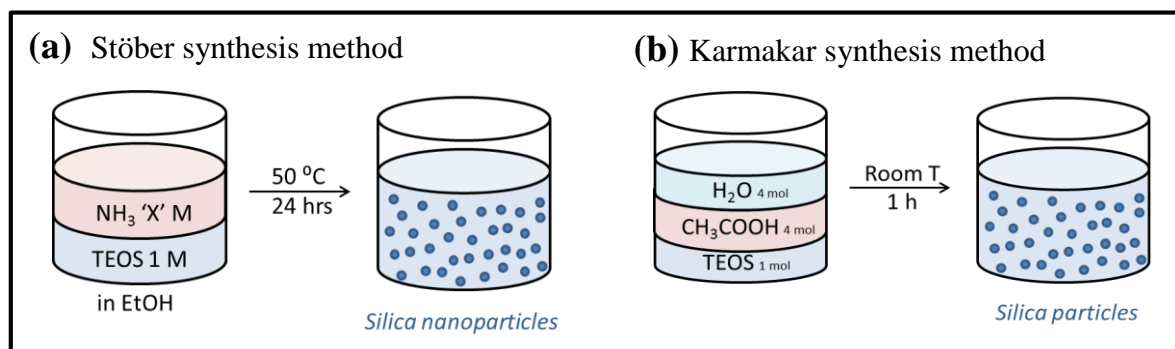


Figure 5.2 Scheme of the growth of silica particles following two different synthesis routes: (a) modified Stöber synthesis method and (b) Karmakar synthesis method.

Following the modified Stöber synthesis method, TEOS and ammonia were chosen as the silica precursor and base, respectively. Both solutions (TEOS and ammonia) were separately prepared. Firstly, 22.3 ml of TEOS solution (98%, reagent grade) was diluted with 76.6 ml of ethanol. Secondly, 21.3 ml of NH_3 stock solution was diluted with 80 ml of ethanol. Following the modified Stöber method, particle size can be manipulated by controlling the ammonia concentration added into the reaction system (Stöber *et al.*, 1968). Presence of ammonium ions in the reaction medium has a twofold role; first, it alters the pH of the medium which promotes hydrolysis and; second, it reduces the amount of the energy required to start the nucleation, thereby, enhancing silica condensation rate (Stöber *et al.*, 1968; Wu *et al.*, 2013). In this study, concentrations of ammonia in a range 0.25 - 10 M were used to achieve the desired particle sizes, from 28 to 210 nm (Figure 5.3). For accurate preparation of the NH_3 stock solutions in a range 0.25 - 10 M, the concentration was determined prior to each experiment by back titrating a mixture of 2 ml NH_3 and 10 ml HCl (1M) with 1 M KOH volumetric standard. Freshly made samples (TEOS and ammonia) were heated in a water bath at $50\text{ }^\circ\text{C}$ for 1 hour prior to the addition of the TEOS solution into the ammonia solution. The mixtures were vigorously stirred and placed again to the water bath at $50\text{ }^\circ\text{C}$ for up to 24 hours. Collected samples were centrifuged at 10000 rpm for 10 minutes to separate any precipitate from the supernatant. Supernatant was carefully separated by the aid of a Pasteur pipette and only ~80% of the supernatant was

drawn from the vial although no precipitates were visibly observed at the bottom of the vial (this was the case of particle size < 100 nm). The precipitates were re-dissolved in ethanol and re-centrifuged using the same conditions as previously mentioned and, finally, washed three times with ddH₂O. For each washing, the samples were centrifuged at 5000 rpm during 5 minutes. Cleaned precipitates were lyophilized at -70°C using a Virtis-110 freeze-dryer. This method allows for the growth of silica particles at the nanoscale, hereafter named Stöber particles.

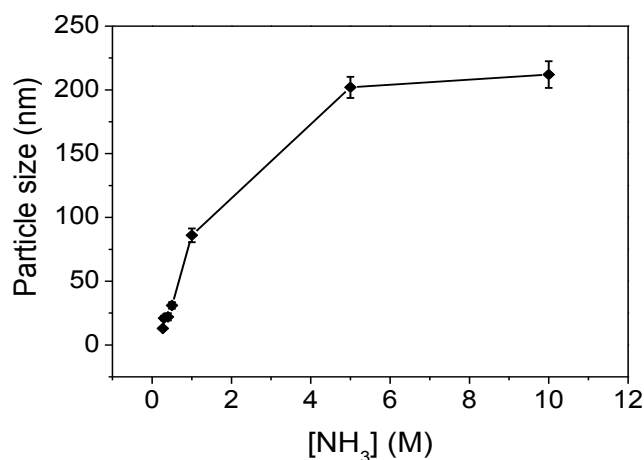


Figure 5.3 Particle size (diameter) of SiO₂ NPs as a function of ammonia concentration.

In the attempt of growing bigger silica particles (> 2 μm) for comparison of the later silica-binding studies, this silica synthesis route (Stöber method) was limited by the reaction conditions, since high pH values achieved by increasing the ammonia fraction can give rise to silica dissolution. Hence, it was followed a simpler (T = 25 °C) and time saving synthesis route: the Karmakar method. TEOS (98%, reagent grade), acetic acid (>99%) and ddH₂O were mixed together at a molar ratio of 1:4:4 and allowed to hydrolyse and condense over the course of 1 hour with the aid of a paddle mixer at moderately high speed. After 1 hour, the silica particles were quickly collected and centrifuged at 3000 rpm during 1 min. Precipitated silica was washed successively with ethanol, water and, finally, acetone. Same volume of solvents was used for each washing step. Cleaned precipitates were dried in the oven at 80°C overnight. This method allows for the growth of silica particles at the microscale, hereafter named Karmakar particles.

5.4.2 Silica Functionalization

The functionalization of the silica particles with methyl (-CH₃) and aminopropyl -(CH₂)₃-NH₂), hereafter named CH₃-SiO₂ and NH₂-(CH₂)₃-SiO₂, was performed using MTEOS and APTES solutions, respectively. Different levels of functionalization were achieved by increasing the concentrations of APTES and MTEOS until saturation was reached (Appendix 5.3). The functionalization of silica particles was initially carried out according to the methodology followed by Wu and colleagues (Wu *et al.*, 2006) in which 4.79 x 10⁻⁴ mol of either APTES or MTEOS were added and vigorously stirred into a Stöber solution after 3.5 hours of reaction allowing the reaction to continue for additional 19 hours at room temperature. However, during the course of reaction, it was observed a gelation effect for those samples containing APTES, being more pronounced for samples containing a higher fraction of APTES (see section 5.6.2). As different levels of functionalization (different concentration of APTES) were one of the purposes of this investigation, the methodology followed for functionalization was then adapted to this study. Henceforth, silica synthesis remained using either the modified Stöber method (50 °C, 24 hours) or Karmakar method (25 °C, 1 hour) and functionalization was performed on the collected silica (after synthesis) during the course of 24 hours at room temperature as shown in Figure 5.4. Collected samples were centrifuged and washed following the same procedure as in Section 5.4.1. The advantage of using this method (post-grafting) was that the silica particles were characterized previously to the functionalization, thus, being of the desired size and properties. For clarification, binding studies were performed only using the post-grafted silica particles.

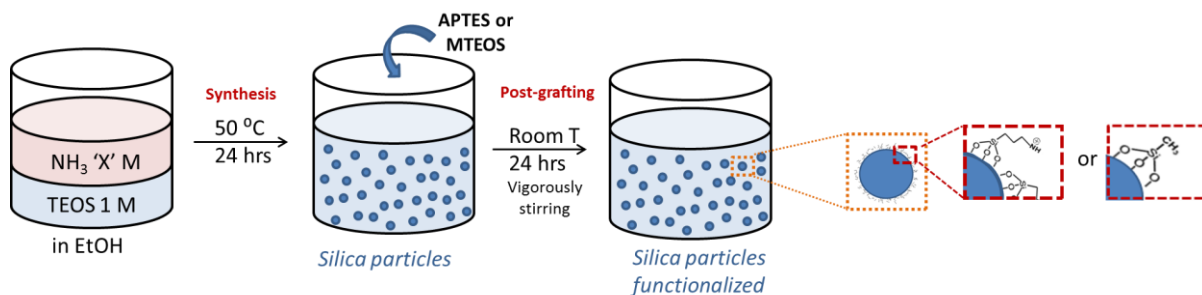


Figure 5.4 Scheme of the silica synthesis following modified Stöber method and post surface functionalization treatment following a modified Wu *et al.* (2006) method.

Note that, the functionalization of silica particles was directly performed on the Stöber solution (80% EtOH solution, with still some non-reacted ammonia), whereas for silica synthesized by the Karmakar method, the dried silica particles were re-dispersed into an 80% EtOH solution and then functionalized. A comparison study was performed in order to see how the different silica solutions affect the levels of functionalization (Appendix 5.4). Although level of functionalization was slightly less when the dried silica particles were re-dispersed into an 80% EtOH solution; the functionalization trends (for MTEOS and APTES) observed were similar between both methods.

5.4.3 Preparation of samples for the binding studies (Fluorescamine assay)

Silica particles were suspended ($1 \text{ mg}\cdot\text{ml}^{-1}$) in phosphate-buffered saline (pH = 7.4) and sonicated for 1 hour, followed by the addition of peptide solution of desired concentration and incubated for another hour. Langmuir adsorption isotherms have been reported when a protein approaches a solid interface (Rabe *et al.*, 2011; Roach *et al.*, 2005); however, previous studies in our group have shown that the adsorption isotherms of the peptides of this study follow the Freundlich model, where saturation is achieved at values higher than 1.0 mM (Puddu and Perry, 2012). Hence, the peptide concentrations range chosen for this study was from 0.1 - 1.0 mM. HPLC and Mass Spec results were considered for the calculations of the preparation of peptide solutions at different concentrations. Finally, samples were centrifuged at 13000 rpm for 5 minutes at 20 °C, as shown in Figure 5.5. For the assay, 180 μl of the supernatant was dispensed into a black 96-well plate. To this aliquot, 20 μl of fluorescamine solution ($5 \text{ mg}\cdot\text{ml}^{-1}$ in acetone) was added and mixed (shaking of 60 seconds) immediately prior to the measurement of the fluorescence intensity.

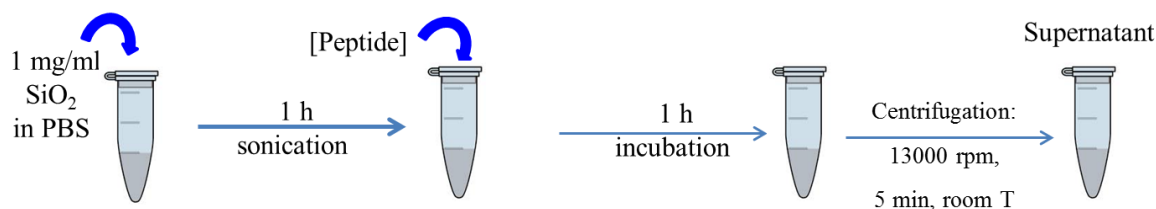


Figure 5.5 Scheme of methodology followed for the silica-peptide binding studies.

5.5 Characterization

The morphology and size of selected precipitates were studied using SEM (JEOL JSM-840A, 20 kV) and TEM (JEOL 2010, 200 kV). For SEM analysis, samples were attached using double-sided carbon adhesive tape to SEM stubs and carbon coated (Edwards, sputter coater S150B). For TEM analysis, samples were dissolved in ethanol prior to addition onto the copper grids and analyzed after solvent evaporation was ensured. Silica particles size (diameter) was determined by average of more than 50 particles from a SEM and TEM image using Java-based image processing program (*ImageJ* software). DLS (Zetasizer Nano S) was also employed for particle size analysis (silica particles in 5% EtOH solution) and for zeta potential determination of silica samples (silica particles in PBS solution, pH = 7.4). All samples were sonicated prior to DLS analysis. ATR (Perkin Elmer Spectrum 100 Series Spectrometer with Diamond/KRS-5 crystal) was used to detect the functional groups present in the lyophilized precipitates. Spectra were averaged from 32 scans at 4 cm⁻¹ resolution with air as background. The organic content in the samples was determined by thermogravimetric analysis, TGA (Mettler Toledo TGA/SDTA 851^e) where samples were heated at 10 °C·min⁻¹ from 30 °C to 900 °C in air to ensure complete combustion of all organic material. The sample surface area and the N₂ adsorption-desorption isotherms were obtained on approximately 100 mg of sample powder by Gas adsorption analysis (Quantochrome Nova 3200e). Samples were degassed at 100 °C overnight prior to each analysis. The surface area was determined by the Brunauer–Emmett–Teller (BET) method (Brunauer *et al.*, 1938) using a five-point adsorption isotherm in the relative pressure range of $P/P_0 = 0.05/0.3$ at 77.35 K. Sample porosity (pore size distribution) was obtained by the Barrett-Joyner-Halenda (BJH) method (Barrett *et al.*, 1951) from the desorption branch of the isotherm. The chemical constitution of the precipitates was investigated by XPS using a VG Scientific ESCALab MkII X-ray photoelectron spectrometer with an Al K α X-ray source ($h\nu = 1486.6$ eV). Samples were ground and then mounted on standard sample holders. Before analysis, the calibration and linearity of the binding energy scale was checked with a pure silver sample using the peak positions of the Ag3d_{5/2} photoelectron line (at 368.26 eV) and the AgM₄NN Auger line (at 1128.78 eV). Survey spectra of precipitates were collected covering the full BE range from 0 - 1200 eV using a step size of

1 eV, a dwell time of 0.2 seconds and PE of 50 eV. High resolution core level spectra of the Si 2p, C 1s, O 1s and N 1s peaks were collected using a PE of 20 eV, a step size of 0.2 and a dwell time of 0.4 seconds, which were subsequently deconvoluted and fitted using standard mixed Gaussian-Lorentzian components using CasaXPS software. To compensate for surface charging effects in the insulating samples, all binding energies were corrected with reference to the saturated hydrocarbon C 1s peak at 285.0 eV using the CasaXPS software. In order to minimize the amount of ubiquitous carbonaceous contamination which proportionally increases with time, samples were in this case individually loaded in the chamber. Finally, the silica-peptide binding measurements were performed using fluorescence spectroscopy (TECAN i-control M200) on Corning[®] black polystyrene 96-well plates. The excitation wavelength was set at 360 nm and the emission (sample reading) was at 465 nm. The gain of the photomultiplier was adjusted to 60 a.u. for the best signal-noise.

5.6 Results and Discussion

5.6.1 Silica Particles Synthesis and Properties

The morphology of the silica particles was characterized by TEM and/or SEM as seen in Figure 5.6. Microscope images showed that smaller particles were more aggregated and less spherical compared with larger particles which also seem to have a much smoother surface. Specially, Karmakar particles have been shown to be highly dense, between 2.10-2.16 g·cm⁻³ (Karmakar *et al.*, 2000) being also named glass-like silica spheres (De *et al.*, 2000). The particle size (diameter) measured ($n \geq 30$) was 27 ± 3 nm, 212 ± 22 nm and 37 ± 8 μ m. Note that, for the Karmakar samples, particles with a size < 10 μ m was not taken into account for average size as population was lower than 10% of the total sample composition. The size of the silica spheres was also determined using DLS for the Stöber SiO₂ particles, these values being 28 ± 1 nm and 229 ± 5 nm, respectively. Slightly exaggerated diameters are commonly measured by DLS (compared with TEM/SEM) due to the surrounding water molecules and/or the swelling effect on the particles surface (Jung *et al.*, 2012). DLS of Karmakar particles was not satisfactorily achieved as sedimentation of the particles occurred immediately; hence, sample readings were not representative of

the particle size. Additionally, the scattering envelope of such large particles is not symmetrical and this also has an effect on the size of particles measured. Silica particles with different sizes will be named hereafter SiO₂-28 nm, SiO₂-210 nm and SiO₂-40 μ m.

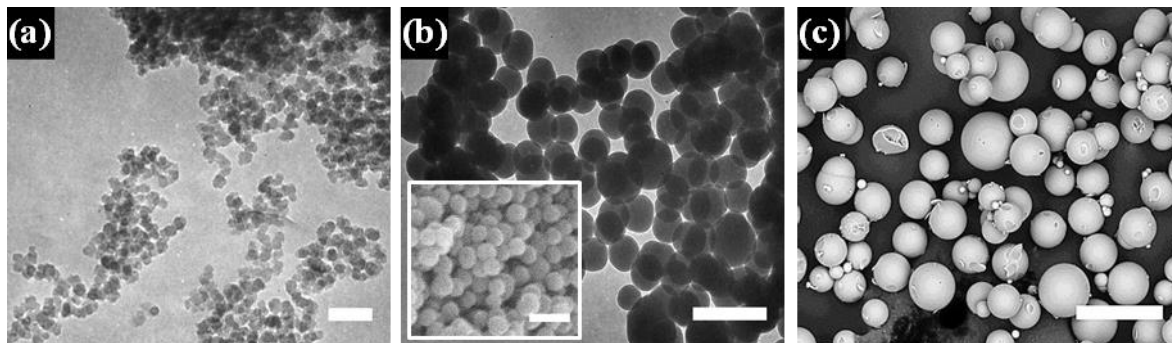


Figure 5.6 Electron microscopy images of (a) SiO₂-28 nm, (b) SiO₂-210 nm and (c) SiO₂-40 μ m. Scale bars are 0.1 μ m (a), 0.5 μ m (b) and 100 μ m (c).

The charge of the silica particles synthesized was determined by zeta potential measurements at the working pH for the binding studies (PBS solution, pH \sim 7.4). For Stöber particles, the bigger the particle size, the more negative zeta potential value was achieved (Table 5.1). During the Stöber synthesis, larger concentrations of ammonia used in the formation of larger size particles ionized more silanol groups; hence, an increase of the surface ionization with particle size is believed to be by the presence of a higher population of isolated silanol groups (Si-OH) compared to the smaller particles, leading to a higher surface acidity for bigger particles (Patwardhan *et al.*, 2012). For the Karmakar particles, even if particles were the largest, the zeta potential values were less negative than for the SiO₂-210 nm sample. In this case, ammonia was no longer present during synthesis (acetic acid instead), thus a higher ionization of silanol groups was not expected, and if it occurred due to the synthesis conditions, the reduced surface area of the big particles may decrease the number of silanol groups that can be accommodated on the silica surface. It should also be mentioned that large particles (>1 μ m) are less likely to be uniformly suspended in solution (or they may sediment); thus, the zeta values obtained may not be representative of the overall silica particle size in the sample. Further, Karmakar samples showed to be non-monodispersed (particles with size <10 μ m were also present), hence, zeta values could be only a contribution of the small particles in the sample. In any case,

the binding studies were carried out in the same conditions; therefore, zeta values are representative of the charge of the particles interacting with the peptides. Theoretical surface area was investigated in order to predict the expected surface area for a sphere with smooth or non-porous surface (Appendix 5.5) and values were compared for those determined by using BET method (Table 5.1). For SiO₂-28 nm, determined surface area values deviate more from the theoretical value compared with the SiO₂-210 nm due to the irregular sphere shape commonly observed for very small silica particles (< 100 nm). The additional surface area found for the SiO₂-210 nm particles is most likely also a result of surface irregularities or low level presence of pores. Inspection of the BJH treated data (Appendix 5.6), showed the major pore domains in terms of cumulative pore volume correlate with the particle size, that is, these pores are mostly inter-particle voids caused by the aggregation of particles. The diameter of the silica pores are also of interest as previous studies have shown that protein adsorption on silica is pore-size dependent (Katiyar *et al.*, 2005; Schlipf *et al.*, 2013). In this study, the pore size (diameter) values for Stöber particles were bigger as particle size increased and, conversely, pore volume decreased. In the case of the SiO₂-28 nm particles, these were found to be mesoporous (~10 nm) whereas the SiO₂-210 nm particles showed the majority of their pore volume between 20-200 nm (Appendix 5.6, BJH graph), typical of inter-particle voids. Since a very smooth surface was observed for the Karmakar particles, low pore volume and diameter values were expected (Table 5.1). In this case, particles were found to be non-porous with only significant levels of nitrogen being adsorbed at high P/P₀ (liquid infill of inter-particle space) and therefore, experimental surface area could not be obtained. The N₂ sorption-desorption isotherms and BJH graph for this sample are given in Appendix 5.7. Karmakar particles have been described as high dense silica microspheres with reported density, 2.10–2.16 g cm⁻³, is similar to that of silica glass.

Table 5.1 Zeta potential and N₂ gas adsorption data for SiO₂ particles of different size.

<i>Sample</i>	ξ (mV) <i>pH 7.4</i>	SSA (m ² ·g ⁻¹)	SSA _{theoret.} (m ² ·g ⁻¹)	V _{pore} (cm ³ ·g ⁻¹)	S _{pore} (nm)
SiO ₂ -28 nm	-18.3 ± 0.6	277.8 ± 3.5	97.4	0.548	9.6
SiO ₂ -210 nm	-33.3 ± 3.6	16.2 ± 0.6	13.0	0.303	31.7
SiO ₂ -40 μm	-21.1 ± 1.1	0.0 ^a	0.7	0.059	2.2

^aSSA values lower than the limits of detection of the instrumentation.

Thermal decomposition of silica samples showed an increase of the total % weight loss when increasing particle size (Figure 5.7a) and in all three silica samples two main stages of weight loss was observed (Figure 5.7b). First, desorption of water molecules at $T < 190$ °C (Zhuravlev, 2000), followed by subsequent dehydroxylation due to the condensation of silanol groups on the silica surface at temperatures from 200-900 °C (Iler, 1979), where vicinal, internal, geminal and isolated silanols can be completely removed from the surface at ~400 °C, 400 - 900 °C, 800 - 900 °C and ~900 °C, respectively (Zhuravlev, 2000). The observed % weight lost suggested that a higher fraction of water (Stage 1) and silanol groups (Stage 2) is present in larger particles (Figure 5.7c-d). Note that, for the Karmakar silica particles some of the weight loss in the Stage 2 was thought to be due to the presence of some remaining acetic acid (from the reaction) and/or acetone (from the washing process), since samples collected after thermal treatment were dark brown coloured instead of the original white powder, indicating the presence of residual carbon in the samples. Further, the main weight loss in Stage 2 for the Karmakar particles could also be attributed to decomposition of acetate groups at 250-400 °C (Wang *et al.*, 2011) and/or formation of volatile products (i.e. CO₂) from 225 to 440 °C (Devalencourt *et al.*, 1995) originated from any remaining acetic acid present in the samples. It should be taken into account the washing procedure and isolation of silica particles was different following the Stöber and Karmakar method (Appendix 5.8) which could affect either the elimination of non-reacted products and/or the amount of water molecules since these samples were not freeze-dried (only dried in an oven at 80 °C). Therefore, Karmakar silica particles were washed and isolated following the same procedure employed for the Stöber particles. TGA analysis (Appendix 5.9) showed that the % weight loss decreased from ~16% to ~15% when the particles were re-washed; however, the difference in weight loss was mainly observed in the Stage 1 (water content), these values being ~10% for the original Karmakar particles and ~9% for the re-washed Karmakar particles, indicating that the drying process affected the final content of water in the silica particles. Besides this, no significant difference of weight loss was observed for the weight loss in Stage 2. Further, remaining C was still present in the samples since the dark brown colour was still observed after TGA analysis. These results suggested that acetic acid may be intercalated within the SiO₂ particles and trapped up to very high temperatures (30-900 °C) due to the high density and non-porous

nature of this material. It was concluded that the increase of silanol groups with particle size could be uniquely confirmed for Stöber silica particles (28 and 210 nm). The silanol density in fully hydroxylated silica has been reported from 4.5 to 5.8 OH·nm⁻² (Davydov *et al.*, 1964; Ek *et al.*, 2001; Zhuravlev, 2000). However, these values (bulk material) include different silanol groups that can be present on a silica particle (isolated, geminal, vicinal and internal); and for larger particles, a higher fraction of internal silanol groups has been reported compared with smaller particles (Davydov *et al.*, 1964); which will not contribute to the functionalization of the particle surface. As surface chemistry is very important for silica functionalization, the chemical surface composition was investigated by XPS.

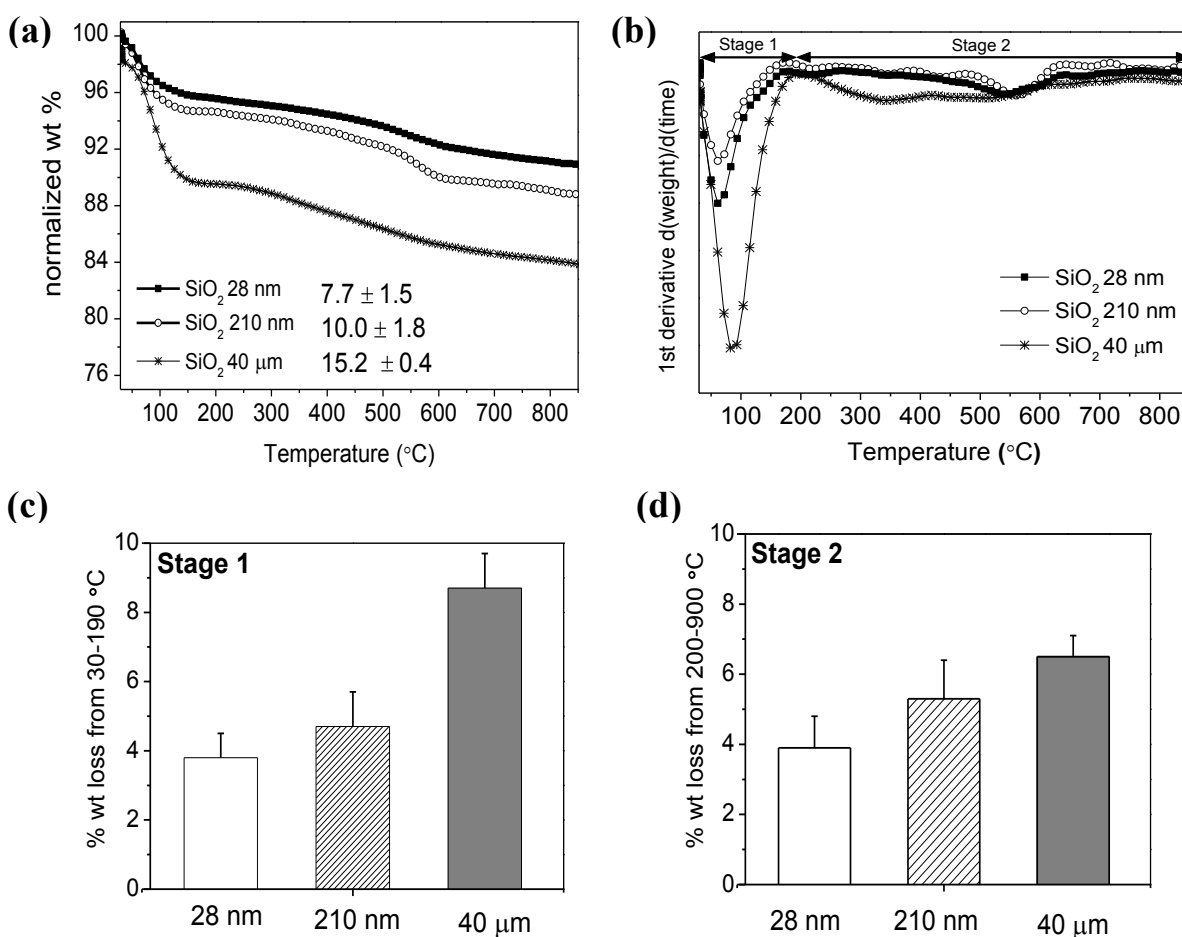


Figure 5.7 Thermal decomposition of silica particles of size 28 nm, 210 nm and 40 μm (a) TGA curves, (b) DTG plots, (c) % wt loss in Stage 1 (from 30 - 200 °C) and (d) % wt loss in Stage 2 (from 200 - 900 °C).

From XPS analysis, the presence of Si, O and ‘possibly’ C in the silica samples was studied by detailed analysis of the Si 2p_{3/2}, O 1s and C 1s regions, at 103.5 ± 0.1 eV, 533.0 ± 0.0 eV, 285.0 ± 0.0 eV, respectively; cf. the survey scan of the SiO₂-210 nm (Figure 5.8a). The ratio of Si/O for all the samples was around 0.6 (Figure 5.8a inset). Theoretically, taking into account moles of oxygen per moles of silicon this Si/O relation for silica should be around 0.9, however; due to the presence of silanol groups on the surface, the amount of oxygen is expected to be higher as shown in Figure 5.8a inset; and consequently, decrease the Si/O ratio. Although, higher % of weight loss for larger particle has been proposed to be due to a higher amount of silanol groups (bulk material), the higher % of O detected for the nano-scaled particles (Figure 5.8a), suggested a higher amount of –OH groups on the surface. In addition, a higher amount of water molecules was observed for the micro sized particles (TGA data); thus, a higher fraction of this % of O detected accounted for water molecules instead of Si-OH or SiO₂. It was also observed that the % of carbon detected in the SiO₂-40 μm (Karmakar particles) was much higher than for the Stöber particles (Figure 5.8a). Although XPS is a surface technique, X-rays may penetrate deep into the sample and photoelectrons from depths up to 10 nm can be detected (Fairley, 2009). Therefore, the detection of a large amount of C in the Karmakar particles suggested that acetic acid could be present within the silica network of the particles as shown in Figure 5.8b. On the other hand, the C detected in the Stöber particles was attributed to adventitious C present in the XPS chamber during analysis.

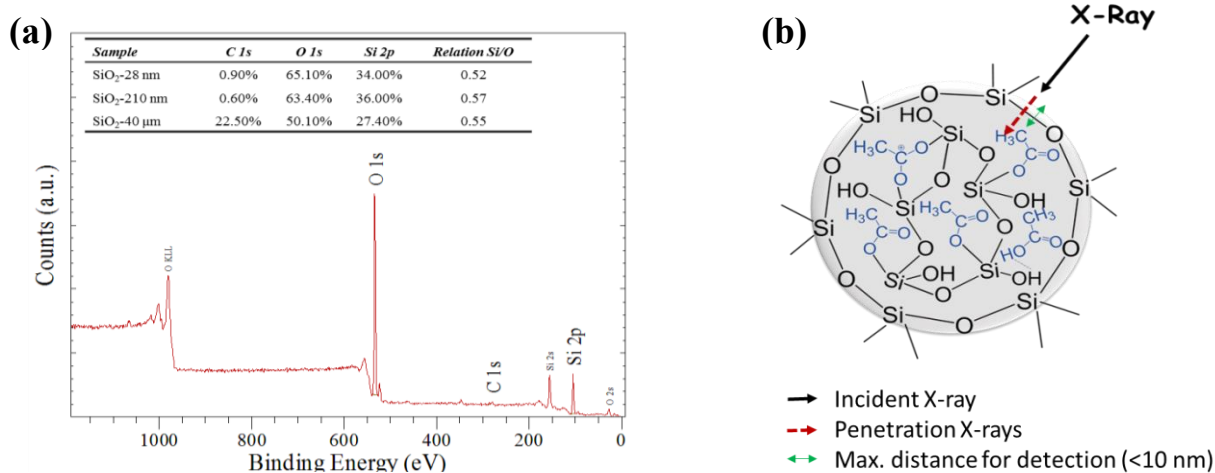


Figure 5.8 (a) XPS survey spectrum recorded from an as-deposited SiO₂-210 nm sample and inset atomic % of carbon, oxygen and silicon and the calculated ratio of Si/O. (b) representation of a

Karmakar particle with the acetic acid forming part of the silica network and the penetration of the incident X-rays (discontinuous red arrow) and depth from which photoelectrons can still be emitted (double sided green arrow) using the XPS technique.

ATR spectra of the samples (Figure 5.9a) presented characteristic silica peaks at ~ 1050 cm^{-1} (peak ii), ~ 950 cm^{-1} (peak iii) and ~ 790 cm^{-1} (peak iv), corresponding to the antisymmetric Si-O-Si stretching mode, Si-OH stretching mode and symmetric Si-O-Si stretching mode, respectively (Smith, 1960). A broad peak observed at 3500 - 3000 cm^{-1} was attributed to vibrational mode of water (3500 - 3000 cm^{-1}) (Smith, 1960) and/or silanol groups (3400 - 3200 cm^{-1}) (Smith, 1960). Although it is difficult to distinguish between these two species only based on this band as they are similar in position and shape, the detection of the Si-OH stretching mode as well as a band at ~ 1636 cm^{-1} (peak i) attributed to the scissoring of the two O-H bonds (Smith, 1960) in a water molecule suggested that the band at 3500 - 3000 cm^{-1} can either be due to the presence of silanol groups and/or the presence of water in the samples. Besides this, no evidence of acetic acid was detected by ATR in the Karmakar samples. Samples were then analysed by FTIR-KBr (Figure 5.9b) and the presence of carboxyl groups could be confirmed by a peak arising at 1706 cm^{-1} (Max and Chapados, 2004).

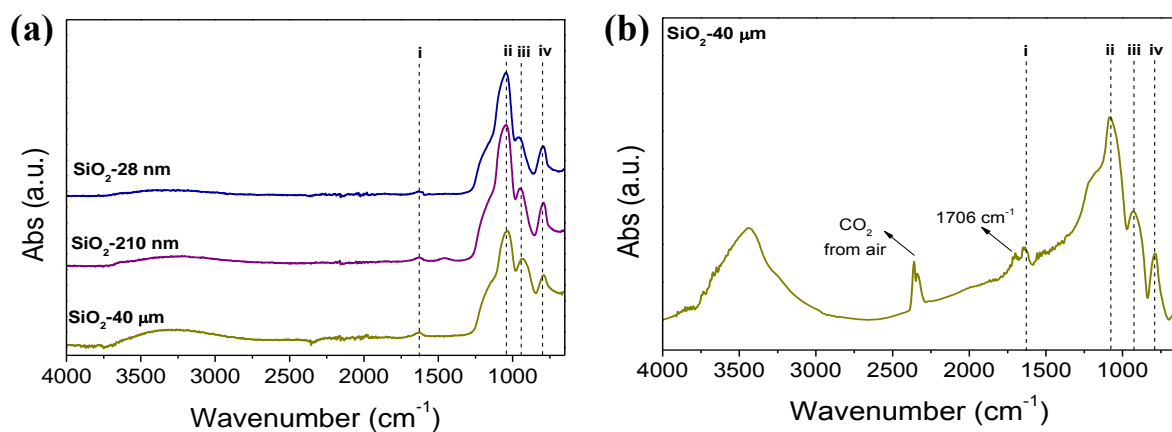


Figure 5.9 (a) ATR of SiO₂-28 nm, SiO₂-210 nm and SiO₂-40 μm particles and (b) FTIR-KBr analysis of Karmakar particles (SiO₂-40 μm); peaks corresponding to (i) scissoring of the two O-H bonds in a water molecule (ii) antisymmetric Si-O-Si stretching mode, (iii) Si-OH stretching mode, and (iv) symmetric Si-O-Si stretching mode. The peak assigned to CO₂ from air is due to experimental analysis. The broad peak at 3500 - 3000 cm^{-1} is due to vibrational mode of water. The

slope observed for the SiO₂-40 μm particles is typically a result of scattering from coarsely ground particles, i.e. silica glass type materials.

5.6.2 Silica Particle Functionalization and Properties

During the course of reaction, a gelation effect for those samples containing APTES was observed, being more pronounced for samples containing a higher fraction of APTES (Figure 5.10). Synthesis parameters, such as temperature has been shown to be a significant factor for the formation of gels, especially during silica synthesis, where an increase of the temperature into the system gives place to an increase of the aggregation kinetics and, hence, gelation time is reduced (Amiri *et al.*, 2011; Colby *et al.*, 1986). On the other hand, the addition of APTES has also been shown to favour gel formation (Kong *et al.*, 2012; Zhmud and Sonnefeld, 1996).

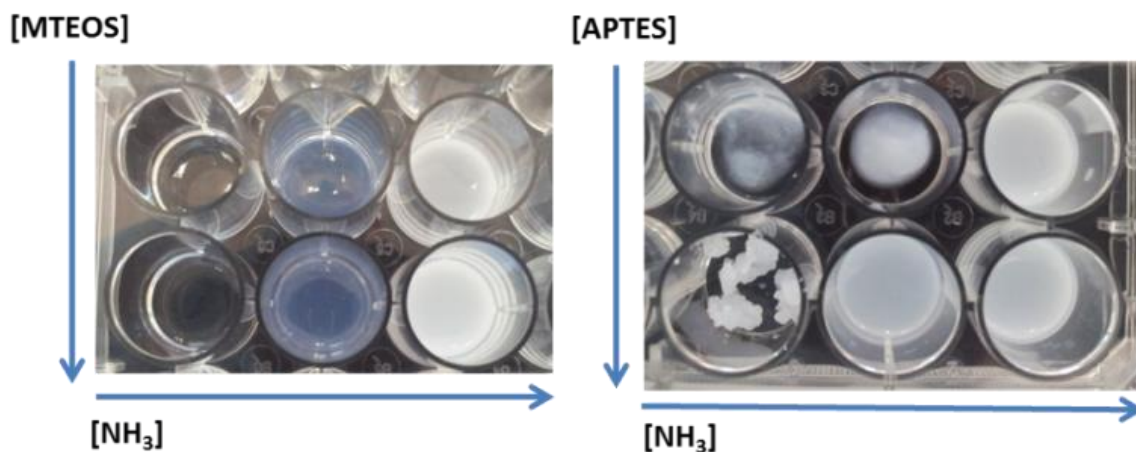


Figure 5.10 Functionalized silica samples collected after 24 hours of reaction containing different concentrations of MTEOS or APTES (concentration increasing from top to bottom) and different ammonia concentrations (concentration increasing from left to right).

As previously mentioned (section 5.1) APTES can also catalyse the sol-gel process (enhancement in the rate of hydrolysis and condensation reaction). The presence of -NH₂ groups can lead to a larger and more agglomerated species (Bagwe *et al.*, 2006; Digigow *et al.*, 2014; Rahman *et al.*, 2009). Essentially, the amine-functionalized silica particles can bind through other active sites of the molecule (i.e. amine group) with the silanol groups on the surface, aiding aggregation of the particles as there is no driving force

on the particles surface to keep them apart (Bagwe *et al.*, 2006). In Figure 5.11 is shown the effect of APTES addition during the silica synthesis method followed. Particle size measured (*ImageJ*, $n \geq 30$) showed an increase when adding a higher fraction of APTES in the system compared with the Blank (27 ± 3 nm), being these values of 35 ± 4 , 36 ± 3 and 53 ± 6 nm, respectively. Hence, the methodology described in Section 5.4.2 was followed in which no heating was employed for the functionalization of the silica particles as grafting method was chosen for modification of the silica surface.

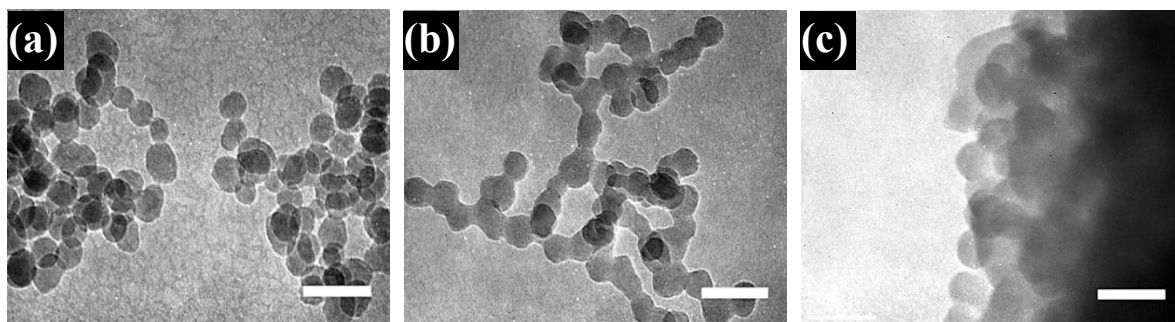


Figure 5.11 TEM images of SiO₂ NPs synthesized in the presence of APTES at concentrations of (a) 10 mM, (b) 100 mM and (c) 500 mM. All scale bars are 100 nm.

Methyl and 3-aminopropyl silica samples were first characterized by ATR in order to know if functionalization was successfully achieved. Si-alkoxy compounds, such Si-CH₃, have one or more strong bands in the 1100-1000 cm⁻¹ region; however, if silica (Si-O-Si linkage) is present in the sample, these bands can be masked by the strong Si-O-Si absorption bands (1130-1000 cm⁻¹) (Smith, 1960). Even so, ATR spectra (Figure 5.12) showed the presence of two sharp peaks (α) at 2973-2863 cm⁻¹ and a band (β) at ~ 1460 cm⁻¹ attributed to C-H stretch mode (Jung *et al.*, 2012) and C-H scissoring, respectively; confirming the presence of either methyl or propyl groups in the silica samples. It was also observed that the intensity of the peaks corresponding to the stretching mode of C-H increased with APTES addition, suggesting higher levels of functionalization for samples treated with higher concentrations of APTES (Figure 5.12 inset). The two weak characteristic peaks from the amine group (-NH₂) expected at ~ 3362 cm⁻¹ and ~ 3296 cm⁻¹ (Li *et al.*, 2013), could not be detected due to the broad peak in the region of 3500-3000 cm⁻¹ attributed to silanol groups and/or water molecules. Besides this, the peak at ~ 1628 cm⁻¹ (peak i) previously assigned

to scissoring of the two O-H groups in a water molecule could, in this case, also be attributed to the deformation mode of -NH₂ (Li *et al.*, 2013). However, the detection of this peak in both methyl and amino-functionalized surfaces suggested that it was more likely to be from O-H bonds rather than -NH₂ groups. Hence, due to the dubious existence of amino functionalized silica surfaces by ATR analysis, the presence of amine groups on the silica surface was best confirmed by the Ninhydrin Test which is a qualitative method for the detection of ammonia or primary and secondary amines (Harding and Warneford, 1916; Soto-Cantu *et al.*, 2012) (Appendix 5.10). The results from this test also revealed that the non-functionalized Stöber particles did not contain traces of ammonia from the synthesis process, which could have interfered with the later binding studies.

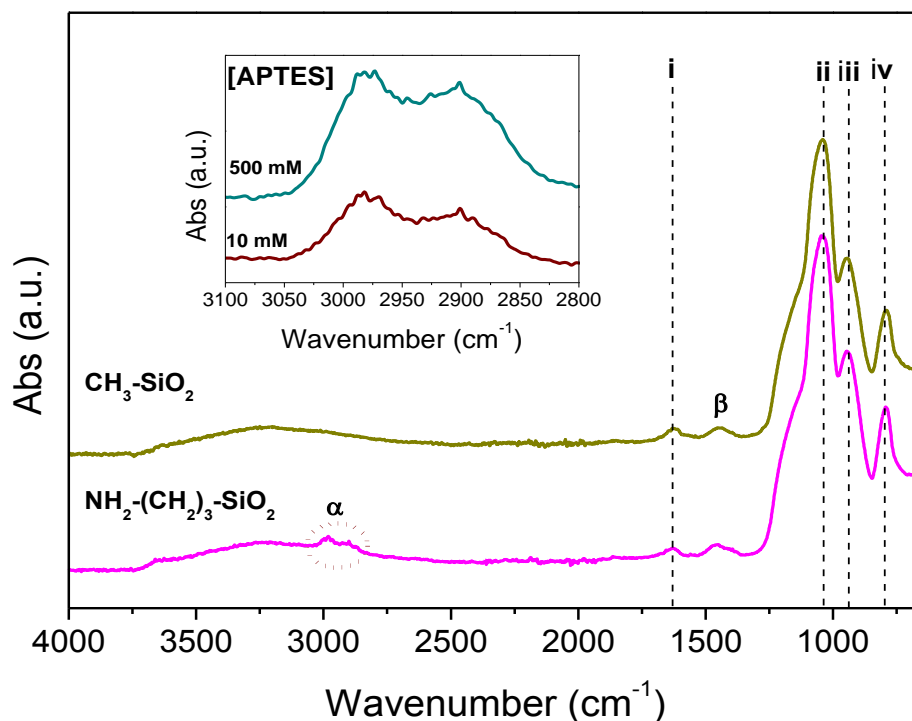


Figure 5.12 ATR of functionalized silica particles. Peaks corresponding to only silica are: (i) scissoring of the two O-H bonds in a water molecule and/or deformation mode of -NH₂ (ii) antisymmetric Si-O-Si stretching mode, (iii) Si-OH stretching mode and (iv) symmetric Si-O-Si stretching mode. Peaks corresponding to functional groups: (α) C-H stretch mode and (β) C-H scissoring. Inset shows highlighted region between 3100-2800 cm⁻¹.

The zeta values for functionalized samples are shown in Table 5.2. The addition of either MTEOS or APTES reduced the surface charge of the silica particles, and for higher amounts of amino-propyl groups on the surface, the zeta values became positive in the case of the nano-scaled silica particles.

Table 5.2 Zeta potential values (mV) of functionalized SiO₂ particles.

ζ (mV) pH	10 mM MTEOS	500 mM MTEOS	10 mM APTES	500 mM APTES
SiO ₂ -28 nm	-17.9 ± 1.6	-14.9 ± 0.2	-13.1 ± 0.6	+9.1 ± 1.8
SiO ₂ -210 nm ^b	-28.0 ± 1.1	-22.3 ± 2.1	-17.8 ± 1.2	+2.2 ± 0.4
SiO ₂ -40 μm	-18.4 ± 6.2	-11.9 ± 0.7	-11.7 ± 3.3	-11.4 ± 2.5

^a ζ (mV) values for non-functionalized SiO₂ were -18.3 ± 0.6 (28 nm), -33.3 ± 3.6 (210 nm) and -21.1 ± 1.1 (40 μm). ^b ζ (mV) values for amino-functionalized SiO₂ with 2.5 mM and 100 mM were -18.5 ± 2.4 and -12.9 ± 1.2, respectively.

TGA analysis showed for smaller particles a higher % of weight loss when functionalized with APTES compared with larger particles and a lower % of weight loss when functionalized with MTEOS (Figure 5.13a-b); cf. graphs of samples functionalized with 500 mM of MTEOS or APTES. For the three different sizes of functionalized silica particles samples containing 3-aminopropyl groups, it was observed a common peak of weight loss at ~531 °C (Figure 5.13c). The decomposition of bonded phase aminopropyl ligands has been shown to take place between temperatures from 400 to 600 °C, being the maximum rate of wt loss at ~ 500 °C (Jaroniec *et al.*, 1997). The presence of peaks at lower temperatures (between 200-400 °C) could be associated to the condensation of silanol groups between neighbouring aminopropyl ligands (Vansant *et al.*, 1995). For the silica particles containing methyl groups, the weight loss observed between 200-800 °C (Figure 5.13d) was mainly associated with the decomposition of methyl groups leading to the formation of carbon where combustion occurs later on at temperatures around 500-650 °C. Note that, Karmakar samples were still coloured after TGA analysis indicating the presence of acetic acid, hence, the peak of weight loss observed from 250 to 400 °C could still be attributed to decomposition of acetic acid. Appendix 5.11 shows the total % of weight loss and % of weight loss in Stage 2 for all different concentrations of MTEOS or APTES added into the system. The % of weight loss of the organic content (Stage 2) showed an increase of weight loss with silica functionalization (Appendix 5.11).

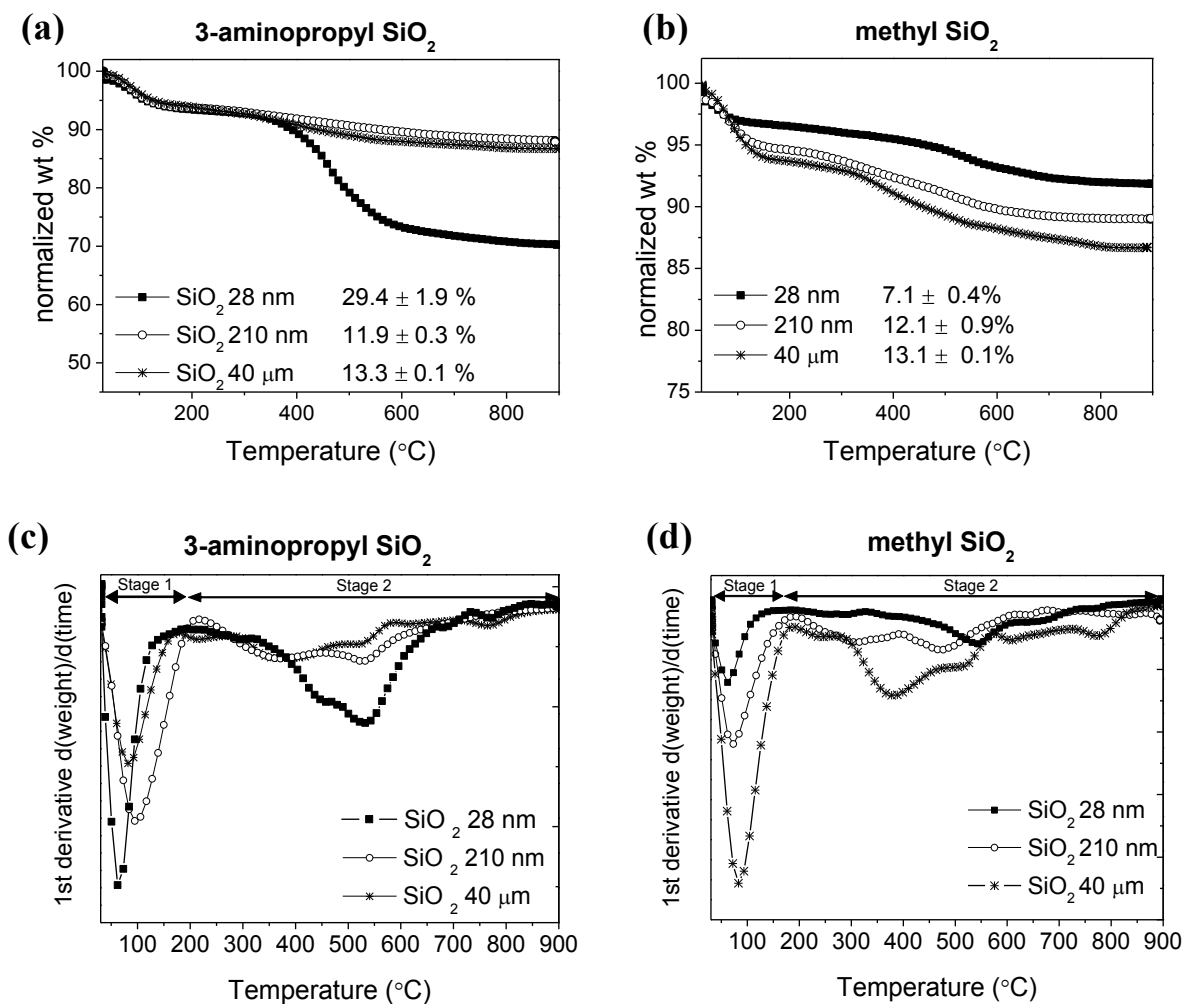


Figure 5.13 (a) TGA curves and (b) DTG plots for functionalized SiO₂ particles (500 mM) of different size.

Surface functionalization was also confirmed by XPS analysis. Similarly to the non-functionalized silica samples, XPS spectra showed the characteristic peaks of Si 2p and O 1s, at 103 eV and 532 eV, respectively; as well as the incorporation of C and/or N by detection of peaks in the region of C 1s (285 eV) and N 1s (399 eV); cf spectra of a SiO₂-210 nm sample (Figure 5.14a-b). In general, the area of the C 1s peak increased with extent of functionalization as well as the N 1s peak for the samples containing APTES (Figure 5.14c). The atomic % of Si, O, C and N for the different silica sizes studied is shown in Appendix 5.12. Remarkably, for the Karmakar particles, the % of C was less than that observed for the blank (non-functionalized SiO₂ particles). As explained in Section 5.7.1, the presence of remaining acetic acid (from the reaction) was observed in the samples.

Knowing that the XPS technique has an X-ray depth penetration up to 10 nm, acetic acid could be detected for the Blanks whereas for the functionalized particles the X-ray may penetrate first into the organic molecules on the surface as shown in Figure 5.14d.

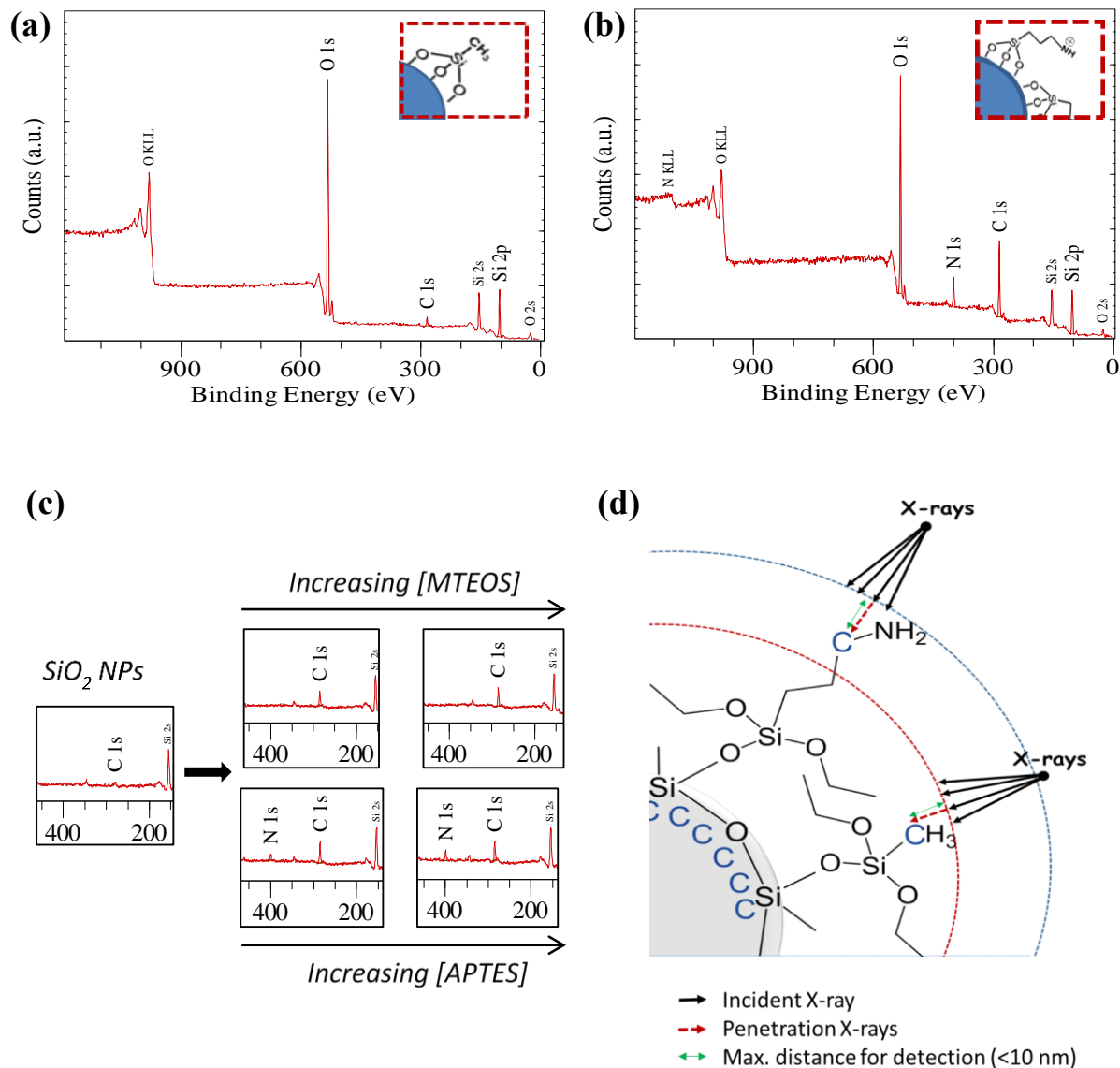


Figure 5.14 XPS survey spectra for 210 nm SiO₂ NPs (a) methyl functionalized (MTEOS) and (b) 3-aminopropyl functionalized (APTES) corresponding to the high concentration added (500 mM). (c) XPS spectra highlighted between 180-240 eV to show the variation of the peak intensity by adding MTEOS or APTES. (d) Representation of Karmakar particles with acetic acid intercalated throughout the silica particles and the penetrations of the X-rays.

For the 3-aminopropyl surfaces, an increase of % of N in smaller particles (~ 8% for SiO₂-28 nm) compared with bigger particles (~3% for SiO₂-210 nm and ~ 1% for SiO₂-40 μm) was observed. From silica surface charge values, it would be expected that the more negative the surface charge, the more amino groups are attracted to the surface; however, these results showed the opposite trend. Hence, it is suggested that the higher surface area of the particles, the more 3-aminopropyl groups could be attached to the surface; giving rise to smaller particles having higher degree of amino-functionalization, independently of the particle surface charge. For SiO₂-28 nm particles, the % of atomic of N remained more or less constant with APTES addition indicating no further functionalization was achieved (Appendix 5.12). As previously mentioned, the high reactivity of aminoalkoxysilanes towards water can induce its uncontrolled polymerization/oligomerization in solution, being these no longer available to attach onto the silica surface (Asenath Smith and Chen, 2008). Further, these self-condensed side products can be easily removed by repeating centrifugation/redispersion processes (Jung *et al.*, 2012) as followed in this study. However, the positive net charge (Table 5.2) and the % of weight loss observed (TGA data) for the higher concentrations of APTES (500 mM), suggested a higher degree of amino groups present in these samples. Therefore, it was believed the formation of multilayered APTES interfaces due to intermolecular polymerization. For the higher concentrations of APTES (500 mM) suggested a higher degree of amino groups present in the samples. Therefore, multilayered APTES interfaces due to intermolecular polymerization were proposed. On the other hand, for the 210-SiO₂ NPs, although the % of N was much less than observed for the smaller particles, an increase of % of N was detected by increasing the concentration of APTES added into the system, indicating the coverage was below that of a monolayer as previously reported in our group (Puddu and Perry 2014). Note that, for Karmakar particles even though the % wt loss was higher than for smaller particles when functionalizing with low concentrations of APTES (TGA data, see Appendix 5.11), the % of N detected was lower. It was believed that some % wt loss in the karmakar particles accounted from acetate groups detected in the silica network and it was not from its functionalization. For methyl functionalized surfaces, an increase of the % of C was observed with addition of higher amounts of MTEOS into the system (Appendix 5.12).

The extent of methyl and 3-aminopropyl functionalization for the different particle sizes was also studied by comparing the ratio of C:Si and N:Si on the silica surface, respectively (Figure 5.15). Note that, the C:Si ratio data for non-functionalized Karmakar particles were not included due to the possible presence of acetic acid. It was observed that for smaller particles a higher grafting of amino groups onto silica particles was achieved (as previously shown for the % of N), whereas methyl groups were more likely to accommodate onto larger particles. These results also corroborate that independently of the particle charge, amino groups attach preferentially to smaller particles. On the other hand, methyl functionalized surfaces showed a higher % of C for larger particles. The presence of less % of O in larger particles (XPS analysis of non-functionalized SiO₂ particles) suggested lower amounts of silanol groups on the surface; hence, a higher hydrophobicity of the silica particles is expected due to the presence of Si-O-Si linkages on the surface. Therefore, hydrophobic molecules such as methyl groups will tend to interact preferentially with larger particles through hydrophobic-hydrophobic interactions.

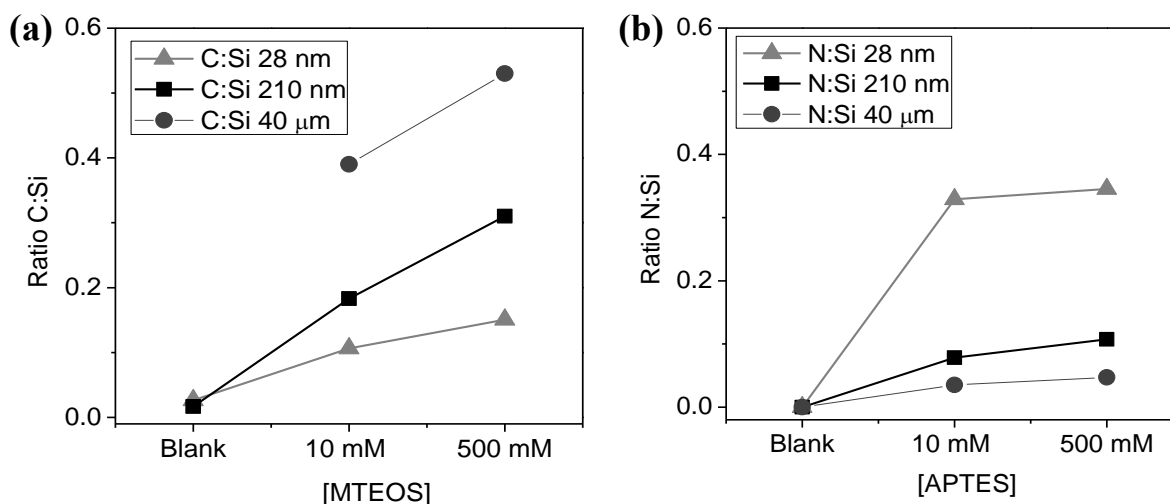


Figure 5.15 From XPS data, (a) C:Si ratio and (b) N:Si ratio on the silica particles showing trend of functionalization vs. particle size.

5.6.3 Silica-Peptide Binding Studies

The peptides chosen for the study of the silica-peptide interface interactions were previously identified in our group by the phage-display technique (Puddu and Perry, 2012).

In Table 5.3 are shown the properties of these peptides, K7 (KLPGWWSG), A7 (AFILPTG) and L7 (LDHSHS), which are believed to affect the type of interactions taking place at the silica-aqueous interface.

Table 5.3 Amino acid chain and peptide properties

Peptide name	Peptide Sequence	pI	ζ^a	Average Hydrophilicity ^b	Number of side-chain functionalities					
					Basic	acidic	Polar ^c	Non-polar ^d	amino	hydroxyl
K7	KLPGWWSG	10	+1	-0.3	1	0	3	3	0	1
A7	AFILPTG	6	0	-1.0	0	0	2	5	0	1
L7	LDHSLHS	6	-1	-0.1	2	1	2	2	0	2

^aNet charge pH 7.4 ^bCalculated from <http://www.bachem.com/service-support/peptide-calculator/>, ^cuncharged and ^dhydrophobic.

Although the adsorption process highly depends on the nature/chemistry of the solid surface, other factors such as binding/kinetic energies and/or orientation/conformation of the peptide also play an important role on peptide adsorption (Gray, 2004; Rabe *et al.*, 2011; Roach *et al.*, 2005). The mechanism of protein or peptide binding has been shown to be a complex process involving electrostatic, hydrophobic, van der Waals interactions, and hydrogen bonding (Natte, 2013; Patwardhan *et al.*, 2012; Puddu and Perry, 2012; Rabe *et al.*, 2011; Roach *et al.*, 2005). These peptide sequences have been selected essentially for their difference in the net charge at the working pH (7.4) as well as for their different hydrophobic/hydrophilic character. In Appendix 5.13, the theoretical net charge at the range of pH from 0 to 14 is presented.

5.6.3.1 Effect of Silica Particle Size on Binding

Adsorption curves for each peptide as a function of the initial peptide concentration are shown in Figure 5.15. In Appendix 5.14 are shown the calibration curves for the three peptides. The amount of peptide adsorbed was expressed per unit surface area due to silica particles of different size differ by surface area. Note that, theoretical surface areas were used instead BET values since the later do not represent particle surface area in solution (i.e. sonication will give rise to less aggregated particles). The results showed a higher peptide affinity for larger particles (Figure 5.16) independently of the peptide properties,

which suggested that the binding mechanism depends upon the properties of the different sized silica particles. It was also noted that the peptide affinity increased generally from L7 < A7 < K7 (Figure 5.16), which was in accordance with the results previously reported by Puddu and Perry (2014). The high affinity of the peptide K7 was due to interactions between the positively charged amino-terminated side chains in the peptide (i.e. Lys) and the negatively charged (deprotonated hydroxyl groups) silica surface (Patwardhan *et al.*, 2012; Puddu and Perry, 2014). It has been shown for this peptide that an increase of pH in the system lead to a higher affinity towards silica particles due to an increase of the net charge which further supports the role of electrostatic forces in adsorption (Puddu and Perry, 2012). Besides this, the overall neutral and negatively charged peptides (A7 and L7, respectively) also showed a significant affinity towards silica, suggesting that binding mechanisms were governed by other types of interactions such as hydrogen bonding and other non-ionic interactions (Patwardhan *et al.*, 2012; Puddu and Perry, 2014). In other biological scenarios, bacterial adhesion to cellular surfaces has been shown to not only be influenced by physicochemical properties (such as surface charge) but by thermodynamic properties of the bacteria cells and surface (such as hydrophobicity) (Li and McLandsborough, 1999). The presence of nonpolar amino acids in A7 (i.e. Isoleucine, Proline and Leucine) increase its hydrophobic character; hence, it was suggested that hydrophobic interactions dominate/contribute to the peptide binding mechanism (Puddu and Perry, 2012). Similarly, the peptide L7 was shown to interact with silica surfaces by hydrophobic interactions due to the presence of Leu as well as hydrogen bonding due to the presence of polar and charged amino acids (Emami *et al.*, 2014; Patwardhan *et al.*, 2012; Puddu and Perry, 2014) . Hydrogen bonding takes place, in general, between amide and carbonyl groups of the polypeptide chain. Nevertheless, hydrogen bonding is not the main driving force for protein adsorption. Previous studies showed that the formation of hydrogen bonded multilayers was observed for L7 as no saturation was reached by adding higher amounts of peptide into the system (Patwardhan *et al.*, 2012). As this type of interaction (hydrogen bonding) is weaker than electrostatic interactions, a higher initial peptide concentration threshold is required for significant adsorption (Patwardhan *et al.*, 2012). Further, peptide multilayer formation was suggested to be due to peptide-peptide interactions (Puddu and Perry, 2012; Roach *et al.*, 2005).

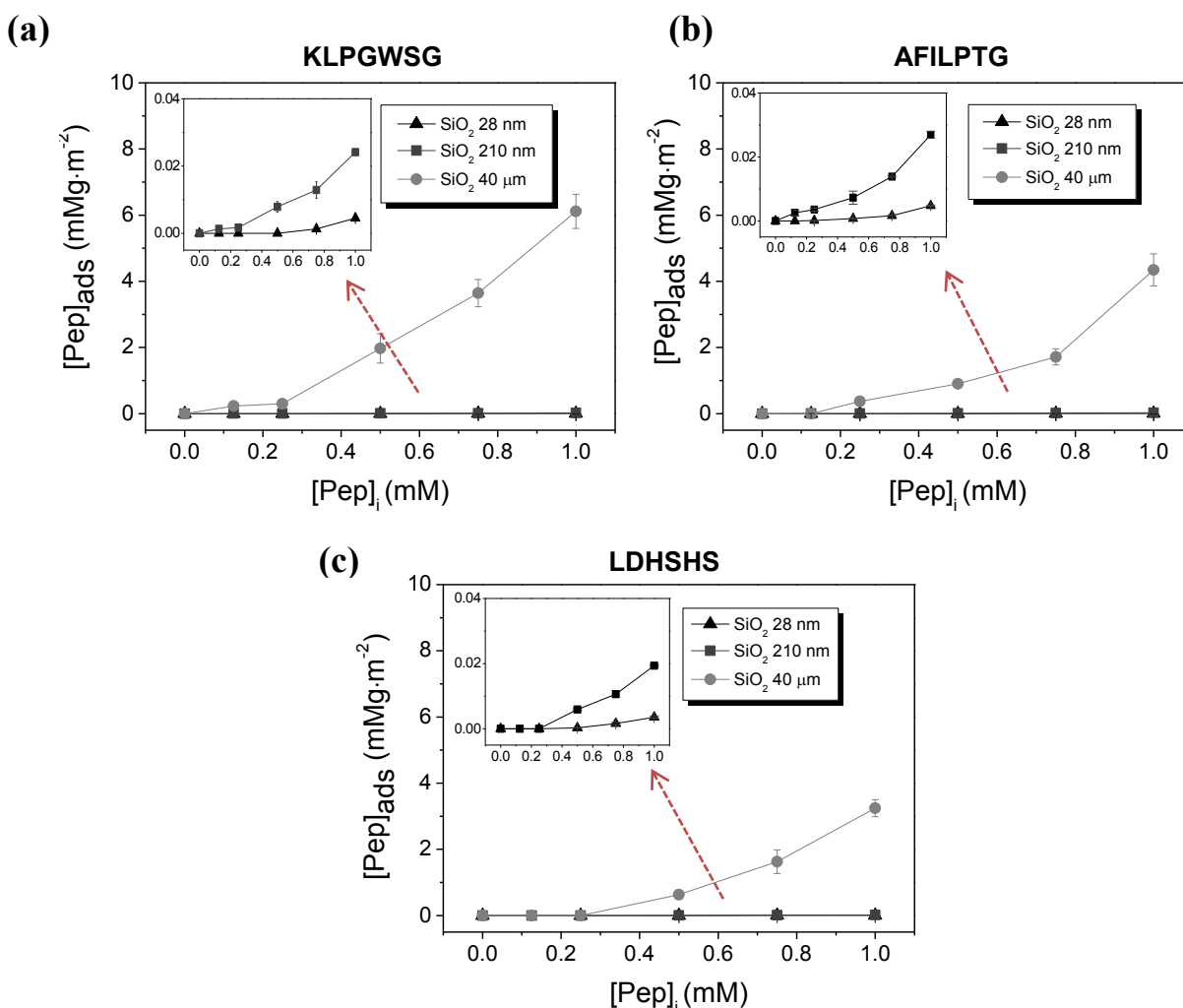


Figure 5.16 Adsorption isotherms of (a) K7 (KLPGWSG), (b) A7 (AFILPTG) and (c) L7 (LDHSHS) on non-functionalized silica particles of different size. The adsorbed peptide was normalized to the BET surface area of each corresponding size. Insets show an amplification of the curves for the Stöber particles (28 and 210 nm).

5.6.3.2 Effect of Silica Functionalization on Binding

The silica-peptide binding response was shown to be influenced by the surface chemistry of the surface and similar trends were obtained for all different sized silica particles. In this section, silica particles of 210 nm are shown due to the greater differences between net charge of the pristine silica (-33 mV), methyl-functionalized (-28 mV) and amino-functionalized (-18 mV). Adsorption isotherms for 28 nm and 40 μm SiO₂ particles are shown in Appendix 5.15. The study of the binding behaviour depending on the degree of

functionalization is explained in section 5.6.3.3; hence, these results only show a comparison between pristine silica and low levels of functionalized surfaces (methyl and 3-aminopropyl groups).

The positively charged peptide (K7) showed a greater affinity for the pristine silica compared with the methyl- and amino-functionalized surfaces (Figure 5.17a). Therefore, electrostatic interactions as the mechanism of binding was confirmed as interaction decreased with decreasing silica surface charge (-33 mV for SiO₂, -28 mV for CH₃-SiO₂ and -18 mV for NH₂-(CH₂)₃-SiO₂). For the peptide A7 (neutral), no significant differences were found for the 210 nm silica surfaces (Figure 5.17b). However, for smaller particles it was observed that slightly lower amounts of peptide adsorbed on amino-functionalized surfaces as was previously reported by Puddu and Perry (2014) due to the more hydrophilic character of this surface. It should be noted that the 28 nm silica particles present a higher degree of functionalization compared with larger particles (XPS data); hence, these results may suggest that a certain level of amino groups might be needed to reach significant adsorption differences. On the other hand, Karmakar particles showed a higher affinity for either methyl- and amino-functionalized surfaces compared with pristine silica (Appendix 5.15). Due to the hydrophobic character of the peptide A7, a higher affinity for methyl-functionalized surface was expected. Although, the level of methyl functionalization for Kamakar silica could not be totally ensured (due to the possible presence of acetic acid within the sample), the correlation of methyl functionalization with particle size was demonstrated by comparing 28 and 210 nm silica particles (XPS data). Hence, a higher degree of methyl groups on larger particles would increase hydrophobicity of such particles and show a higher affinity for peptide A7. For the negatively charge peptide (L7), all three sized silica particles had a much higher affinity to the amino-functionalized surface (Figure 5.17c) suggesting that, in this case, the peptide interacted by electrostatic interactions. This remarkable change in the binding mechanism from hydrophobic interactions and hydrogen bonding for non-functionalized SiO₂ (Patwardhan *et al.*, 2012; Puddu and Perry, 2014) to electrostatic interactions for amino-functionalized surfaces, showed how peptide-surface response can easily be modified by slight changes at the silica-peptide interface. It should be noted, that for the 28 nm SiO₂ particles (Appendix 5.1), adsorption occurred even at the very low initial peptide concentrations, which may be due to the higher degree of surface

amino groups. Slightly less affinity towards methyl-functionalized surfaces was observed for larger particles (210 nm and 40 μm) compared with the pristine silica which could be due to the less hydrophobic character of this peptide (Table 5.3). For the for SiO₂-28 nm particles, no significant difference were observed possibly due to the lower degree of methyl coverage present in this sample.

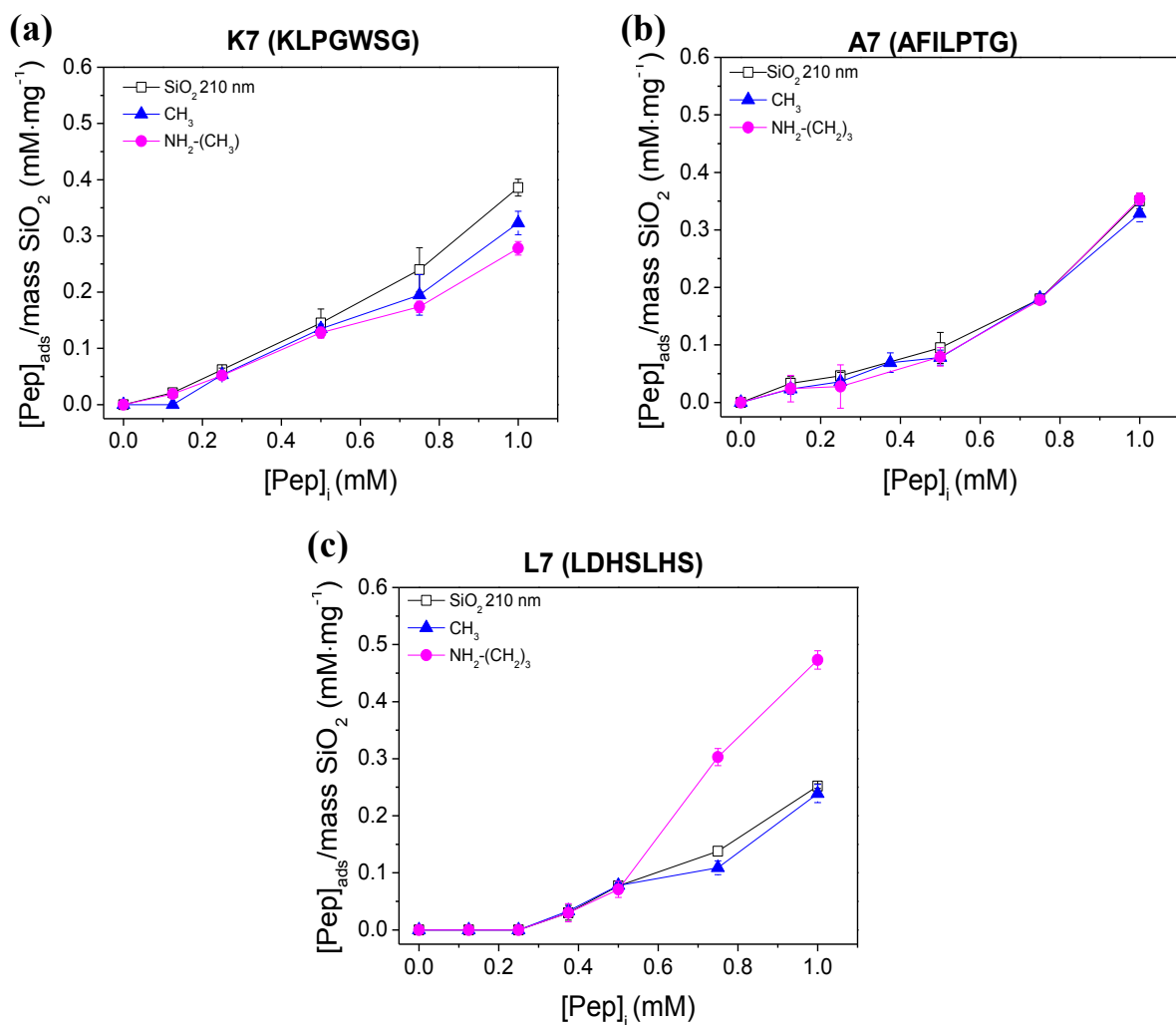


Figure 5.17 Adsorption isotherms of the peptide (a) K7, (b) and (c) L7 on non-functionalized and functionalized silica particles of 210 nm size. Functionalized surfaces shown are the low level (10 mM) of methyl- and amino-functionalization.

5.6.3.3 Effect of Level of Functionalization on Binding

Silica-BPs interactions were first studied with the peptide K7 (Figure 5.18). This positively charged peptide at the working pH (7.4) have been shown to interact preferentially with a

negatively charged surface, and decreasing interaction as follows: Si-OH > CH₃-SiO₂ > NH₂-(CH₂)₃-SiO₂ (Puddu and Perry, 2014). As mentioned in Section 5.6.3.2, the same trend was observed when samples were functionalized following the Wu *et al.* methodology (Wu *et al.*, 2013), where only 10 mM of APTES or MTEOS were added to the system (previous section, Figure 5.17). However, when increasing surface functionalization by adding higher concentrations of APTES (500 mM), a higher interaction compared with the pristine SiO₂ was observed. Further, interaction seemed to be higher for those particles with higher level of amino groups on the surface (smaller particles), decreasing with increasing particle size (Figure 5.18i), being observed for SiO₂-40 μm no significant difference in binding for the lower and higher levels of functionalization. The reason for this could be that increased levels of amine functionalization may enhance particle aggregation by limiting levels of charge and by increasing hydrophobicity (Belton *et al.*, 2008). The presence of hydrophobic character amino acids in the peptide (i.e. Leucine and Proline) may induce hydrophobic-hydrophobic interactions as a component of the peptide binding mechanism. On the other hand, the positive charges observed for the nano-scaled particles (~ 9 mV for 28 nm and ~2 mV for the 210 nm silica particles) suggested a switch from nucleophile groups (free amines) to electrophile groups (protonated amine groups) on the silica surface; hence, nucleophilic attack of Serine due to the presence of -OH groups to form a new covalent bond could also occur (Petsko and Ringe, 2009). Since covalent bonds are much stronger than molecular interactions (attractive or repulsive forces) the possibly release of adsorbed peptide into solution due to the centrifugation process would not be expected. For the methyl functionalized surfaces (Figure 5.18ii), all three sized particles showed slightly less interaction compared with pristine silica due to the less negative surface (Table 5.2). Therefore, peptide adsorption decreased with particle size. Further, it has been reported that steric hindrance by the presence of methyl groups on the surface can decrease the amount of peptide adsorbed onto the surface (Puddu and Perry, 2014). Although, Karmakar particles present a higher degree of methylation, more steric effects are expected on smaller particles which would explain the lower peptide adsorption observed compared with the pristine silica.

Peptide K7 (KLPGWSG)

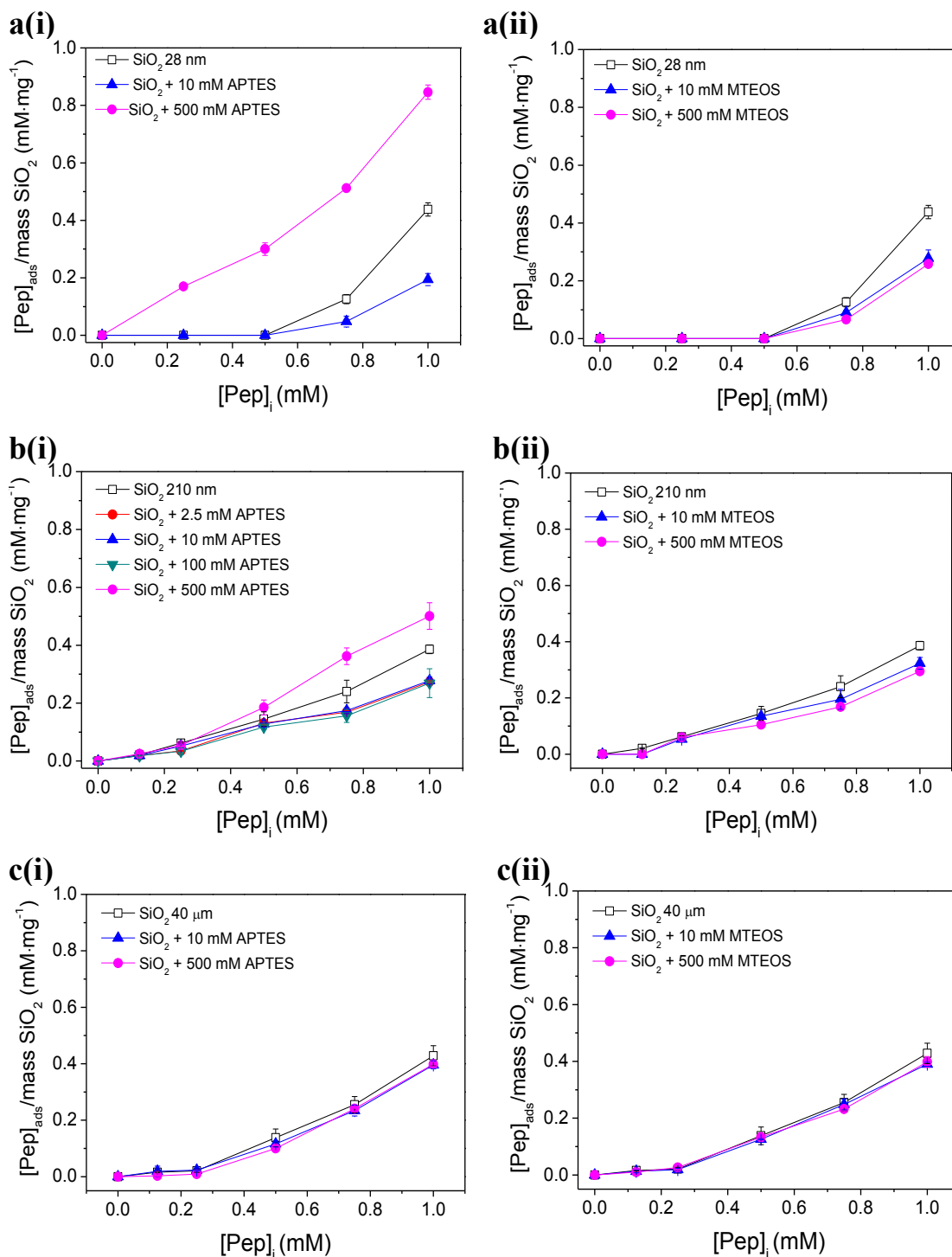


Figure 5.18 Adsorption isotherms of the peptide K7 (KLPGWSG) on silica particles of different size (a) 28 nm, (b) 210 nm and (c) 40 μm functionalized with (i) APTES and (ii) MTEOS.

For the neutral peptide A7, slightly different behaviour on binding was seen for all three sized silica particles (Figure 5.19). In the case of the amino functionalized surfaces, it was also observed a higher interaction compared with the pristine SiO₂ for the highest level of functionalization, even though this peptide has been shown to interact by hydrophobic interactions and lower affinity towards the hydrophilic 3-aminopropyl-SiO₂ was expected (Puddu and Perry, 2014). Similarly to the peptide K7, nucleophilic attack could occur, in this case, through the –OH group of threonine. The slightly lower peptide adsorption compared with the peptide K7 could be because the threonine (in A7) is a secondary alcohol whereas serine is a primary alcohol; hence, lower binding due to steric hindrance. It should be mentioned, that the peptide conformation is also crucial for binding. A higher amount of hydrophobic residues can contribute to the folding of protein structures (Kauzmann, 1959). The higher hydrophobic character of A7 in respect of the peptide K7 may induce cluster formation (Janin, 1979) and; hence, inaccessibility to specific amino acid sites. For Karmakar particles, binding affinity was higher than the pristine silica for both the lowest and the highest levels of functionalization. The higher peptide affinity observed for the low level of amino-functionalized Karmakar particles did not correlate with statements previously proposed as this surface was still negatively charge (Table 5.2). During the experiments, it was observed that smaller particles are suspended throughout the solution even after sonication, being easily accessible for the peptide during the one hour incubation. On the other hand, Karmakar particles sediment rapidly, being only the particles on the top readily to interact. When samples were functionalized with APTES, the presence of amine groups sticking out of the particles could facilitate peptide accessibility on the particles and, therefore, this may explain higher values of peptide adsorbed. These results show that physicochemical processes should be taken into account when looking at the interface interactions and, in this case, agitation of the sample during incubation period may be required to study particle-interface interactions. For methyl functionalized surfaces, a higher interaction was expected compared with pristine SiO₂ due to the hydrophobic nature of the peptide and this surface. This binding mechanism (hydrophobic-hydrophobic interactions) was more significant for larger particles (40 μm) due to the higher extent of methylation achieved.

Peptide A7 (AFILPTG)

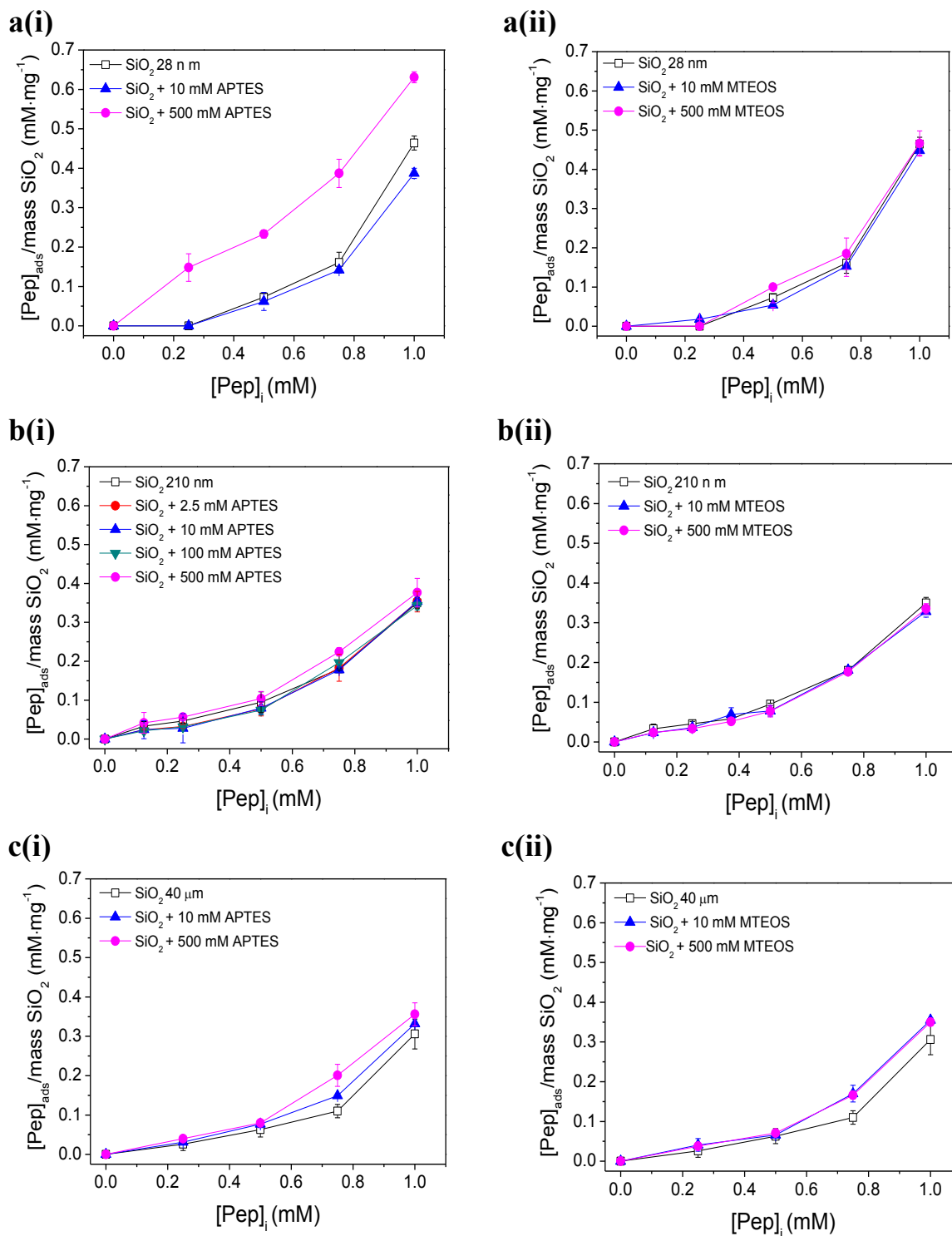


Figure 5.19 Adsorption isotherms of the peptide A7 (AFILPTG) on silica particles of different size (a) 28 nm, (b) 210 nm and (c) 40 μm functionalized with (i) APTES and (ii) MTEOS.

For the negative charged peptide L7, similar behaviour on binding was seen for all three sized silica particles (Figure 5.20). As previously mentioned, this peptide interacts by electrostatic interactions to the 3-amino-propyl surfaces. Level of amino functionalization did affect more significantly the peptide adsorption with decreasing particle size. Although more interaction was expected for higher levels of amine groups on the surface (positively charged surfaces), adsorption isotherms showed the opposite trend, being very significant for the SiO₂-28 nm particles. These results may indicate that for high levels of amino-functionalized surfaces the peptide L7 might interact via the basic amino residues (i.e. histidine) instead of the overall charge of the peptide under experimental conditions. However, a 'switch' on peptide adsorption behaviour towards the highly amino-functionalized surface observed for all three peptides suggested that the peptide binding mechanism may occur through the C-terminus (-COOH group) of the peptide and the surface -NH₃⁺ groups. It should be noted that for smaller particles (28 nm), significant differences of L7 uptake between amino functionalized surfaces and pristine silica was observed at very low initial concentrations whereas for larger particles a threshold concentration was required to observe such differences. For methyl-functionalized surfaces, less affinity was observed due to the more hydrophobic character of the surface. Further, more significant differences on level of functionalization were observed for larger particles, which would support a higher amount of methyl groups on those particles. In general, affinity decreased with increasing hydrophobicity (higher extent of methylation) as expected due to the more hydrophilic character of this peptide (Table 5.3).

From these studies, it was concluded that the extent of functionalization is key for determining peptide affinity and its binding. It is essential to know the chemistry and topography of the solid surface under study to understand their effect on protein adsorption, as it was shown that the interaction with specific peptide sites was not only influenced by the surface functionalities but also by the extent of functionalization of a particular moiety. It was also shown that a wide range of interactions can occur at the silica-peptide interface, such as electrostatic and hydrophobic interactions, hydrogen bonding as well as nucleophile driven reactions. And, further, a 'switch' of peptide adsorption behaviour due to a change on the binding mechanism was demonstrated by increasing level of functionalization on the silica surface.

Peptide L7 (LDHSLHS)

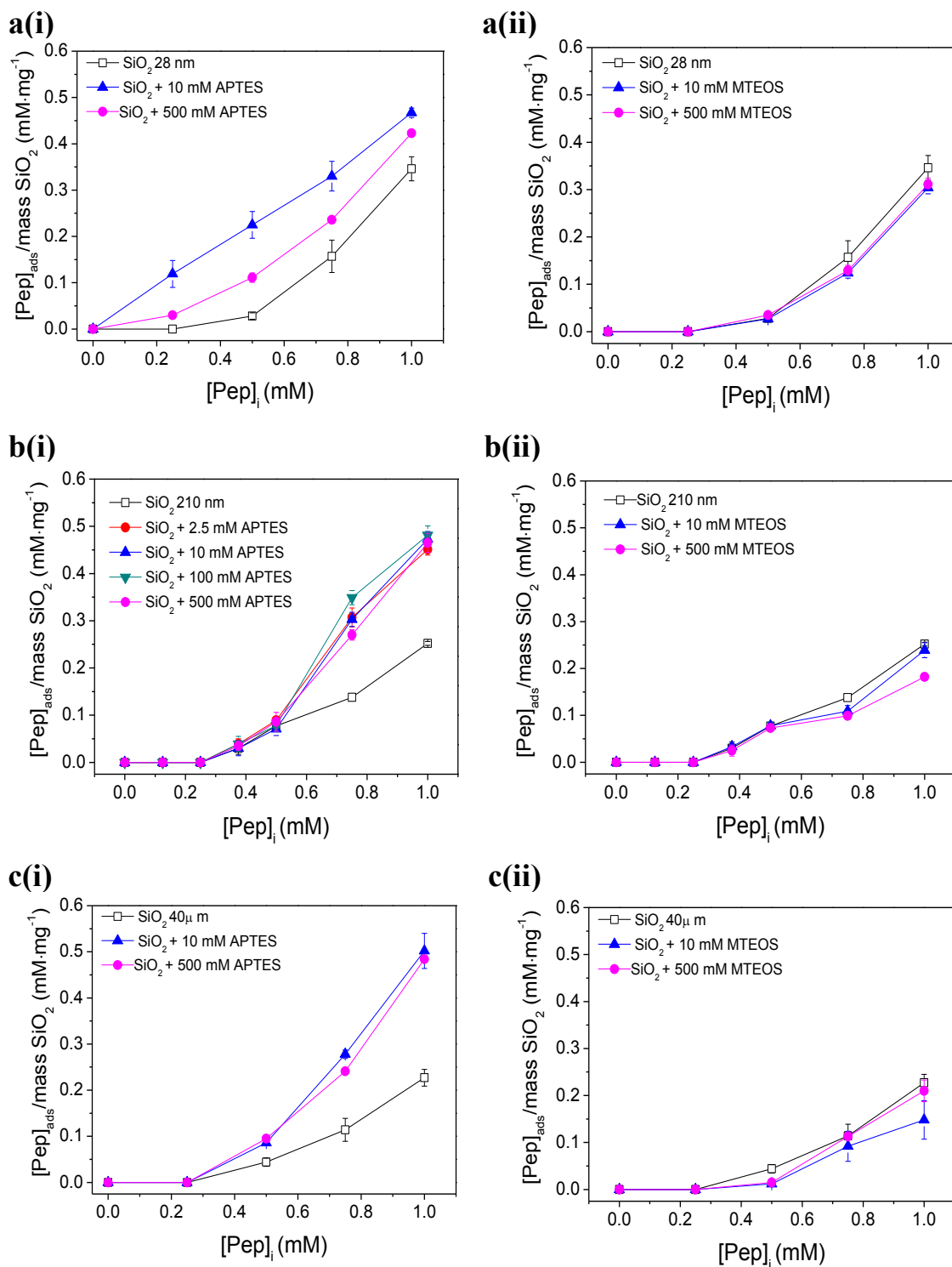


Figure 5.20 Adsorption isotherms of the peptide L7 (LDHSLHS) on silica particles of different size (a) 28 nm, (b) 210 nm and (c) 40 μm functionalized with (i) APTES and (ii) MTEOS.

5.7 Conclusions

The effect of particle size and surface chemistry on peptide binding response was studied; and, a specific emphasis and novel aspect was given to investigate the extent of functionalization on binding. Silica particles synthesised either by the Stöber method (nano-scaled particles) or Karmakar method (micro-scaled particles) showed significant different chemistry properties. Particularly, for the Karmakar silica particles, the presence of acetic acid intercalating through the silica network was proposed and demonstrated by TGA, XPS and FTIR analysis. Level of surface functionalization was shown to be particle-size dependent. It was observed that a higher amount of 3-aminopropyl functionality was achieved for smaller particles, while a higher degree of methyl groups was more likely to be found on larger particles. This different extent of functionalization showed significant differences on the surface properties (i.e. net charge) for the different particle sizes, with positive net charge values in the case of nano-scaled particles when functionalized with high concentrations of APTES, but still a negatively charged surface for the micro sized particles. As peptide binding response depends on the nature/chemistry of the solid surface, remarkable differences were observed at the silica-peptide interface. A higher peptide affinity for larger particles independent on the peptide properties suggested that the binding mechanism significantly depends on the properties of the different sized silica particles. For the non-functionalized surfaces (negatively charged), the peptide affinity was shown to be higher for the positively charged peptide (K7) due to electrostatic interactions. Less but still significant affinity was found for the neutral peptide (A7) and negatively charged peptide (L7) due to hydrophobic-hydrophobic interactions and hydrogen bonding. The presence of functional groups on the silica surface was shown to alter or modify the binding mechanism at the silica-peptide interface. However, interactions with specific peptide sites were shown not to be only influenced by the surface functionalities but also by the extent of functionalization where a 'switch' of peptide adsorption behaviour was demonstrated by increasing levels of functionalization on the silica surface. Therefore, this work provides a better understanding of silica-peptide interactions at the aqueous interface and highlights the importance of knowing the chemistry and topography of the solid surface under study to understand their effect on protein adsorption.

Chapter VI

Conclusions and Future Work

6.1. Conclusions

The investigation presented in this thesis aimed to explore peptide-mineral interactions either during the process of biomineralization (*in vitro* studies) or at the mineral-aqueous interface; with crystalline ZnO and amorphous SiO₂, respectively, being used as examples for the studies. The main objectives were to identify the peptide binding mechanism(s) and, for the *in vitro* studies, their effect on mineral formation.

For ZnO, a study was first conducted where mineral formation (precursors ZnAc₂ and NH₃) via a hydrothermal synthesis method was monitored over time to understand the ZnO crystal growth mechanism for the selected synthesis conditions (**Chapter 3**). Through this hydrothermal method, it was shown that a small change of pH can play an important role on ZnO morphology, with elongated ZnO hexagonal rods being formed at pH 7.1, short ZnO hexagonal rods at pH 7.2 and multi-needle ZnO particles at pH > 8. For further studies, the reaction was conducted at pH 7.0 ± 0.1 to initiate nucleation (reach supersaturation) and to ensure the growth of wurtzite structured ZnO hexagonal rods. Through the characterization of precipitates formed during the reaction process, it was shown that this synthesis route occurs *via* intermediate(s), layered structures that only later transform to the oxide phase. The identities of the solid-phases formed were confirmed by SEM, XRD, ATR, XPS and TGA analysis. The first intermediate identified was LBZA (Layered Basic Zinc Acetate), followed by the formation of LBZAC (Layered Basic Zinc Acetate-Carbonate) where carbonates originated from dissolved CO₂ present in solution (Jang *et al.*, 2010). The observation of ZnO crystals growing out of the layered structures gave further evidence of LBZA being an intermediate of the reaction. Further, the influence of synthesis conditions on product formation, precipitation processes and phase transformation was demonstrated by comparison with another hydrothermal synthesis route using zinc nitrate and HMTA as precursors that are also known to result in the formation of

ZnO hexagonal rods. As demonstrated, depending on the reaction conditions chosen, ZnO growth can take place via dissolution/re-precipitation processes and/or solid-phase transformation. In the $\text{ZnAc}_2\text{-NH}_3$ system, solid-phase transformation from intermediates to ZnO involved a dissolution and re-precipitation process, resulting in an immediate precipitation of LBZA, partial dissolution of LBZAC releasing Zn^{2+} ions back into solution, consequently leading to a re-precipitation process facilitating further growth of ZnO crystals. For the $\text{Zn}(\text{NO}_3)_2\cdot 6\text{H}_2\text{O-HMTA}$ system, no dissolution/re-precipitation process was observed; and growth of ZnO crystals occurred via solid-phase transformation from an intermediate identified as LBZN.

The effect of the peptide EM-12 (identified by phage display) and its mutant EC-12 during ZnO formation was then investigated. A specific aim of the investigation was to explore the effect of increasing the number of potential complexing groups on ZnO formation, for instance, the replacement of methionine (M_5) with cysteine (C_5) in the peptide sequence (**Chapter 4**). Although both peptides affected the crystal formation process, only EC12 was shown to interact with the solid phase(s) formed during the reaction. The presence of EM-12 caused a delay and/or suppression of ZnO formation when increasing the peptide concentration, with LBZA being the major compound present at the highest concentration of EM-12 added. Further, addition of EM-12 not only caused the delayed formation of ZnO (conversion from LBZA to ZnO) but also caused the inhibition of crystal growth (wurtzite structured hexagonal rods) along the c-axis corresponding to the (0002) plane. These results also revealed that the mechanism of ZnO crystallisation occurs by the formation of a first hexagonal rod ($\text{R}_{1\text{st}}$) followed by the growth of a second rod ($\text{R}_{2\text{nd}}$) on the first one, generating symmetrical twinned ZnO crystals (Blanks). This was demonstrated as at increasing EM-12 concentrations, crystal growth equilibrated before/at the end of growth of the first rod ($\text{R}_{1\text{st}}$) where untwinned ZnO crystals having comparable diameters with those observed for the Blanks were obtained. The presence of EC-12; however, caused a more drastic change in the mineral morphology with sphere-like ZnO crystals being formed, and remarkably, no ZnO suppression was observed for the highest EC-12 concentrations added. From experimental data (XPS and ATR), it was shown that EM-12 interacted with Zn^{2+} species in solution, whereas EC-12 could also interact with species in the solid phase(s). The interaction with Zn^{2+} species in solution was suggested to be the

cause of the delay in ZnO formation. Further, from XPS data, the interaction of EC-12 with the solid phase was proposed to be via Zn^{2+} -sulphur (from cysteine). However, the exact solid phase(s) which EC-12 interacted with could not be uniquely identified due to the presence of other solid phases (LBZs) in the samples. The interlayer spacing of LBZA formed in the presence of EC-12 did not change significantly compared with the Blanks which implied that either EC-12 was not intercalated or it was oriented parallel to the zinc hydroxide layer while intercalated. In order to explore this further, the ZnO lattice strain modification was studied. The results showed that the crystal lattice was modified when EC-12 was added into the system suggesting that this peptide may be incorporated into the lattice of ZnO. It was also suggested that the ZnO morphology modification was due to adsorption of EC-12 onto ZnO surface. As Zn^{2+} in the crystal can form bonds with those in the peptide that are stronger than the bonds of solvation; a decrease of the interfacial free energy could occur, allowing for the growth of spherical shape ZnO crystals. A smaller interfacial energy was demonstrated by the smaller crystallite domain sizes obtained for ZnO when increasing the concentration of EC-12 added into the system. This investigation showed that although ZnO crystals are preferentially expressed elongated along the *c*-axis, the presence of additives such as peptides can modulate nucleation and crystal growth processes (i.e. modify the surface energy of the growing facets) to direct ZnO formation and, in some other cases, stabilize the formation of reaction intermediates as is the case of LBZs.

For the studies on silica, the effect of particle size and surface chemistry (i.e. hydroxyl, methyl or amino groups) on peptide binding response was studied; and, a specific emphasis and novel aspect was given to investigate the extent of functionalization on binding (**Chapter 5**). SiO_2 -BPs (silica-binding peptides) previously identified by phage-display (Patwardhan *et al.*, 2012; Puddu and Perry, 2012) were chosen for this study: K7 (KLPGWSG), A7 (AFILPTG) and L7 (LDHSHS), due to their different net charge at the working pH (7.4), being positively, neutral and negatively charged; respectively. Henceforth, peptide affinity with the negatively charged silica surface was expected to decrease as follows $K7 > A7 > L7$. Careful characterization of the particles and levels of surface functionalization was carried out. Silica particles were synthesised either by the Stöber method (nano-scaled particles: 28 and 210 nm) or Karmakar method (micro-scaled

particles: 40 μm), hereafter named Stöber or Karmakar particles, respectively. By increasing the size, particles were less aggregated and more spherical with a smoother surface. As expected, surface area decreased with particle size; however, for SiO_2 -28 nm particles, the determined surface area values deviate more from the theoretical value compared with the SiO_2 -210 nm sample due to the irregular sphere shape observed. For Karmakar particles, particles were found to be non-porous and a very smooth surface was observed. Karmakar particles have been described as highly dense silica microspheres which reported density, 2.10–2.16 g cm^{-3} , similar to that of silica glass (Karmakar *et al.*, 2000). The charge of the silica particles was size-dependent but was also affected by the synthesis method used. During the Stöber synthesis, the higher concentrations of ammonia used in the formation of larger size particles generated higher levels of ionized silanol groups; hence, an increase of the surface ionization with particle size was believed to be by the presence of a higher population of isolated silanol groups (Si-OH) compared to the smaller particles, leading to a higher surface acidity for bigger particles as found in previous studies by Patwardhan *et al.* (2012). For the Karmakar particles, even if particles were the biggest in size, the zeta potential values were less negative than for the SiO_2 -210 nm particles. In this case, a higher ionization of silanol groups was not expected as acetic acid was used during synthesis, thus, it was suggested that the reduced surface area of big particles decreased the number of silanol groups that can be accommodated on the silica surface. However, one of the most remarkable and non-expected findings in this study (not previously reported) was during the characterization of the Karmakar particles. The presence of acetic acid intercalating through the silica network was proposed and demonstrated by TGA, XPS and FTIR analysis. Silica particles were functionalized by using APTES (amine groups) and MTEOS (methyl groups) as this allowed the study of the effect of (positive) electrostatic interactions and hydrophobic interactions with peptides, respectively. Functionalization of the silica particles was first studied by comparison of two methods (i) post modification (or grafting) and (ii) in situ modification (or co-condensation). In situ modification showed a gelation effect for those samples containing APTES, being more pronounced for samples containing a higher fraction of APTES. Previous reported studies have shown that synthesis parameters, such as temperature (applied in Stöber synthesis) or a higher population of $-\text{NH}_2$ groups can give place to an

increase of the aggregation kinetics and, hence, favouring gel formation (Amiri *et al.*, 2011; Colby *et al.*, 1986). Moreover, for amine-functionalized silica particles an increase of the size of the silica particles (compared with the Blank) was observed when adding APTES into the reaction system due to the presence of aminopropyl and alkoxy silane groups quickly induces hydrolysis and condensation of TEOS catalysing the sol-gel process and allowing for the growth of bigger articles (Wang *et al.*, 2012). Henceforth, as different levels of functionalization for a specific particles size were one of the purposes of this investigation, silica functionalization was followed by grafting of the silica particles at room temperature. The extent of surface functionalization was shown to be particle-size dependent. It was observed that a higher amount of 3-aminopropyl functionality was achieved for smaller particles, while a higher degree of methyl groups was more likely to be found on the larger particles. These results also suggested that functionalization occurred independently on the particle surface charge since smaller particles (less negative charged) presented a higher degree of amino-functionalization. Thus, the higher amount of 3-aminopropyl groups found on the surface of the smaller particles was thought to be due to the higher surface area of these particles. This different extent of functionalization showed significant differences on the surface properties (i.e. net charge) for the different particle sizes, positive net charge values being observed in the case of the nanoscale particles functionalized with high concentrations of APTES, but still negatively charged surface for the microscale particles. As peptide binding response depends on the nature/chemistry of the solid surface, remarkable differences due to the net charge were observed at the silica-peptide interface. A higher peptide affinity for larger particles independent of the peptide properties suggested that the binding mechanism significantly depends upon the properties of the different sized silica particles. For the non-functionalized surfaces (negatively charged), the peptide affinity was shown to be higher for the positively charged peptide (K7 \rightarrow KLPGWSG) due to electrostatic interactions. Reduced affinity was found for the neutral peptide (A7 \rightarrow AFILPTG) and negative charged peptide (L7 \rightarrow LDHSLHS) due to hydrophobic-hydrophobic interactions and hydrogen bonding as previously reported by Puddu and Perry (2012). The presence of functional groups on the silica surface was shown to modify the binding affinity and/or mechanism at the silica-peptide interface. In this case, the peptide A7 (neutral) had more affinity for the

more hydrophobic surfaces (i.e. methyl-functionalized) due to its hydrophobic character while the peptide L7 (-) interacted preferentially with the amine-functionalized surface by electrostatic interactions. Besides this, the peptide K7 (+) still preferred pristine SiO₂ (non-functionalized surface) due to higher negative surface charge. As extent of functionalization was shown to be particle-size-dependent, higher or lower affinity of the peptides towards the different sized particles could be correlated with the degree of functionalization. Silica-peptide interactions were shown to be not only influenced by the surface functionalities but also by the extent of functionalization where a ‘switch’ on peptide adsorption behaviour was demonstrated by increasing levels of functionalization on the silica surface. Particularly for the high level of amine-functionalized nano-scaled silica particles, a ‘not expected’ much higher interaction (compared to the pristine SiO₂) with the peptides K7 (+) and A7 (neutral/hydrophobic character) and lower interaction (compared with the low extent of amine functionalized SiO₂) with the peptide L7 (-) since these particles were positively charged and hydrophilic was observed. It was proposed that in this case, peptide binding mechanism may be through the peptide C-terminus (-COO⁻ group) and the surface -NH₃⁺ groups. These findings provide a deeper understanding of silica-peptide interactions at the aqueous interface and highlight the importance of knowing the chemistry and topography of the solid surface under study to understand their effect on peptide adsorption.

The ultimate goal of this thesis was to explore the effect/behaviour of peptides in (bio)mineralising systems and to identify the interactions governing the peptide binding mechanism. This work has contributed to the knowledge on peptide-directed crystal growth modification, the role of specific amino acids on mineral binding and has led to a more comprehensive view of mechanisms concerning mineral-peptide interactions. These results are applicable to the design and development of interfaces with specific adsorption/affinity response for biomedical applications, where uptake is important, such as drug delivery systems. The establishment of unique binding sites may shed light on the understanding of the epitopes involved for example in neural cell recognition or cell adhesion in biological systems. The insights gained from this peptide-mineral study may allow for the design and synthesis of novel (nano)materials with properties tailored for specific applications such as biomineralization of hydroxyapatite/titania composites avoiding implant rejection. Finally,

the studies presented here also led to two publications (listed in section Publications) that have significant contributions to the field.

6.2. Future work

This investigation was able to provide a better understanding of peptide-mineral binding mechanisms. For ZnO, the effect of the peptides (for *in vitro* studies) and possible interactions were proposed; however, these assumptions were largely made by analysis of the surface *ex-situ* (solid phase removed from solution). The complementary use of techniques such as Quartz Crystal Microbalance (QCM) and ITC can provide information about interactions at the biotic-abiotic interface *in situ* giving a better view of processes happening in solution. Since EC-12 was shown to interact with the solid-phase, this thesis focused on studying EC12-ZnO interactions in solution, as performed by ITC, which showed that reaction took place spontaneously. However, further XPS analysis suggested that EC-12 was interacting via a thiol group with the Zn^{2+} species of the solid phase, which could either exist as ZnO or LBZA. Henceforth, a comparative ITC study using LBZA instead ZnO would be of great interest, as it may clarify which specific zinc containing phase the peptide is interacting with. An extensive study may be needed since although ITC is a powerful tool on determining the molecular nature of non-covalent interactions involved in binding (Limo and Perry, 2015), strong interactions such as those showing the thiol group covalently attached to the zinc might be misunderstood from the data obtained. In particular, it has been reported that when more cysteines contribute to Zn^{2+} coordination, the enthalpy of binding becomes less favourable due to deprotonation of Cys while an entropy gain can be observed from the loss of protons (Rich *et al.*, 2012). It would also be interesting to take into account ZnO synthesis conditions such as pH and T as these will strictly affect the protonated species in solution and reaction rates, respectively (Amin *et al.*, 2011; Baruah and Dutta, 2009). The use of buffers to adjust pH should be carefully monitored as any additional salt into the system will affect the isotherm heat changes, thus subtraction of buffer contributions to the calorimetric data should be applied. In the same manner, this technique can be performed for the SiO_2 -peptide studies to characterize thermodynamics of interaction, giving further prove of our findings.

QCM has also been used to determine the affinity of certain molecules (i.e. proteins) to specific surfaces such as metal oxides (Chen *et al.*, 2006) and, can provide further information about monolayer or multilayer formation (Marx, 2003). The main limitation of this technique is that the sensor (provided by the manufacturer) is coated with the surface of interest, thus, interactions can only be studied with the ZnO/SiO₂ surface available by the supplier. Crystalline ZnO with preferred crystal planes can be purchased; however, SiO₂ sensors coated with different particle size and/or surface functionalized are not easily obtained/formed. Besides this, it could be interesting to not only study the silica-peptide interactions (for a determined SiO₂ surface but also to study the level of functionalization that can be achieved and when saturation is reached by, for example, adding APTES onto a silica coated sensor.

Peptide conformation is also key for mineral-peptide interactions. It has been suggested that a higher amount of hydrophobic residues can contribute to the folding of protein structures (Kauzmann, 1959). However, conformation changes will be affected by given solution parameters such as pH (White *et al.*, 2015). Circular dichroism analyses can be used to determine the secondary structure and folding properties of the proteins. Therefore, combining this tool with interactions observed during this investigation may give new insights or better understanding on the binding mechanisms.

For SiO₂ studies, the remarkable ‘switch’ of peptide adsorption behaviour for the different levels of amine-functionalized surfaces was proposed to arise from different binding mechanisms. To confirm the possibility of the peptide interacting at the C-terminus, it might would be desirable to do a comparison study having the peptide with the C-terminus blocked. Several methods can be applied to inactivate the –COOH group of a peptide such as amidation and glycosylphosphatidylinositol (GPI anchor) (Paulick and Bertozzi, 2008). GPI attachment, however, may induce other type of interactions as it will change the hydrophobic/hydrophilic character of the peptide. On the other hand, amidation may reduce the overall charge of the peptide; therefore, its overall solubility may decrease. Henceforth, a deep analysis of the properties of the modified peptides will be required to predict and study the mechanisms concerning silica-peptide interactions.

References

- Ababou, A.; Ladbury, J. E. Survey of the year 2005: literature on applications of isothermal titration calorimetry. *Journal of Molecular Recognition* **2007**, *20*, 4-14.
- Aguado, J.; Arsuaga, J. M.; Arencibia, A.; Lindo, M.; Gascón, V. Aqueous heavy metals removal by adsorption on amine-functionalized mesoporous silica. *J. Hazard. Mater.* **2009**, *163*, 213-221.
- Aisawa, S.; Takahashi, S.; Ogasawara, W.; Umetsu, Y.; Narita, E. Direct intercalation of amino acids into layered double hydroxides by coprecipitation. *Journal of Solid State Chemistry* **2001**, *162*, 52-62.
- Albericio, F.; Kates, S. A. In *Solid-phase synthesis : a practical guide*; Marcel Dekker: New York, 2000; pp 79-91.
- Al-Gaashani, R.; Radiman, S.; Daud, A. R.; Tabet, N.; Al-Douri, Y. XPS and optical studies of different morphologies of ZnO nanostructures prepared by microwave methods. *Ceram. Int.* **2013**, *39*, 2283-2292.
- Amekura, H.; Sakuma, Y.; Yoshitake, M.; Takeda, Y.; Kishimoto, N.; Buchal, C. Defect-band-free luminescence from ZnO nanoparticles fabricated by ion implantation and thermal oxidation. *Nuclear Inst. and Methods in Physics Research, B* **2007**, *257*, 64-67.
- Amin, G.; Asif, M. H.; Zainelabdin, A.; Zaman, S.; Nur, O.; Willander, M. Influence of pH, Precursor Concentration, Growth Time, and Temperature on the Morphology of ZnO Nanostructures Grown by the Hydrothermal Method. *J. Nanomater* **2011**, *2011*, 269-692.
- Amiri, A.; Oye, G.; Sjoblom, J. Temperature and pressure effects on stability and gelation properties of silica suspensions. *Colloids Surf. Physicochem. Eng. Aspects* **2011**, *378*, 14-21.
- An, Y.; Chen, M.; Xue, Q.; Liu, W. Preparation and self-assembly of carboxylic acid-functionalized silica. *J. Colloid Interface Sci.* **2007**, *311*, 507-513.
- Arizaga, G. G. C.; Satyanarayana, K. G.; Wypych, F. Layered hydroxide salts: synthesis, properties and potential applications. *Solid State Ionics* **2007**, *178*, 1143-1162.
- Asenath Smith, E.; Chen, W. How to prevent the loss of surface functionality derived from aminosilanes. *Langmuir* **2008**, *24*, 12405-12409.
- Bae, S. Y.; Seo, H. W.; Park, J. Vertically aligned sulfur-doped ZnO nanowires synthesized via chemical vapor deposition. *The Journal of Physical Chemistry B* **2004**, *108*, 5206-5210.
- Bagwe, R. P.; Hilliard, L. R.; Tan, W. Surface modification of silica nanoparticles to reduce aggregation and nonspecific binding. *Langmuir* **2006**, *22*, 4357-4362.
- Bai, H.; Xu, F.; Anjia, L.; Matsui, H. Low temperature synthesis of ZnO nanowires by using a genetically-modified collagen-like triple helix as a catalytic template. *Soft Matter* **2009**, *5*, 966-969.
- Baier, J.; Naumburg, T.; Blumenstein, N. J.; Jeurgens, L. P. H.; Welzel, U.; Do, T. A.; Pleiss, J.; and Bill, J. Bio-inspired mineralization of zinc oxide in presence of ZnO-binding peptides. **2012**, *2*, 380-291.

- Ballerini, G.; Ogle, K.; Barthés-Labrousse, M. G. The acid–base properties of the surface of native zinc oxide layers: An XPS study of adsorption of 1,2-diaminoethane. *Appl. Surf. Sci.* **2007**, *253*, 6860-6867.
- Barrett, E. P.; Joyner, L. G.; Halenda, P. P. The determination of pore volume and area distributions in porous substances. I. Computations from nitrogen isotherms. *J. Am. Chem. Soc.* **1951**, *73*, 373-380.
- Baruah, S.; Dutta, J. Hydrothermal growth of ZnO nanostructures. *Science and Technology of Advanced Materials* **2009**, *10*, 013001.
- Baruah, S.; Dutta, J. pH-dependent growth of zinc oxide nanorods. *J. Cryst. Growth* **2009**, *311*, 2549-2554.
- Belton, D.; Paine, G.; Patwardhan, S. V.; Perry, C. C. Towards an understanding of (bio) silicification: the role of amino acids and lysine oligomers in silicification. *Journal of Materials Chemistry* **2004**, *14*, 2231-2241.
- Belton, D. J.; Patwardhan, S. V.; Annenkov, V. V.; Danilovtseva, E. N.; Perry, C. C. From biosilicification to tailored materials: optimizing hydrophobic domains and resistance to protonation of polyamines. *Proc. Natl. Acad. Sci. U. S. A.* **2008**, *105*, 5963-5968.
- Bernecker, A.; Ziomkowska, J.; Heitmüller, S.; Wieneke, R.; Geyer, A.; Steinem, C. Formation of Silica Precipitates on Membrane Surfaces in Two and Three Dimensions. *Langmuir* **2010**, *26*, 13422-13428.
- Bertini, I. *Biological inorganic chemistry: structure and reactivity*; University Science Books: Sausalito, California, 2007; .
- Bharali, D. J.; Klejbor, I.; Stachowiak, E. K.; Dutta, P.; Roy, I.; Kaur, N.; Bergey, E. J.; Prasad, P. N.; Stachowiak, M. K. Organically modified silica nanoparticles: a nonviral vector for in vivo gene delivery and expression in the brain. *Proc. Natl. Acad. Sci. U. S. A.* **2005**, *102*, 11539-11544.
- Bhat, H. L. *Introduction to crystal growth principles and practice*; CRC Press: London, 2015; .
- Bragg, W. L. LXII. The crystalline structure of zinc oxide. *Philosophical Magazine Series 6 Philosophical Magazine Series 6* **1920**, *39*, 647-651.
- Brayner, R.; Ferrari-Iliou, R.; Brivois, N.; Djediat, S.; Benedetti, M. F.; Fiévet, F. Toxicological impact studies based on Escherichia coli bacteria in ultrafine ZnO nanoparticles colloidal medium. *Nano Letters* **2006**, *6*, 866-870.
- Brif, A.; Ankonina, G.; Drathen, C.; Pokroy, B. Bio-inspired band gap engineering of zinc oxide by intracrystalline incorporation of amino acids. *Adv. Mater.* **2014**, *26*, 477-81.
- Briggs, D.; Beamson, G. Primary and Secondary Oxygen-Induced C1s Binding-Energy Shifts in X-Ray Photoelectron-Spectroscopy of Polymers. *Anal. Chem.* **1992**, *64*, 1729-1736.
- Brinker, C. J.; Scherer, G. W. *Sol-gel science : the physics and chemistry of sol-gel processing*; Academic Press: London, 1990; .
- Brunauer, S.; Emmett, P. H.; Teller, E. Adsorption of gases in multimolecular layers. *J. Am. Chem. Soc.* **1938**, *60*, 309-319.
- Castner, D. G.; Hinds, K.; Grainger, D. W. X-ray Photoelectron Spectroscopy Sulfur 2p Study of Organic Thiol and Disulfide Binding Interactions with Gold Surfaces. *Langmuir* **1996**, *12*, 5083-5086.

- Cavalleri, O.; Gonella, G.; Terreni, S.; Vignolo, M.; Floreano, L.; Morgante, A.; Canepa, M.; Rolandi, R. High resolution X-ray photoelectron spectroscopy of L-cysteine self-assembled films. *Phys. Chem. Chem. Phys.* **2004**, *6*, 4042-4046.
- Cazes, J.; Ewing, G. W. In *Ewing's analytical instrumentation handbook*. Marcel Dekker: New York, 2005; pp 57-71.
- Cha, J. N.; Shimizu, K.; Zhou, Y.; Christiansen, S. C.; Chmelka, B. F.; Stucky, G. D.; Morse, D. E. Silicatein filaments and subunits from a marine sponge direct the polymerization of silica and silicones in vitro. *Proc. Natl. Acad. Sci. U. S. A.* **1999**, *96*, 361-365.
- Chen, H.; Su, X.; Neoh, K.; Choe, W. QCM-D analysis of binding mechanism of phage particles displaying a constrained heptapeptide with specific affinity to SiO₂ and TiO₂. *Anal. Chem.* **2006**, *78*, 4872-4879.
- Chen, Y.; Bagnall, D.; Koh, H.; Park, K.; Hiraga, K.; Zhu, Z.; Yao, T. Plasma assisted molecular beam epitaxy of ZnO on c-plane sapphire: growth and characterization. *J. Appl. Phys.* **1998**, *84*, 3912-3918.
- Chiad, K.; Stelzig, S. H.; Gropeanu, R.; Weil, T.; Klapper, M.; Muullen, K. Isothermal titration calorimetry: A powerful technique to quantify interactions in polymer hybrid systems. *Macromolecules Macromolecules* **2009**, *42*, 7545-7552.
- Cho, N.; Cheong, T.; Min, J. H.; Wu, J. H.; Lee, S. J.; Kim, D.; Yang, J.; Kim, S.; Kim, Y. K.; Seong, S. A multifunctional core-shell nanoparticle for dendritic cell-based cancer immunotherapy. *Nature nanotechnology* **2011**, *6*, 675-682.
- Cihlár, J. Hydrolysis and polycondensation of ethyl silicates. 1. Effect of pH and catalyst on the hydrolysis and polycondensation of tetraethoxysilane (TEOS). *Colloids Surf. Physicochem. Eng. Aspects* **1993**, *70*, 239-251.
- Clark, D. T.; Peeling, J.; Colling, L. Experimental and Theoretical Investigation of Core Level Spectra of a Series of Amino-Acids, Dipeptides and Polypeptides. *Biochim. Biophys. Acta* **1976**, *453*, 533-545.
- Cliff, M. J.; Gutierrez, A.; Ladbury, J. E. A survey of the year 2003 literature on applications of isothermal titration calorimetry. *Journal of Molecular Recognition* **2004**, *17*, 513-523.
- Colby, M. W.; Osaka, A.; Mackenzie, J. D. Effects of temperature on formation of silica gel. *J. Non Cryst. Solids* **1986**, *82*, 37-41.
- Cölfen, H.; Mann, S. Higher-order organization by mesoscale self-assembly and transformation of hybrid nanostructures. *Angewandte Chemie International Edition* **2003**, *42*, 2350-2365.
- Collins, J. M.; Lambert, J. J.; Collins, M. J. US7550560 B2, 2009.
- Coradin, T.; Livage, J. Aqueous silicates in biological sol-gel applications: New perspectives for old precursors. *Acc. Chem. Res.* **2007**, *40*, 819-826.
- Coradin, T.; Livage, J. Effect of some amino acids and peptides on silicic acid polymerization. *Colloids and Surfaces B: Biointerfaces* **2001**, *21*, 329-336.
- Cox, S. J.; Raza, Z.; Kathmann, S. M.; Slater, B.; Michaelides, A. The microscopic features of heterogeneous ice nucleation may affect the macroscopic morphology of atmospheric ice crystals. *Faraday Discuss.* **2013**, *167*, 389-403.

- Crenshaw, M. In *Mechanisms of normal biological mineralization of calcium carbonates*; Biological mineralization and demineralization; Springer: Berlin Heidelberg, 1982; pp 243-257.
- Cui, Q.; Yu, K.; Zhang, N.; Zhu, Z. Porous ZnO nanobelts evolved from layered basic zinc acetate nanobelts. *Appl. Surf. Sci.* **2008**, *254*, 3517-3521.
- Das, I.; Mishra, M. K.; Medda, S. K.; De, G. Durable superhydrophobic ZnO–SiO₂ films: a new approach to enhance the abrasion resistant property of trimethylsilyl functionalized SiO₂ nanoparticles on glass. *RSC Advances* **2014**, *4*, 54989-54997.
- Davis, M. E. Ordered porous materials for emerging applications. *Nature* **2002**, *417*, 813-821.
- Davydov, V. Y.; Kiselev, A.; Zhuravlev, L. Study of the surface and bulk hydroxyl groups of silica by infrared spectra and D₂O-exchange. *Transactions of the Faraday Society* **1964**, *60*, 2254-2264.
- De Jong, W. H.; Borm, P. J. Drug delivery and nanoparticles: applications and hazards. *Int. J. Nanomedicine* **2008**, *3*, 133-149.
- De La Rica, R.; Matsui, H. Urease as a nanoreactor for growing crystalline ZnO nanoshells at room temperature. *Angewandte Chemie International Edition* **2008**, *47*, 5415-5417.
- De, G.; Karmakar, B.; Ganguli, D. Hydrolysis–condensation reactions of TEOS in the presence of acetic acid leading to the generation of glass-like silica microspheres in solution at room temperature. *Journal of Materials Chemistry* **2000**, *10*, 2289-2293.
- deBoer, J. H. *The structure and properties of porous materials*; Butterworths: London, UK, 1958; .
- Deroubaix, G.; Marcus, P. X-Ray Photoelectron-Spectroscopy Analysis of Copper and Zinc-Oxides and Sulfides. *Surf. Interface Anal.* **1992**, *18*, 39-46.
- Devallencourt, C.; Saiter, J.; Fafet, A.; Ubrich, E. Thermogravimetry/Fourier transform infrared coupling investigations to study the thermal stability of melamine formaldehyde resin. *Thermochimica acta* **1995**, *259*, 143-151.
- Dickerson, M. B.; Sandhage, K. H.; Naik, R. R. Protein- and Peptide-Directed Syntheses of Inorganic Materials. *Chem. Rev.* **2008**, *108*, 4935-4978.
- Digigow, R. G.; Dechézelles, J.; Dietsch, H.; Geissbühler, I.; Vanhecke, D.; Geers, C.; Hirt, A. M.; Rothen-Rutishauser, B.; Petri-Fink, A. Preparation and characterization of functional silica hybrid magnetic nanoparticles. *J Magn Magn Mater* **2014**, *362*, 72-79.
- Djurišić, A. B.; Chen, X.; Leung, Y. H.; Ng, A. M. C. ZnO nanostructures: growth, properties and applications. *Journal of Materials Chemistry* **2012**, *22*, 6526-6535.
- Dodero, G.; De Michieli, L.; Cavalleri, O.; Rolandi, R.; Oliveri, L.; Dacca, A.; Parodi, R. L-cysteine chemisorption on gold: an XPS and STM study. *Colloids Surf. , A* **2000**, *175*, 121-128.
- Dove, P. M.; Yoreo, J. J.; Weiner, S., Eds.; In *Biomineralisation: Reviews in Mineralogy and Geochemistry*; Mineralogical Society of America and the Geochemical Society: Washington D.C., 2003; Vol. 54, pp 381.
- Ek, S.; Root, A.; Peussa, M.; Niinistö, L. Determination of the hydroxyl group content in silica by thermogravimetry and a comparison with ¹H MAS NMR results. *Thermochimica acta* **2001**, *379*, 201-212.

- Ellmer, K.; Klein, A.; Rech, B., Eds.; In *Transparent conductive zinc oxide basics and applications in thin film solar cells*; Springer: Berlin, 2008; .
- Emami, F. S.; Puddu, V.; Berry, R. J.; Varshney, V.; Patwardhan, S. V.; Perry, C. C.; Heinz, H. Force Field and a Surface Model Database for Silica to Simulate Interfacial Properties in Atomic Resolution. *Chemistry of Materials* **2014**, *26*, 2647-2658.
- Erdemir, D.; Lee, A. Y.; Myerson, A. S. Nucleation of crystals from solution: classical and two-step models. *Acc. Chem. Res.* **2009**, *42*, 621-629.
- Eteshola, E.; Brillson, L. J.; Lee, S. C. Selection and characteristics of peptides that bind thermally grown silicon dioxide films. *Biomol. Eng.* **2005**, *22*, 201-204.
- Fairley, N. *CasaXPS Manual 2.3.15*; Casa Software Ltd.: [S.l.], 2009; .
- Freire, E.; Mayorga, O. L.; Straume, M. Isothermal titration calorimetry. *Anal.Chem.Analytical Chemistry* **1990**, *62*, 950A-959A.
- Freyer, M. W.; Lewis, E. A. Isothermal titration calorimetry: experimental design, data analysis, and probing macromolecule/ligand binding and kinetic interactions. *Methods Cell Biol.* **2008**, *84*, 79-113.
- Funk, G. M.; Hunt, C. E.; Epps, D. E.; Brown, P. K. Use of a rapid and highly sensitive fluorescamine-based procedure for the assay of plasma lipoproteins. *J. Lipid Res.* **1986**, *27*, 792-795.
- Gao, Y. K.; Traeger, F.; Shekhah, O.; Idriss, H.; Woell, C. Probing the interaction of the amino acid alanine with the surface of ZnO(10-10). *J. Colloid Interface Sci.* **2009**, *338*, 16-21.
- Gardener, M.; Perry, C. C. Novel thermochromism in silica sol-gel materials. *Sol-Gel Optics V* **2000**, *3943*, 249-257.
- Gerstel, P.; Lipowsky, P.; Durupthy, O.; Hoffmann, R. C.; Bellina, P.; Bill, J.; Aldinger, F. Deposition of zinc oxide and layered basic zinc salts from aqueous solutions containing amino acids and dipeptides. *J. Ceram. Soc. Jpn.* **2006**, *114*, 911-917.
- Gibbs, J. W. On the equilibrium of heterogeneous substances. *Am. J. Sci.* **1878**, 441-458.
- Girelli, A. M.; Mattei, E. Application of immobilized enzyme reactor in on-line high performance liquid chromatography: a review. *Journal of Chromatography B* **2005**, *819*, 3-16.
- Goldstein, J. *Scanning electron microscopy and X-ray microanalysis : a text for biologists, materials scientists, and geologists*; Plenum Press: New York, 1981; .
- Goldstein, J. I. *Scanning electron microscopy and X-ray microanalysis*; Springer: New York, N.Y., 2003; .
- Golec, P.; Karczewska-Golec, J.; Łoś, M.; Węgrzyn, G. Novel ZnO-binding peptides obtained by the screening of a phage display peptide library. *Journal of Nanoparticle Research* **2012**, *14*, 1-6.
- Golec, P.; Karczewska-Golec, J.; Łoś, M.; Węgrzyn, G. Novel ZnO-binding peptides obtained by the screening of a phage display peptide library. *J. Nanopart. Res.* **2012**, *14*, 1-6.

- Golić, D. L.; Branković, G.; Nešić, M. P.; Vojisavljević, K.; Rečnik, A.; Daneu, N.; Bernik, S.; Šćepanović, M.; Poleti, D.; Branković, Z. Structural characterization of self-assembled ZnO nanoparticles obtained by the sol-gel method from Zn (CH₃COO) 2· 2H₂O. *Nanotechnology* **2011**, *22*, 395603.
- Goormaghtigh, E.; Cabiaux, V.; Ruyschaert, J. Secondary structure and dosage of soluble and membrane proteins by attenuated total reflection Fourier-transform infrared spectroscopy on hydrated films. *European Journal of Biochemistry* **1990**, *193*, 409-420.
- Govender, K.; Boyle, D. S.; Kenway, P. B.; O'Brien, P. Understanding the factors that govern the deposition and morphology of thin films of ZnO from aqueous solution. *Journal of Materials Chemistry* **2004**, *14*, 2575-2591.
- Gray, J. J. The interaction of proteins with solid surfaces. *Curr. Opin. Struct. Biol.* **2004**, *14*, 110-115.
- Guan, K. L.; Dixon, J. E. Evidence for Protein-Tyrosine-Phosphatase Catalysis Proceeding Via a Cysteine-Phosphate Intermediate. *J. Biol. Chem.* **1991**, *266*, 17026-17030.
- Guzzo, A. V. The Influence of Amino Acid Sequence on Protein Structure. *Biophysical Journal* **1965**, *5*, 809.
- Hamada, T.; Fujii, E.; Chu, D.; Kato, K.; Masuda, Y. Aqueous synthesis of single-crystalline ZnO prisms on graphite substrates. *J. Cryst. Growth* **2011**, *314*, 180-184.
- Harding, V. J.; Warneford, F. H. S. *The ninhydrin reaction with amino-acids and ammonium salts*. Montreal, 1916; .
- Held, P. Fluorimetric Quantitation of Protein using the Reactive Compound Fluorescamine. *Nature Methods/ Application Notes* **2006**.
- Hickman, G. J.; Boocock, D.; Pockley, G.; Perry, C. C. The importance and clinical relevance of surfaces in tissue culture. *ACS Biomater.Sci.Eng.ACS Biomaterials Science & Engineering* **2015**.
- Hickman, G. J.; Rai, A.; Boocock, D. J.; Rees, R. C.; Perry, C. C. Fabrication, characterisation and performance of hydrophilic and super-hydrophilic silica as cell culture surfaces. *Journal of Materials Chemistry* **2012**, *22*, 12141-12148.
- Hofmann, S. *Auger- and x-ray photoelectron spectroscopy in materials science: a user-oriented guide*; Springer: Berlin; Heidelberg, 2013; .
- Hosono E; Fujihara S; Kimura T; Imai H Growth of layered basic zinc acetate in methanolic solutions and its pyrolytic transformation into porous zinc oxide films. *J. Colloid Interface Sci.* **2004**, *272*, 391-8.
- Hosono, E.; Fujihara, S.; Kimura, T.; Imai, H. Growth of layered basic zinc acetate in methanolic solutions and its pyrolytic transformation into porous zinc oxide films. *J. Colloid Interface Sci.* **2004**, *272*, 391-8.
- Hu, H.; Huang, X.; Deng, C.; Chen, X.; Qian, Y. Hydrothermal synthesis of ZnO nanowires and nanobelts on a large scale. *Mater. Chem. Phys.* **2007**, *106*, 58-62.
- Huang, C.; Li, C.; Wang, H.; Lin, T. Effects of formic acid on the chemical state and morphology of as-synthesized and annealed ZnO films. *World Acad. Sci. Eng. Technol.* **2010**, *41*, 266-270.
- Huang, Z.; Yan, D.; Yang, M.; Liao, X.; Kang, Y.; Yin, G.; Yao, Y.; Hao, B. Preparation and characterization of the biomaterialized zinc oxide particles in spider silk peptides. *J. Colloid Interface Sci.* **2008**, *325*, 356-362.

- Huang, J. X.; Bishop-Hurley, S. L.; Cooper, M. A. Development of anti-infectives using phage display: biological agents against bacteria, viruses, and parasites. *Antimicrob. Agents Chemother.* **2012**, *56*, 4569-4582.
- Hüsing, N.; Schubert, U.; Mezei, R.; Fratzl, P.; Riegel, B.; Kiefer, W.; Kohler, D.; Mader, W. Formation and Structure of Gel Networks from Si (OEt)₄/(MeO)₃Si (CH₂)₃NR'₂ Mixtures (NR'₂= NH₂ or NHCH₂CH₂NH₂). *Chemistry of materials* **1999**, *11*, 451-457.
- Hutson, A. Piezoelectricity and Conductivity in ZnO and CdS. *Phys. Rev. Lett. Physical Review Letters* **1960**, *4*, 505-507.
- Iler, R. K. *The chemistry of silica : solubility, polymerization, colloid and surface properties, and biochemistry*; Wiley: New York, 1979; .
- Inoue, S.; Fujihara, S. Liquid-Liquid Biphasic Synthesis of Layered Zinc Hydroxides Intercalated with Long-Chain Carboxylate Ions and Their Conversion into ZnO Nanostructures. *Inorg. Chem.* **2011**, *50*, 3605-3612.
- Izutsu, H.; Mizukami, F.; Nair, P. K.; Kiyozumi, Y.; Maeda, K. Preparation and characterization of porous silica spheres by the sol-gel method in the presence of tartaric acid. *J.Mater.Chem.* **1997**, *7*, 767-771.
- Jang, E.; Won, J.; Kim, Y.; Cheng, Z.; Choy, J. Dynamic transition between Zn-HDS and ZnO; growth and dissolving mechanism of dumbbell-like ZnO bipod crystal. *CrystEngComm* **2011**, *13*, 546-552.
- Jang, J. S.; Yu, C.; Choi, S. H.; Ji, S. M.; Kim, E. S.; Lee, J. S. Topotactic synthesis of mesoporous ZnS and ZnO nanoplates and their photocatalytic activity. *Journal of Catalysis* **2008**, *254*, 144-155.
- Jang, E.; Won, J.; Kim, Y.; Cheng, Z.; Choy, J. Synthesis of porous and nonporous ZnO nanobelt, multipod, and hierarchical nanostructure from Zn-HDS. *J. Solid State Chem.* **2010**, *183*, 1835-1840.
- Janin, J. Surface and inside volumes in globular proteins. **1979**.
- Jaroniec, C. P.; Gilpin, R. K.; Jaroniec, M. Adsorption and Thermogravimetric Studies of Silica-Based Amide Bonded Phases. *J Phys Chem B* **1997**, *101*, 6861-6866.
- Jin, T.; Sun, D.; Su, J.; Zhang, H.; Sue, H. Antimicrobial Efficacy of Zinc Oxide Quantum Dots against *Listeria monocytogenes*, *Salmonella Enteritidis*, and *Escherichia coli* O157:H7. *J. Food Sci.* **2009**, *74*, M46-M52.
- Jing, L.; Wang, D.; Wang, B.; Li, S.; Xin, B.; Fu, H.; Sun, J. Effects of noble metal modification on surface oxygen composition, charge separation and photocatalytic activity of ZnO nanoparticles. *Journal of Molecular Catalysis A-Chemical* **2006**, *244*, 193-200.
- Jitianu, M.; Goia, D. V. Zinc oxide colloids with controlled size, shape, and structure. *J. Colloid Interface Sci.* **2007**, *309*, 78-85.
- Jung, H.; Moon, D.; Lee, J. Quantitative analysis and efficient surface modification of silica nanoparticles. *Journal of Nanomaterials* **2012**, *2012*, 48.
- Karmakar, B.; De, G.; Ganguli, D. Dense silica microspheres from organic and inorganic acid hydrolysis of TEOS. *J. Non Cryst. Solids* **2000**, *272*, 119-126.
- Kasai, A.; Fujihara, S. Layered single-metal hydroxide/ethylene glycol as a new class of hybrid material. *Inorg. Chem.* **2006**, *45*, 415-418.

- Katlyar, A.; Ji, L.; Smirniotis, P.; Pinto, N. G. Protein adsorption on the mesoporous molecular sieve silicate SBA-15: effects of pH and pore size. *Journal of chromatography A* **2005**, *1069*, 119-126.
- Kauzmann, W. Some factors in the interpretation of protein denaturation. *Adv. Protein Chem.* **1959**, *14*, 1.
- Kawaguchi, T.; Ono, K. Spherical silica gels precipitated from acid catalyzed TEOS solutions. *J. Non Cryst. Solids* **1990**, *121*, 383-388.
- Khatri, V.; Halász, K.; Trandafilović, L. V.; Dimitrijević-Branković, S.; Mohanty, P.; Djoković, V.; Csóka, L. ZnO-modified cellulose fiber sheets for antibody immobilization. *Carbohydr. Polym.* **2014**, *109*, 139-147.
- Kimitsuka, Y.; Hosono, E.; Ueno, S.; Zhou, H.; Fujihara, S. Fabrication of Porous Cubic Architecture of ZnO Using Zn-terephthalate MOFs with Characteristic Microstructures. *Inorg. Chem.* **2013**, *52*, 14028-14033.
- Kirkland, J.; Truszkowski, F.; Dilks, C.; Engel, G. Superficially porous silica microspheres for fast high-performance liquid chromatography of macromolecules. *Journal of Chromatography A* **2000**, *890*, 3-13.
- Klingshirn, C. ZnO: Material, physics and applications. *Chem. Phys. Chem* **2007**, *8*, 782-803.
- Klug, H. P.; Alexander, L. E. *X-ray diffraction procedures for polycrystalline and amorphous materials*; John Wiley: New York, 1974; .
- Knecht, M. R.; Wright, D. W. Functional analysis of the biomimetic silica precipitating activity of the R5 peptide from *Cylindrotheca fusiformis*. *Chemical Communications* **2003**, 3038-3039.
- Koleva, V.; Stoilova, D. Infrared and Raman studies of the solids in the Mg(CH₃COO)(2)-Zn(CH₃COO)(2)-H₂O system. *J. Mol. Struct.* **2002**, *611*, 1-8.
- Kong, Y.; Zhong, Y.; Shen, X.; Cui, S.; Yang, M.; Teng, K.; Zhang, J. Facile synthesis of resorcinol-formaldehyde/silica composite aerogels and their transformation to monolithic carbon/silica and carbon/silicon carbide composite aerogels. *J. Non Cryst. Solids* **2012**, *358*, 3150-3155.
- Kong, J.; Yu, S. Fourier transform infrared spectroscopic analysis of protein secondary structures. *Acta Biochim. Biophys. Sin. (Shanghai)* **2007**, *39*, 549-559.
- Kroger, N.; Deutzmann, R.; Bergsdorf, C.; Sumper, M. Species-specific polyamines from diatoms control silica morphology. *Proc. Natl. Acad. Sci. U. S. A.* **2000**, *97*, 14133-14138.
- Kroger, N.; Deutzmann, R.; Sumper, M. Polycationic peptides from diatom biosilica that direct silica nanosphere formation. *Science* **1999**, *286*, 1129-1132.
- Kroger, N.; Lorenz, S.; Brunner, E.; Sumper, M. Self-assembly of highly phosphorylated silaffins and their function in biosilica morphogenesis. *Science* **2002**, *298*, 584-586.
- Krunk, M.; Mellikov, E. Zinc oxide thin films by the spray pyrolysis method. *Thin Solid Films* **1995**, *270*, 33-36.
- Kumar, N.; Mittal, H.; Reddy, L.; Nair, P.; Ngila, J. C.; Parashar, V. Morphogenesis of ZnO nanostructures: role of acetate (COOH⁻) and nitrate (NO₃⁻) ligand donors from zinc salt precursors in synthesis and morphology dependent photocatalytic properties. *RA RSC Advances* **2015**, *5*, 38801-38809.

- Kupiec, T. Quality-control analytical methods: High-performance liquid chromatography. *International journal of pharmaceutical compounding* **2004**, *8*, 223-227.
- Lagashetty, A.; Havanoor, V.; Basavaraja, S.; Balaji, S.; Venkataraman, A. Microwave-assisted route for synthesis of nanosized metal oxides. *Science and Technology of Advanced Materials* **2007**, *8*, 484-493.
- Lakowicz, J. R. *Principles of fluorescence spectroscopy*; Springer Science & Business Media: New York, 2013; .
- Lee, W.; Jeong, M.; Myoung, J. Catalyst-free growth of ZnO nanowires by metal-organic chemical vapour deposition (MOCVD) and thermal evaporation. *Acta Materialia* **2004**, *52*, 3949-3957.
- Li, J.; McLandsborough, L. The effects of the surface charge and hydrophobicity of Escherichia coli on its adhesion to beef muscle. *Int. J. Food Microbiol.* **1999**, *53*, 185-193.
- Li, S. Y.; Ma, W.; Zhou, Y.; Chen, X.; Ma, M.; Xu, Y.; Ding, Z.; Wu, X. 3-aminopropyltriethoxysilanes modified porous silicon as a voltammetric sensor for determination of Silver ion. *Int.J.Electrochem.Sci* **2013**, *8*, 1802-1812.
- Li, W.; Shi, E.; Zhong, W.; Yin, Z. Growth mechanism and growth habit of oxide crystals. *J. Cryst. Growth* **1999**, *203*, 186-196.
- Lian, J.; Ding, Z.; Kwong, F.; Ng, D. H. Template-free hydrothermal synthesis of hexagonal ZnO micro-cups and micro-rings assembled by nanoparticles. *CrystEngComm* **2011**, *13*, 4820-4822.
- Liang, M. Study of peptide-mineral interactions, Nottingham Trent University, Nottingham, 2010.
- Liang, M.; Deschaume, O.; Patwardhan, S. V.; Perry, C. C. Direct evidence of ZnO morphology modification via the selective adsorption of ZnO-binding peptides. *J. Mater. Chem.* **2011**, *21*, 80-89.
- Liang, M.; Limo, M. J.; Sola-Rabada, A.; Roe, M. J.; Perry, C. C. New insights into the mechanism of ZnO formation from aqueous solutions of zinc acetate and zinc nitrate. *Chem. Mater.* **2014**, *26*, 4119-4129.
- Lim, J.; Kang, C.; Kim, K.; Park, I.; Hwang, D.; Park, S. UV electroluminescence emission from ZnO light-emitting diodes grown by high-temperature radiofrequency sputtering. *Adv Mater* **2006**, *18*, 2720-2724.
- Limo, M. J.; Ramasamy, R.; Perry, C. C. ZnO Binding Peptides: Smart Versatile Tools for Controlled Modification of ZnO Growth Mechanism and Morphology. *Chem.Mater.Chemistry of Materials* **2015**, *27*, 1950-1960.
- Limo, M. J. The study of peptide inorganic interactions, Nottingham Trent University, Nottingham, 2014.
- Limo, M. J.; Perry, C. C. Thermodynamic Study of Interactions between ZnO and ZnO Binding Peptides Using Isothermal Titration Calorimetry. *Langmuir* **2015**.
- Limo, M. J.; Perry, C. C.; Thyparambil, A. A.; Wei, Y.; Latour, R. A. In *Experimental Characterization of Peptide-Surface Interactions*; Knecht, M. R., Walsh, T. R., Eds.; Bio-inspired nanotechnology : from surface analysis to applications; 2014; pp 37-94.
- Liu, B.; Zeng, H. C. Room temperature solution synthesis of monodispersed single-crystalline ZnO nanorods and derived hierarchical nanostructures. *Langmuir* **2004**, *20*, 4196-4204.

- Liu, B.; Zeng, H. C. Hydrothermal synthesis of ZnO nanorods in the diameter regime of 50 nm. *J. Am. Chem. Soc.* **2003**, *125*, 4430-4431.
- Lofgreen, J. E.; Ozin, G. A. Controlling morphology and porosity to improve performance of molecularly imprinted sol-gel silica. *Chem. Soc. Rev.* **2014**, *43*, 911-933.
- Lofgren, P.; Krozer, A.; Lausmaa, J.; Kasemo, B. Glycine on Pt(111): A TDS and XPS study. *Surf. Sci.* **1997**, *370*, 277-292.
- Lopez, P. J.; Gautier, C.; Livage, J.; Coradin, T. Mimicking biogenic silica nanostructures formation. *Current Nanoscience* **2005**, *1*, 73-83.
- Lovingood, D. D.; Owens, J. R.; Seeber, M.; Kornev, K. G.; Luzinov, I. Preparation of Silica Nanoparticles Through Microwave-assisted Acid-catalysis. *JoVE (Journal of Visualized Experiments)* **2013**, e51022-e51022.
- Lowenstam, H. A.; Weiner, S. *On Biomineralisation*; Oxford University Press: Oxford, 1989; .
- Lu, C.; Yeh, C. Influence of hydrothermal conditions on the morphology and particle size of zinc oxide powder. *Ceram. Int.* **2000**, *26*, 351-357.
- Luechinger, M.; Prins, R.; Pirngruber, G. D. Functionalization of silica surfaces with mixtures of 3-aminopropyl and methyl groups. *Microporous and mesoporous materials* **2005**, *85*, 111-118.
- Madelung, O.; Rössler, U.; Schulz, M. *Semiconductors*; Springer: Berlin; New York, 1998; .
- Malvern Instruments Ltd., Ed.; In *Zetasizer Nano Series User Manual*; Malvern Instruments Ltd.: Worcestershire, 2004; .
- Mann, S. *Biomimetic materials chemistry*; Wiley: New York, 1998; .
- Marx, K. A. Quartz crystal microbalance: a useful tool for studying thin polymer films and complex biomolecular systems at the solution-surface interface. *Biomacromolecules* **2003**, *4*, 1099-1120.
- Masuda, Y.; Kinoshita, N.; Koumoto, K. Morphology control of ZnO crystalline particles in aqueous solution. *Electrochim. Acta* **2007**, *53*, 171-174.
- Matijevic, E. Preparation and properties of uniform size colloids. *Chemistry of materials* **1993**, *5*, 412-426.
- Max, J.; Chapados, C. Infrared spectroscopy of aqueous carboxylic acids: Comparison between different acids and their salts. *The Journal of Physical Chemistry A* **2004**, *108*, 3324-3337.
- McBride, R. A.; Kelly, J. M.; McCormack, D. E. Growth of well-defined ZnO microparticles by hydroxide ion hydrolysis of zinc salts. *Journal of Materials Chemistry* **2003**, *13*, 1196-1201.
- McPeak, K. M.; Le, T. P.; Britton, N. G.; Nickolov, Z. S.; Elabd, Y. A.; Baxter, J. B. Chemical bath deposition of ZnO nanowires at near-neutral pH conditions without hexamethylenetetramine (HMTA): understanding the role of HMTA in ZnO nanowire growth. *Langmuir* **2011**, *27*, 3672-3677.
- Merrifield, R. B. Solid phase peptide synthesis. I. The synthesis of a tetrapeptide. *J. Am. Chem. Soc.* **1963**, *85*, 2149-2154.

- Milea, C.; Bogatu, C.; Duta, A. The influence of parameters in silica sol-gel process. *Bulletin of The Transilvania University of Brasov* **2011**, *4*, 53.
- Milev, S. Isothermal titration calorimetry: Principles and experimental design. *General Electric* **2013**, *9*.
- Minegishi, K.; Koiwai, Y.; Kikuchi, Y.; Yano, K.; Kasuga, M.; Shimizu, A. Growth of p-type zinc oxide films by chemical vapor deposition. *Japanese Journal of Applied Physics* **1997**, *36*, L1453.
- Moon, C. H.; Tousi, M.; Cheeney, J.; Ngo-Duc, T. T.; Zuo, Z.; Liu, J.; Haberer, E. D. Effects of 8-mer acidic peptide concentration on the morphology and photoluminescence of synthesized ZnO nanomaterials. *Applied Physics a Materials Science and Processing* **2015**, *121*, 757-763.
- Morioka, H.; Tagaya, H.; Kadokawa, J.; Chiba, K. Studies on layered basic zinc acetate. *J. Mater. Sci. Lett.* **1999**, *18*, 995-998.
- Moulder, J. F.; Stickle, W. F.; Sobol, P. E.; and Bomben, K. D., Eds.; In *Handbook of X-Ray Photoelectron Spectroscopy*; Perkin-Elmer Corporation (Physical Electronics): 1992; .
- Muthukumar, M. Theory of competitive adsorption-nucleation in polypeptide-mediated biomineralization. *J. Chem. Phys.* **2009**, *130*, 161101.
- Muthukumar, M. Theory of competitive adsorption-nucleation in polypeptide-mediated biomineralization. *J. Chem. Phys.* **2009**, *130*, 161101.
- Naik, R. R.; Brott, L. L.; Clarkson, S. J.; Stone, M. O. Silica-precipitating peptides isolated from a combinatorial phage display peptide library. *Journal of nanoscience and nanotechnology* **2002**, *2*, 95-100.
- Naik, R. R.; Jones, S. E.; Murray, C. J.; McAuliffe, J. C.; Vaia, R. A.; Stone, M. O. Peptide templates for nanoparticle synthesis derived from polymerase chain reaction-driven phage display. *Advanced Functional Materials* **2004**, *14*, 25-30.
- Nakamoto, K. *Infrared and Raman Spectra of Inorganic and Coordination Compounds*; Infrared and Raman Spectra of Inorganic and Coordination Compounds; John Wiley & Sons Inc: New York, 1986; .
- Nara, M.; Torii, H.; Tasumi, M. Correlation between the vibrational frequencies of the carboxylate group and the types of its coordination to a metal ion: An ab initio molecular orbital study. *J. Phys. Chem.* **1996**, *100*, 19812-19817.
- Natte, K. Synthesis of novel polymeric hybrid nanoparticles with enhanced interfacial and colloidal properties for biomedical studies. **2013**.
- Nesbitt, H.; Bancroft, G.; Pratt, A.; Scaini, M. Sulfur and iron surface states on fractured pyrite surfaces. *Am. Mineral.* **1998**, *83*, 1067-1076.
- Newman, S. P.; Jones, W. Comparative study of some layered hydroxide salts containing exchangeable interlayer anions. *Journal of Solid State Chemistry* **1999**, *148*, 26-40.
- Nicklin, M.; Rees, R. C.; Pockley, A. G.; Perry, C. C. Development of an hydrophobic fluoro-silica surface for studying homotypic cancer cell aggregation–disaggregation as a single dynamic process in vitro. *Biomaterials Science* **2014**, *2*, 1486-1496.

- Nie, X.; Wei, S.; Zhang, S. Bipolar doping and band-gap anomalies in delafossite transparent conductive oxides. *Phys. Rev. Lett.* **2002**, *88*, 066405.
- Nohynek, G. J.; Lademann, J.; Ribaud, C.; Roberts, M. S. Grey goo on the skin? Nanotechnology, cosmetic and sunscreen safety. *Crit. Rev. Toxicol.* **2007**, *37*, 251-277.
- Nudelman, F.; Sommerdijk, N. A. Biomineralization as an inspiration for materials chemistry. *Angewandte Chemie International Edition* **2012**, *51*, 6582-6596.
- Ogata, S.; Miyazaki, I.; Tasaka, Y.; Tagaya, H.; Kadokawa, J.; Chiba, K. Preparation method for organic-inorganic layered compounds including fibrous materials by the reaction of Zn(OH)(2) with organic compounds. *Journal of Materials Chemistry* **1998**, *8*, 2813-2817.
- Ohya, Y.; Saiki, H.; Takahashi, Y. Preparation of transparent, electrically conducting ZnO film from zinc acetate and alkoxide. *J. Mater. Sci.* **1994**, *29*, 4099-4103.
- Okochi, M.; Sugita, T.; Furusawa, S.; Umetsu, M.; Adschiri, T.; Honda, H. Peptide Array-Based Characterization and Design of ZnO-High Affinity Peptides. *Biotechnol. Bioeng.* **2010**, *106*, 845-851.
- Osseo-Asare, K.; Arriagada, F. Preparation of SiO₂ nanoparticles in a non-ionic reverse micellar system. *Colloids and surfaces* **1990**, *50*, 321-339.
- Osterholtz, F.; Pohl, E. Kinetics of the hydrolysis and condensation of organofunctional alkoxysilanes: a review. *J. Adhes. Sci. Technol.* **1992**, *6*, 127-149.
- Patrinoiu, G.; Calderon-Moreno, J. M.; Culita, D. C.; Birjega, R.; Ene, R.; Carp, O. Eco-friendly synthetic route for layered zinc compound and its conversion to ZnO with photocatalytic properties. *Solid State Sci.* **2013**, *23*, 58-64.
- Patwardhan, S. V.; Emami, F. S.; Berry, R. J.; Jones, S. E.; Naik, R. R.; Deschaume, O.; Heinz, H.; Perry, C. C. Chemistry of Aqueous Silica Nanoparticle Surfaces and the Mechanism of Selective Peptide Adsorption. *J. Am. Chem. Soc.* **2012**, *134*, 6244-6256.
- Paulick, M. G.; Bertozzi, C. R. The Glycosylphosphatidylinositol Anchor: A Complex Membrane-Anchoring Structure for Proteins†. *Biochemistry (N. Y.)* **2008**, *47*, 6991-7000.
- Pearton, S.; Norton, D.; Ip, K.; Heo, Y.; Steiner, T. Recent progress in processing and properties of ZnO. *Prog. Mater. Sci.* **2005**, *50*, 293-340.
- Perry, C. C.; Keeling-Tucker, T. Model studies of colloidal silica precipitation using biosilica extracts from *Equisetum telmateia*. *Colloid Polym. Sci.* **2003**, *281*, 652-664.
- Perry, C. C.; Patwardhan, S. V.; Deschaume, O. From biominerals to biomaterials: the role of biomolecule-mineral interactions. *Biochem. Soc. Trans.* **2009**, *37*, 687-691.
- Petsko, G. A.; Ringe, D. *Protein structure and function*; London New Science Press Ltd: London, Oxford, New York, 2009; , pp 78-80.
- Pietruszka, R.; Witkowski, B. S.; Luka, G.; Wachnicki, L.; Gieraltowska, S.; Kopalko, K.; Zielony, E.; Bieganski, P.; Placzek-Popko, E.; Godlewski, M. Photovoltaic properties of ZnO nanorods/p-type Si heterojunction structures. *Beilstein journal of nanotechnology* **2014**, *5*, 173-179.

- Polsongkram, D.; Chamninok, P.; Pukird, S.; Chow, L.; Lupan, O.; Chai, G.; Khallaf, H.; Park, S.; Schulte, A. Effect of synthesis conditions on the growth of ZnO nanorods via hydrothermal method. *Physica B: Condensed Matter* **2008**, *403*, 3713-3717.
- Poul, L.; Jouini, N.; Fievet, F. Layered Hydroxide Metal Acetates (Metal = Zinc, Cobalt, and Nickel): Elaboration via Hydrolysis in Polyol Medium and Comparative Study. *Chem. Mater.* **2000**, *12*, 3123-3132.
- Poulsen, N.; Kröger, N. A new molecular tool for transgenic diatoms. *Febs Journal* **2005**, *272*, 3413-3423.
- Poulsen, N.; Kroger, N. Silica morphogenesis by alternative processing of silaffins in the diatom *Thalassiosira pseudonana*. *J. Biol. Chem.* **2004**, *279*, 42993-42999.
- Puddu, V.; Perry, C. C. Interactions at the Silica-Peptide Interface: The Influence of Particle Size and the Surface Functionality. *Langmuir* **2014**, *30*, 227-233.
- Puddu, V.; Perry, C. C. Peptide Adsorption on Silica Nanoparticles: Evidence of Hydrophobic Interactions. *ACS Nano* **2012**, *6*, 6356-6363.
- Qiu, Y.; Chen, W.; Yang, S. Facile hydrothermal preparation of hierarchically assembled, porous single-crystalline ZnO nanoplates and their application in dye-sensitized solar cells. *Journal of Materials Chemistry* **2010**, *20*, 1001-1006.
- Rabe, M.; Verdes, D.; Seeger, S. Understanding protein adsorption phenomena at solid surfaces. *Adv. Colloid Interface Sci.* **2011**, *162*, 87-106.
- Rahman, I.; Jafarzadeh, M.; Sipaut, C. Synthesis of organo-functionalized nanosilica via a co-condensation modification using γ -aminopropyltriethoxysilane (APTES). *Ceram. Int.* **2009**, *35*, 1883-1888.
- Ramimoghadam, D.; Hussein, M. Z. B.; Taufiq-Yap, Y. H. The effect of sodium dodecyl sulfate (SDS) and cetyltrimethylammonium bromide (CTAB) on the properties of ZnO synthesized by hydrothermal method. *International journal of molecular sciences* **2012**, *13*, 13275-13293.
- Rao, C. N. R.; Müller, A.; Cheetham, A. K. *The chemistry of nanomaterials: synthesis, properties and applications*; Wiley-VCH: Weinheim, 2006; Vol. 1.
- Rich, A. M.; Bombarda, E.; Schenk, A. D.; Lee, P. E.; Cox, E. H.; Spuches, A. M.; Hudson, L. D.; Kieffer, B.; Wilcox, D. E. Thermodynamics of Zn²⁺ binding to Cys²His² and Cys²HisCys zinc fingers and a Cys⁴ transcription factor site. *J. Am. Chem. Soc.* **2012**, *134*, 10405-10418.
- Richthammer, P.; Börmel, M.; Brunner, E.; van Pée, K. Biomineralization in diatoms: The role of silacidins. *Chembiochem* **2011**, *12*, 1362-1366.
- Rimola, A.; Sodupe, M.; Ugliengo, P. Affinity scale for the interaction of amino acids with silica surfaces. *The Journal of Physical Chemistry C* **2009**, *113*, 5741-5750.
- Roach, P.; Farrar, D.; Perry, C. C. Interpretation of protein adsorption: surface-induced conformational changes. *J. Am. Chem. Soc.* **2005**, *127*, 8168-8173.
- Rodríguez-hornedo, N.; Murphy, D. Significance of controlling crystallization mechanisms and kinetics in pharmaceutical systems. *J. Pharm. Sci.* **1999**, *88*, 651-660.

- Rombach, M.; Gelinsky, M.; Vahrenkamp, H. Coordination modes of aminoacids to zinc. *Inorg. Chim. Acta* **2002**, *334*, 25-33.
- Rothenstein, D.; Claasen, B.; Omiecienski, B.; Lammel, P.; Bill, J. Isolation of ZnO-Binding 12-mer Peptides and Determination of Their Binding Epitopes by NMR Spectroscopy. *J. Am. Chem. Soc.* **2012**, *134*, 12547-12556.
- Russell, P.; Batchelor, D.; Thornton, J. SEM and AFM: complementary techniques for high resolution surface investigations. *Microscopy and Analysis* **2001**, 9-12.
- Sanchez, C.; Arribart, H.; Guille, M. M. G. Biomimetism and bioinspiration as tools for the design of innovative materials and systems. *Nature materials* **2005**, *4*, 277-288.
- Sanchez, C.; Arribart, H.; Guille, M. M. Biomimetism and bioinspiration as tools for the design of innovative materials and systems. *Nat. Mater.* **2005**, *4*, 277-88.
- Sanford, K.; Kumar, M. New proteins in a materials world. *Curr. Opin. Biotechnol.* **2005**, *16*, 416-421.
- Sanjay, S. L.; Annaso, B. G.; Chavan, S. M.; Rajiv, S. V. Recent progress in preparation of superhydrophobic surfaces: a review. *Journal of Surface Engineered Materials and Advanced Technology* **2012**, *2012*.
- Schlipf, D. M.; Rankin, S. E.; Knutson, B. L. Pore-Size Dependent Protein Adsorption and Protection from Proteolytic Hydrolysis in Tailored Mesoporous Silica Particles. *ACS applied materials & interfaces* **2013**, *5*, 10111-10117.
- Sewell, S. L.; Wright, D. W. Biomimetic Synthesis of Titanium Dioxide Utilizing the R5 Peptide Derived from *Cylindrotheca fusiformis*. *Chemistry of materials* **2006**, *18*, 3108-3113.
- Shaporev, A.; Ivanov, V.; Baranchikov, A.; Tret'yakov, Y. D. Microwave-assisted hydrothermal synthesis and photocatalytic activity of ZnO. *Inorganic Materials* **2007**, *43*, 35-39.
- Shen, X.; Belcher, A. M.; Hansma, P. K.; Stucky, G. D.; Morse, D. E. Molecular cloning and characterization of lustrin A, a matrix protein from shell and pearl nacre of *Haliotis rufescens*. *J. Biol. Chem.* **1997**, *272*, 32472-32481.
- Simkiss, K.; Wilbur, K. M. *Biom mineralization*; Elsevier Science: Burlington, 2012; .
- Singh, O.; Singh, M. P.; Kohli, N.; Singh, R. C. Effect of pH on the morphology and gas sensing properties of ZnO nanostructures. *Sensors Actuators B: Chem.* **2012**, *166*, 438-443.
- Singh, S.; Gopal, R. Zinc nanoparticles in solution by laser ablation technique. *Bull. Mater. Sci.* **2007**, *30*, 291-293.
- Skoog, D. A.; Holler, F. J.; Nieman, T. A. *Principles of Instrumental Analysis*; Saunders College Pub: Philadelphia, 1998; .
- Slowing, I. I.; Trewyn, B. G.; Giri, S.; Lin, V. Mesoporous silica nanoparticles for drug delivery and biosensing applications. *Advanced Functional Materials* **2007**, *17*, 1225-1236.
- Smith, A. L. Infrared spectra-structure correlations for organosilicon compounds. *Spectrochimica Acta* **1960**, *16*, 87-105.

- Smith, G. P.; Petrenko, V. A. Phage display. *Chem. Rev.* **1997**, *97*, 391-410.
- Sola-Rabada, A.; Liang, M.; Roe, M. J.; Perry, C. C. Peptide-directed crystal growth modification in the formation of ZnO. *Journal of Materials Chemistry B* **2015**, *3*, 3777-3788.
- Soto-Cantu, E.; Cueto, R.; Koch, J.; Russo, P. S. Synthesis and rapid characterization of amine-functionalized silica. *Langmuir* **2012**, *28*, 5562-5569.
- Srivastava, O. K.; Secco, E. A. Studies on on metal hydroxy compounds. II. Infrared spectra of zinc derivatives ϵ -Zn(OH)₂, β -ZnOHCl, ZnOHF, Zn₅(OH)₈Cl₂, and Zn₅(OH)₈Cl₂·H₂O. *Canadian Journal of Chemistry* **1967**, *45*, 585-588.
- Stein, S.; Böhlen, P.; Udenfriend, S. Studies on the kinetics of reaction and hydrolysis of fluorescamine. *Arch. Biochem. Biophys.* **1974**, *163*, 400-403.
- Stöber, W.; Fink, A.; Bohn, E. Controlled growth of monodisperse silica spheres in the micron size range. *J. Colloid Interface Sci.* **1968**, *26*, 62-69.
- Strano, V.; Urso, R. G.; Scuderi, M.; Iwu, K. O.; Simone, F.; Ciliberto, E.; Spinella, C.; Mirabella, S. Double Role of HMTA in ZnO Nanorods Grown by Chemical Bath Deposition. *The Journal of Physical Chemistry C* **2014**, *118*, 28189-28195.
- Stricks, W.; Kolthoff, I. M. Reactions between Mercuric Mercury and Cysteine and Glutathione. Apparent Dissociation Constants, Heats and Entropies of Formation of Various Forms of Mercuric Mercapto-Cysteine and -Glutathione. *J. Am. Chem. Soc.* **1953**, *75*, 5673-5681.
- Stuart, B. *Infrared spectroscopy fundamentals and applications*; J. Wiley & Sons: Chichester, 2004; .
- Sugunan, A.; Warad, H. C.; Boman, M.; Dutta, J. Zinc oxide nanowires in chemical bath on seeded substrates: role of hexamine. *J. Sol Gel Sci. Technol.* **2006**, *39*, 49-56.
- Sumerel, J. L.; Yang, W.; Kisailus, D.; Weaver, J. C.; Choi, J. H.; Morse, D. E. Biocatalytically templated synthesis of titanium dioxide. *Chemistry of materials* **2003**, *15*, 4804-4809.
- Sumper, M.; Kroger, N. Silica formation in diatoms: the function of long-chain polyamines and silaffins. *Journal of Materials Chemistry* **2004**, *14*, 2059-2065.
- Sun, X.; Liu, B.; Sun, Y.; Yu, Y. DNA-length-dependent fluorescent sensing based on energy transfer in self-assembled multilayers. *Biosensors and Bioelectronics* **2014**, *61*, 466-470.
- Sun, Y.; Hu, J.; Wang, N.; Zou, R.; Wu, J.; Song, Y.; Chen, H.; Chen, H.; Chen, Z. Controllable hydrothermal synthesis, growth mechanism, and properties of ZnO three-dimensional structures. *New Journal of Chemistry* **2010**, *34*, 732-737.
- Tamerler, C.; Sarikaya, M. Molecular biomimetics: utilizing nature's molecular ways in practical engineering. *Acta biomaterialia* **2007**, *3*, 289-299.
- Tanford, C. *The Hydrophobic Effect: Formation of Micelles and Biological Membranes*; Krieger: Malabar, 1991; .
- Teng, H. H. How ions and molecules organize to form crystals. *Elements* **2013**, *9*, 189-194.

- Thiele, E. Relation between catalytic activity and size of particle. *Industrial & Engineering Chemistry* **1939**, *31*, 916-920.
- Tian, Z. R.; Voigt, J. A.; Liu, J.; McKenzie, B.; McDermott, M. J.; Rodriguez, M. A.; Konishi, H.; Xu, H. Complex and oriented ZnO nanostructures. *Nature materials* **2003**, *2*, 821-826.
- Tian, Z. R.; Voigt, J. A.; Liu, J.; McKenzie, B.; McDermott, M. J. Biomimetic arrays of oriented helical ZnO nanorods and columns. *J. Am. Chem. Soc.* **2002**, *124*, 12954-5.
- Togashi, T.; Yokoo, N.; Umetsu, M.; Ohara, S.; Naka, T.; Takami, S.; Abe, H.; Kumagai, I.; Adschiri, T. Material-binding peptide application—ZnO crystal structure control by means of a ZnO-binding peptide. *J. Biosci. Bioeng.* **2011**, *111*, 140-145.
- Tokumoto, M. S.; Pulcinelli, S. H.; Santilli, C. V.; Briois, V. Catalysis and temperature dependence on the formation of ZnO nanoparticles and of zinc acetate derivatives prepared by the sol-gel route. *J. Phys. Chem. B* **2003**, *107*, 568-574.
- Tomczak, M. M.; Glawe, D. D.; Drummy, L. F.; Lawrence, C. G.; Stone, M. O.; Perry, C. C.; Pochan, D. J.; Deming, T. J.; Naik, R. R. Polypeptide-templated synthesis of hexagonal silica platelets. *J. Am. Chem. Soc.* **2005**, *127*, 12577-12582.
- Tomczak, M. M.; Gupta, M. K.; Drummy, L. F.; Rozenzhak, S. M.; Naik, R. R. Morphological control and assembly of zinc oxide using a biotemplate☆. *Acta Biomaterialia* **2009**, *5*, 876-882.
- Turnbull, D. Formation of crystal nuclei in liquid metals. *J. Appl. Phys.* **1950**, *21*, 1022-1028.
- Umar, A.; Kim, S.; Lee, Y.; Nahm, K.; Hahn, Y. Catalyst-free large-quantity synthesis of ZnO nanorods by a vapor–solid growth mechanism: structural and optical properties. *J. Cryst. Growth* **2005**, *282*, 131-136.
- Umetsu, M.; Mizuta, M.; Tsumoto, K.; Ohara, S.; Takami, S.; Watanabe, H.; Kumagai, I.; Adschiri, T. Bioassisted Room-Temperature Immobilization and Mineralization of Zinc Oxide-The Structural Ordering of ZnO Nanoparticles into a Flower-Type Morphology. *Adv. Mater.* **2005**, *17*, 2571.
- Vallee, B. L.; Auld, D. S. Zinc coordination, function, and structure of zinc enzymes and other proteins. *Biochemistry (N. Y.)* **1990**, *29*, 5647-5659.
- Van Blaaderen, A.; Van Geest, J.; Vrij, A. Monodisperse colloidal silica spheres from tetraalkoxysilanes: particle formation and growth mechanism. *J. Colloid Interface Sci.* **1992**, *154*, 481-501.
- Vansant, E. F.; Van Der Voort, P.; Vrancken, K. C. *Characterization and chemical modification of the silica surface*; Elsevier: Amsterdam, 1995; .
- Verges, M. A.; Mifsud, A.; Serna, C. J. Formation of Rod-Like Zinc-Oxide Microcrystals in Homogeneous Solutions. *Surf. Interface Anal.* **1990**, *86*, 959-963.
- Vogler, R.; Gelinsky, M.; Guo, L. F.; Vahrenkamp, H. Solution behaviour and zinc complexation of di- and tripeptides with two cysteine units. *Inorg. Chim. Acta* **2002**, *339*, 1-8.
- Volmer, M.; Stratmann, M.; Viefhaus, H. Electrochemical and electron spectroscopic investigations of iron surfaces modified with thiols. *Surf. Interface Anal.* **1990**, *16*, 278-282.

- Wagner, C. D.; Riggs, W. M.; Davis, L. E.; Moulder, J. F. *Handbook of X-ray Photoelectron Spectroscopy*; Perkin-Elmer Corporation (Physical Electronics): Eden Prairie, 1979; .
- Wan, Q.; Li, Q. H.; Chen, Y. J.; Wang, T. H.; He, X. L.; Li, J. P.; Lin, C. L. Fabrication and ethanol sensing characteristics of ZnO nanowire gas sensors. *Appl.Phys.Lett.Applied Physics Letters* **2004**, *84*, 3654.
- Wang, H.; Zepeda-Ruiz, L. A.; Gilmer, G. H.; Upmanyu, M. Atomistics of vapour–liquid–solid nanowire growth. *Nature communications* **2013**, *4*.
- Wang, S.; Xue, J.; Ge, X.; Fan, H.; Xu, H.; Lu, J. R. Biomimetic synthesis of silica nanostructures with controllable morphologies and sizes through tuning interfacial interactions. *Chemical Communications* **2012**, *48*, 9415-9417.
- Wang, X.; Song, J.; Wang, Z. L. Nanowire and nanobelt arrays of zinc oxide from synthesis to properties and to novel devices. *Journal of Materials Chemistry* **2007**, *17*, 711-720.
- Wang, Z. L. Zinc oxide nanostructures: growth, properties and applications. *Journal of Physics: Condensed Matter* **2004**, *16*, R829.
- Wang, Z.; Qian, X.; Yin, J.; Zhu, Z. Large-scale fabrication of tower-like, flower-like, and tube-like ZnO arrays by a simple chemical solution route. *Langmuir* **2004**, *20*, 3441-3448.
- Wang, H. H.; Xie, C. S.; Zeng, D. W.; Yang, Z. H. Controlled organization of ZnO building blocks into complex nanostructures. *J. Colloid Interface Sci.* **2006**, *297*, 570-577.
- Wang, Y.; Li, Y.; Zhou, Z.; Zu, X.; Deng, Y. Evolution of the zinc compound nanostructures in zinc acetate single-source solution. *J. Nanopart. Res.* **2011**, *13*, 5193-5202.
- Weiner, S.; Traub, W.; Lowenstam, H. In *Organic matrix in calcified exoskeletons*; Biomineralization and biological metal accumulation; Springer: Netherlands, 1983; pp 205-224.
- Weiner, S.; Addadi, L. Calcium Carbonate formation in biology: the involvement of an amorphous calcium carbonate precursor phase. *Geochim. Cosmochim. Acta* **2002**, *66*, A827-A827.
- Wenzl, S.; Hett, R.; Richthammer, P.; Sumper, M. Silacidins: highly acidic phosphopeptides from diatom shells assist in silica precipitation in vitro. *Angewandte Chemie* **2008**, *120*, 1753-1756.
- White, S. J.; Johnson, S. D.; Sellick, M. A.; Bronowska, A.; Stockley, P. G.; Wälti, C. The Influence of Two-Dimensional Organization on Peptide Conformation. *Angewandte Chemie* **2015**, *127*, 988-992.
- Wieneke, R.; Bernecker, A.; Riedel, R.; Sumper, M.; Steinem, C.; Geyer, A. Silica precipitation with synthetic silaffin peptides. *Organic & biomolecular chemistry* **2011**, *9*, 5482-5486.
- Williams, R. An introduction to biominerals and the role of organic molecules in their formation. *Philosophical Transactions of the Royal Society B: Biological Sciences* **1984**, *304*, 411-424.
- Wong, E. M.; Searson, P. C. ZnO quantum particle thin films fabricated by electrophoretic deposition. *Appl. Phys. Lett.* **1999**, *74*, 2939-2941.
- Wu, Q.; Chen, X.; Zhang, P.; Han, Y.; Chen, X.; Yan, Y.; Li, S. Amino acid-assisted synthesis of ZnO hierarchical architectures and their novel photocatalytic activities. *Crystal Growth and Design* **2008**, *8*, 3010-3018.

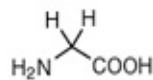
- Wu, S.; Mou, C.; Lin, H. Synthesis of mesoporous silica nanoparticles. *Chem. Soc. Rev.* **2013**, *42*, 3862-3875.
- Wu, Y.; Yang, P. Direct observation of vapor-liquid-solid nanowire growth. *J. Am. Chem. Soc.* **2001**, *123*, 3165-3166.
- Wu, Z.; Xiang, H.; Kim, T.; Chun, M.; Lee, K. Surface properties of submicrometer silica spheres modified with aminopropyltriethoxysilane and phenyltriethoxysilane. *J. Colloid Interface Sci.* **2006**, *304*, 119-124.
- Wyckoff, R. W. G. *Crystal structures*. Interscience Publishers: New York, 1963; .
- Xia, Z.; Wang, Y.; Fang, Y.; Wan, Y.; Xia, W.; Sha, J. Understanding the Origin of Ferromagnetism in ZnO Porous Microspheres by Systematic Investigations of the Thermal Decomposition of Zn-5(OH)(8)Ac-2 center dot 2H(2)O to ZnO. *Journal of Physical Chemistry C* **2011**, *115*, 14576-14582.
- Xie, T.; Song, S.; Schwenke, K.; Singh, M.; Gonzalez, L. E.; Del Gado, E.; Hahm, J. Low-Index ZnO Crystal Plane-Specific Binding Behavior of Whole Immunoglobulin G Proteins. *Langmuir* **2015**, *31*, 10493-10499.
- Xu, A.; Ma, Y.; Coelfen, H. Biomimetic mineralization. *J. Mater. Chem.* **2007**, *17*, 415-449.
- Yang, L.; Wang, Y.; Luo, G.; Dai, Y. Functionalization of SBA-15 mesoporous silica with thiol or sulfonic acid groups under the crystallization conditions. *Microporous and mesoporous materials* **2005**, *84*, 275-282.
- Yin, J.; Gao, F.; Wei, C.; Lu, Q. Water amount dependence on morphologies and properties of ZnO nanostructures in double-solvent system. *Scientific reports* **2014**, *4*, 3736.
- Yokoo, N.; Togashi, T.; Umetsu, M.; Tsumoto, K.; Hattori, T.; Nakanishi, T.; Ohara, S.; Takami, S.; Naka, T.; Abe, H.; Kumagai, I.; Adschiri, T. Direct and Selective Immobilization of Proteins by Means of an Inorganic Material-Binding Peptide: Discussion on Functionalization in the Elongation to Material-Binding Peptide. *J. Phys. Chem. B* **2010**, *114*, 480-486.
- Yoreo, J. J.; Vekilov, P. G. Principles of Crystal Nucleation and Growth. *Rev. Mineral. Geochem.* **2003**, *54*, 57-93.
- Yoshimura, M.; Byrappa, K. Hydrothermal processing of materials: past, present and future. *J Mater Sci Journal of Materials Science : Full Set - Includes `Journal of Materials Science Letters'* **2008**, *43*, 2085-2103.
- Zeng, J.; Hou, J.; Wang, X. *Colloidal Hybrid Nanocrystals: Synthesis, Properties, and Perspectives*; INTECH Open Access Publisher: 2011; .
- Zhang, J.; Liu, H.; Wang, Z.; Ming, N. Low-temperature growth of ZnO with controllable shapes and band gaps. *J. Cryst. Growth* **2008**, *310*, 2848-2853.
- Zhang, J.; Liu, H.; Wang, Z.; Ming, N. Synthesis and band gap of ZnO particles with hexagonal bilayer structure. *Appl. Phys. Lett.* **2007**, *90*, 113117.
- Zhang, Y.; Nayak, T. R.; Hong, H.; Cai, W. Biomedical applications of zinc oxide nanomaterials. *Curr. Mol. Med.* **2013**, *13*, 1633-1645.
- Zhmud, B.; Sonnefeld, J. Aminopolysiloxane gels: production and properties. *J. Non Cryst. Solids* **1996**, *195*, 16-27.

- Zhou, H.; Alves, H.; Hofmann, D.; Kriegseis, W.; Meyer, B.; Kaczmarczyk, G.; Hoffmann, A. Behind the weak excitonic emission of ZnO quantum dots: ZnO/Zn(OH)₂ core-shell structure. *Appl. Phys. Lett.* **2002**, *80*, 210-212.
- Zhou, X.; Xie, Z.; Jiang, Z.; Kuang, Q.; Zhang, S.; Xu, T.; Huang, R.; Zheng, L. Formation of ZnO hexagonal micro-pyramids: a successful control of the exposed polar surfaces with the assistance of an ionic liquid. *Chem. Commun.* **2005**, 5572-5574.
- Zhou, Y.; Shimizu, K.; Cha, J. N.; Stucky, G. D.; Morse, D. E. Efficient catalysis of polysiloxane synthesis by silicatein α requires specific hydroxy and imidazole functionalities. *Angewandte Chemie International Edition* **1999**, *38*, 779-782.
- Zhuravlev, L. The surface chemistry of amorphous silica. Zhuravlev model. *Colloid Surf. A-Physicochem. Eng. Asp.* **2000**, *173*, 1-38.
- Zou, H.; Wu, S.; Shen, J. Polymer/silica nanocomposites: preparation, characterization, properties, and applications. *Chem. Rev.* **2008**, *108*, 3893-3957.
- Zucca, P.; Sanjust, E. Inorganic materials as supports for covalent enzyme immobilization: methods and mechanisms. *Molecules* **2014**, *19*, 14139-14194.

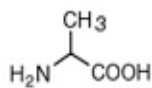
APPENDIX 1.1

Amino acids structures and properties

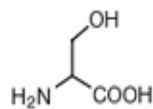
Small



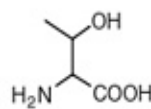
Glycine (Gly, G)
MW: 57.05



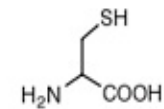
Alanine (Ala, A)
MW: 71.09



Serine (Ser, S)
MW: 87.08, pK_a ~ 16



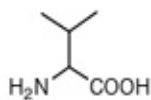
Threonine (Thr, T)
MW: 101.11, pK_a ~ 16



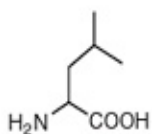
Cysteine (Cys, C)
MW: 103.15, pK_a = 8.35

Nucleophilic

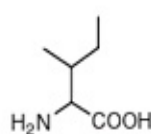
Hydrophobic



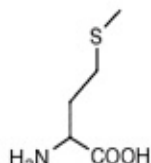
Valine (Val, V)
MW: 99.14



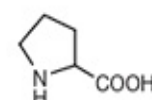
Leucine (Leu, L)
MW: 113.16



Isoleucine (Ile, I)
MW: 113.16

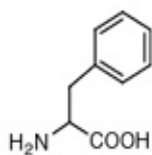


Methionine (Met, M)
MW: 131.19

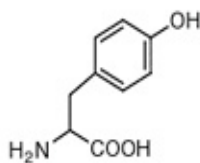


Proline (Pro, P)
MW: 97.12

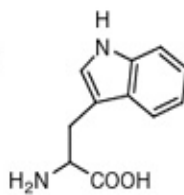
Aromatic



Phenylalanine (Phe, F)
MW: 147.18

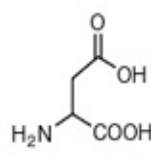


Tyrosine (Tyr, Y)
MW: 163.18

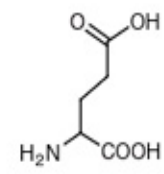


Tryptophan (Trp, W)
MW: 186.21

Acidic

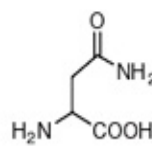


Aspartic Acid (Asp, D)
MW: 115.09, pK_a = 3.9

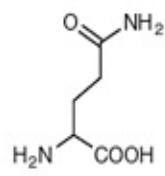


Glutamic Acid (Glu, E)
MW: 129.12, pK_a = 4.07

Amide

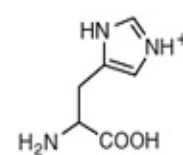


Asparagine (Asn, N)
MW: 114.11

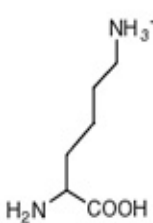


Glutamine (Gln, Q)
MW: 128.14

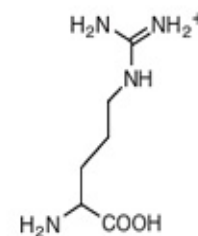
Basic



Histidine (His, H)
MW: 137.14, pK_a = 6.04



Lysine (Lys, K)
MW: 128.17, pK_a = 10.79



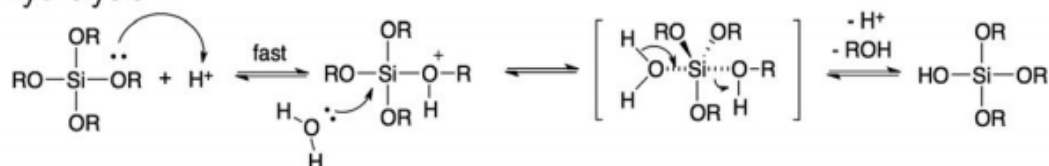
Arginine (Arg, R)
MW: 156.19, pK_a = 12.48

APPENDIX 1.2

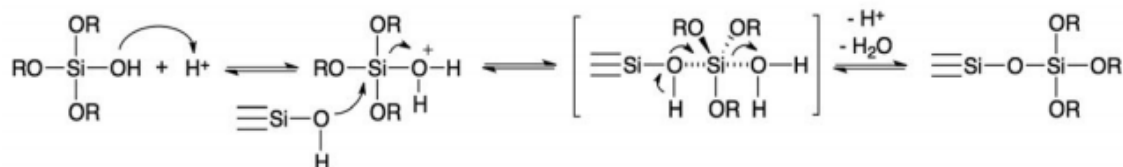
Mechanisms of hydrolysis and condensation of alkoxy silane precursors to form Silica in (a) acid-catalyzed conditions, and (b) base catalyzed conditions according to [Lofgreen et al. 2014](#).

a) acid-catalyzed - pH < 2

hydrolysis

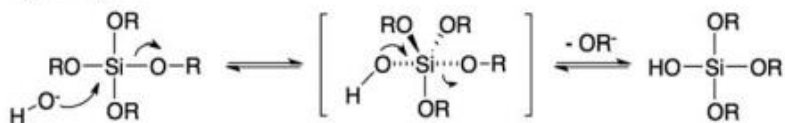


condensation

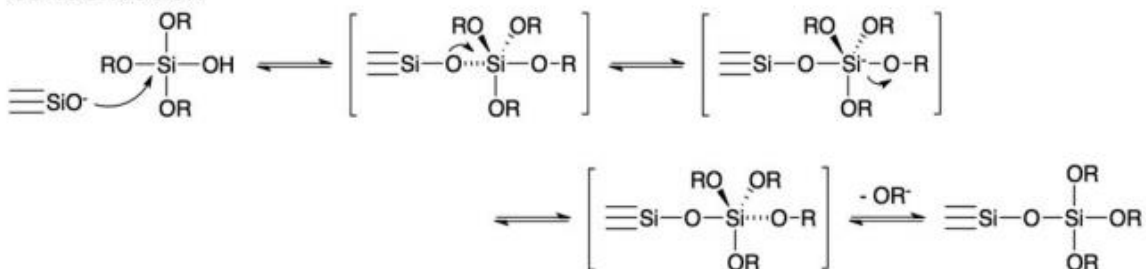


b) base-catalyzed - pH > 2

hydrolysis

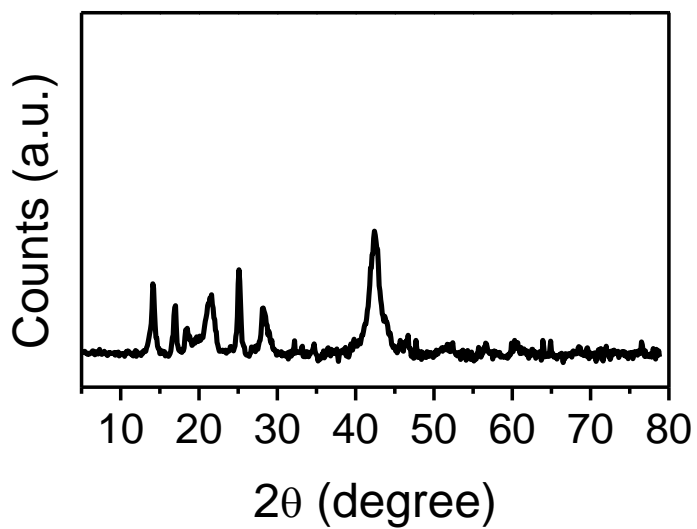


condensation



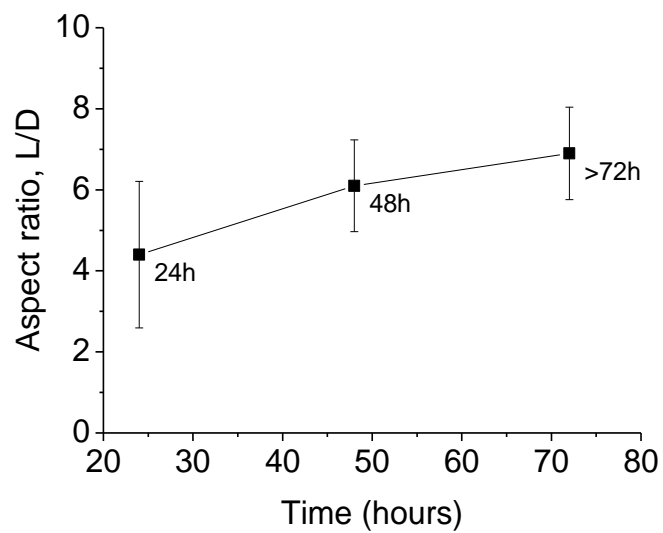
APPENDIX 2.1

XRD for the polypropylene (PP) sample holder used in experiments with small amount of sample.



APPENDIX 3.1.

Dimension analysis ($n \geq 30$) of ZnO crystals for aspect ratio (L/D) of blanks at different time reaction



APPENDIX 3.2.

ATR spectra of precipitates collected at different reaction times and identification of the peaks is given in the Table A1.

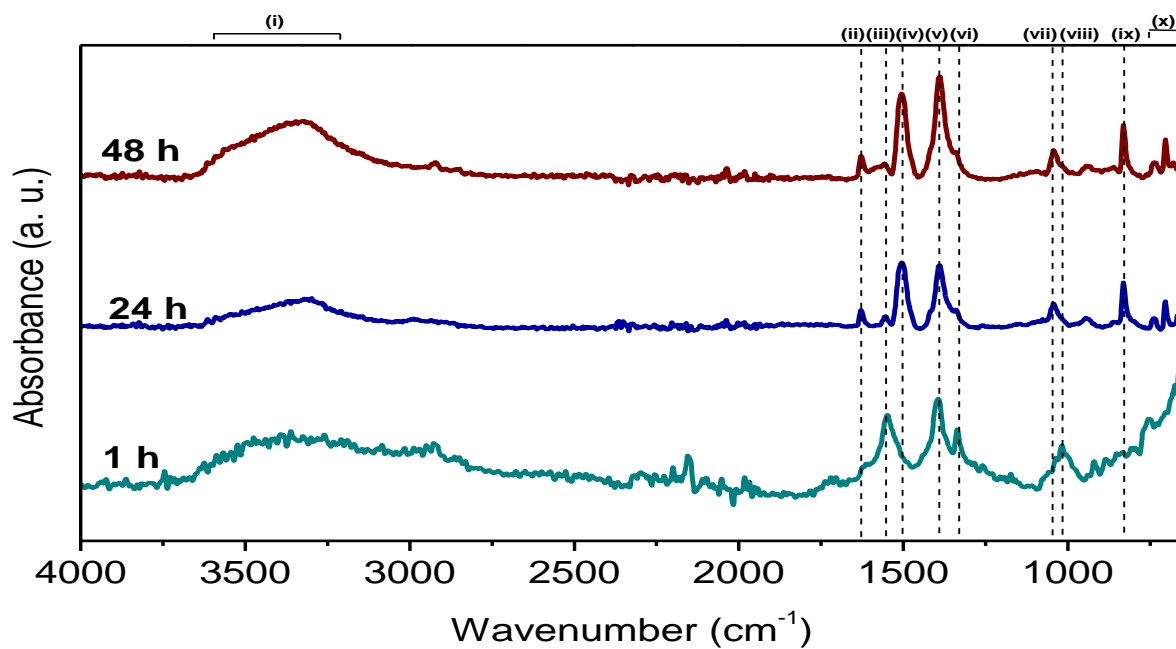
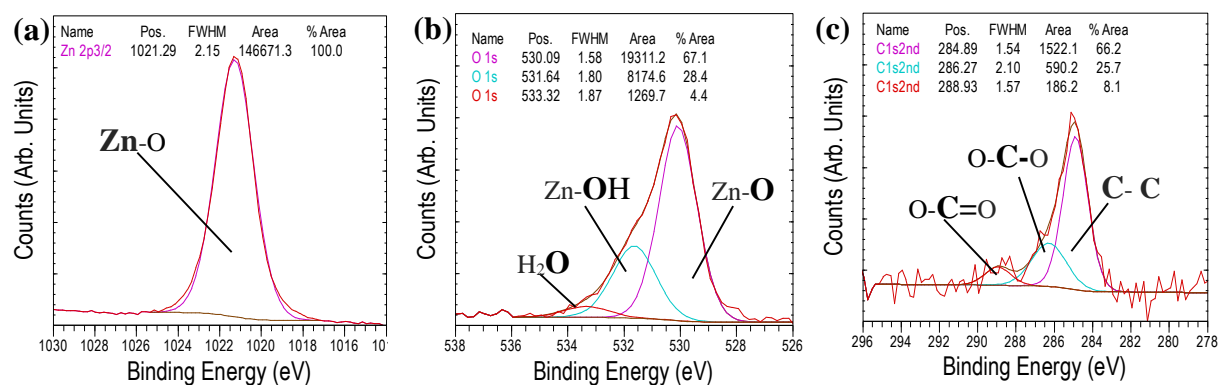


Table A1. ATR absorption peaks identified in precipitates collected at different reaction times

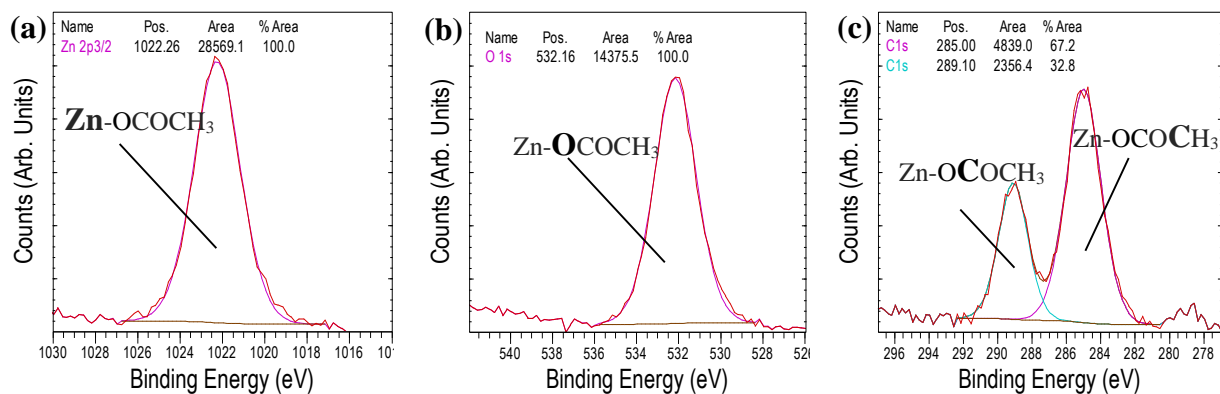
Peak	Wavenumber (cm ⁻¹)	Assignment
i	3000-3600	O-H group of hydroxide or intercalated water in LBZA
ii	~ 1620	O-H vibrational mode attributed to the hydroxide slab in LBZA
iii	~ 1550	antisymmetric stretching (ν_{as}) of CO ₂ ⁻
iv	~ 1505	antisymmetric stretching (ν_{as}) of CO ₃ ²⁻
v	~ 1390	symmetric stretching (ν_s) of CO ₂ ⁻ and/or ν_3 (CO ₃ ²⁻)
vi	~ 1340	in-plane bending (δ_s) or deformation of CH ₃
vii	~ 1045	symmetric stretching (ν_s) of CO ₃ ²⁻
viii	~ 1020	CH ₃ rocking (ρ_r)
ix	~ 830	out-of-plane deformation of CO ₃ ²⁻ and/or Zn(OH) ₂ vibration mode
x	600-800	out-of-plane bending (π) of CH or COO

APPENDIX 3.3

Core-level spectra for purchased ZnO (99.999%) for the regions (a) Zn 2p_{3/2}, (b) O 1s and (c) C 1s. Note that, the detection of water in the O 1s is due to ZnO having a natural affinity to hold some moisture from humidity in the air. The C 1s peaks at ~284.9 eV, 286 eV and 288.9 eV can be attributed to C-C, C-O-C and O-C=O; all of them from adventitious carbon contamination.



Core-level spectra for purchased ZnAc₂ (99.99%) of (a) Zn 2p_{3/2}, (b) O 1s and (c) C 1s regions.



APPENDIX 3.4

Study carried out to test the washing procedure used to clean precipitates collected during the ZnO synthesis process. Suspensions of pure ZnO ($1 \text{ mg}\cdot\text{ml}^{-1}$) were prepared in 15 mM zinc acetate solution (the same concentration used in the synthesis process). The mixtures were incubated for an hour at room temperature then centrifuged at 13000 rpm for 3 minutes to separate precipitates that may contain adsorbed material from supernatants. Precipitates were then subjected to three treatments (each performed in triplicate);

- 1) Not washed: Precipitates were lyophilized at $-70 \text{ }^{\circ}\text{C}$ using a Virtis-110 freeze-dryer.
- 2) Washed once: Precipitates were washed once in 3 volumes of ddH₂O and lyophilized at $-70 \text{ }^{\circ}\text{C}$ using a Virtis-110 freeze-dryer.
- 3) Washed thrice: Precipitates were washed three times in 3 volumes of ddH₂O and lyophilized at $-70 \text{ }^{\circ}\text{C}$ using a Virtis-110 freeze-dryer. This was the procedure followed in the study presented in the manuscript.

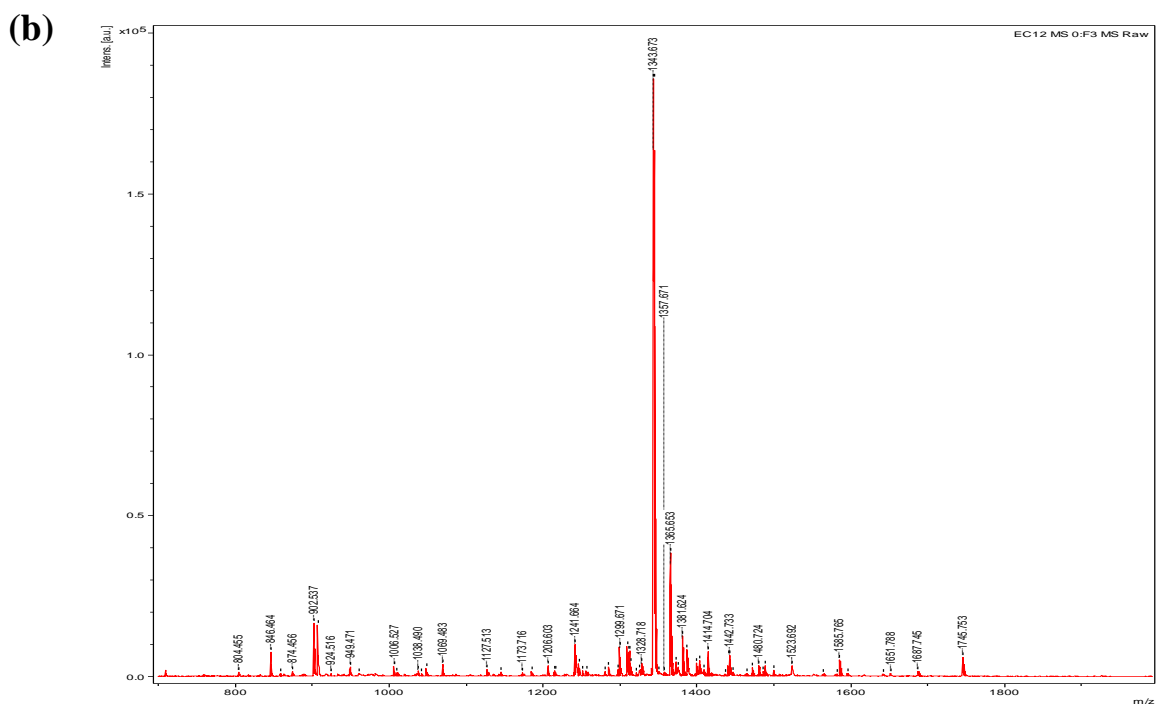
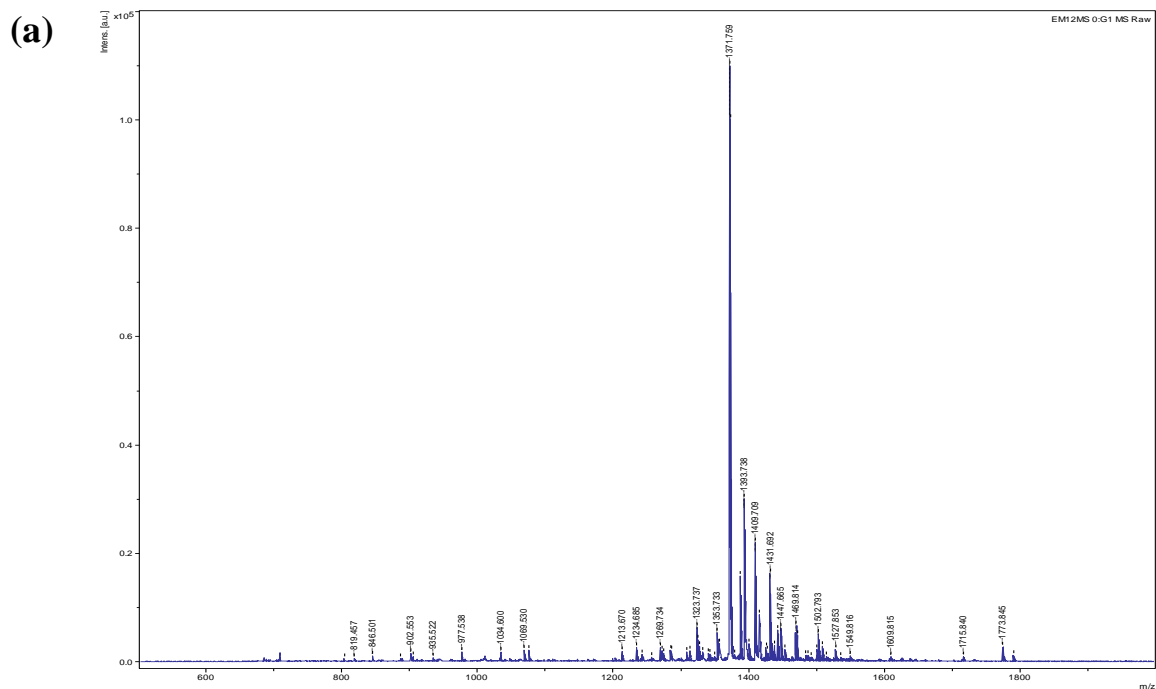
All samples were then subjected to thermal decomposition (TGA) and the weight loss determined.

Table shows TGA determined % weight loss of organic material in precipitates subjected to three treatments; not washed, washed once and washed thrice.

<i>Treatment</i>	<i>Organic Weight Loss %</i>
Not washed	4.0 ± 1.0
Washed once	1.8 ± 0.6
Washed thrice	1.6 ± 0.3

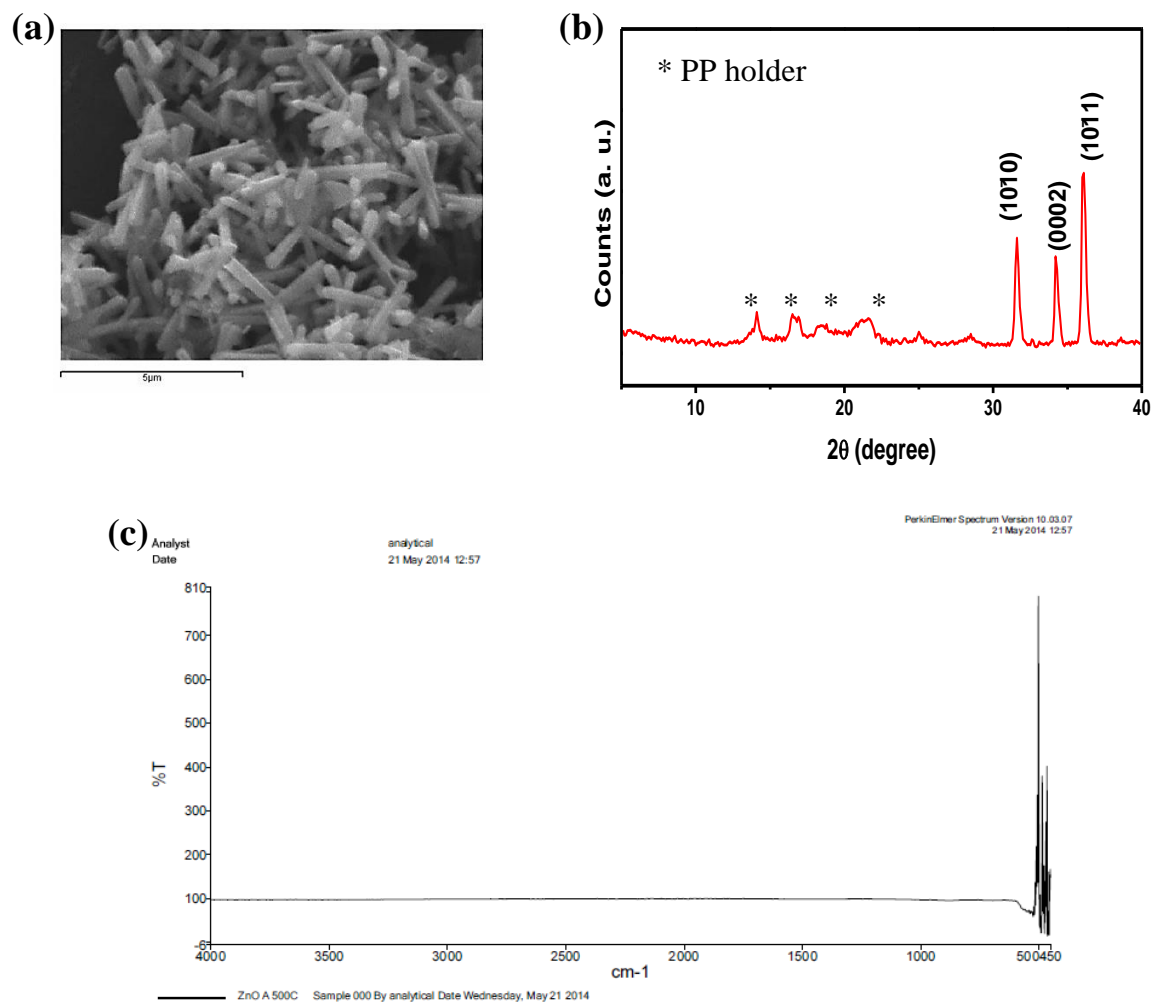
APPENDIX 4.1

Mass spectra of (a) EM-12 and (b) EC-12



APPENDIX 4.2

Characterisation of the calcined ZnO sample by (a) SEM image showing ZnO rods, (b) XRD where peaks at 31.6° , 34.2° , and 36.1° matched with the (1010), (0002), and (1011) planes of ZnO, respectively; and (c) ATR, where peaks around 460 cm^{-1} are assigned to M–O vibrational band (Ghule et al. 2006) which in this case can be attributed to vibrational stretching of ZnO (Yang et al. 2004).



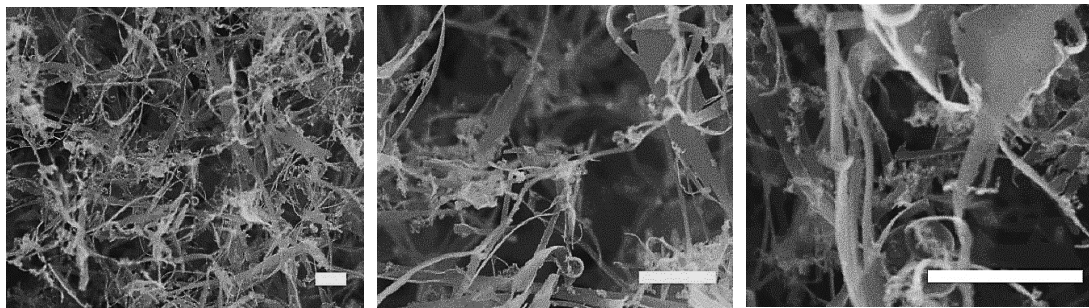
Ghule, Kalyani, Ghule, Anil Vithal, Chen, Bo-Jung, Ling, Yong-Chien, Preparation and characterization of ZnO nanoparticles coated paper and its antibacterial activity study. *Green Chem.* **2006**, 8, 1034-1041.

Yang, Xinghua, Shao, Changlu, Guan, Hongyu, Li, Xiliang, Gong, Jian, Preparation and characterization of ZnO nanofibers by using electrospun PVA/zinc acetate composite fiber as precursor. *Inorganic Chemistry Communications Inorganic Chemistry Communications* **2004**, 7, 176-178.

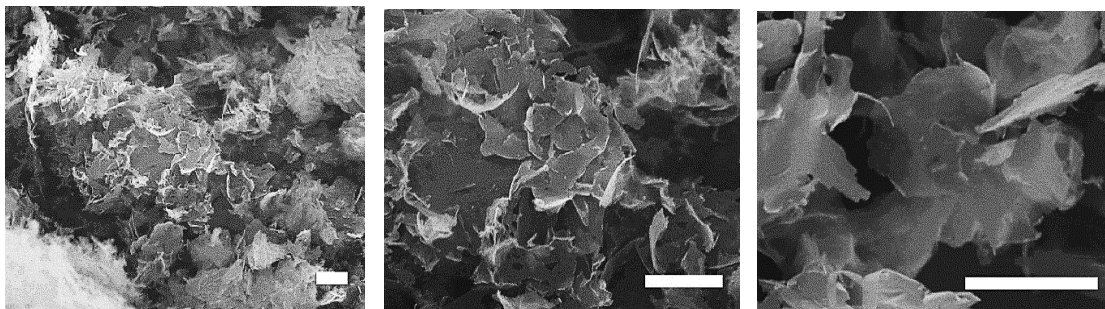
APPENDIX 4.3

SEM pictures (all scale bars are 5 μm) of LBZA for different concentrations of EM-12:

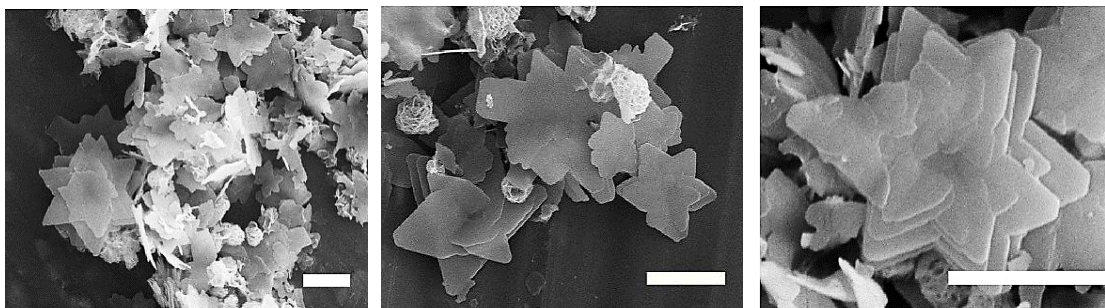
(a) 0.2 mM



(b) 0.4 mM

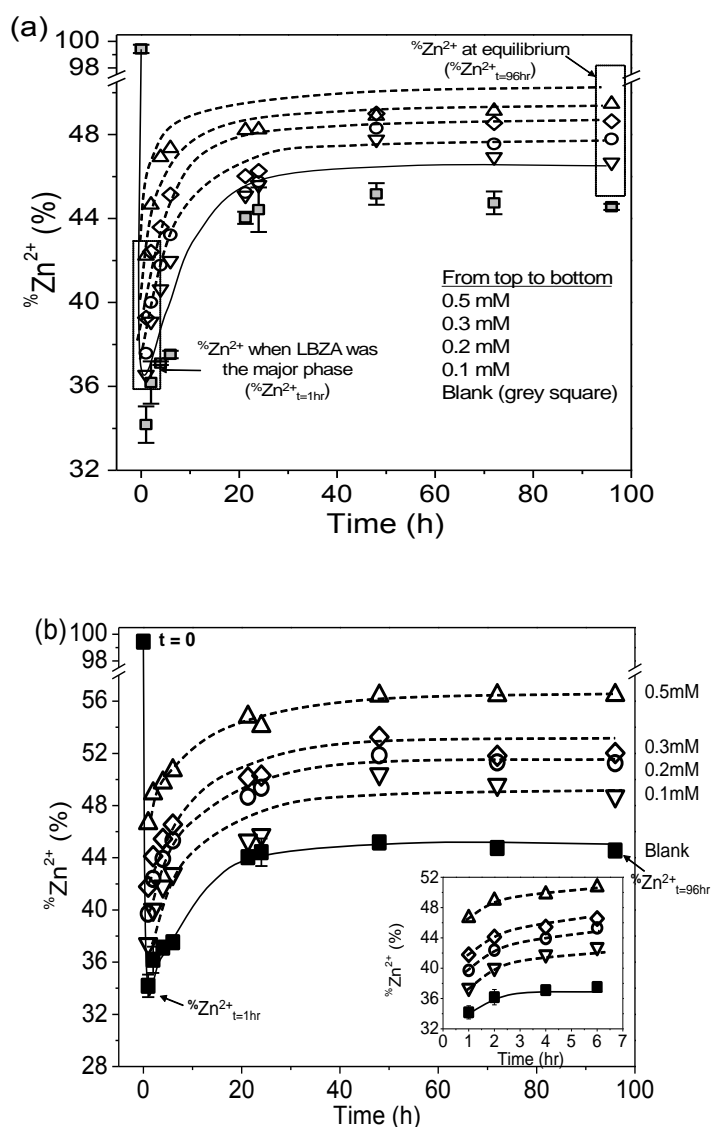


(c) 0.5 mM



APPENDIX 4.4

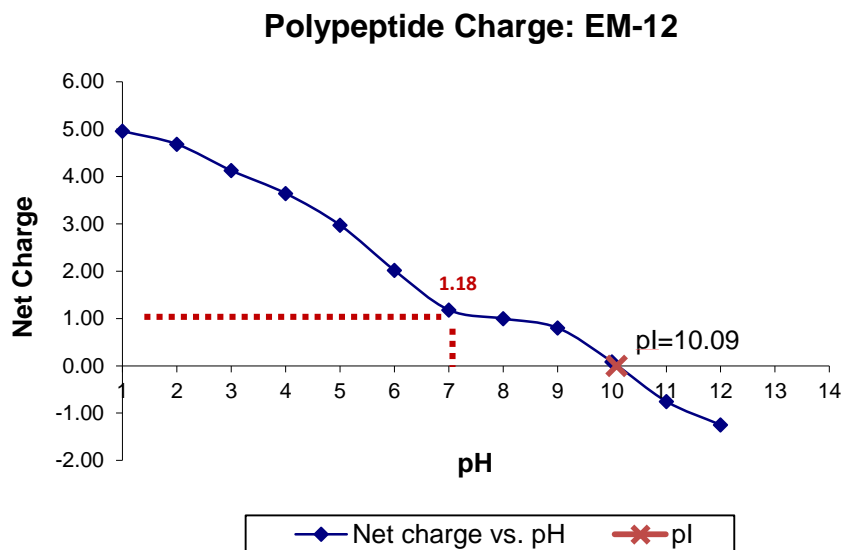
ICP-OES data obtained by Dr Liang showing the percentage of Zn^{2+} in solution with respect to the initial Zn^{2+} concentration, in the presence of (a) EM-12 and (b) EC-12 at different concentrations. The addition of EC-12 to the $\text{ZnAc}_2\text{-NH}_3$ reaction under identical conditions retained more Zn^{2+} in solution throughout the reaction compared to EM-12 and the increase was proportional to the concentration of the EC-12 added. In the presence of EM-12 (0.1–0.5mM), ~36–42% and ~46–50% of Zn^{2+} was retained in solution at $t = 1$ hour and $t = 96$ hours, respectively; compared to 34% and 45% for the Blank. In the presence of EC-12 at comparable concentrations, ~37–47% of Zn^{2+} was retained in solution at $t = 1$ hour while 48–57% was retained at $t = 96$ hours.



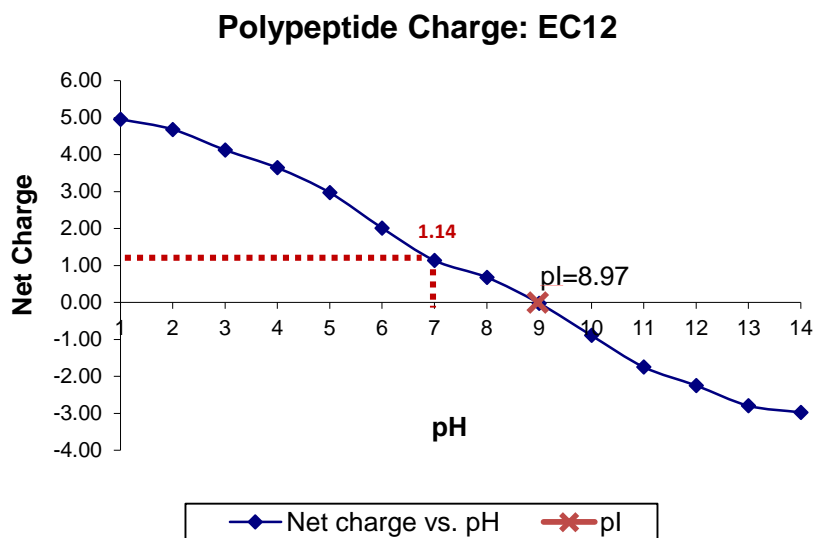
APPENDIX 4.5

Peptide charge graphs of (a) EM-12 and (b) EC-12. Based on the pK_a values for all the ionizable groups of the amino acids present in the peptide sequence.

(a)

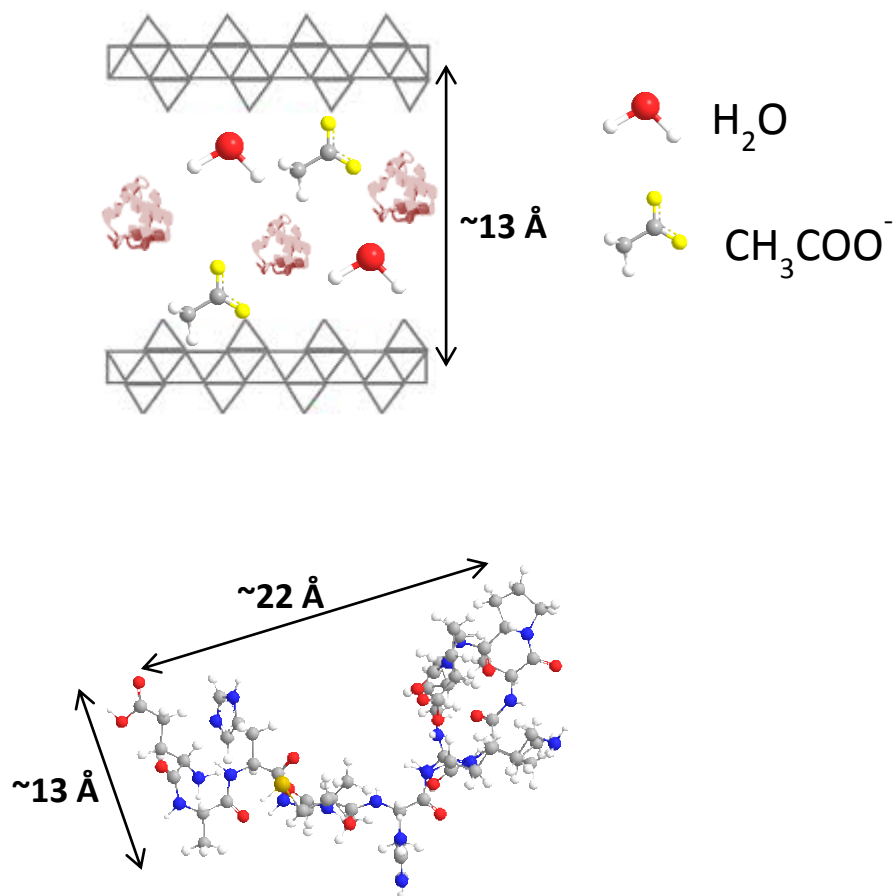


(b)



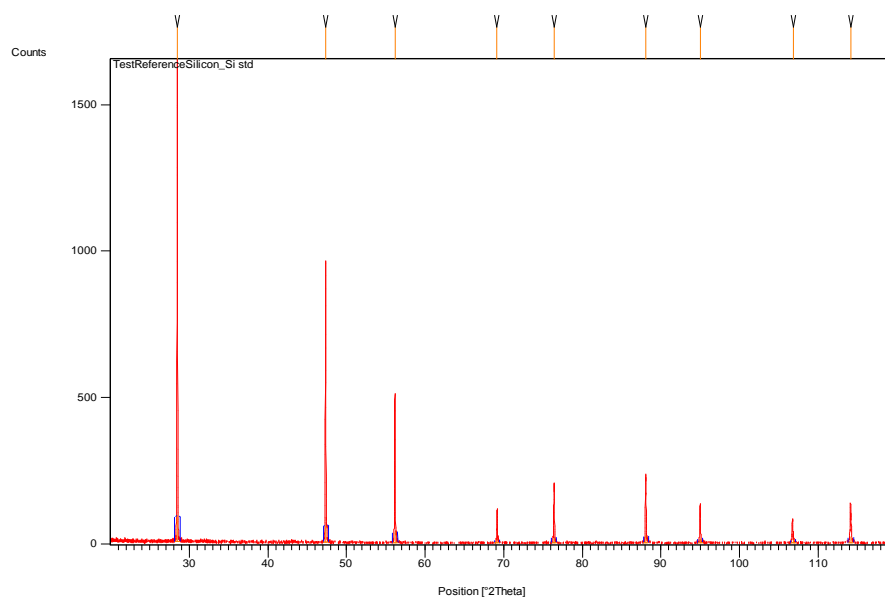
APPENDIX 4.6

Representation of (a) zinc hydroxide layers in LBZA and (b) EC-12 in ChemDraw 3D.



APPENDIX 4.7

The lattice strain of ZnO along the axes was calculated following Brif and co-workers studies (Brif *et al.*, 2014) in which a high-resolution powder diffraction was used. Our study; however, due to the facilities available, has been carried out using a X-ray diffractometer as described in Section 2.5. Therefore, the wavelength of the X-ray diffractometer was calculated prior the analysis to ensure accurate d-spacing values. The wavelength of the instrument is calculated by analysis of a reference Silicon standard:



(hkl)	Rel. Int %	$2\theta(^{\circ})$	$\theta(^{\circ})$	$\theta(rad)$	$Sin \theta$	n	d -spacing	$\lambda=d*\sin\theta (\text{\AA})$
(111)	100.00	28.473	14.236	0.248	0.246	1	3.132	0.770
(220)	67.60	47.362	23.681	0.413	0.402	2	1.919	0.771
(311)	42.26	56.196	28.098	0.490	0.471	3	1.636	0.770
(400)	13.52	69.155	34.578	0.603	0.568	4	1.357	0.770
(331)	21.08	76.387	38.194	0.667	0.618	5	1.245	0.770
(422)	29.84	88.101	44.050	0.769	0.695	6	1.108	0.770
(333)	16.81	95.010	47.505	0.829	0.737	7	1.045	0.770

The d-spacing values are calculated using Bragg equation: $d = (n \cdot \lambda) / 2 \cdot \sin \theta$, where $n = 1$, $\lambda =$ average of wavelength calculated and $\theta = 15.828^\circ$ and 15.810° ; Blank and EC-12, respectively.

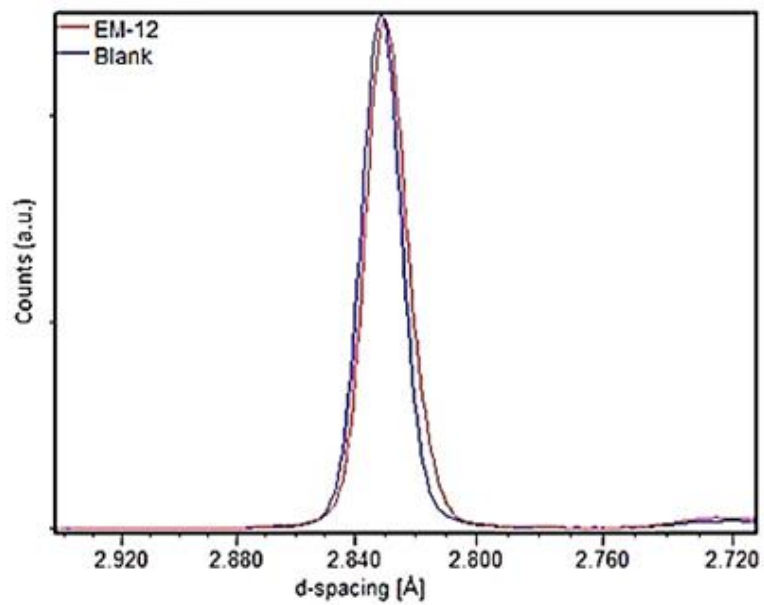
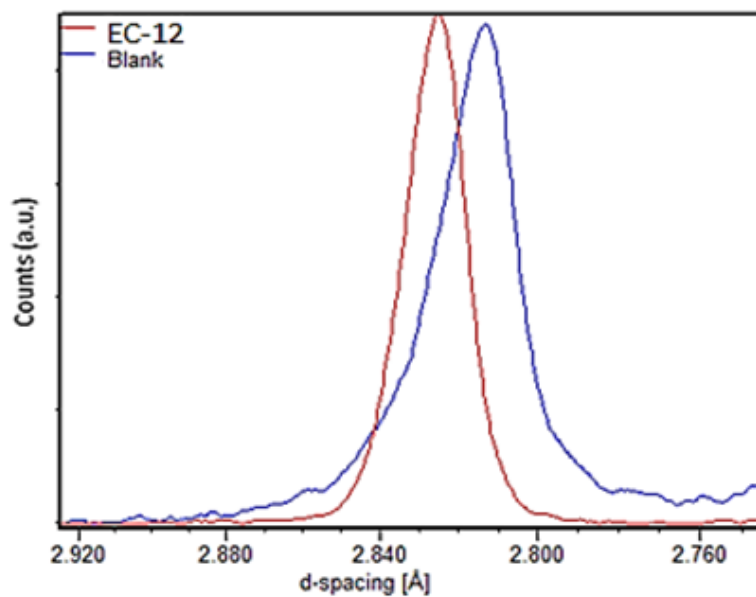
<i>d-spacing</i>	<i>measured</i>	<i>calculated</i>
Blank	2.824	2.823
EC12	2.827	2.826

As an example, the lattice strain of ZnO along the a-axis in the presence of EC-12 was calculated as follows:

$$\frac{d_{Blank} - d_{EC-12}}{d_{Blank}} * 100 = 0.108\%$$

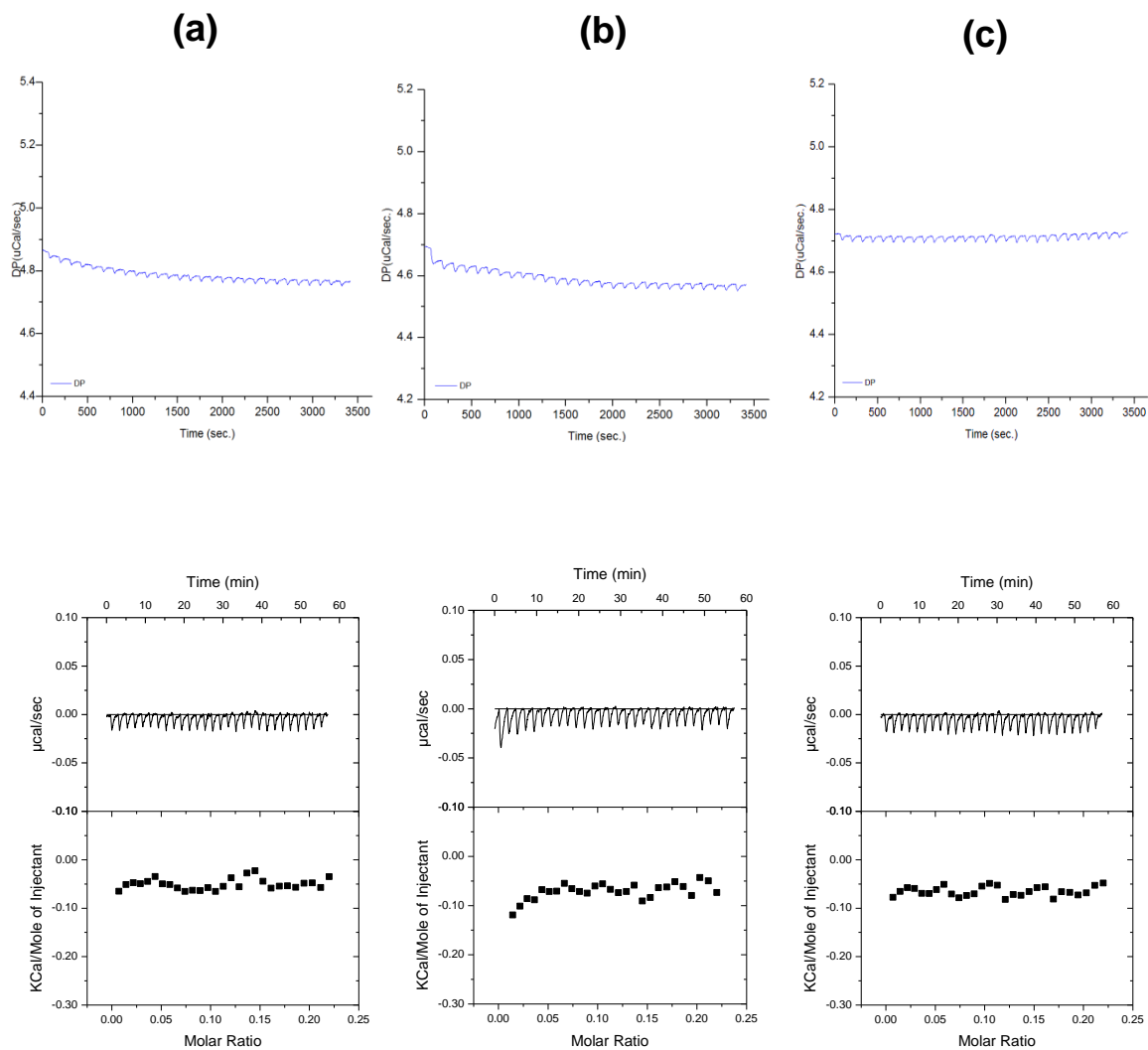
APPENDIX 4.8

Comparison of the lattice strain modification along the (0002) plane (or c-axis) for the peptides EC-12 and EM-12.



APPENDIX 4.9

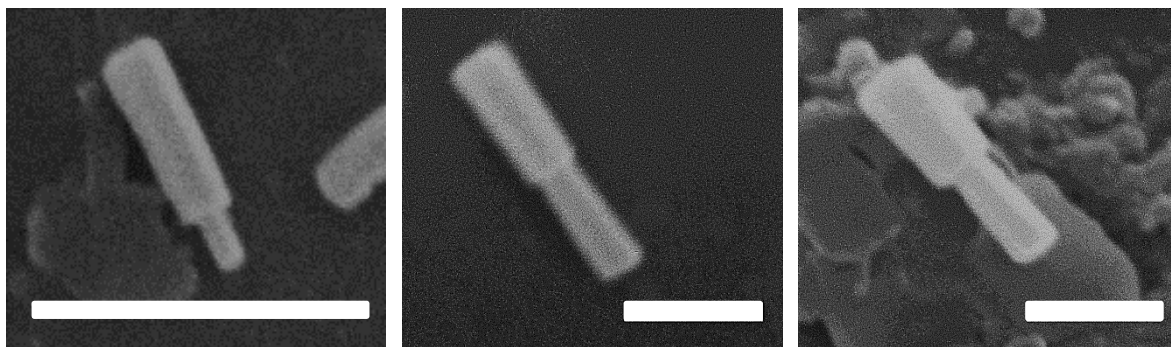
From ITC analysis, isothermal profiles (raw and processed data) of the water-water method obtained prior to (a) ZnO-water method, (b) water-EC12 method and (c) ZnO-EC12 method.



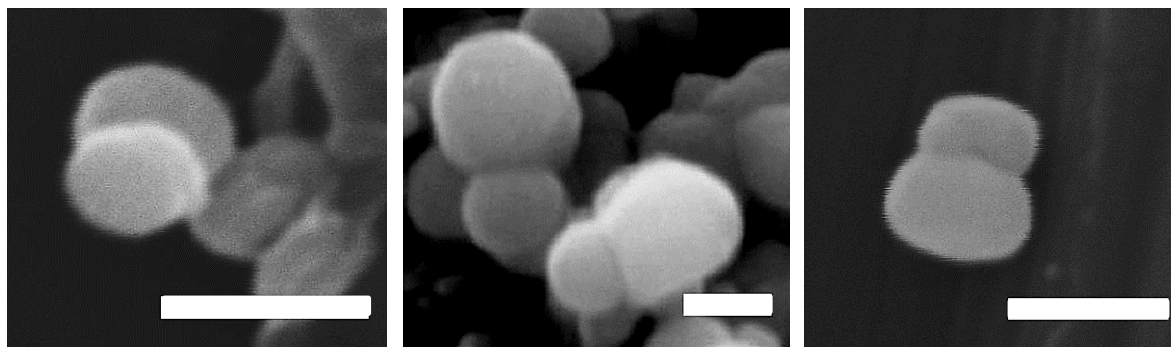
APPENDIX 4.10

SEM images of ZnO crystals in the presence of EM-12 and EC-12, showing twinned crystals with a second rod or sphere, respectively, smaller than the first one. All scale bars are 1 μm

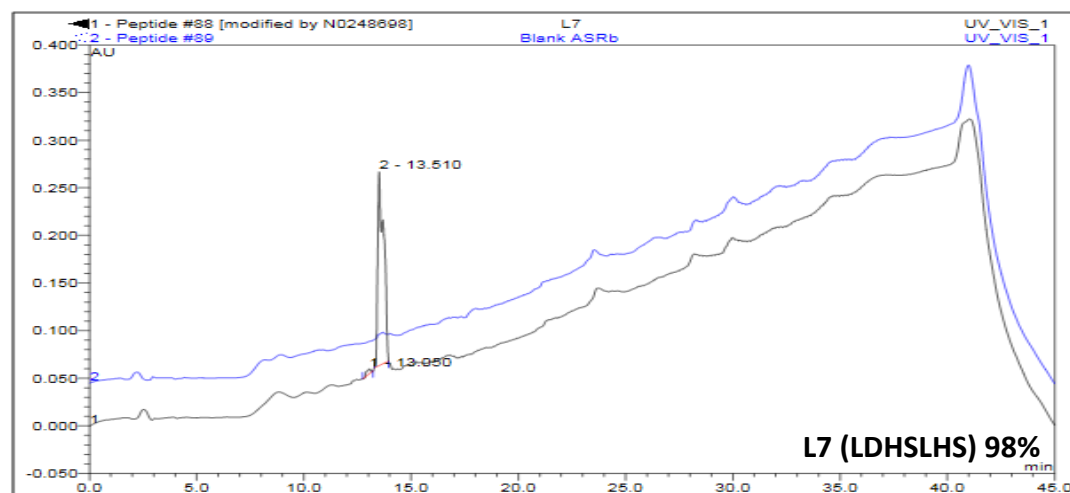
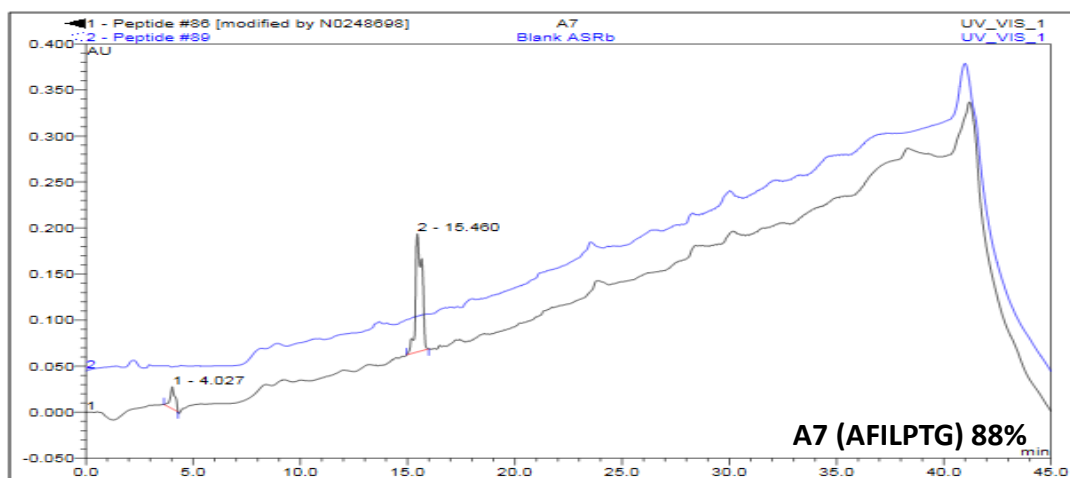
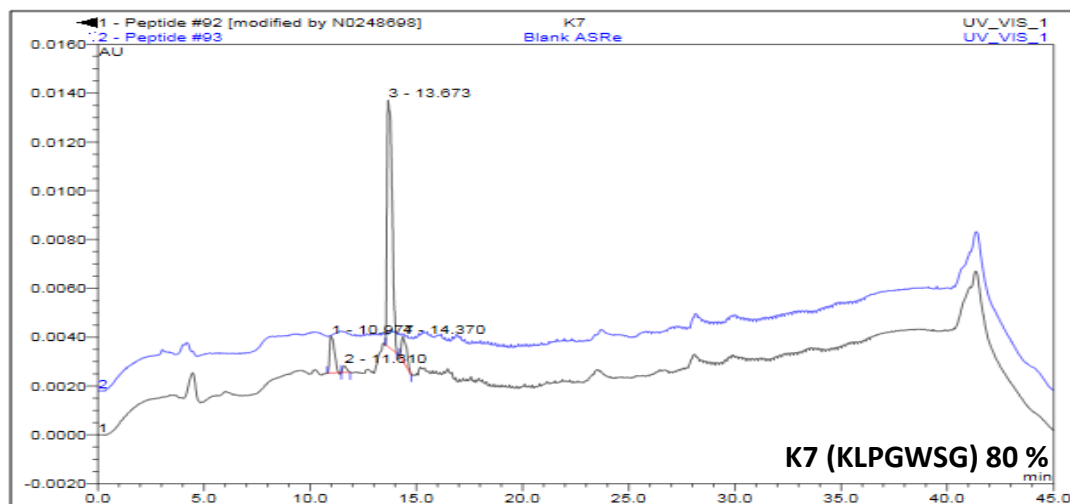
(a) In the presence of EM-12



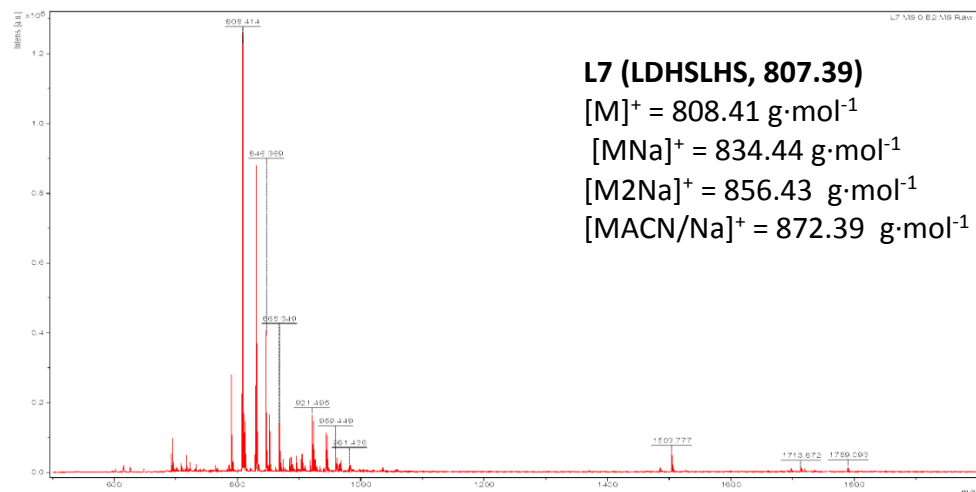
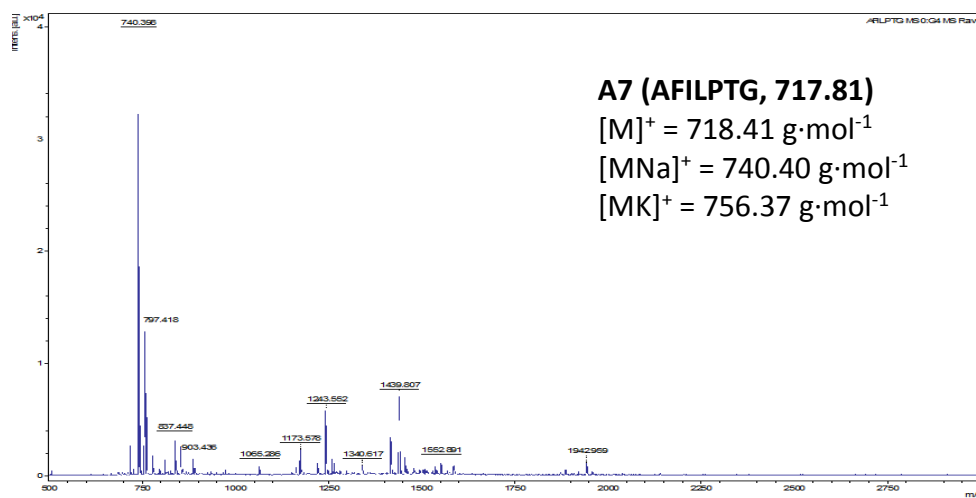
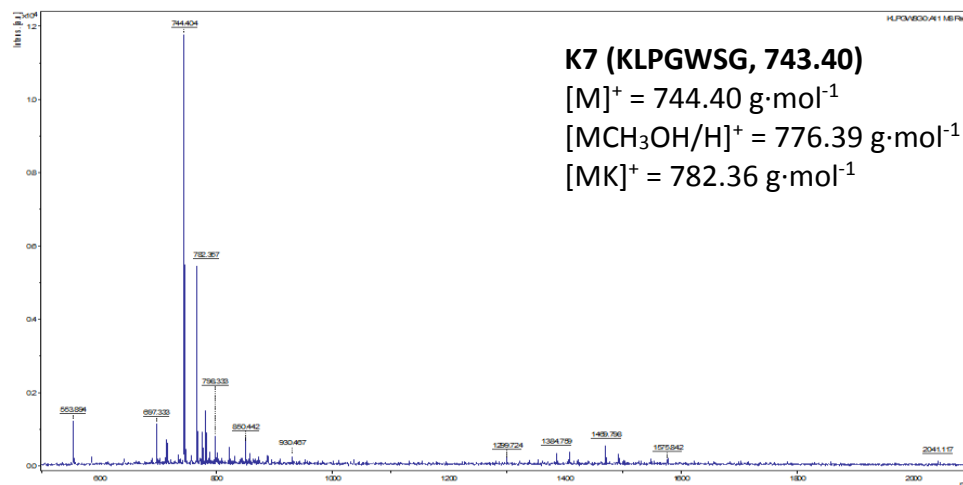
(b) In the presence of EC-12



APPENDIX 5.1

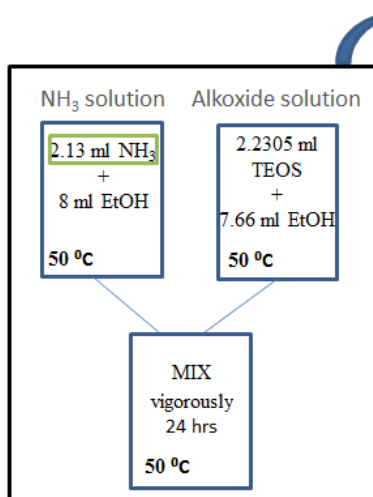
HPLC chromatograms of the synthesized SiO₂-BPs.

APPENDIX 5.2

Mass spectra of the synthesized SiO₂-BPs.

APPENDIX 5.3

Calculations to reach saturation of the functionalized SiO₂ NPs surfaces.



$$2.2305 \text{ ml TEOS} \times \frac{0.933 \text{ g}}{1 \text{ ml}} \times \frac{1 \text{ mol}}{208.33 \text{ g}} = 0.00998 \text{ mols TEOS}$$

$$\text{mols TEOS} = \text{mols MTEOS/APTES}$$

$$[\text{MTEOS/APTES}] = \frac{0.00998 \text{ mols}}{0.02 \text{ l}} = 0.5 \text{ M} \equiv 500 \text{ mM}$$

Concentration in the reaction vessel is $\sim 10 \text{ mM}$ Wu *et al.* method

Volumes to reach saturation (Vt = 20 ml):

(a) MTEOS (98%)

$$0.00998 \text{ mol MTEOS} \times \frac{152.3 \text{ g}}{1 \text{ mol}} \times \frac{1 \text{ ml}}{1.032 \text{ g}} \times \frac{100}{98} = 1.5 \text{ ml}$$

(b) APTES (99%)

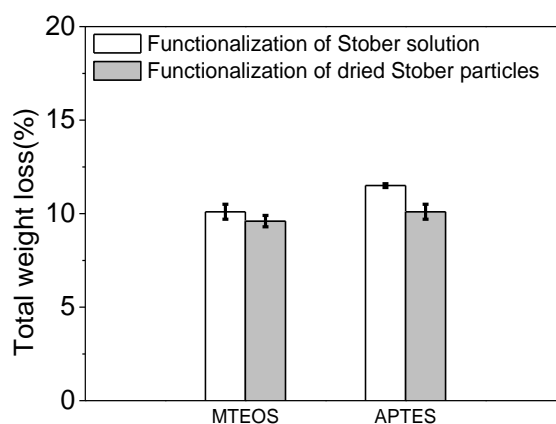
$$0.00998 \text{ mol APTES} \times \frac{221.37 \text{ g}}{1 \text{ mol}} \times \frac{1 \text{ ml}}{0.946 \text{ g}} \times \frac{100}{99} = 2.35 \text{ ml}$$

APPENDIX 5.4

Comparison study of functionalization when MTEOS or APTES is added to:

- (1) The collected Stöber solution (80% EtOH + NH₃) (pH = 11.1 ± 0.1).
- (2) The dried Stöber silica particles re-dispersed into a 80% EtOH solution (pH = 8.0 ± 0.3).

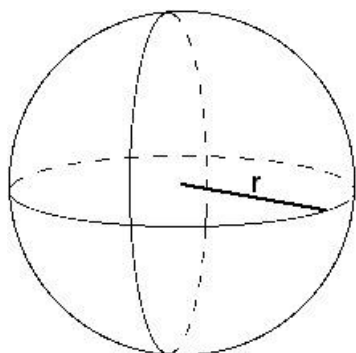
From TGA data, it was observed lower values of total % of weight loss where observed when the functionalization was performed following method 2. This can be explained as the nature of the species in solution highly depends on the working pH conditions. The pK_a of APTES is 10.8, thus, at pH ~ 8 amino groups will be positive charged and at pH ~11 only the 50% of the amine functions will be protonated (Mittal 2007). The presence of more charged amine moieties may induce self-condensation of the aminoalkoxysilanes, thus lower grafting of silica surface is achieved. Additionally the silanol groups of the particles and hydrolysed functionalization reagent will carry more negative charge at higher pH and this is known to favour the anionic reaction mechanism proposed for the condensation reaction. Besides this, same trends of functionalization were achieved for the methyl- and amino-silanes. As Karmakar silica particles were not included in this study until the very end and the Stöber silica particles were already functionalized and mostly characterized and, further, functionalization trends observed were alike between both methods, it was thought suitable to functionalize the Karmakar silica particles following the second method above described.



Mittal, K. L., Silanes and Other Coupling Agents, Volume 4.

APPENDIX 5.5

Theoretical surface area:



$$A = 4\pi r^2$$

$$V = \frac{4}{3}\pi r^3$$

Mass SiO_2 = Volume * density
 SSA = area * mass SiO_2

SiO₂-28 nm:

$$A = 2.5 \cdot 10^{-15} \text{ m}^2, V = 1.2 \cdot 10^{-21} \text{ L} \rightarrow SSA = 97.403 \text{ m}^2 \cdot \text{g}^{-1}$$

SiO₂-210 nm:

$$A = 1.4 \cdot 10^{-13} \text{ m}^2, V = 4.9 \cdot 10^{-18} \text{ L} \rightarrow SSA = 12.987 \text{ m}^2 \cdot \text{g}^{-1}$$

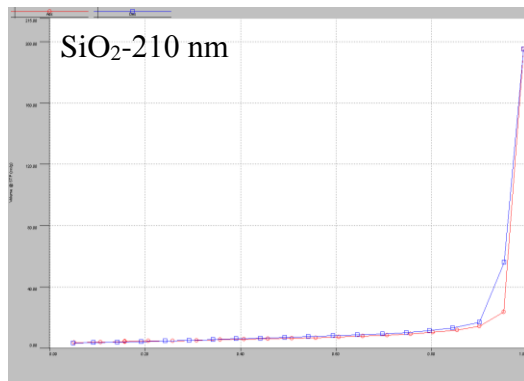
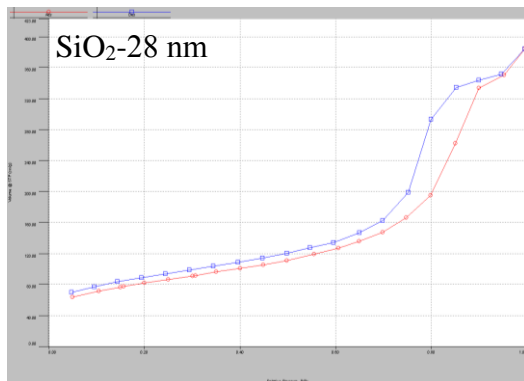
SiO₂-40 μm:

$$A = 5.0 \cdot 10^{-9} \text{ m}^2, V = 3.4 \cdot 10^{-11} \text{ L} \rightarrow SSA = 0.0682 \text{ m}^2 \cdot \text{g}^{-1}$$

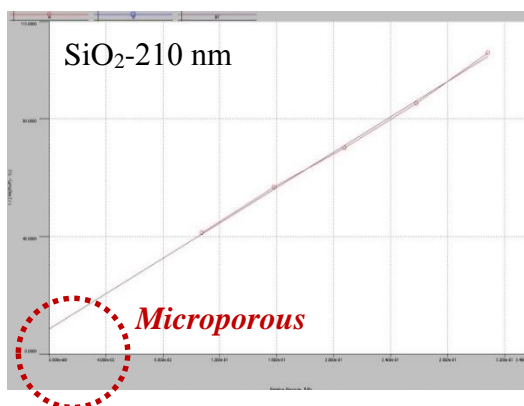
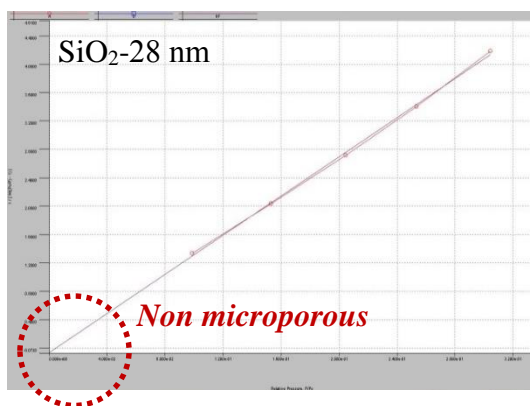
APPENDIX 5.6

From gas adsorption analysis (a) N₂ sorption-desorption isotherms, (b) BET and (c) BJH graphs for 28 nm and 210 nm SiO₂ NPs.

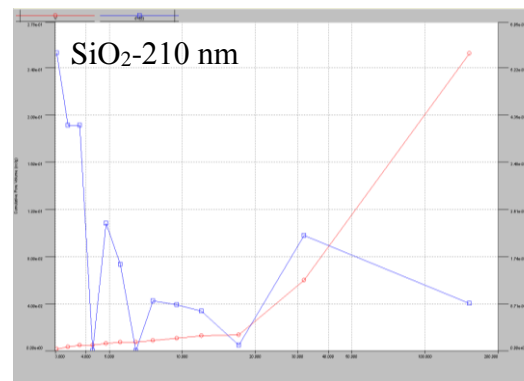
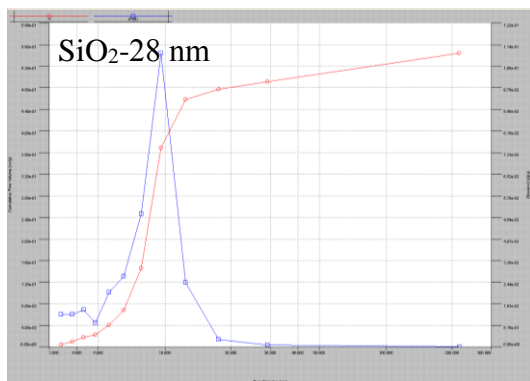
(a) Isotherm



(b) BET



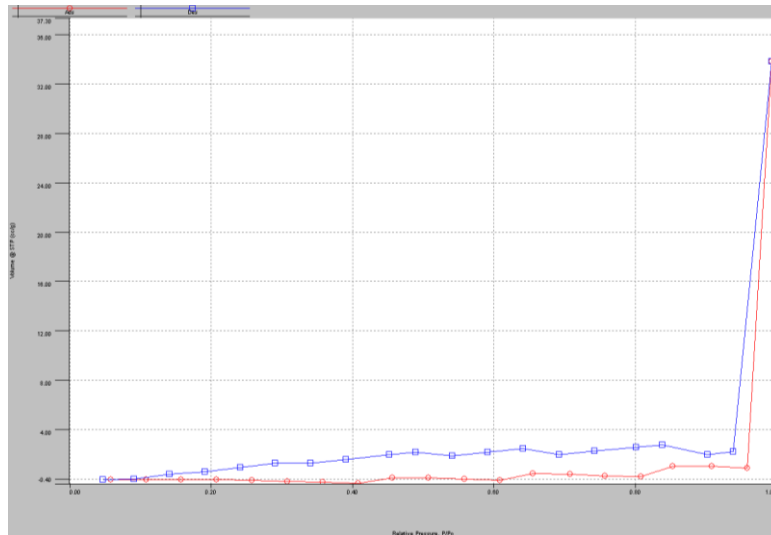
(c) BJH



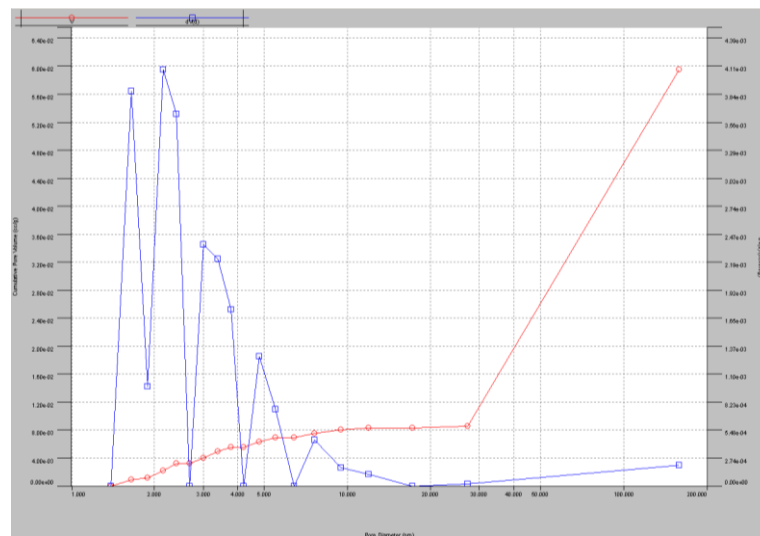
APPENDIX 5.7

From gas adsorption analysis (a) N_2 sorption-desorption isotherm and (b) BJH graph for 40 μm SiO_2 particles (Karmakar). Particles were found to be non-porous with only significant levels of nitrogen being adsorbed at high P/P_0 (liquid infill of inter-particle space).

(a) Isotherm

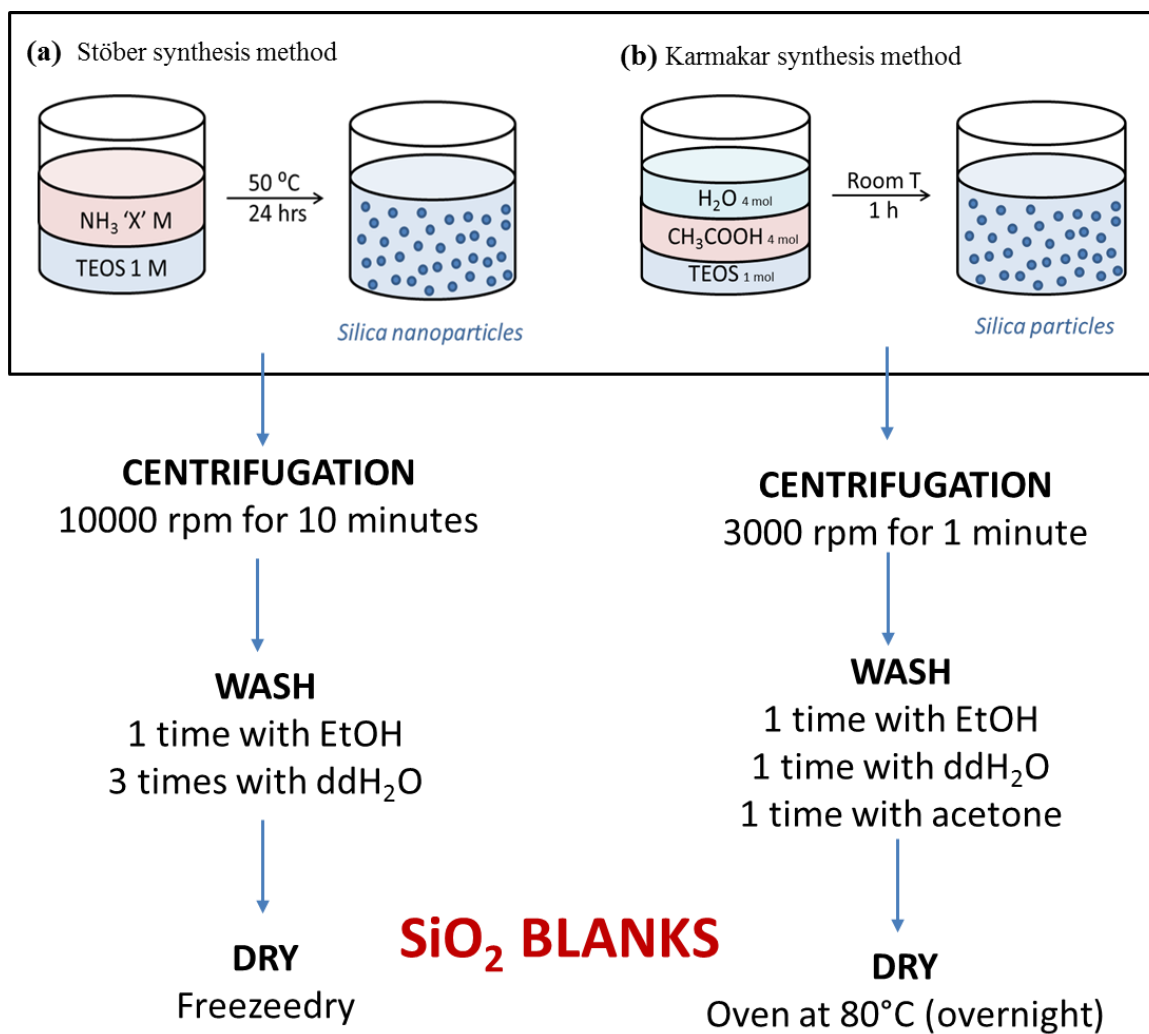


(b) BJH



APPENDIX 5.8

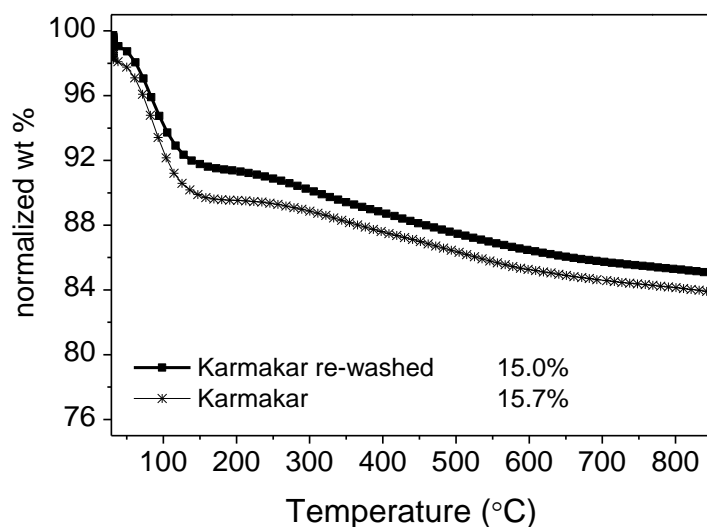
Methodology followed for isolation of silica particles (powder) after synthesis.



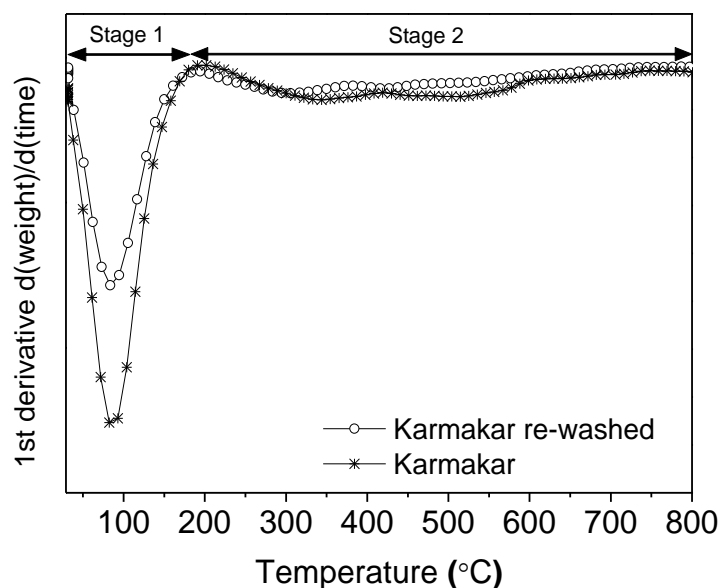
APPENDIX 5.9

TGA analysis for Karmakar silica particles obtained after applying Kamakar method and obtained after applying the same washing procedure as Stöber particles (see Appendix 5.8). Therefore, Karmakar washed involves extra washing with EtOH (1 time) and ddH₂O water (3 times) as well as freeze-drying of the sample.

(a) **Normalized TGA curve:** shows less % of total wt loss of the sample being washed

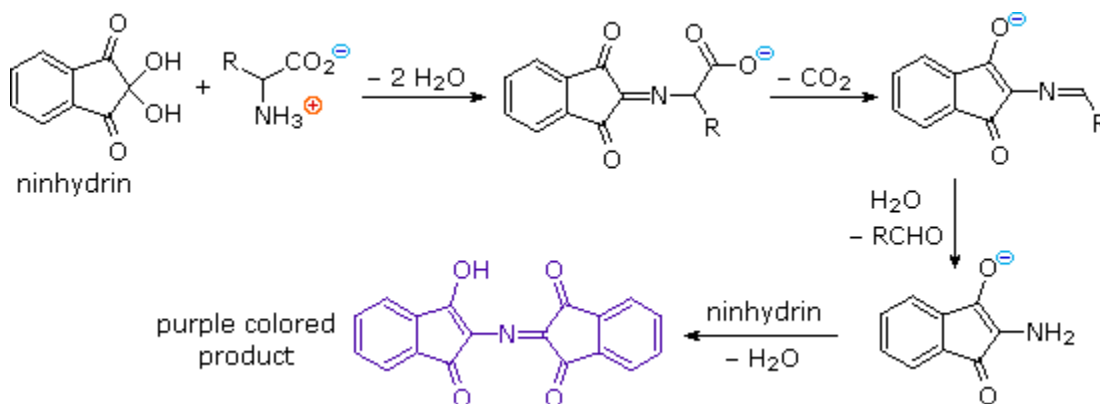


(b) **Normalized DTG curve:** shows the main difference of wt loss is in Stage 1 (water content)



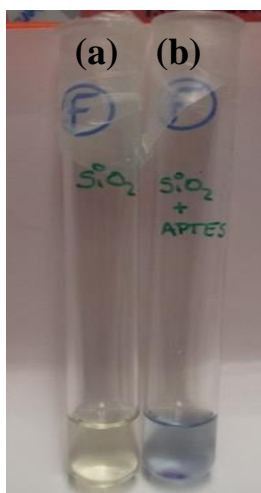
APPENDIX 5.10

Ninhydrin test is commonly used to identify the presence of amino acids in samples. In the pH range of 4-8, all α - amino acids react with ninhydrin (triketohydrindene hydrate), a powerful oxidizing agent to give a purple colored product (diketohydrin) termed Rhuemann's purple. All primary amines and ammonia react similarly but without the liberation of carbon dioxide.



Note: initial Ninhydrin solution is yellow coloured.

Figure below shows the solution after the Ninhydrin solution was added to the silica particles (a) non-functionalized and (b) functionalized with APTES:



APPENDIX 5.11

The % of total weight loss from TGA analysis for the blanks and functionalized silica particles are shown in the table below.

<i>% Total wt loss</i>	<i>Blank</i>	<i>10 mM MTEOS</i>	<i>500 mM MTEOS</i>	<i>10 mM</i>	<i>500 mM APTES</i>
SiO ₂ -28 nm	7.7 ± 1.1	9.4 ± 1.9	10.3 ± 0.8	8.8 ± 1.5	29.4 ± 1.9
SiO ₂ -210 nm	10.0 ± 1.8	10.0 ± 1.7	11.3 ± 2.4	10.6 ± 1.0	11.9 ± 0.3
SiO ₂ -40 μm	15.2 ± 0.4	12.3 ± 1.0	13.1 ± 1.5	13.1 ± 1.5	13.3 ± 1.2

The % of weight loss in Stage 2 from TGA analysis for the blanks and functionalized silica particles are shown in the table below.

<i>% wt loss</i>	<i>Blank</i>	<i>10 mM MTEOS</i>	<i>500 mM MTEOS</i>	<i>10 mM</i>	<i>500 mM APTES</i>
<i>Stage 2</i>				<i>APTES</i>	
SiO ₂ -28 nm	4.7 ± 0.3	5.5 ± 0.8	6.5 ± 0.2	6.4 ± 1.7	24.7 ± 4.8
SiO ₂ -210 nm	6.4 ± 0.6	6.7 ± 0.9	7.6 ± 0.8	7.7 ± 0.5	9.3 ± 2.1
SiO ₂ -40 μm	6.5 ± 0.2	7.3 ± 0.5	7.7 ± 0.6	7.6 ± 0.7	7.2 ± 0.8

APPENDIX 5.12

Atomic % of Si, O, C and N for the non-functionalized and functionalized samples employing different [MTEOS] or [APTES]

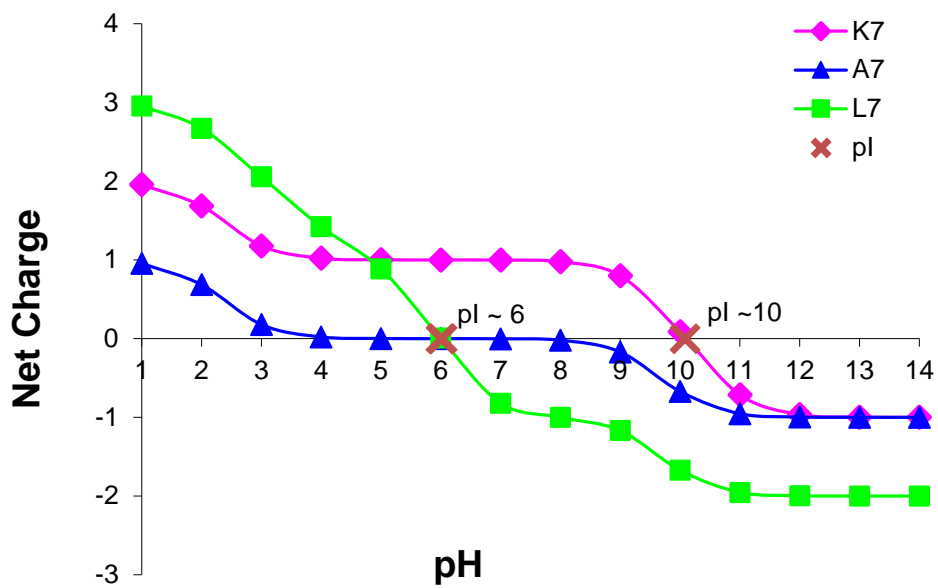
	C 1s	O 1s	Si 2p	N 1s
SiO₂-28 nm	0.90%	65.10%	34.00%	---
10 mM MTEOS	3.60%	62.50%	33.90%	---
500 mM MTEOS	5.20%	60.20%	34.50%	---
10 mM APTES	29.80%	38.60%	23.70%	7.80%
500 mM APTES	32.50%	37.80%	22.00%	7.60%

	C 1s	O 1s	Si 2p	N 1s
SiO₂-210 nm	0.60%	63.40%	36.00%	---
10 mM MTEOS	6.10%	59.10%	33.30%	---
500 mM MTEOS	10.30%	56.50%	33.20%	---
2.5 mM	14.70%	53.60%	30.00%	1.70%
10 mM APTES	11.70%	55.30%	30.70%	2.40%
100 mM APTES	15.10%	53.00%	29.70%	2.30%
500 mM APTES	11.30%	53.60%	31.70%	3.40%

	C 1s	O 1s	Si 2p	N 1s
SiO₂-40 μm	22.50%	50.10%	27.40%	---
SiO₂-40 μm re- washed	25.10%	53.90%	21.00%	---
10 mM MTEOS	11.70%	58.20%	30.00%	---
500 mM MTEOS	15.30%	55.90%	28.80%	---
10 mM APTES	15.90%	54.70%	28.40%	1.00%
500 mM APTES	21.10%	47.90%	29.70%	1.40%

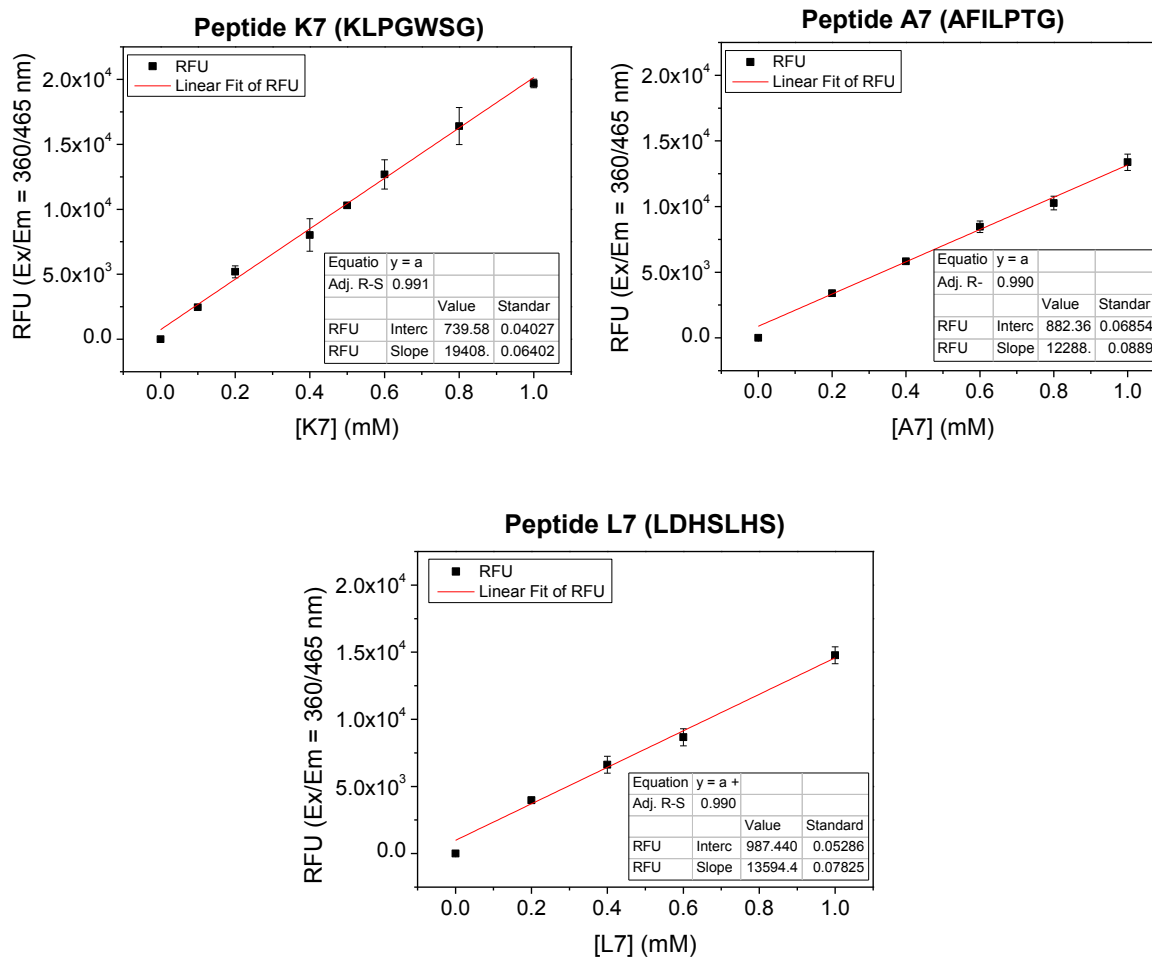
APPENDIX 5.13

Theoretical change in net charge versus pH for KLPGWSG (K7), AFILPTG (A7) and LDHSHS (L7).



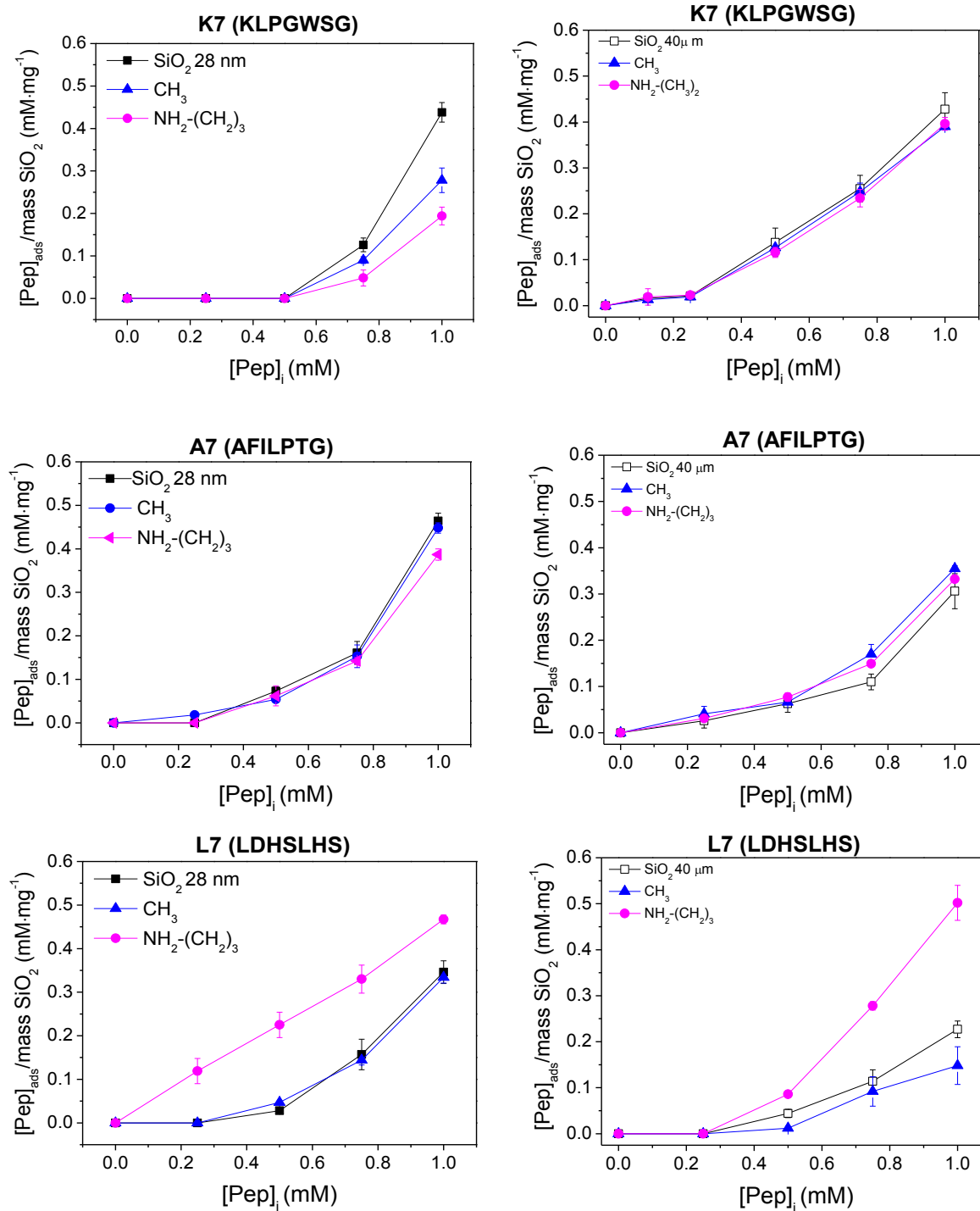
APPENDIX 5.14

Calibration curves for the peptides K7, A7 and L7 obtained when non-functionalized surfaces experiments were performed. Note that, a calibration curve was plotted for each batch of experiments performed, and due to the magnitude of experiments carried out (over 50 samples for each silica surface chemistry and for each peptide), the calibration curves shown below are an example of type of curves obtained in which final results were extracted when $R^2 > 0.98$.



APPENDIX 5.15

Comparison study between amino- and methyl-functionalized surfaces for 28 nm and 40 μm SiO_2 particles.



GLOSSARY

1D	One dimensional
aa	Amino acid
ACN	Acetonitrile
ΔG	Change in Gibbs free energy (ΔG_s for surface and ΔG_v for volume)
ΔH	Change in enthalpy
ΔS	Change in entropy
APTES	3-aminopropyltriethoxysilane
ATR	Attenuated total reflectance
a.u.	Arbitrary units
BE (or E_B)	Binding energy
BET	Brunauer-Emmett-Teller (method for surface area measurements)
BPs	Binding peptides
BJH	Barret, Joyner and Halenda (method for total pore volume measurements)
BSE	Back-scattered electrons
°C	Celsius (temperature)
-CH ₃	Methyl groups
DCM	Dichloromethane
ddH ₂ O	Distilled deionised water
DIPEA	N,N'-Diisopropylethylamine
DLS	Dynamics light scattering
DMF	N,N-dimethylformamide
DNA	Deoxyribonucleic acid
DOTD	3,6-Dioxa-1,8-octanedithiol
DP	Differential Power
DTG (curve)	1 st derivative of sample weight loss versus temperature °C

EDX	Energy dispersive X-ray analysis
EM-12	EAHVMHKVAPRP (peptide sequence)
EC-12	EAHVCHKVAPRP (peptide sequence)
eV	Electronvolt
FWHM	Half width of the maximum intensity
FTIR-KBr	Fourier transform infrared spectroscopy- Potassium bromide
G-12	GLHVMHKVAPPR (peptide sequence)
GT-16	GLHVMHKVAPPR-GGGC (peptide sequence)
h	Hours
HCl	Hydrochloric acid
HMTA	Hexamethylenetetramine
HPLC	High Performance Liquid Chromatography
Hz	Hertz (frequency)
ICP-OES	Inductively coupled plasma-optical emission spectrometry
ITC	Isothermal titration calorimetry
J	Joules
K _B	Binding constant
Kcal	Kilocalories
KE	Kinetic energy
KeV	Kiloelectron volt
K _D	Dissociation constant (for desorption)
KV	Kilovolt
L/D	Length/Diameter (=aspect ratio)
LBZA	Layered basic zinc acetate
LBZAC	Layered basic zinc acetate carbonate
LBZN	Layered basic zinc nitrate
LBZs	Layered basic zinc structures
M13	Phage coat protein

MALDI-TOF MS Matrix-assisted laser desorption ionization time-of-flight mass spectrometry

min	Minutes
mM	Millimolar
Mw	Molecular weight
m/z	Mass to charge ratio
NH ₃	Ammonia
-NH ₂	Amino groups
nm	Nanometers
NMP	N-methyl-2-pyrrolidinone
NPs	Nanoparticles
N ₂	Nitrogen
PD	Phage display
PE	Pass energy
Pep1	KSLSRHDHIIHHH (Peptide sequence)
pI	Isoelectric point
PP	Polypropylene
ppm	Parts per milion
P/P_0	Relative Pressure
QCM	Quartz crystal microbalance
R ²	Correlation coefficient
R5	SSKKSGSYSGSKGSKRRIL(peptide sequence)
s	Seconds
SEM	Scanning electron microscope
SDAs	Structure directing agents
Si4-1	MSPHPHPRHHHT (Peptide sequence)
Si1-1A ₁	Silaffin (silica-associated biomolecule)
SiO ₂	Silicon oxide (silica)
Si(OH) ₄	Silicon hydroxide

Si-OH	Silanols
SiO ₂ -BPs	Silica binding peptides
SiO ₂ -NPs	Silica nanoparticles
SiNPs	Synthetic amorphous silica nanoparticles
SPPS	Solid phase peptide synthesis
TEM	Transmission electron microscope
TFA	Trifluoroacetic acid
TGA	Thermogravimetric analysis
TEOS	Tetraethoxysilane
XPS	X-ray photoelectron spectroscopy
Zn ²⁺	Zinc ions
ZnAc ₂	Zinc acetate or Zn(CH ₃ COO) ₂
ZnO	Zinc oxide
ZnO-BPs	ZnO binding peptides
μl	Microliters
μm	Micrometers

Publications

Liang, M. K.;[‡] Limo, M. J.;[‡] Sola-Rabada, A.;[‡] Roe, M. J.; Perry, C. C. New insights into the mechanism of ZnO formation from aqueous solutions of zinc acetate and zinc nitrate. *Chem. Mater.* **2014**, *26*, 4119-4129. ([‡]Authors contributed to this paper equally)

Sola-Rabada, A.; Liang, M.; Roe, M. J.; Perry, C. C. Peptide-directed crystal growth modification in the formation of ZnO. *Journal of Materials Chemistry B* **2015**, *3*, 3777-3788.

Sola-Rabada, A.; Rinck, J.; Belton, D. J.; Powell, A. K.; Perry, C. C. Isolation of a wide range of minerals from a thermally treated plant: *Equisetum arvense*, a Mare's Tale. *J. Biol. Inorg. Chem.* **2016**. (Accepted 08 Dec 2015, DOI: 10.1007/s00775-015-1320-0)

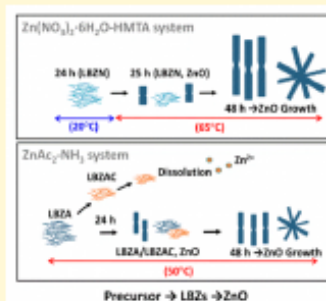
New Insights into the Mechanism of ZnO Formation from Aqueous Solutions of Zinc Acetate and Zinc Nitrate

Mei-Keat Liang,[‡] Marion J. Lim,[‡] Anna Sola-Rabada,[‡] Martin J. Roe,[†] and Carole C. Perry*[‡]

Biomolecular and Materials Interface Research Group, Interdisciplinary Biomedical Research Centre, School of Science and Technology, Nottingham Trent University, Clifton Lane, Nottingham NG11 8NS, U.K.

Supporting Information

ABSTRACT: The controlled synthesis of ZnO at the micro- and nanoscale has been the focus of significant research due to its importance in electrical and optoelectronic applications, and the potential of tuning its properties at the crystal formation stage. We present a detailed study of ZnO growth processes which supports and consolidates previous findings and gives a clearer understanding of the mechanism of ZnO formation. The influence of synthesis conditions on ZnO formation was investigated by comparison of two different growth routes ($\text{Zn}(\text{CH}_3\text{COO})_2\text{-NH}_3$ and $\text{Zn}(\text{NO}_3)_2\cdot 6\text{H}_2\text{O-HMTA}$) both known to result in the formation of wurtzite structured, twinned hexagonal rods of ZnO. The identities of the solid phases formed and supernatants were confirmed by data from SEM, XRD, FTIR, XPS, TGA, and ICP-OES analysis; giving insight into the involvement of multistep pathways. In both cases, reaction takes place via intermediates known as layered basic zinc salts (LBZs) which only later transform to the oxide phase. In the $\text{ZnAc}_2\text{-NH}_3$ system, crystal growth evolves as $\text{Zn}(\text{CH}_3\text{COO})_2 \rightarrow \text{LBZA}$ (A: acetate) $\rightarrow \text{ZnO}$ through a dissolution/precipitation process, with the formation of an additional product identified as LBZAC (C: carbonate). In contrast, in the $\text{Zn}(\text{NO}_3)_2\cdot 6\text{H}_2\text{O-HMTA}$ system, solid-phase transformation occurs as $\text{Zn}(\text{NO}_3)_2\cdot 6\text{H}_2\text{O} \rightarrow \text{LBZN}$ (N: nitrate) $\rightarrow \text{ZnO}$ with no evidence of dissolution. Similar comprehensive studies can be applied to other solid-state processes to further advance functional materials design.



INTRODUCTION

From as early as 1935, studies on characterization of ZnO had begun,^{1–3} however, with improvements in technology to produce ZnO using synthetic processes, the past decade has seen a significant rise in research interest in developing the uses of ZnO especially for its potential electrical and optoelectronic applications.^{1,4–6} Emerging technological and industrial applications include the making of field emitters, varistors, acoustic wave devices, piezoelectric devices, solar cells, photocatalysts, transparent conducting materials, and possibly even chemical/biosensors.^{7–9} Its biocompatible, biodegradable, and antimicrobial nature also encourages further developments for biomedical applications.^{10–12}

As the physical/chemical properties and functions of a given material are dictated by its structure and/or morphology, controlled synthesis of materials at the micro- and nanoscale has been of research interest but is still met by challenges with a rising need for more facile, reproducible, efficient, economic, and environmentally friendly fabrication routes.^{13–16} Solution synthesis methods using alkoxides or simple salts as precursors^{17–20} have become a favored bottom-up synthesis route for metals/metal oxides as they allow for the fine-tuning of growth parameters such as solution composition, chemistry, temperature, reactant concentration, reaction rate, and solubility which are intricately linked and together influence the parameters of crystal growth and hence crystal morphol-

ogy.^{21–24} A wide range of 1D nanometer to micrometer ZnO structures have been formed using solution synthesis methods such as rods, plates, tubes, rings, tetrapods, prisms, pyramids, spheres, hollow structures, flowerlike, and multineedle-shaped crystals.^{18,20,25–30}

The driving force for chemical reactions leading to nucleation and crystal growth from solution is the need to minimize the free energy of the whole system, and the direction of crystal growth is dictated by the surface activities of the growing facets under specific growth conditions.^{23,31,32} Observations from biomineralization studies suggest that nucleation may follow more complex routes than proposed by classical nucleation theory.^{33,34} Crystallization could proceed through a multistep pathway involving structural and compositional transformation of amorphous precursors which subsequently crystallize, forming intermediates that are transformed to give the final crystalline structure.^{33–36} The progress of phase transformation usually occurs through dissolution and renucleation processes in a phenomenon referred to as Ostwald's Law of phases which depends on the free energy of activation and the solubility of the intermediates.^{33,37–39} Ultimately, the resulting crystal morphology is thought to be governed by contributions from

Received: March 27, 2014

Revised: June 20, 2014



Cite this: DOI: 10.1039/c5tb00253b

Peptide-directed crystal growth modification in the formation of ZnO†

Anna Sola-Rabada,^a Mei-Keat Liang,^a Martin J. Roe^b and Carole C. Perry^{a*}

Biomolecule-mediated synthesis is fascinating in terms of the level of control and the intricate hierarchical structures of the materials that can be produced. In this study we compare the behavior of a phage display identified peptide, EAHVMHKVAPRP (EM-12) with that of a mutant peptide EAHVCHKVAPRP (EC-12), having additional complexation capability, on the formation of ZnO from solution. The synthesis conditions ($\text{Zn}(\text{CH}_3\text{COO})_2\text{-NH}_3$ hydrothermal method at 50 °C) were chosen to generate rod-shaped ZnO via layered basic zinc salts (LBZs) as intermediates. Both peptides affected the crystal formation process by moderating the amount of Zn^{2+} ions in solution (EC12 having a greater effect than EM12) but only EC12 was shown to interact with the solid phase(s) formed during the reaction. Depending on the peptide concentration used, EM-12 was shown to delay and/or suppress ZnO formation. In contrast, additions of EC-12, although leading to the retention of higher levels of Zn^{2+} ions in solution did not similarly delay the transformation of the intermediate phases to ZnO but were found to dramatically modify the morphology of ZnO crystallites with mushroom shaped crystals being formed. From the results of detailed materials characterization and changes in the morphology observed, the interactions between the peptide(s) and solution and solid state species present during the process of ZnO crystal formation in the presence of EM-12 and EC-12 are proposed.

Received 4th February 2015,
Accepted 2nd April 2015

DOI: 10.1039/c5tb00253b

www.rsc.org/MaterialsB

Introduction

The identification of biomineral-associated biomolecules has shed light on how biominerals are formed in living organisms. This has also led to the use of the bioinspired/biomimetic approach for materials synthesis,^{1–4} even for non-biologically produced minerals such as ZnO.⁵ Despite ZnO not being found in living organisms, to date, more than twenty ZnO-binding peptides (ZnO-BPs) have been identified from either cell surface display^{6,7} or phage display libraries.^{8–11} However, only a few peptides such as GLHVMHKVAPRP (G-12),^{12,13} EAHVMHKVAPRP (EM-12)^{9,14}

and derivatives GLHVMHKVAPRP-GGGC (GT-16)^{12,15} and EAHVMHKVAPRP-GGGSC (ET-17)^{9,15} have been studied further. The addition of GT-16 during ZnO synthesis has been shown to reduce the aspect ratio of the ZnO crystals formed.⁸ In order to unravel the cause(s) of aspect ratio reduction by this ZnO-BP, our group conducted some studies using G-12^{12,13} and/or GT-16.¹² The direct evidence obtained suggested that (i) ZnO aspect ratio reduction occurs *via* an adsorption-growth inhibition mechanism, (ii) G-12 adsorbing on both (0001) and (10 $\bar{1}0$) planes of ZnO is sufficient to reduce ZnO aspect ratio (GGGC-tag is not essential); and, (iii) that the GGGC-tag is responsible for the selective adsorption of GT-16 on the (0001) plane of ZnO crystals. Also, the addition of G-12 in different ZnO experimental systems led to a modification of the growth mechanisms.¹³ Studies by others have shown that the addition of ET-17 into stable Zn(OH)₂ sols catalyzes ZnO formation, directing a flower-type anisotropic crystal growth.⁹ The catalytic effect of ET-17 is generated either by the presence of the EM-12 segment or GGGC-tag.⁹ The catalytic effect of ET-17 was further confirmed as ET-17 attached to a genetically modified-collagen template was able to generate ZnO nanowires.¹⁶ A study proposed to understand the interactions taking place between the ZnO surface and EM-12 showed that conformational changes as well as charged amino acids and residues adjacent to the charged aminoacids are critical to the binding to ZnO.¹⁷ It was concluded that the electrostatic interaction between ZnO particles and

^a Biomolecular and Materials Interface Research Group, Interdisciplinary Biomedical Research Centre, School of Science and Technology, Nottingham Trent University, Clifton Lane, Nottingham, NG11 9NS, UK. E-mail: Carole.Perry@ntu.ac.uk

^b Advanced Materials Research Group, X-ray Photoelectron Spectroscopy, Faculty of Engineering, The University of Nottingham, University Park, Nottingham, NG7 2RD, UK

† Electronic supplementary information (ESI) available: XPS analysis for the study of the ubiquitous carbonaceous contamination, and XPS data including the relative ratio of Zn/O and BE (eV) for O 1s, C 1s and Zn 2p_{3/2} for samples analyzed; calibration curves used for peptide quantification in solution; calculated pK_a of peptide side chains using Marvin calculator; Zn²⁺ in solution for EC-12-added reactions; XRD and TGA results for 24 hour-precipitates produced in the presence of EC-12; dimension analysis of ZnO crystals obtained from EM-12-added reactions (48 hours); lattice strain modification for ZnO planes in the presence of EC-12; and mass spectra for peptides. See DOI: 10.1039/c5tb00253b



Isolation of a wide range of minerals from a thermally treated plant: *Equisetum arvense*, a Mare's tale

Anna Sola-Rabada¹ · Julia Rinck^{2,3} · David J. Belton¹ · Annie K. Powell² · Carole C. Perry¹

Received: 4 November 2015 / Accepted: 8 December 2015
© The Author(s) 2016. This article is published with open access at Springerlink.com

Abstract Silica is the second most abundant biomineral being exceeded in nature only by biogenic CaCO₃. Many land plants (such as rice, cereals, cucumber, etc.) deposit silica in significant amounts to reinforce their tissues and as a systematic response to pathogen attack. One of the most ancient species of living vascular plants, *Equisetum arvense* is also able to take up and accumulate silica in all parts of the plant. Numerous methods have been developed for elimination of the organic material and/or metal ions present in plant material to isolate biogenic silica. However, depending on the chemical and/or physical treatment applied to branch or stem from *Equisetum arvense*; other mineral forms such glass-type materials (i.e. CaSiO₃), salts (i.e. KCl) or luminescent materials can also be isolated from the plant material. In the current contribution, we show the chemical and/or thermal routes that lead to the

formation of a number of different mineral types in addition to biogenic silica.

Keywords Silica · *Equisetum arvense* · Wollastonite · Calcium sulphide · Vitrification

Introduction

Silica is one of the most common materials in nature and is the second most common biogenic mineral after carbonates [1], and it is deposited in living organisms, including animals, plants and diatoms [2]. Horsetail (*Equisetum* spp.) is classified as one of the most ancient species of living vascular plants [3]. A remarkable characteristic of *Equisetum* species is their ability to take up and accumulate silica in their tissues giving the epidermis a rough texture [4]. Back in the 1980s, Williams and co-workers were one of the first groups to characterize the nature of silica in biological systems by using transmission electron microscopy, FTIR and NMR spectroscopy [5]. This natural silica, often referred to as biogenic silica, is present in the form of amorphous silica [5, 6] and for some plants seems to be an essential mineral for growth [7]. The ability of plants to produce biogenic silica with a wide range of morphologies under mild physiological conditions is of great interest to scientists (and industry); as it gives the material exceptional properties, such as ordered hierarchical porous structures applicable for catalysis [8], biosensing [9] and biomedical applications [9]. Further, plants and other biological organisms (i.e. sponges or diatoms) produce silica in amounts of gigatons per annum, whereas industrial processes only produce mere megatons. Biogenic silica in plants is present together with the organic matrix, including polymers (i.e. cellulose), proteins, other carbohydrates, lipids, metal ions (such

This article is a contribution to the current volume in memory of Professor R. J. P. Williams, FRS, the DPhil advisor of CCP and arose from research initiated whilst CCP was Gast professor at the Institute of Inorganic Chemistry, Karlsruhe Institute for Technology (KIT), Germany in 2012.

Electronic supplementary material The online version of this article (doi:10.1007/s00775-015-1320-0) contains supplementary material, which is available to authorized users.

✉ Carole C. Perry
carole.perry@ntu.ac.uk

¹ Interdisciplinary Biomedical Research Centre, Nottingham Trent University, Clifton Lane, Nottingham NG11 8NS, UK

² Karlsruhe Institute of Technology, Institute of Inorganic Chemistry, Engesserstrasse 15, 76131 Karlsruhe, Germany

³ Karlsruhe Institute of Technology DFG-Center for Functional Nanostructures (CFN), Wolfgang-Gaede-Straße 1a, 76131 Karlsruhe, Germany